(21)

National Library of Canada
Bibliothèque nationale du Canada

Ottawa, Canada
K1A 0N4

TC - 66154

ISBN 0-315-18245-8

CANADIAN THESES ON MICROFICHE SERVICE – SERVICE DES THESES CANADIENNES SUR MICROFICHE

PERMISION TO MICROFILM – AUTORISATION DE MICROFILMER

- Please print or type – Écrire en lettres moulées ou dactylographier

AUTHOR – AUTEUR

Full Name of Author – Nom complet de l'auteur: Hani Sabri Mitri

Date of Birth – Date de naissance: August 4, 1953

Canadian Citizen – Citoyen canadien: ☐ Yes Oui ☒ No Non

Country of Birth – Lieu de naissance: United Arab Republic

Permanent Address – Résidence fixe:
16 Giza Street,
Giza, United Arab Republic.

THESIS – THÈSE

Title of Thesis – Titre de la thèse: Separated Double Chord RHS Joints

Degree for which thesis was presented / Grade pour lequel cette thèse fut présentée: Ph.D.

Year this degree conferred / Année d'obtention de ce grade: 1985

University – Université: McMaster

Name of Supervisor – Nom du directeur de thèse:
Dr. R.M. Korol
Dr. F.A. Mirza

AUTHORIZATION – AUTORISATION

Permission is hereby granted to the NATIONAL LIBRARY OF CANADA to **microfilm** this thesis and to **lend** or **sell copies of the film.**

The author reserves other publication rights, and neither the thesis nor extensive extracts from it may be printed or otherwise reproduced without the author's written permission.

L'autorisation est, par la présente, accordée à la BIBLIOTHÈQUE NATIONALE DU CANADA de **microfilmer** cette thèse et de **prêter** ou de **vendre des exemplaires du film.**

L'auteur se réserve les autres droits de publication; ni la thèse ni de longs extraits de celle-ci ne doivent être imprimés ou autrement reproduits sans l'autorisation écrite de l'auteur.

ATTACH FORM TO THESIS – VEUILLEZ JOINDRE CE FORMULAIRE À LA THÈSE

Signature

Date: December 7, 1984.

NL 91 (r. 84/03)

Canada

Separated Double Chord RHS Joints

by

Hani Sabri Mitri, B.Sc., M. Eng.

A Thesis
Submitted to the School of Graduate Studies
in Partial Fulfilment of the Requirements
for the Degree
Doctor of Philosophy

McMaster University

© December 1984

Separated Double Chord RHS Joints

To My Dear Wife

MIRANDA

DOCTOR OF PHILOSOPHY (1984)
(Civil Engineering and Engineering Mechanics)

McMASTER UNIVERSITY
Hamilton, Ontario

TITLE: Separated Double Chord RHS Joints

AUTHOR: Hani Sabri Mitri, B.Sc. (Cairo University)
M.Eng. (McMaster University)

SUPERVISORS: Dr. R.M. Korol and Dr. F.A. Mirza

NUMBER OF PAGES: xxii, 231

ABSTRACT

The central focus of research undertaken concerned the strength and behaviour of separated double chord rectangular hollow section (RHS) K-joints. Peripherally, the concept of the twin member shear beam is introduced as a simple and inexpensive bridging device for revealing the intrinsic structural properties of such joints.

The finite element method has been used to investigate the stiffness characteristics of the separated joint. The RHS chord member is idealized by a thin plate representing the inner web and a channel representing the top and bottom flanges and the outer web. The stiffening effect offered by the channel is incorporated through its condensation into a boundary stiffness matrix to be added to the inner web stiffness matrix.

The proposed finite element formulation includes rectangular plate elements in the inner web plate and a variety of beam elements in the channel forming a grillage. The formulation considers both bending and in-plane actions. Material nonlinearities of the joint are assumed to be adequately represented by the Von Mises yield criterion and the associated plastic flow rule. While geometric nonlinearities have been excluded, this was deemed reasonable for the range of displacements considered in this study.

To verify the finite element model, a number of experiments were conducted on twin shear beams with the objective of making definitive statements about the joint performance to be anticipated for the finite element model. Twenty-four specimens were tested in the Applied Dynamics Laboratory of McMaster University. Test results showed a definite improvement in structural performance for both increased depth and a decrease in the gap.

From experimental results, a local deflection limit criterion was suggested to define a range of permissible displacements in double chord joints. Such a criterion was based upon that presented in the literature for single chord joints.

A verification of the finite element model was made using the experimental data of the twin shear beams and it exhibited good correlation. A model sensitivity analysis was then carried out with the objective of furthering understanding of the behaviour of such structural components.

The model was extended to the general model called EPAC-RHS (Elasto-Plastic Analysis of RHS Connections). In the process of this extension, triangular plane stress-plate bending elements were introduced to accommodate an arbitrary joint assembly of K and N configuration. In addition, member preloads were accounted for in EPAC-RHS.

Theoretical results of simulated K-joint models were compared

with experimental data of K-joints obtained from the literature. While strength predictions were somewhat conservative, very good agreement of elastic response was observed for all tests.

A yield line theory was developed for which two strength models, trapezoidal and conical were proposed. Their predicted strengths were compared with experimental loads at the limiting deflection suggested. Good agreement with the tests was found particularly for the trapezoidal model. The twin shear beam models were then extended to be applicable to K-joints by taking into account both the reduction in strength due to chord axial preload and the horizontal component of the diagonal force. Theoretical results were compared with previous experiments on K-joints and exhibited reasonable correlation.

ACKNOWLEDGEMENTS

I would like to express my sincere appreciation to my research supervisors, Dr. R.M. Korol and Dr. F.A. Mirza, for their invaluable guidance, utmost interest and dashing encouragement throughout the course of this study. It has been a privilege and a pleasure to work under their supervision.

I am very grateful to the other members of my supervisory committee, Dr. G.A. Oravas, Dr. J. Duncan and Dr. J.A. Packer for their valuable comments and suggestions.

This research investigation was made possible by funding from the Natural Sciences and Engineering Research Council and the Canadian Steel Construction Council. My personal involvement with the study would not have been possible without the financial support of McMaster University for which I am most thankful. The provision of hollow structural sections for the experimental work by the Steel Company of Canada, is gratefully acknowledged.

I would also like to express special thanks to David Perrett for his cooperation during the testing programme undertaken at the Applied Dynamics Laboratory and to express my appreciation for the assistance offered by the staff of Academic Computing Services during the develop-

ment of the computer models.

The remarkable speed and accuracy in typing the manuscript is due to the staff in the Burke Science Word Processing Centre, to whom I am indebted.

Finally, I would like to thank my parents for their continuing support and encouragement to pursue graduate studies.

This work is dedicated to my lovely wife, Miranda, in recognition of the sacrifices she has made during the period of this study.

TABLE OF CONTENTS

PAGE

ABSTRACT iv

ACKNOWLEDGEMENTS vii

TABLE OF CONTENTS ix

LIST OF FIGURES xiv

LIST OF TABLES xviii

LIST OF SYMBOLS xix

CHAPTER 1 INTRODUCTION 1

1.1 Hollow Structural Sections 1

1.2 Double Chord Systems 2

1.3 Literature Review 3

1.4 Study Problem 7

1.5 Scope and Objectives 8

CHAPTER 2 EXPERIMENTAL PROGRAM ON SEPARATED TWIN MEMBER SHEAR BEAMS 14

2.1 Introduction 14

2.2 Description of Experimental Procedure 15

PAGE

2.2.1 Parameters Considered 15
2.2.2 Connection Detail 15
2.2.3 Specimen Data 15
2.2.4 Measuring Devices 16
2.2.5 Loading 17
2.2.6 Material Properties 17
2.3 Test Results 17
2.4 Effect of Chord Aspect Ratio 19
2.5 Influence of Gap Distance 20
2.6 Deflection Limit-Criterion 21
CHAPTER 3 STRENGTH ANALYSIS 36
3.1 Introduction 36
3.2 Trapezoidal Mechanism 38
3.3 Conical Mechanism 43
3.4 Comparison with Twin Shear Beam Experiments 47
3.5 Application to K-joints 49
3.5.1 Basic Modifications to Beam Models 49
3.5.2 Trapezoidal Mechanism Model 52
3.5.3 Conical Mechanism Model 53
3.6 Comparison of K-Joint Results with Tests 54

TABLE OF CONTENTS (cont'd) PAGE

3.7 Variation of Parameters 55

3.8 Discussion 56

CHAPTER 4 FINITE ELEMENT MODEL FOR RHS TWIN MEMBER SHEAR BEAM 75

4.1 Introduction 75

4.2 Modelling of RHS Joints-Historical Review 76

4.3 Basic Finite Element Model 78

4.4 Inner Web Plate-Discretization and Boundary Conditions 82

4.5 Top Flange, Bottom Flange and Outer Web 83

4.6 Modelling of Material Properties 84

CHAPTER 5 FINITE ELEMENT FORMULATION AND NONLINEAR ANALYSIS 96

5.1 Equilibrium Equation 96

5.2 Finite Element Formulation 98

5.2.1 Inner Web Plate 98

5.2.2 Top and Bottom Flanges and Outer Web 103

5.3 Analysis of the Channel Frame 107

5.3.1 Feasible Strategies 107

5.3.2 Uncoupled Model 108

TABLE OF CONTENTS (cont'd) PAGE

5.3.3 Coupled Model 112

5.4 Plasticity Relations for Elasto-Plastic Analysis 116

5.4.1 Introduction 116

5.4.2 Elasto-Plastic Compliance Matrix 117

5.5 Nonlinear Finite Element Analysis 122

5.5.1 Newton-Raphson Method 122

5.5.2 Algorithm for Computer Model 124

CHAPTER 6 MODEL VERIFICATION AND SENSITIVITY ANALYSIS 137

6.1 Introduction 137

6.2 Comparison Between Uncoupled and Coupled Finite Element Twin Shear Beam Models 138

6.3 Verification 140

6.4 Sensitivity Analysis 145

CHAPTER 7 EXTENSION OF TWIN BEAM FINITE ELEMENT MODEL TO SEPARATED DOUBLE CHORD JOINTS 179

7.1 Introduction 179

7.2 Special Considerations 181

7.3 Triangular Plate Element 182

7.4 Chord/Web Member Preloads 189

TABLE OF CONTENTS (cont'd)

PAGE

7.5 Solution Technique for Nonlinear Analysis 191
7.6 Comparison with Previous Experiments on K-Joints 193
7.7 Discussion 195

CHAPTER 8 CONCLUSION 212

8.1 Summary and Conclusions 212
8.2 Suggestions for Future Research 216

APPENDIX A 219

A.1 Shape Functions for the Rectangular Plate Bending Element 219
A.2 Shape Functions for the Rectangular Plane Stress Element 220
A.3 Shape Functions for the Boundary Spring Element 220

APPENDIX B 223

B.1 Shape Functions for the Triangular Plate Bending Element (Ref. 34) 223
B.2 Transformation Between Bending Slopes and Triangular Element Nodal Displacements (Ref. 41) 224
B.3 Matrix $[\overline{B}]$ of Triangular Plate Bending Element (Ref. 42) 225

BIBLIOGRAPHY 228

LIST OF FIGURES

PAGE

1.1 RHS Double Chord K-Joints 11

1.2 K-Joint Specimens Tested Previously (Ref. 2) 12

1.3 RHS Twin Shear Beam 13

2.1 Nominal Dimensions of RHS Twin Shear Beam 25

2.2 Weldment Locations 26

2.3 Gauge Locations 27

2.4 Load-Central Displacement Curves 30

2.5 Typical Shear Beam Specimens 31

2.6 Load-Shear Strain Relationships 34

2.7 Influence of Gap Distance on Outer Web Shearing Efficiency 35

3.1 Trapezoidal Mechanism Model for Double Shear Beam 60

3.2 Hodograph 61

3.3 Lower Limit Failure Mechanism 62

3.4 Upper Limit Failure Mechanism 63

3.5 Conical Mechanism Model for Double Shear Beam 65

3.6 Various Conical Mechanisms 66

3.7 Comparison of Experimental and Analytical Shear Beam Loads — Trapezoidal Mechanism 67

3.8 Comparison of Experimental and Analytical Shear Beam Loads — Conical Mechanism 68

3.9 Form of Stress Lines Developed in a K-Joint 69

LIST OF FIGURES (cont'd) PAGE

3.10 Correlation Between Trapezoidal Model and Test Results of K-Joints 70

3.11 Correlation Between Conical Model and Test Results of K-Joints 71

3.12 Variation of Parameters for RHS Double Chord K-Joints — Conical Mechanism Model 73

3.13 Interaction Between K-Joint Strength and its Chord Preload 74

3.14 Effect of Web-to-Chord Member Angle 74

4.1 Various Models of RHS T-Joints 88

4.2 Modelling of Twin Shear Beam 89

4.3 Idealization of Inner Web Plate and Overlapping Branch Members 90

4.4 Grid for a and b Type of Twin Beam Specimens 91

4.5 Grid for c and d Type of Twin Beam Specimens 92

4.6 Channel Grillage of Beam Elements 93

4.7 Beam Elements Employed in the Channel Grillage 94

4.8 Discretization of C-frame into Beam-Column Elements 95

4.9 Typical Distribution of Beam Elements in $\tilde{z}$ Direction 95

5.1 Rectangular Plate Element 131

5.2 Beam Element 131

5.3 Channel Grillage with Notation for Uncoupled Analysis 132

5.4 Boundary Spring Element 133

LIST OF FIGURES (cont'd)

PAGE

5.5 Channel Node Numbering for Coupled Model - First Method 134
5.6 Channel Node Numbering for Coupled Model - Second Method 135
5.7 Newton-Raphson Iterative Method 136
6.1 Comparison of Performance Between Uncoupled and Coupled Models 154
6.2 Data and Results of Test 2V 155
6.3 Data and Results of Test 3V 156
6.4 Typical Inner Web Plate Grid for Verification and Sensitivity Analysis 157
6.5 Comparison of Experimental and Theoretical P-_ curves - Shallow Beams 161
6.6 Comparison of Experimental and Theoretical P-_ curves - Square Beams 165
6.7 Comparison of Experimental and Theoretical P-_ curves - Deep Beams 169
6.8 Correlation Between Experimental and Theoretical Elastic Stiffness 170
6.9 Correlation Between Experimental and Theoretical Deflection Limit Loads 171
6.10 Variation of Chord Member Depth 172
6.11 Variation of Chord Member Width 172
6.12 Variation of Chord Member Thickness 173
6.13 Variation of Gap Distance 173

LIST OF FIGURES (cont'd) PAGE

6.14 Variation of Vertical Member Depth 174

6.15 Variation of Vertical Member Width 174

6.16 Variation of Vertical Member Thickness 175

6.17 Variation of Tangent Modulus 175

6.18 Wider Range of Variation of Vertical Member Depth 176

6.19 Influence of the Weldment Type on the Behaviour of Twin Beam 176

6.20 Stiffening Effect of the Channel Portion of the RHS Chord Member 177

6.21 Progression of Yield Zones in the Inner Web Plate 178

7.1 Longitudinal Section in a Separated Double Chord K-Joint 198

7.2 Idealization of Inner Web Plate and Overlapping Branch Members in a K-Joint 199

7.3 Triangular Plate Element 200

7.4 Finite Element Assemblage for Group 1 K-Joints 201

7.5 Finite Element Assemblage for Group 2 K-Joints 202

7.6 Finite Element Assemblage for Group 3 K-Joints 203

7.7 Comparison of Experiments and EPAC-RHS model for Group 1 K-Joints 204

7.8 Comparison of Experiments and EPAC-RHS model for Group 2 K-Joints 205

7.9 Comparison of Experiments and EPAC-RHS model for Group 3 K-Joints 206

7.10 Effect of K-Joint Eccentricity on its Elasto-Plastic Behaviour 207

7.11 Effect of Chord Axial Preload on the Behaviour of K-Joint 208

LIST OF TABLES

PAGE

2.1 Dimensional and Physical Properties of Twin Shear Beam Specimens 23

2.2 Shear Beam Experimental Results 24

3.1 Twin Shear Beam Experimental and Analytical Results 59

4.1 Material Properties of Twin Beam Specimens 87

6.1 Test Data for Sensitivity Analysis 151

6.2 Additional Test Data for Sensitivity Analysis 152

7.1 Computed Central Deflection of a Square Plate for Several Meshes Using Triangular Plate Bending Elements - 21 Integration Points 196

7.2 Dimensions of Separated Double Chord K-Joints (Ref. 2) 197

LIST OF SYMBOLS

$a, b, t,$	length, width and thickness of plate element
$b, \ \ , t$	width, length and depth of beam element
b_o, h_o, t_o	width, height and wall thickness of single RHS chord member
b_1, h_1, t_1	width, height and wall thickness of single RHS branch member
$2c$	clearance between branch members for K-joint
C_e, C_e^*	experimental and theoretical elastic stiffness
d	truss depth
e_c	eccentricity in a K-joint
E	modulus of elasticity
E_T	tangent modulus
f	nondimensional normal stress
F	yield function
H	chord force transferred from diagonal member
$2\ \ {}_c$	total chord length
j	length of yield line
s	span of truss
w	branch member length
M	computed moment
M_p, M_p'	fully and reduced plastic moments per unit length

LIST OF SYMBOLS (cont'd)

N, N_y	single chord preload and yield forces
P	twin beam or K-joint load
P_{exp}	experimental twin shear beam loads
P_b	theoretical twin shear beam strength
P_d	shear beam deformation limit load
P_{int}	shear beam load by interaction equation
P_{ult}	shear beam ultimate load by test
P_w	theoretical K-joint strength
P_{wd}	K-joint deformation limit load
P_w^o	K-joint deformation limit load at zero chord axial preload
r	ratio of outer to inner web displacements
r_i, r_o	radii defining conical mechanism
R	reduction in shear beam strength
s	gap spacing
u, v	dimensions of loading column (Figure 3.5)
$u_i, v_i, w_i, \Theta_{xi}, \Theta_{yi}$	nodal displacements at point i
V	computed shearing force
$V_p, V_{p'}$	fully and reduced plastic shearing forces
α, β, γ	angles defined in Figures 3.1 and 3.5
ξ, η, z	nondimensional co-ordinates of rectangular element
Δ	relative deflection of inner web plate
Δ_1, Δ_2	inner and outer web displacements

LIST OF SYMBOLS (cont'd)

ψ_i	hinge line rotation
ϕ	hinge line to chord axis angle
Θ	chord to diagonal member angle
γ	web maximum shearing strain
γ_j	web shearing strain
ε_D	percent tolerance based on determinant value
ε_E	tolerance based on energy computation
ε_y	yield normal strain
μ	elastic limit load factor
τ_y	shear yield stress
σ_y	normal yield stress
σ^1	deviatoric stress
$\bar{\sigma}$	effective stress
ν	Poisson's ratio
λ	plastic multiplier
$[A],[\bar{B}]$	matrices for triangular plate bending element
$[B]$	strain matrix
$[D]$	elasticity matrix
$[D_{ep}]$	elasto-plastic compliance matrix
$[K_b]$	boundary element stiffness matrix
$[K_c]$	condensed channel matrix
$[K_{CH}]$	channel global stiffness matrix
$[K^e]$	element stiffness matrix

LIST OF SYMBOLS (cont'd)

$[K_{sp}]$	boundary spring matrix
$[K_T]$	total stiffness matrix
$[K_w]$	inner web stiffness matrix
$[N]$	shape functions matrix
$[T]$	transformation matrix
$\{P\}, \{R\}$	load vectors
$\{\varepsilon\}$	strain vector
$\{\sigma\}$	stress vector
$\{\delta^e\}$	nodal displacement vector
$\{\Psi\}$	residual load vector

CHAPTER 1

INTRODUCTION

1.1 Hollow Structural Sections

The growing popularity of steel rectangular hollow sections (RHS) in structural applications stems from the fact that they possess several advantages over the traditional rolled profile steel sections. In addition to their favoured architectural appearance, they exhibit excellent structural performance due to their high torsional rigidity, high resistance to local buckling and effective bending strength about all axes. Moreover, their cost to develop a specified fire resistance rating and maintenance is less than that of rolled profile sections since the outside perimeter area of a hollow structural section (HSS) is less than the exposed surfaces of an equivalent open section.

At present, HSS have become better accepted by the engineering profession than previously. They have been used successfully in a large number of commercial buildings, industrial plants, recreation and convention centres, pedestrian walkways and overpasses. However, there are two aspects of which HSS construction has suffered in competition with open sections. These relate to size limitation available to the designer and behaviour of member connections. These considerations are the basis for the investigation of which this thesis forms a part.

1.2 Double Chord Systems

The largest sized square RHS produced in Canada is 304.8 × 304.8 × 12.7 mm. If this size were employed in a single chord truss application such as the Warren type, then the clear span would need to be restricted to about the thirty to forty metre range. Some applications, such as long overpasses and recreation centres, necessitate a considerably longer span. This gave rise to the concept of the double chord truss of which there are different arrangements for connecting branch members to the double chord. Basically, a double chord joint is known as separated when the chords are spaced apart (Figure 1.1(a)). Otherwise, the chords are placed back-to-back as shown in Figure 1.1(b). In the former, the diagonals are sandwiched between the chords whereas in the latter they are attached to the flanges. Diagonals of the separated joint type may be directly welded to the inner webs of the chords or to a pair of gusset plates that are welded to the inner webs. The back-to-back type may be stiffened by inserting a sufficiently thick plate onto the top flanges of the chord.

In addition, the type of truss lends itself to joint classification according to:

(a) Single Branch Joints in which a single branch member is connected to the chord such as the T-joint and L-joint of a Vierendeel truss.

(b) Two Branch Joints: Commonly these will be gap joints in which the branch members are mated to the chord and a gap is produced in-between. Such joints are the K and N-joints in Warren and Pratt trusses respectively.

(c) Three Branch Joints: Such joints exist in Pratt trusses where a vertical and two diagonals meet the chord in the middle of a truss.

Double chord systems have certain advantages over single chord systems. While they are applicable to long span structures, their use results in a stiffer structure due to the fact that diagonal forces are transferred to the webs of the double chords, rather than to the flanges of the single chord which are significantly weaker. In addition, double chord systems provide economy in fabrication, particularly the separated type where no special end cuts are necessary for the web members. They also require less lateral bracing because of their high lateral rigidity.

1.3 Literature Review

Since the early 1960's, a considerable amount of research has been conducted on HSS joints. The early efforts focused on testing a large number of isolated joints of T,N and K configuration utilizing single chord RHS members and circular or rectangular HSS web members. Various joint parameters were studied in order to arrive at viable design alternatives and establish some tentative design rules for HSS construction. As will be shown in Section 3.1, the yield line theory was used extensively to assess the capacity of such joints. However, to predict joint deformations, theoretical analyses were first attempted by the finite difference method and subsequently by the finite element method. Such analyses will be reviewed in Section 4.2.

It was not until 1979 that the concept of the double chord was first introduced by Korol and Chidiac (1,2). The following presentation will deal only with the work reported since then on RHS double chord joints and trusses. The initial investigation began by the testing of a total of 29 isolated K-joints comprising four types-standard, channel, bolted and back-to-back. The first three are of a separated chord variety having different web member assemblies while the latter type comprised gapped, overlapped and gapped with stiffening plates. Figure 1.2 shows layouts of the four types tested. It was found that the standard type was particularly attractive because of its relatively low fabrication cost and generally satisfactory structural performance. The channel type appeared to be susceptible to twisting of the chord members and was therefore not recommended as a viable design alternative. The bolted connection was found to be structurally very sound but this was more than offset by its very high fabrication cost. The back-to-back type with a gap did not exhibit adequate strength and stiffness except when the joint was reinforced by a sufficiently thick plate. The fully overlapped joints exhibited good performance at reasonably low cost.

Korol and Chidiac continued their experimental investigation and tested four back-to-back double chord T-joints (3). It was observed that the strength and the stiffness of these joints were improved when the chords were welded together near the joint. Upon comparison with test results of single chord T-joints reported previously by Korol et al. (4), it was concluded that double chord T-joints are more efficient than their equivalent single chord joints. In 1981, Korol and Keen (5) derived two interaction formulae to predict both plastic and ultimate strengths of standard K-joints. The method was based on partitioning the HSS section to resist various stress resultants that were imposed. While good agreement was obtained with test results, it was assumed that inner and outer chord walls were equally effective in shear. Such an assumption was qualified to apply only to square or deep chord joints. No account was taken of localized flange yielding or web distortion, however.

It was then decided to extend the double chord joint work on K-joints to include large scale trusses. A primary objective of the investigation was to ascertain whether the joint test findings would be substantiated in actual truss tests. Chiu (6) tested five simply supported Warren trusses that were one-half to one-third scale of possible long span prototype structures. These included two trusses with back-to-back chords, two standard trusses and one having bolted diagonals attached to gusset plates welded to the inner webs of the chords. It was evident from the test results that the back-to-back as well as the bolted trusses were about 25% stronger than the standard trusses. The separated chord trusses, however, experienced shear failure at the end joints of the top chord. These failures were due to a reduced joint resistance in the gap between the diagonals that sustained the highest axial forces. In all tests, the span to depth ratio (l_s/d) was lower than would be expected in practice (≈ 9.5) for which a joint shear failure is more likely to occur. Korol et al (7) indicated that for longer span applications ($l_s/d \simeq 15$) a member failure could be expected before that of the end joint for separated square RHS chords.

Korol et al. (8,9) developed an elasto-plastic analytical model to predict the strength and behaviour of double chord Warren trusses. Several assumptions were made to simplify the analysis. While local and overall buckling of members were precluded from the analysis, the shearing resistance for gap joints, when they existed, was simulated by a simple elastic-plastic shear spring. Good correlation with experimental results was obtained for the back-to-back truss with overlapped diagonals. The gap joint truss models did not correlate as well, perhaps due to the over-simplistic spring model used for the connections.

Recently, Shehata (10) and Mirza et al. (11) tested ten back-to-back double chord T-joints. The purpose of the experimental program was mainly to obtain more data to verify their finite element model for such joints. Ultimate strength values obtained from a yield line solution and a finite element model were compared with the experimental data and were found to be in very good agreement. The yield line pattern was similar to Mouty's mechanism for single chord T-joints (12) but included shear yielding of the connected webs in the energy dissipation formulation. The finite element model treated the chord face as a thin plate with rectangular subdivisions. Attached to the plate's longitudinal sides was a set of boundary spring elements formulated to simulate the restraining effect that the remainder of the hollow section offers to the chord face plate. Two basic assumptions were made to simplify the analytical model. The area of the top plate inscribed by the branch member was assumed infinitely rigid and, the inner walls of the double chord were assumed to rest on rollers. While the first assumption is almost classical (13,14,15,16,17,18), the second was done to eliminate overall bending of the chord member. Such an assumption, however, may not be valid for two or more branch gap joints. Major shear deformations will normally occur in the crotch between diagonals. Further description of the finite element formulation of the joint model will be made in Section 4.2.

1.4 Study Problem

One of the most popular trusses used in construction is of the Warren type. For long span roof and floor systems, the RHS double chord Warren manifests itself, not only as superior in structural performance but possessing economy as well. However, its use is hampered by a lack of information about the behaviour and capacity of the K-joints which are employed in this structure. A joint may be incapable of withstanding the full compressive and tensile strengths of the branch members if insufficient consideration is taken of the pattern of assembly, the gap distance, the length and location of weldments etc.

As mentioned earlier, Korol and Chidiac (1,2) performed a number of tests on four different types of K-joints. One of their prime conclusions was that the separated type, as well as being economical, held promise both for strength and stiffness requirements. However, their work was limited to square HSS chords; as such the behaviour of joints involving RHS chords remains to be determined. The question of the effectiveness of the top and bottom flanges and the outer webs in carrying the load applied to the diagonals is of prime importance. It has not been known how the gap distance and the chord aspect ratio affect such effectiveness. As was learned from previous tests, a sizable amount of inelastic deformation occurs prior to failure. This, in turn underscores the necessity of investigating joint behaviour beyond the elastic limit.

1.5 Objectives

In conjunction with the results of earlier research, this study will focus on separated double chord gap joints involving square and rectangular HSS chords. One of the principal goals of this study is to assess the shearing resistance of the joint. However, because of the expense and difficulties encountered in testing and fabricating K-joints, it was decided to test a simple, easy-to-fabricate, model that could simulate this shearing action. Such a model is presented in Figure 1.3. All members comprise RHS sections and the method of attachment is either by fillet or bevel groove welding. This specimen, which takes the form of a "twin shear beam", has a major advantage over an isolated K-joint in testing. Such a beam requires only a simple compression testing machine from which load is applied vertically to the upper stub column, as opposed to two hydraulic jacks and an expensive test rig that is needed for a two branch gap joint.

The use of plastic hinge lines for calculating an upper bound load is well known (19). This will be employed in deriving strength expressions for shear beam models and subsequently K and N-truss joints. The results of the shear beam tests will serve to validate the theoretical strength expressions. A variation of parameter study will then be undertaken to determine their influence on the joint bearing capacity. The effect of chord axial forces on the joint capacity will also be investigated.

However, strength is not the only structural property of interest to the design engineer. It is also important to be able to predict the joint stiffness characteristics in and beyond the elastic range. This will be achieved through the formulation of a finite element model that incorporates material nonlinearities. The model will first be formulated for the twin shear beams employing rectangular elements and a grillage of beam elements. Two feasible techniques differing in stiffness analysis of the grillage will be proposed. Comparison with shear beam test results will help identify the more promising one. The twin beam model will then be extended to develop a general computer model "EPAC-RHS", Elasto-Plastic Analysis of RHS Connections, that is applicable to single, two and three branch member double chord joints of the separated type. Special attention will be given to compare two solution methods for selecting the one with a minimum computational effort. Triangular elements will then be included in EPAC-RHS to account for the arbitrary geometry of K and N-joint assemblies. Using the experimental data available on K-joints from previous work (2), validation tests will be performed on EPAC-RHS. Finally, some numerical examples on different joints will be presented to demonstrate the degree to which the model is capable of predicting joint behaviour.

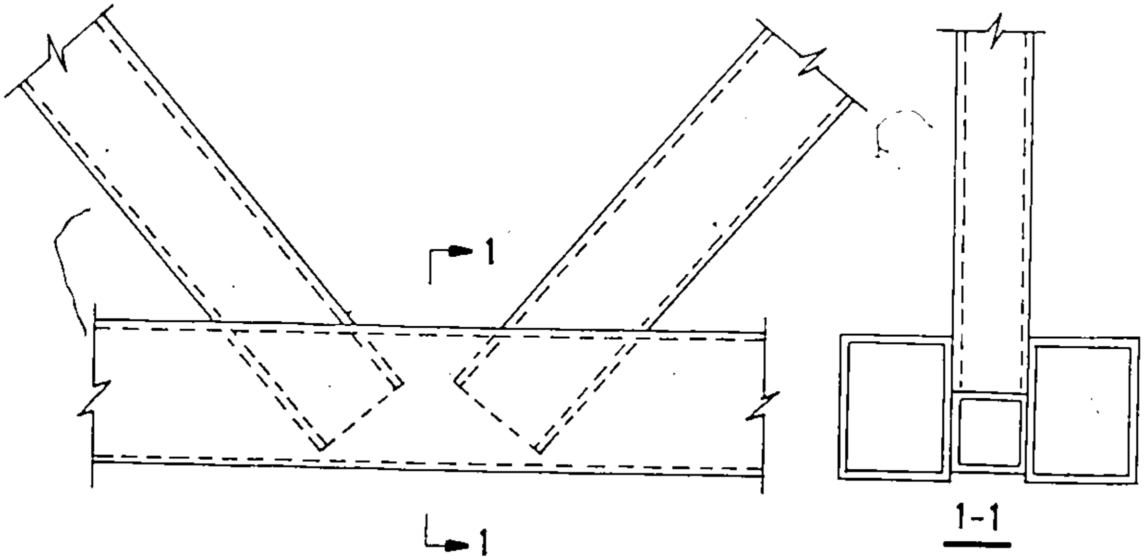

(a) Separated Type

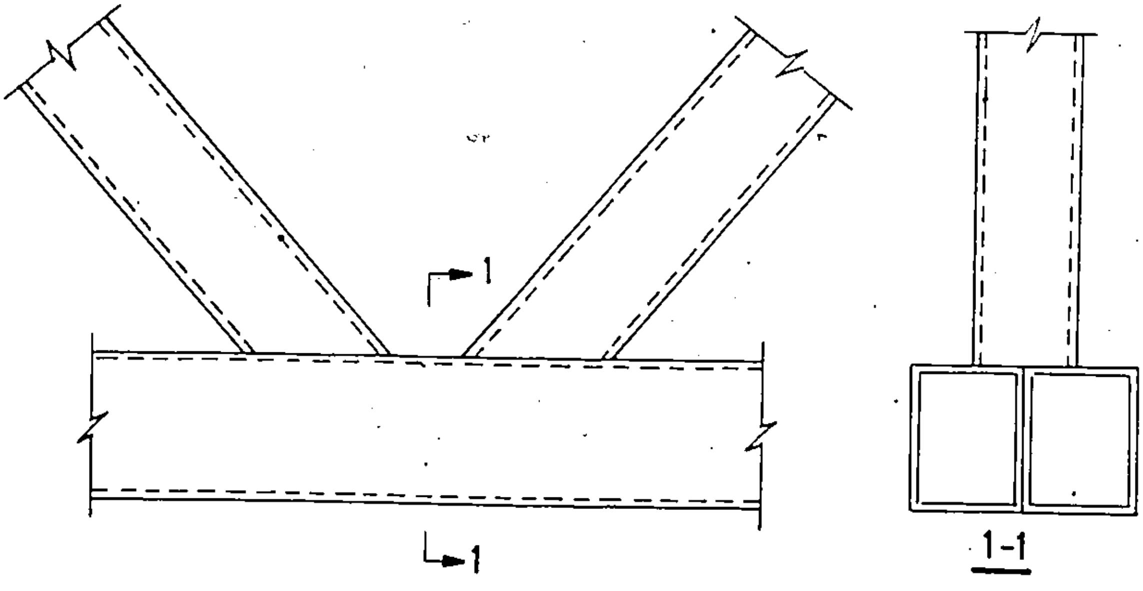

(b) Back-to-Back Type

FIGURE 1.1 : RHS DOUBLE CHORD K-JOINTS

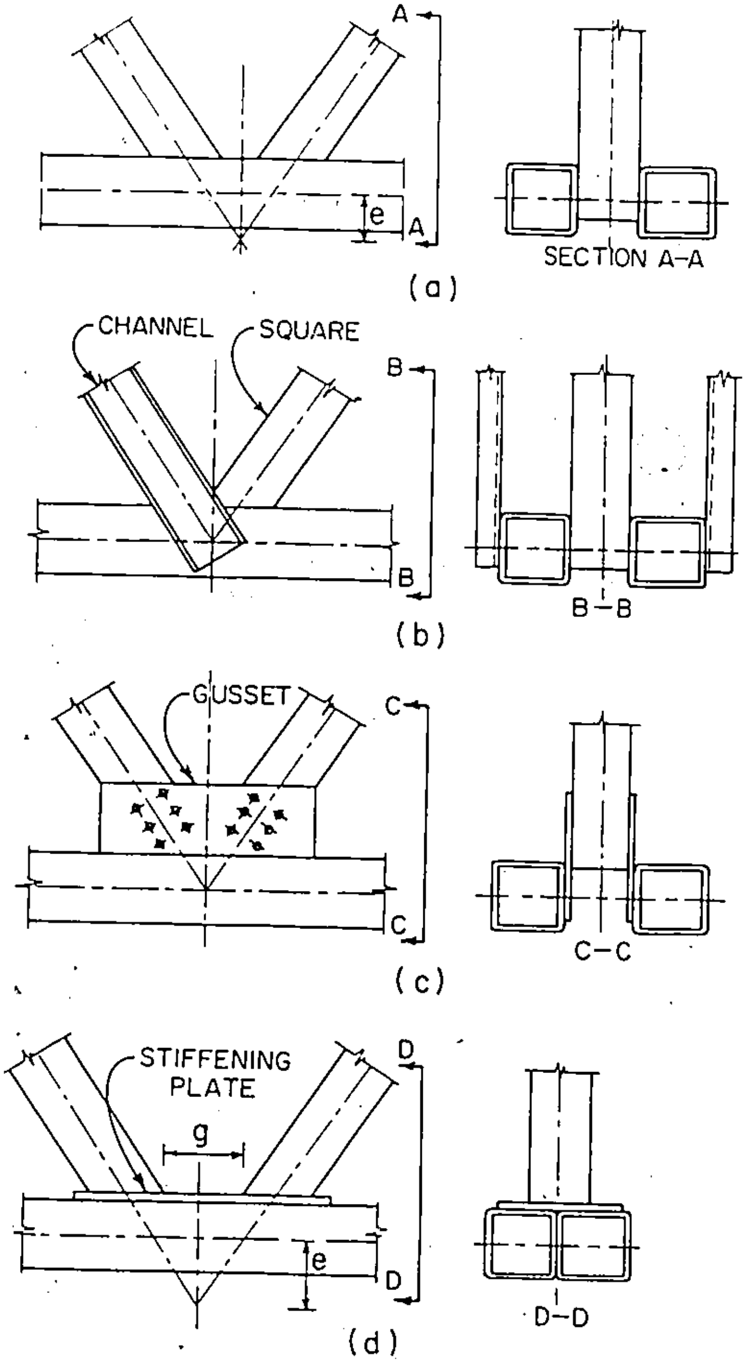
A
e
A
SECTION A-A
(a)
CHANNEL
SQUARE
B
B
B-B
(b)
GUSSET
C
C
C-C
(c)
STIFFENING PLATE
g
D
e
D
D-D
(d)

FIGURE 1.2 : K-JOINT TYPES PREVIOUSLY TESTED (REF.2)

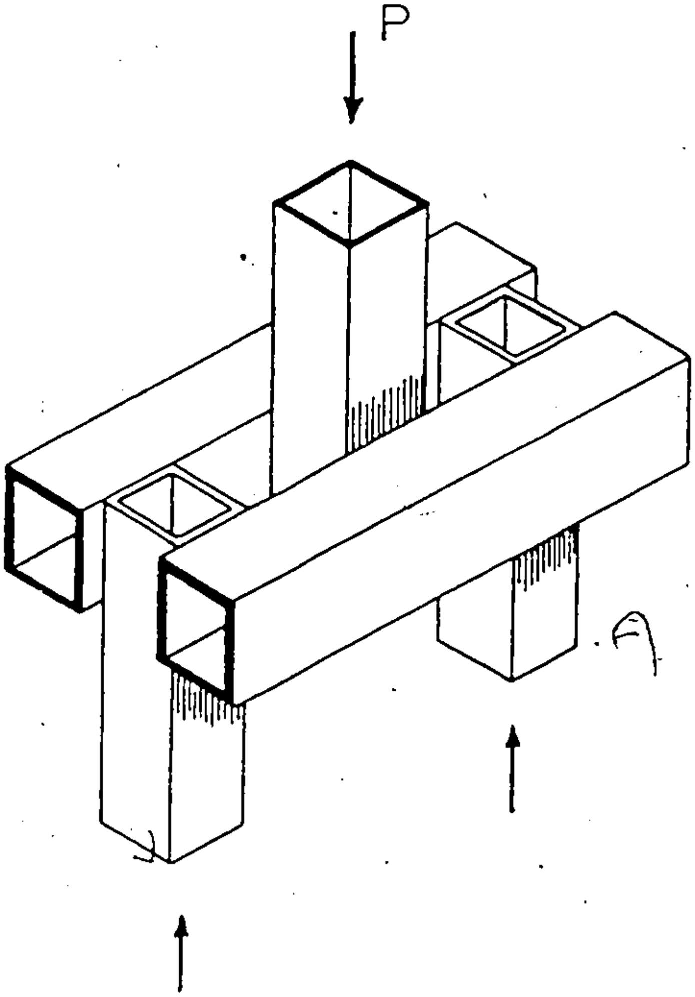

FIGURE 1.3 : RHS TWIN SHEAR BEAM

CHAPTER 2

EXPERIMENTAL PROGRAM OF SEPARATED TWIN MEMBER SHEAR BEAMS

2.1 Introduction

Testing of isolated separated double chord K-joints is complicated by the fact that an elaborate test setup involving a minimum of two hydraulic jacks must be employed. Since it was observed from previous experiments that shear stress resultants are the major cause of a shear failure in the gap (1,2), one can achieve such a behaviour by using the concept of a twin member shear beam.

In the tests undertaken, a total of twenty four shear beam specimens were fabricated from cold and hot formed steel of grade G40.21-350W. The cost of fabrication of such specimens was quite inexpensive due to the need for only fillet or bevel groove welding, either totally or partially, around the perimeter. In addition, flame cutting the member's ends in the vicinity of the joint was adequate. Such simplifications are possible both due to the geometric configurations of the connection and because the load applied to the beam is transmitted to the supporting columns through simple shearing action.

2.2 Description of Experimental Procedure

2.2.1 Parameters Considered

The main objective of the testing programme was to examine the effect of chord aspect ratio (h_o/b_o) and gap-to-depth ratio (s/h_o) on the strength and stiffness of the double chord shear beam. Also, of concern was the shearing efficiency of the outer webs of chords and its variation with the above-mentioned parameters. In the experiments undertaken the chord aspect ratio ranged from 0.4 to 2.5, while the gap-to-depth ratio varied from 0.125 to 1.0.

2.2.2 Connection Detail

As can be seen from Figure 2.1, all members consisted of RHS and were attached by welding. The detail consisted of a double chord beam that spanned the distance s between the upper and lower vertical members. All three verticals were sandwiched between the twin beam members and welded to the inner webs. Support columns of the large gapped specimens (a and b type) were welded along the perimeter whereas those having small gaps (c and d type) were welded only along the top and bottom sides. Figure 2.2 shows the locations of such weldments.

2.2.3 Specimen Data

The 24 specimens that were tested, possessed the geometrical properties indicated in Table 2.1. The vertical members were 127.0 × 127.0 mm in cross section with a thickness sufficient to prevent local buckling. Specimens were classified according to their chord aspect ratio (h_o/b_o) and their gap to depth ratio (s/h_o). Three groups were defined as indicated in Table 2.1: a shallow chord group with $h_o/b_o < 1$, a square chord group ($h_o/b_o = 1$) and a deep chord group ($h_o/b_o > 1$). Within each group, both h_o/b_o and s/h_o are observed to vary. An alphanumeric label was used to identify specific test specimens. The numeral denotes a particular chord aspect ratio whereas the alphabetic character signifies a certain gap to depth ratio. Thus, a further classification into sets was made. Each set consisted of two or more specimens that differed only in the gap distance (constant h_o/b_o). The letters a,b,c and d indicate the relative size of gap where a is the largest and d is the smallest.

2.2.4 Measuring Devices

Initially, only three dial gauges were used in each test to indicate the amount of inner web deformation. For c and d type specimens, a fourth dial was placed under the outer web to measure its vertical deflections. Strain rosettes were mounted on outer webs, and, on inner webs when the gap was sufficiently large to accommodate them. In the latter instance, these were applied at a section mid-way in the gap spacing. Chords having a depth of 127.0 mm or more permitted three rosettes to be positioned along a vertical line on the web face; otherwise one rosette was placed at mid-depth of the chord. Figure 2.3 is a sketch of typical specimens with attached measuring devices.

Measurements were recorded in milli-volts with an Autodata 9 data acquisition system that can monitor up to 80 channels. Knowledge of the gauge factor then permits strains to be easily calculated by multiplying the voltage value with a constant.

2.2.5 Loading

Specimens were loaded using the hydraulic RIEHLE testing machine at McMaster having a capacity of 2500 KN. The load was applied quasi-statically in increments varying from 100 KN to 20 KN depending on the specimen size and the stage of loading. Strain and dial readings were recorded at the end of each load increment.

2.2.6 Material Properties

Upon completion of each test, standard coupons were cut from each specimen remote from the welded seam. Uniaxial tensile tests were then performed on these coupons using the Tinius Olson machine available in the laboratory. The average yield and ultimate stresses σ_y and σ_{ult} for each specimen are listed in Table 2.1.

2.3 Test Results

Load-midspan deflection curves are plotted for each specimen in Figure 2.4 according to the category of shallow, square and deep beam specimens. Of particular interest was the degree to which the outer chord webs contributed to shear resistance as both a function of h_o/b_o and the gap-to-depth ratio s/h_o. For a given aspect ratio, it will be observed from Figure 2.4 and Table 2.2 that greater elastic stiffness C_e and strength were achieved for a decrease in the gap distance (alphabetical letter progression of specimen label) with only two exceptions.

The group I specimens ($h_o/b_o < 1$) suffered severe distortions of their inner webs in the gap zones at high loads, but experienced little deflection of their outer webs even at $P = P_{ult}$. Strain rosettes mounted on the outer webs to measure maximum shear strains confirmed that the stresses remained within the elastic range.

For the group II specimens ($h_o/b_o = 1$), the collapse mechanism was similar to that of group I except that the maximum shear strains as measured in the outer webs were considerably higher, exceeding $\dot{\gamma}_y$ in all instances. This was indicative of a greater effectiveness of the outer webs in sharing the beam's shear resistance. Strength and stiffness characteristics were consistent as both were observed to increase as the gap was reduced.

The deep beams (group III) exhibited a failure mode in which both inner and outer webs underwent significant shear deformation. Measured shear strains in the outer webs were well into the plastic range. In addition, top and bottom flanges were observed to be severely deformed by bending.

Photographs of typical specimens from the deep and shallow groups after testing are presented in Figure 2.5. The taut string line demonstrates the negligible outer web deflection occurring for the shallow specimens (Figure 2.5(a)) whereas visually detectable displacements are evident for those constituting the deep beam group (Figure 2.5(b)).

2.4 Effect of Chord Aspect Ratio

Detailed load strain curves are presented in Figure 2.6 for three representative specimens 1b, 4b and 7b. In each case, the gap spacing s was equal to one-half the beam's depth. Specimen 4b employed square tubular beams ($h_o/b_o = 1$), while 1b and 7b utilized rectangles having extreme aspect ratios (h_o/b_o) of 0.4 and 2.5 respectively. Only single rosettes were mounted on each of the faces for specimen 1b for practical reasons. The increased depth dimension for the other two specimens permitted three rosettes being located along a vertical line of a web face. The curves denoted by T, M and B in Figure 2.6 represent strain measurements taken near the top, the middle and near the bottom of the web. The subscripts i and o refer to inner and outer webs respectively.

A comparison of performance of the three specimens indicates that the outer webs of the section having the greatest depth-to-width ratio were the most effective in sharing the shear load. For example, the measured maximum shear strains, γ_{max}, at ultimate load for the outer web strain rosettes positioned at mid-depth (curves M_0 in Figure 2.6) were about 1000 μ, 2000 μ and 5000 μ for specimens 1b, 4b and 7b, respectively. In fact, it will be noted from Figure 2.6(c) that the maximum shear strains for the outer webs of the deep section specimen, 7b, exceeded the calculated shear strain γ_y, for all three rosettes —

indicative of a distribution of shear stress exceeding yield throughout the depth. From Figure 2.6(b), it is evident that only the top portion of the exterior webs of the square underwent yielding. With a single rosette per web, it is surmised that the entire outer webs of the shallow specimen, 1b, remained elastic up to ultimate load.

It may be noted that the inner web load-strain curves are approximately linear for γ values not exceeding about 1000 μ. This strain level is only about 40% of γ_y. The latter was computed from a nominal yield stress σ_y of 350 N/mm^2 and elastic constants E and ν taken as 210,000 N/mm^2 and 0.3 respectively. (The $\sqrt{3}$ factor from the Mises yield criterion was used to link the shear yield stress τ_y to σ_y.) Early yielding in the shear beam specimens appears to have been due to welding residual stresses in addition to those generated during the HSS manufacturing process itself.

2.5 Influence of Gap Distance

It appears from test results that the beam's outer walls contribute a greater share to its shearing strength when the gap distance is increased. This behaviour can be easily discerned from consideration of the load-outer web shear strain curves of the "2" and "4" series specimens. In these sets, only the gap distance was varied while all other parameters were kept constant (Table 2.1). For example, it is obvious from Figure 2.7(b) that the maximum shear strain attained was smallest for specimen 4d (s = 19.0 mm) whereas it was largest for specimen 4a (s = 127.0 mm). However, this gain in strength was counteracted by the increased bending moment acting on the critical section in the gap spacing. As a result the two effects tended to cancel one another; and hence it may be observed for the range of gaps tested in this investigation, that varying the gap appears to have little influence on the joint ultimate strength. However, for prescribed displacements, as will be discussed below, there is a consistent increase in strength with a reduced gap distance. The elastic stiffness was also found to increase for reduced gap size in all but two specimens (3b and 4c).

2.6 Deflection Limit Criterion

For every specimen tested, it was observed that major distortions in geometry occurred at the maximum load P_{ult}. As such, the original geometry had evidently been altered substantially with tensile stress fields in the inner webs being particularly obvious. However, for practical design purposes, a serviceability deformation criterion is normally required to prevent major distortions occurring in a structure. Such a deflection criterion was previously proposed by Mouty (12) in applications of RHS single chord K and T-joints. He suggested a maximum chord face displacement of 1% b_o for unequal width connections. Implicit in his limitation is the need to restrict the slope of the chord face. No account was taken of the section's depth; perhaps because flexing action of the connecting flange plate for the single chord joint tends to be little influenced by the chord's depth. For the separated double chord, the situation is quite different. The connection relies on a combination of web shearing and flange flexing actions to resist applied loads. Distortions will involve both the chord flanges and the webs, and as such, a deflection criterion ought to include both h_0 and b_0. For square double chords, the equivalent limitation to that of Mouty would be 2% b_0 or, in this instance 1% of $(h_0 + b_0)$. This latter criterion is proposed as the deformation limit load P_d for RHS double chord joints. While arbitrary, such a limitation is simple and conforms to that of Mouty when square chords are used.

Table 2.1 Dimensional and Physical Properties of Twin Shear Beam Specimens

Group	Specimen	Depth × Width × Thickness (mm)	s (mm)	σ_y (MPa)	σ_{ult} (MPa)
I (shallow)	1a	50.8 × 127.0 × 4.78	50.8	338	517
	1b	50.8 × 127.0 × 4.78	25.4	343	506
	2a	63.5 × 127.0 × 4.78	63.5	335	497
	2b	63.5 × 127.0 × 4.78	31.8	334	496
	2c	63.5 × 127.0 × 4.78	15.9	325	524
	2d	63.5 × 127.0 × 4.78	12.7	319	547
	3a	76.2 × 127.0 × 4.78	76.2	337	510
	3b	76.2 × 127.0 × 4.78	38.1	349	517
II (square)	4a	127.0 × 127.0 × 4.78	127.0	367	461
	4b	127.0 × 127.0 × 4.78	63.5	365	460
	4c	127.0 × 127.0 × 4.78	38.1	391	506
	4d	127.0 × 127.0 × 4.78	19.0	402	516
	8a	152.4 × 152.4 × 6.35	152.4	413	523
	8b	152.4 × 152.4 × 6.35	76.2	424	534
	8c	152.4 × 152.4 × 6.35	38.1	392	491
	8d	152.4 × 152.4 × 6.35	19.0	400	495
III (deep)	5a	127.0 × 76.2 × 4.78	127.0	343	511
	5b	127.0 × 76.2 × 4.78	63.5	333	501
	6a	127.0 × 63.5 × 4.78	127.0	338	502
	6b	127.0 × 63.5 × 4.78	63.5	337	494
	6c	127.0 × 63.5 × 4.78	31.8	336	530
	6d	127.0 × 63.5 × 4.78	15.9	333	532
	7a	127.0 × 50.8 × 4.78	127.0	351	516
	7b	127.0 × 50.8 × 4.78	63.5	341	505

N.B. Measured dimensions of HSS were found to be very close to the nominal dimensions and as such the latter were employed.

Table 2.2 Shear Beam Experimental Results

Specimen No.	s/h_o	h_o/b_o	C_e (KN/mm)	P_d (kN)	P_{ult} (kN)
1a	1.0	0.40	364	280	496
1b	0.5	0.40	444	324	571
2a	1.0	0.50	400	328	661
2b	0.5	0.50	400	378	552
2c	0.25	0.50	455	401	628
2d	0.20	0.50	769	438	616
3a	1.0	0.60	417	375	680
3b	0.5	0.60	357	421	727
4a	1.0	1.0	385	506	830
4b	0.5	1.0	714	567	932
4c	0.30	1.0	625	617	1042
4d	0.15	1.0	1000	801	1113
8a	1.0	1.0	555	901	1450
8b	0.5	1.0	833	1081	1661
8c	0.25	1.0	1250	1050	1622
8d	0.125	1.0	1300	1184	1618
5a	1.0	1.67	357	506	986
5b	0.5	1.67	833	644	1157
6a	1.0	2.0	400	562	1077
6b	0.5	2.0	800	680	1063
6c	0.25	2.0	833	668	1110
6d	0.125	2.0	833	742	1108
7a	1.0	2.5	400	505	943
7b	0.5	2.5	800	679	1218

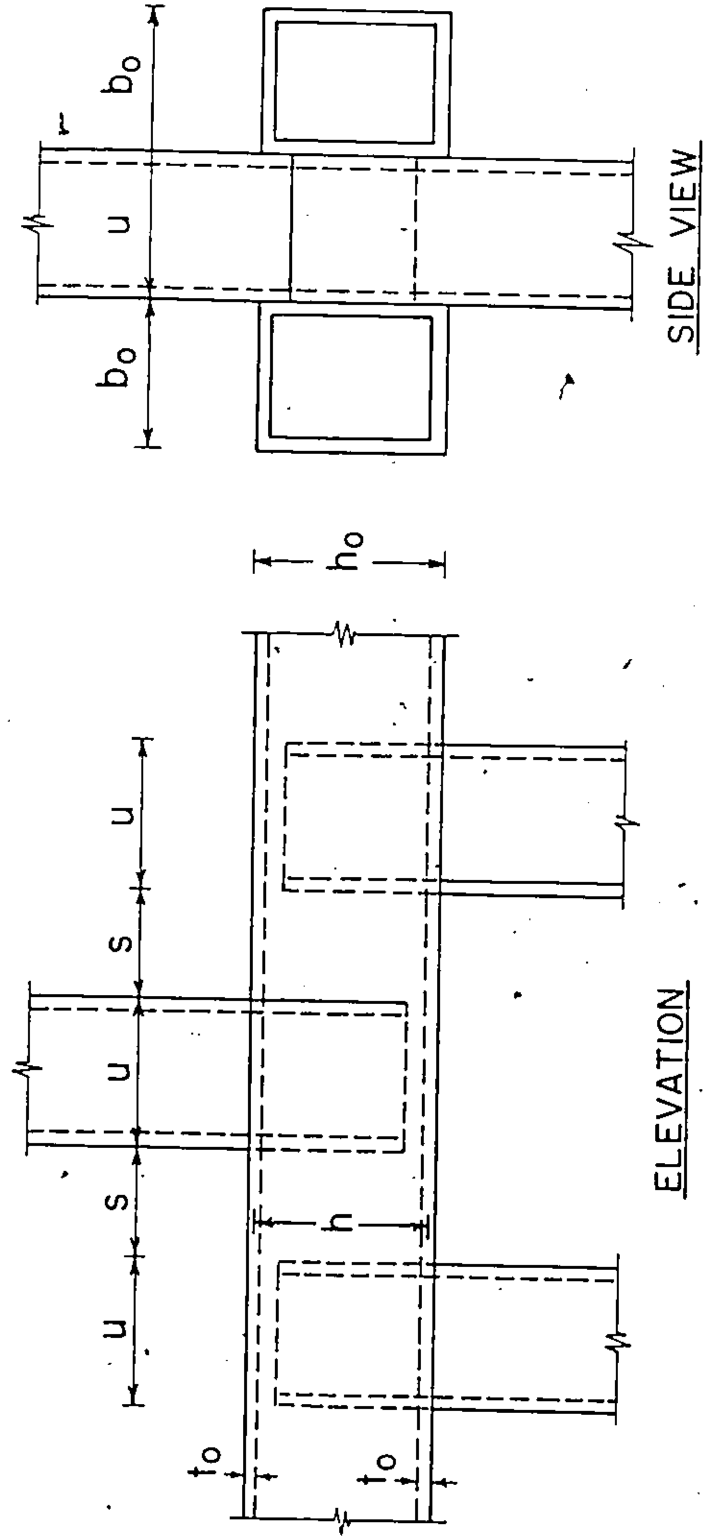
b_o
u
b_o
SIDE VIEW
h_o
u
s
u
s
u
h
t_o
t_o
ELEVATION

FIGURE 2.1 : NOMINAL DIMENSIONS OF RHS TWIN SHEAR BEAM

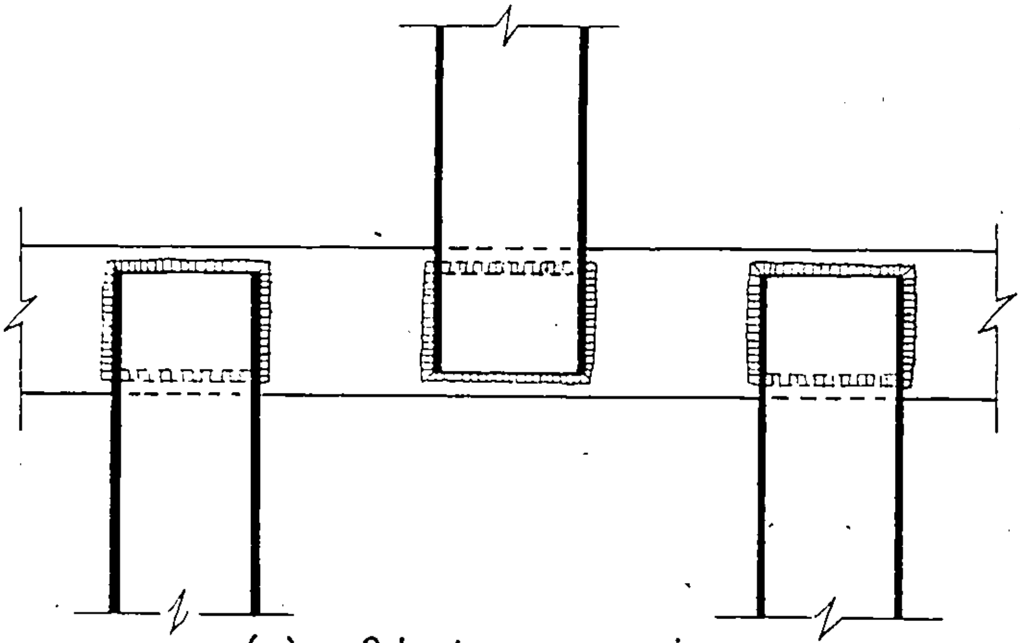

(a) a&b type specimens

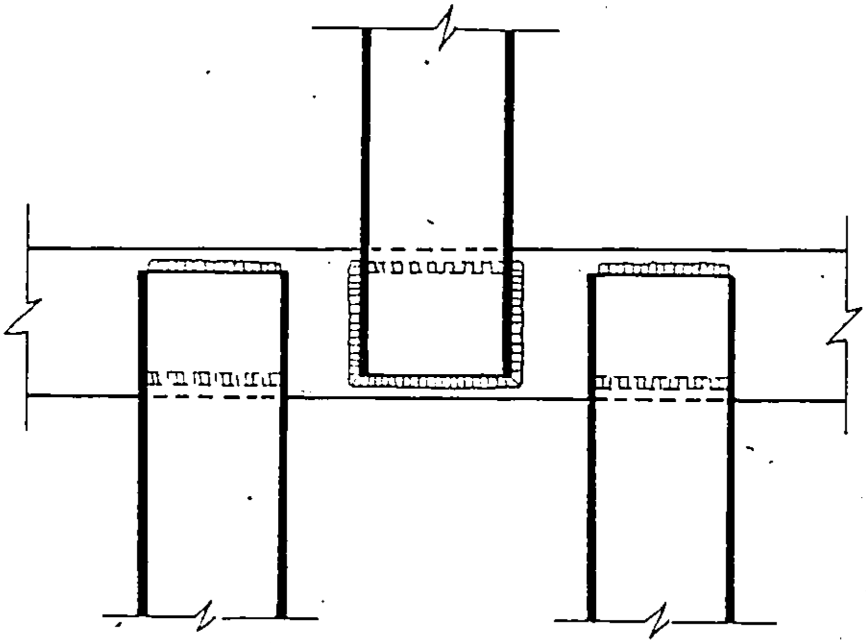

(b) c&d type

FIGURE 2.2 : WELDMENT LOCATIONS

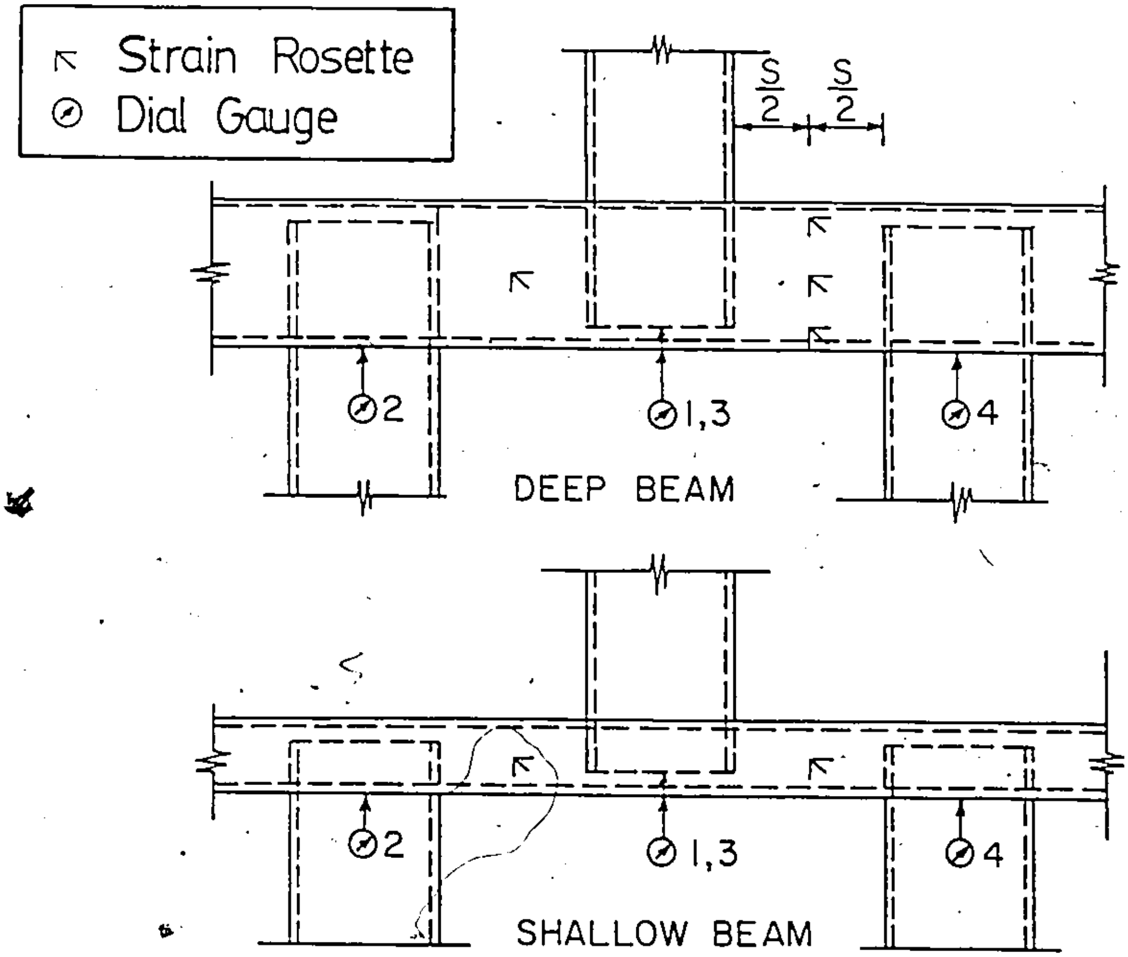
Strain Rosette
Dial Gauge
S/2
S/2
2
1,3
4
DEEP BEAM
2
1,3
4
SHALLOW BEAM

FIGURE 2.3 : GAUGE LOCATIONS FOR TWIN SHEAR BEAM SPECIMENS

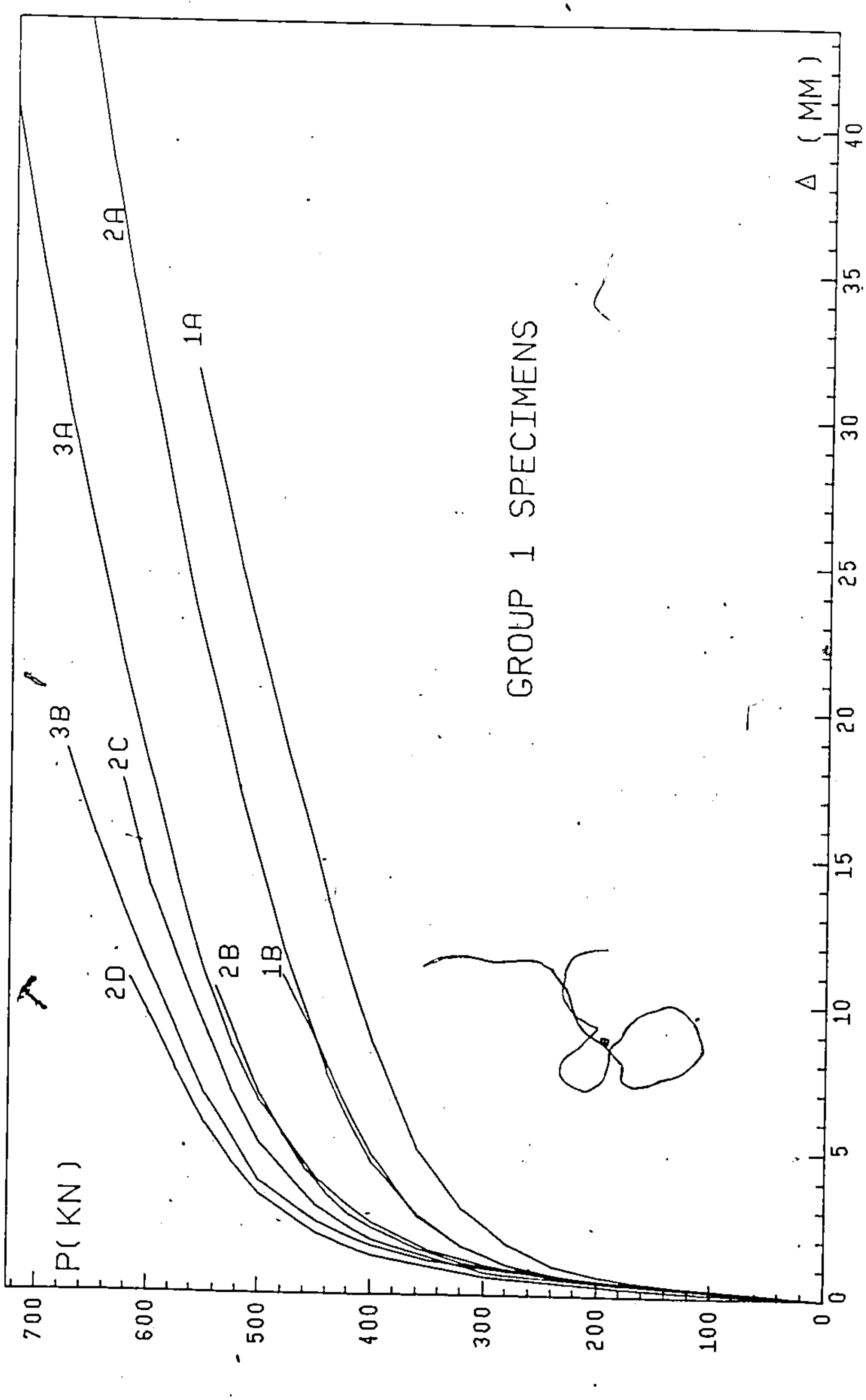
P(KN)
700
600
500
400
300
200
100
0
Δ (MM)
0
5
10
15
20
25
30
35
40
GROUP 1 SPECIMENS
3A
2A
1A
3B
2C
2D
2B
1B

(a)

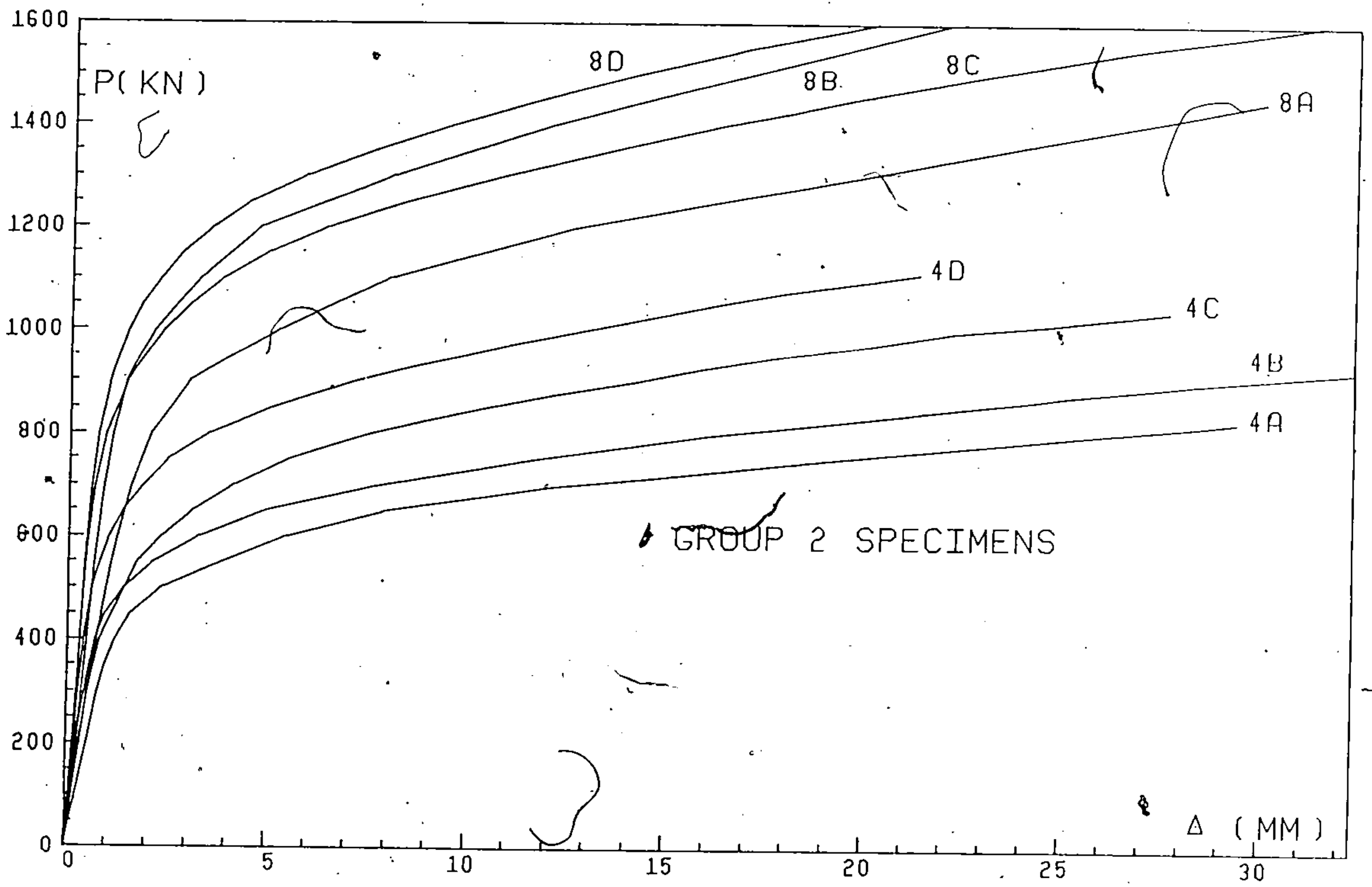
1600
1400
1200
1000
800
600
400
200
0
P(KN)
0
5
10
15
20
25
30
Δ (MM)
8D
8B
8C
8A
4D
4C
4B
4A
GROUP 2 SPECIMENS

(b)

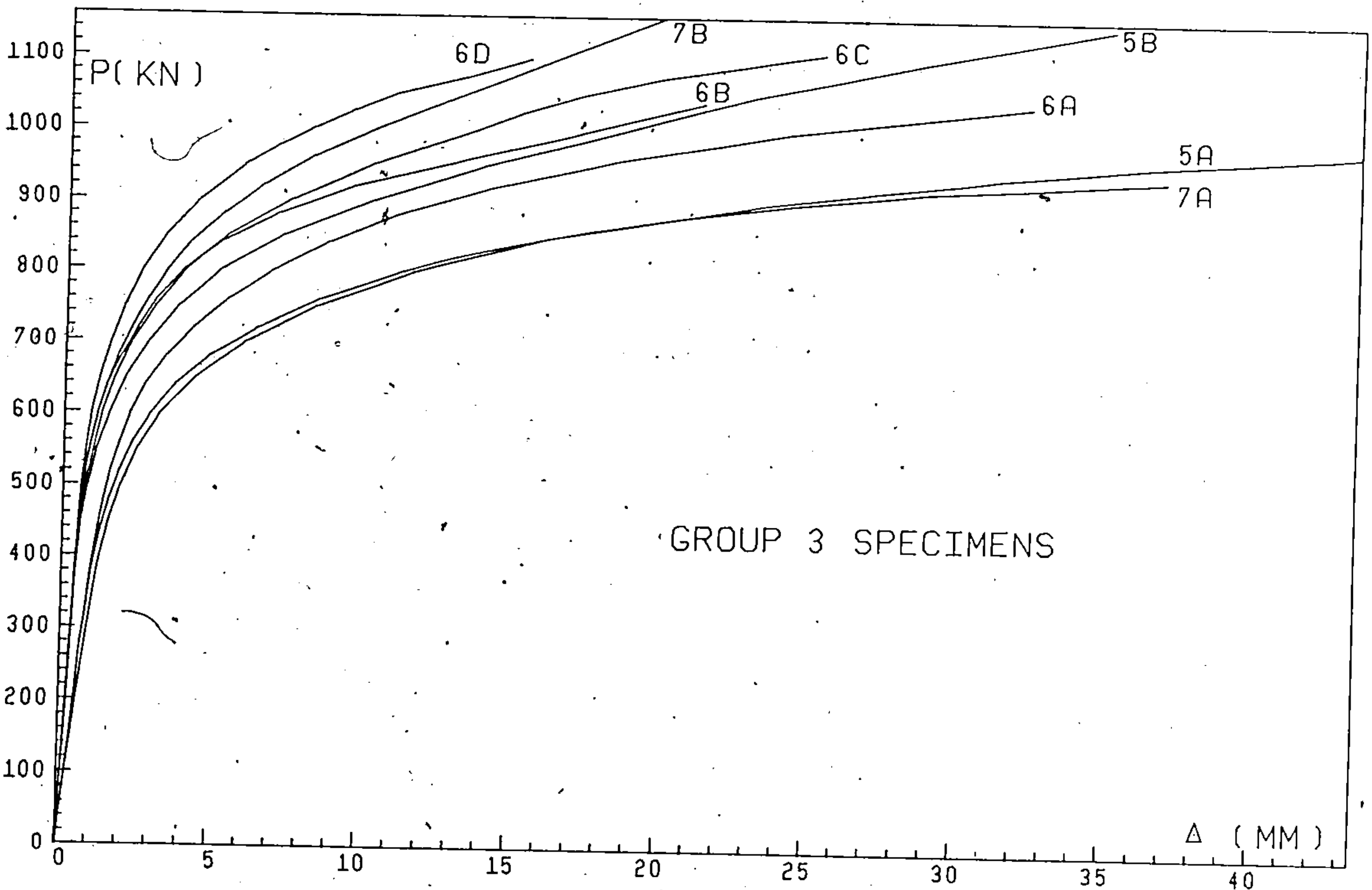

(c)

FIGURE 2.4 : LOAD-CENTRAL DISPLACEMENT CURVES

FIGURE 2.5 : TYPICAL SHEAR BEAM SPECIMENS

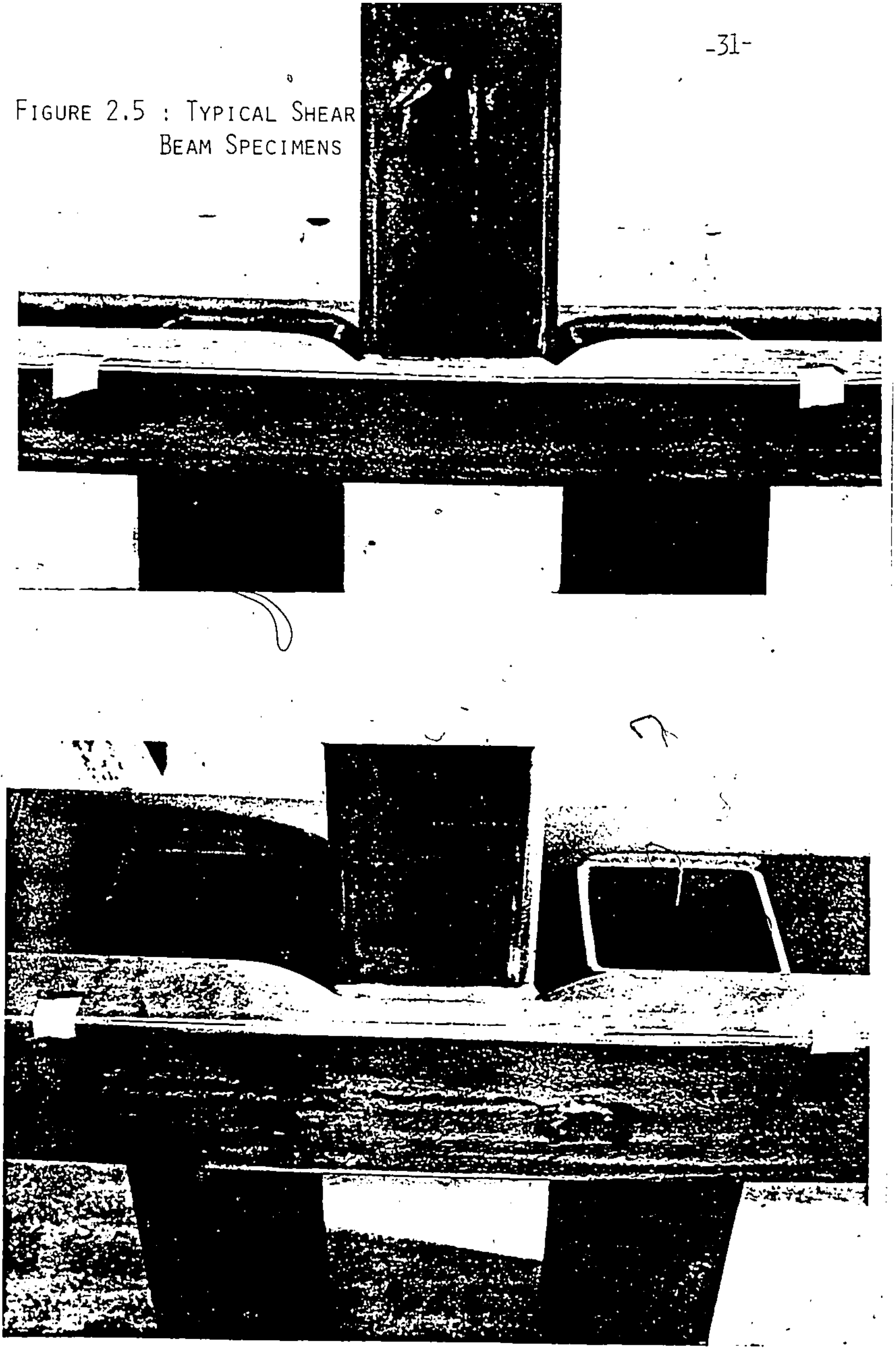

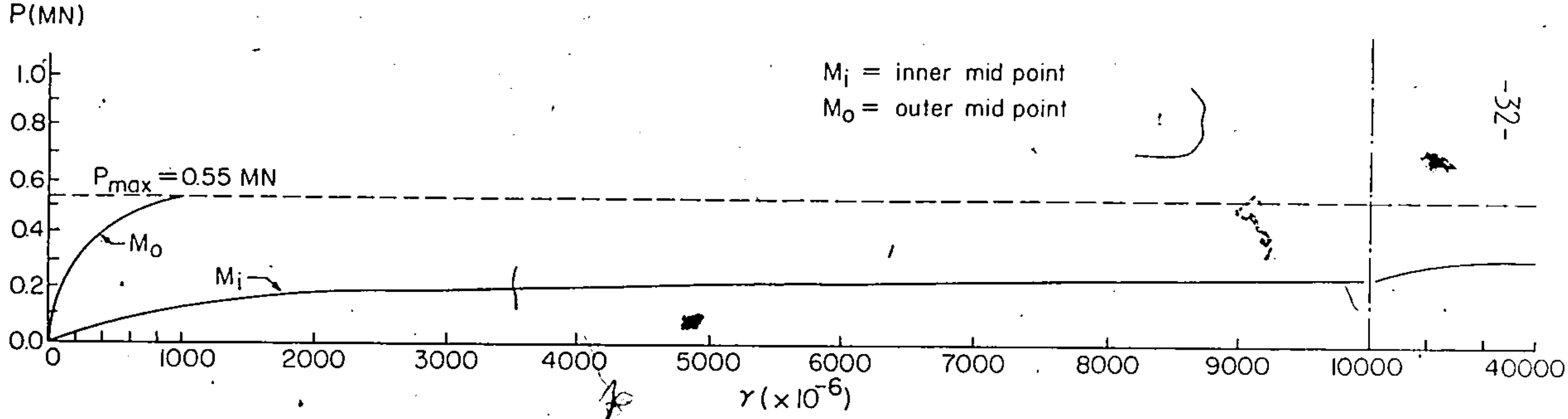

(a) SPECIMEN 1b

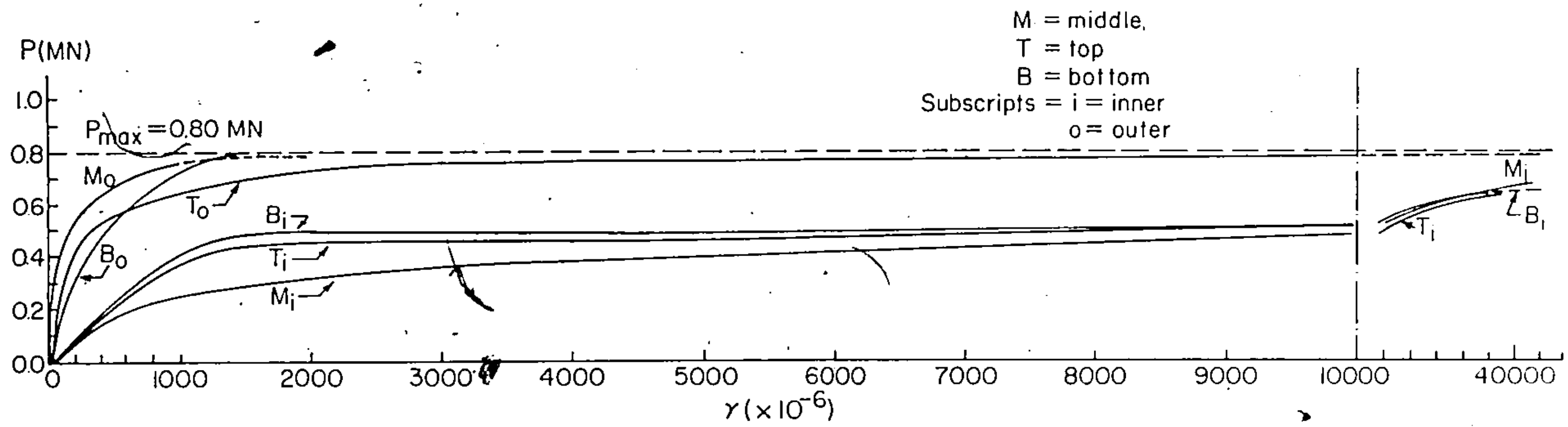

(b) SPECIMEN 4b

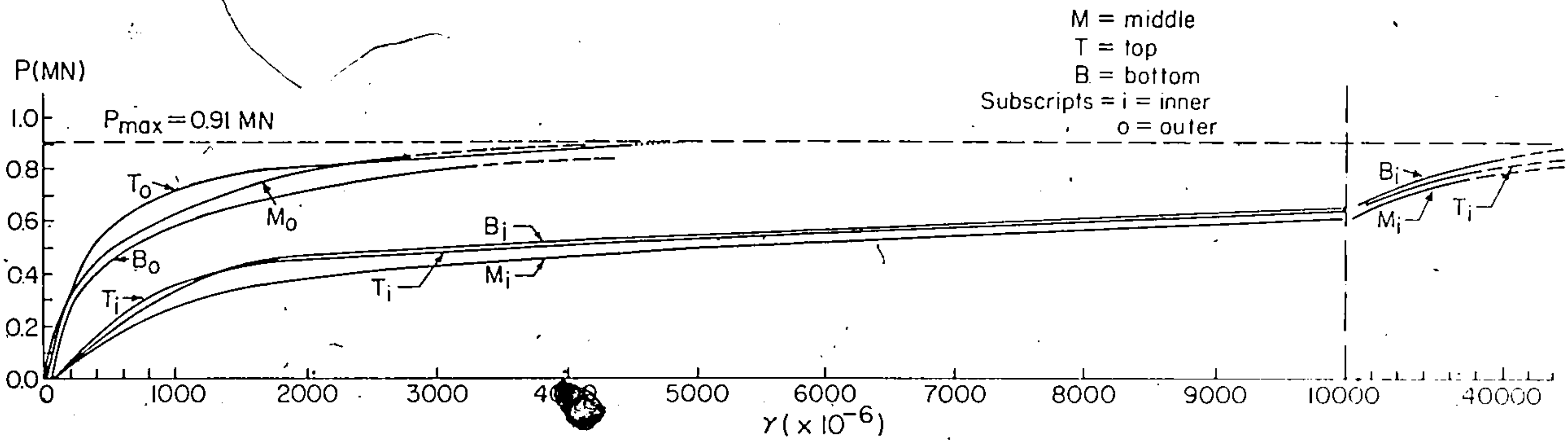

(c) SPECIMEN 7b

FIGURE 2.6 : LOAD SHEAR-STRAIN RELATIONSHIPS

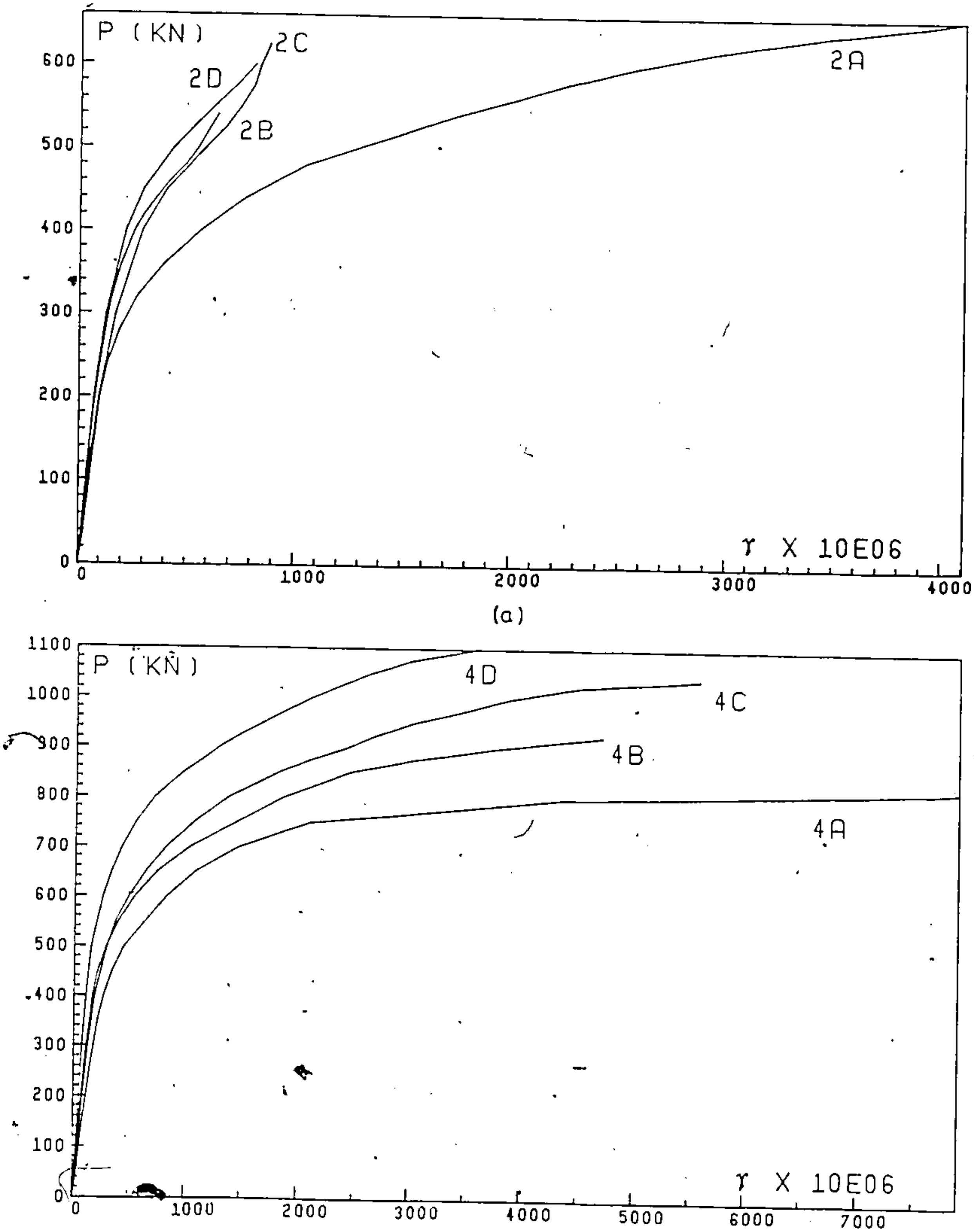

(a)

(b)

FIGURE 2.7 : INFLUENCE OF GAP DISTANCE ON OUTER WEB SHEARING EFFICIENCY

CHAPTER 3

STRENGTH ANALYSIS

3.1 Introduction

The use of plastic hinge lines for calculating an upper bound to the plastic collapse of plates is well known (19). The basic principle involves equating the external work done by an applied load system to the internal work performed by a set of plastic moments and forces operating along hinge lines through changes in angle and displacements respectively. The deformed state must satisfy compatibility requirements and a plausible yield line pattern in order to be acceptable. A minimization of internal energy dissipation with respect to certain geometrical parameters is then required in order to find the lowest upper bound. The method is known as the yield line theory and was originally developed by Johansen (20) in application to reinforced concrete flat slabs. Basic assumptions of the simplified theory include: (1) Rigid-perfectly plastic material; i.e. elastic strains are sufficiently small to be neglected compared to plastic strains, (2) For loadings transverse to the plate, the effect of shear force on the plastic moment capacity may be ignored, and, (3) Deflections are small, and as such, membrane stresses developed in the plate may be assumed to be negligible. With these considerations, the theory appears to be simple to grasp and easy to apply.

In HSS joint applications, the yield line theory has been widely used by several researchers. Early attempts focused on evaluating the punching shear strength of single chord T-joints. This was done initially by Jubb and Redwood (21) followed by Patel et al. (22) using a combined trapezoidal and corner fanned collapse mechanism. Davies and Roper (23,24) then presented similar mechanisms to estimate the strength of N-joints. In their second paper (24), they modified the strength equation to account for the work done by the high shearing forces in the crotch zone. Mouty (12) extended the yield line patterns by Jubb and Redwood and Davies and Roper and derived strength expressions for T, N and K joints considering the effect of chord axial forces. He also addressed the effect of membrane stresses occurring in the chord face on the joint ultimate strength. Packer et al. (25) included such effects in their ultimate strength analysis of gap joints employing Mouty's mechanism. Korol et al. (26) defined three plausible mechanisms for a plate reinforced single chord T-joint subjected to branch punching shear and bending moment. They used these mechanisms to determine the joint strength for prescribed plate dimensions. They also derived optimum plate dimensions for maximum strength. It was not until recently however that the yield line method was applied to RHS double chord connections. Initially, Korol and Mitri (27) derived ultimate strength equations for truss gap connections neglecting the effect of axial forces. They also carried out an ultimate strength analysis (28) for double beam-to-staggered column connections.

In this chapter, the yield line theory is adopted to derive the yield load for twin chord RHS shear beams and subsequently K and N joints. Two mechanism models are presented, namely the trapezoidal and conical types. A comparison between theoretical and experimental results is made to verify the theoretical models proposed. Strength expressions are then modified to apply to real truss joints. These expressions are applied to tested joints to compare predictions with experimental work previously done on K-joints. Finally a variation of parameter study is conducted to indicate their influence on joint strength. Effects of chord axial preload and web member-to-chord angle are also investigated.

3.2 Trapezoidal Mechanism

The yield load of the twin beam, P_b, may be defined as that which causes the inner webs to distort in a vertical plane an amount Δ_1, as shown in Figure 3.1(a), while the four flanges deform in a yield line pattern as indicated in Figure 3.1(c). Furthermore, the outer webs may also distort Δ_2 (Figure 3.1(b)). If the angles formed along the yield lines of the flange segments are compatible with the deflections Δ_1 and Δ_2, a kinematically admissible set of displacements results in the formation of a mechanism. In fact, the deformation pattern proposed is judged to be an acceptable model of the actual distortion of the specimens tested. Figure 2.2 shows two extreme cases illustrating this observation. Indeed, for the shallow twin beam (Figure 2.2(a), the outer webs were visually observed to undergo virtually no displacement, i.e. $\Delta_2 \approx 0$, while an exterior web of a deep beam specimen (Figure

2.2(b) tended to displace as much as did the inner web.

Equating the external work to the internal energy dissipation gives

$$P_b \Delta_1 = \Sigma M_j \Psi_j \ell_j + \Sigma h t_o \tau_j \Delta_j \tag{3.1}$$

where the first term represents the work done by the formation of yield lines developed in the beam flanges, while the second term involves the plastic shearing action of the webs.

The hinge rotations can be simply determined by means of the hodograph method proposed by Johnson (29). As observed from Figure 3.2, these rotations are

$$\Psi_1 = \Psi_2 = OA = \frac{\Delta_1 - \Delta_2}{b} \tag{3.2a}$$

$$\Psi_3 = AC = \frac{\Delta_1}{s \cos\alpha} \tag{3.2b}$$

$$\Psi_4 = EC = \frac{\Delta_1}{s \cos\beta} - \frac{\Delta_2}{b \sin\beta} \tag{3.2c}$$

$$\Psi_5 = EC \sin\beta = \frac{\Delta_1}{s} \tan\beta - \frac{\Delta_2}{b} \tag{3.2d}$$

$$\Psi_6 = OE = \frac{\Delta_2}{b \tan\beta} \tag{3.2e}$$

where the angles α and β are defined in Figure 3.1. Also, the lengths ℓ_j are given as:

$$\ell_1 = u \tag{3.3a}$$

$$\ell_2 = u + 2b \tan\alpha \tag{3.3b}$$

$$\ell_3 = \frac{b}{\cos\alpha} \tag{3.3c}$$

$$\ell_4 = \frac{b}{\cos\beta} \tag{3.3d}$$

$$\ell_5 = s \tag{3.3e}$$

$$\ell_6 = b \tag{3.3f}$$

Substituting (3.2) and (3.3) into (3.1) gives

$$P_b\Delta_1 = 2\sigma_y t_o^2 \{\frac{\Delta_1 - \Delta_2}{b} (b \tan\alpha + u) + \frac{\Delta_1 b}{s \cos^2\alpha}$$

$$+ (\frac{\Delta_1 b}{s \cos^2\beta} - \frac{\Delta_2 b}{b \sin\beta \cos\beta}) + (\Delta_1 \tan\beta - \frac{\Delta_2 s}{b}) + \frac{\Delta_2}{\tan\beta}\}$$

$$+ 4h\, t_o \tau_y (\Delta_1 + \Delta_2)$$

Dividing by Δ_1 and noting that $\tan\beta = \frac{s}{b} - \tan\alpha$, it can be shown that

$$P_b = 2\sigma_y t_o^2 \{(1 - r)(\frac{u}{b} + \frac{2s}{b}) + \frac{2b}{s}(1 + \tan^2\alpha) - 2\tan\alpha\}$$

$$+ 4\tau_y h\ t_o(1 + r) \qquad (3.4)$$

where r is defined as Δ_2/Δ_1.

The minimum value of P_b may be determined by differentiation with respect to $\tan\alpha$ and setting it equal to zero. This results in the yield line pattern defined by α^*. Thus,

$$\frac{\partial P_b}{\partial \tan\alpha} = 0 = \frac{2b}{s}(2\tan\alpha) - 2$$

and

$$\tan\alpha^* = \frac{s}{2b} \qquad (3.5)$$

Substituting this value into (3.4), the upper bound load can be obtained.

$$P_b = 2\sigma_y t_o^2 \{(1 - r)(\frac{u + 2s}{b} + \frac{2b}{s} - \frac{s}{2b}\} + \frac{4h\ t_o}{\sqrt{3}}\sigma_y(1 + r) \qquad (3.6)$$

where τ_y has been replaced by $\sigma_y/\sqrt{3}$ from the Von Mises yield criterion.

If r takes on its minimum value of zero, the outer webs of the twin beam will remain undistorted and the deformation pattern illustrated in Figure 3.3 evolves. In this instance, the failure load represents a lower limit on P_b such that:

$$P_{LL} = \sigma_y t_o^2 \left[\frac{2u + 3s}{b} + \frac{4b}{s} + \frac{4h}{t_o\sqrt{3}}\right] \tag{3.7}$$

If r takes on a maximum value of unity, the outer webs will be most effective. The corresponding mode of failure is depicted in Figure 3.4. The associated load, P_{UL}, is an upper limit on the yield load and is given by

$$P_{UL} = \sigma_y t_o^2 \left[\frac{4b}{s} - \frac{s}{b} + \frac{8h}{t_o\sqrt{3}}\right] \tag{3.8}$$

Comparing Equations 3.7 and 3.8, it can be seen that the lower limit load is less than the upper limit load provided that

$$h\ b > \frac{\sqrt{3}}{2} t_o[u + 2s]$$

In practice, this condition is likely always to be satisfied. Consequently, the lower limit load given by Equation (3.7) will provide the lowest upper bound solution. When calculating the results of the trapezoidal mechanism in discussion to follow, it is therefore to the lower limit solution that reference is being made.

3.3 Conical Mechanism

Conical mechanisms are well known in analyses of collapse for flat slab applications such as floors in buildings and bridge decks subjected to concentrated loadings. In particular, the conical shape commonly utilized is the central fan described by Wood (19). This type of failure mode can be shown to give lower upper bounds to collapse loads as compared with mechanisms consisting of straight yield lines.

A possible circular fan mechanism for the twin beam is shown in Figure 3.5(a). The hatched regions form the conical shape of the deformed top and bottom flanges. A more detailed quarter segment of the deformed state is shown in Figure 3.5(b). Because of symmetry of deformation, the vertex of the cone coincides with the central point of the loaded column. The associated shear distortion of inner and outer webs is hyperbolic and is indicated by the conic sections 1-1 and 2-2 of Figure 3.5(c). The plastic collapse load may be found by equating the internal and external work quantities obtained, as the load displaces an amount Δ_1 (Figure 3.5(c)); elastic strain effects are assumed to be negligible. Thus, the external work term becomes $P_b \Delta_1$ while the total internal work dissipated in causing such a plastic mechanism is given by

$$W_{int} = \sum_{i=1}^{m} \int M_p \ell_i d\Psi_i + \sum_{j=1}^{n} \int \tau_y \gamma_j dV \qquad (3.9)$$

where, for the first term, m is the number of plastic hinge lines, M_p

the plastic moment of the flange plate per unit length (= $\sigma_y t_o^2/4$), and ℓ_i the length of the plastic hinge line with Ψ_i its rotation. In the second term, p is the number of webs distorted by shear, τ_y the yield shear stress, while γ_j is the shear strain in the web (j = 1 for the inner one, 2 for the outer). The right hand side of (3.9), then, represents the plastic strain energy dissipated by bending of the flanges and by the shearing action of the webs. From Figure 3.5(b) it can be seen that the following geometrical relationships hold

$$\ell_1 = r_o \alpha \tag{3.10a}$$

$$\ell_2 = r_o \cos(\alpha + \beta) \tag{3.10b}$$

$$\ell_3 = s \tag{3.10c}$$

$$\ell_4 = (\pi/2 - \gamma) r_i \tag{3.10d}$$

$$\begin{aligned} \ell_5 &= r_o - \frac{v}{2\sin\phi}, \quad \beta < \phi < \gamma \\ &= r_o - r_i, \qquad \gamma < \phi < \alpha + \beta \\ &= \frac{b_o + v/2}{\sin\phi} - r_i, \quad \alpha + \beta < \phi < \pi/2 \end{aligned} \tag{3.10e}$$

The hinge rotations can be easily calculated from Figure 3.5(b). These are

$$\Psi_1 = \Psi_2 = \Psi_3 = \Psi_4 = \frac{\Delta_1}{r_o - r_i} \tag{3.11a}$$

$$d\Psi_5 = \left(\frac{\Delta_1}{r_o - r_i}\right)d\Phi \tag{3.11b}$$

The shear strains in the webs are determined from the equations of the conic sections 1-1 and 2-2. Referring to Figure 3.5(c), it is evident that

$$\gamma_1 = \frac{\partial z_1}{dx} = \frac{\Delta_1 x}{(r_o - r_i)\sqrt{x^2 + (v/2)^2}} \tag{3.12a}$$

and

$$\gamma_2 = \frac{\partial z_2}{dx} = \frac{\Delta_1 x}{(r_o - r_i)\sqrt{x^2 + (b_o + v/2)^2}} \tag{3.12b}$$

The expressions in (3.9) can thus be integrated and equated to the external work quantity. Noting that τ_y may be replaced by $\sigma_y/\sqrt{3}$ from Mises' yield criterion, the plastic shearing capacity of the twin shear beam, P_b, can be obtained as

$P_b = \sigma_y t_o^2 \Big[\frac{2}{r_o - r_i} \{r_o(2\alpha$ [illegible] $\cos(\alpha + \beta)) + s$

$$-(v/2)\ell n\left(\frac{\tan((\alpha+\beta)/2)\tan(\gamma/2)}{\tan(\beta/2)}\right) - b_o \ell n\left(\tan\frac{\alpha+\beta}{2}\right)\}$$

$$+\frac{4h}{\sqrt{3}\,t_o}(1+r)] \quad (3.13)$$

where

$$r_o = \sqrt{(v/2)^2 + \left(s+\frac{u}{2}\right)^2} \quad (3.14a)$$

$$r_i = \sqrt{(v/2)^2 + (u/2)^2} \quad (3.14b)$$

$$\beta = \sin^{-1}\frac{v}{2r_o} \quad (3.14c)$$

$$\alpha = \sin^{-1}\frac{b_o + (v/2)}{r_o} - \beta \quad (3.14d)$$

$$\gamma = \tan^{-1}(u/v) \quad (3.14e)$$

and r is the ratio of outer to inner web deflections, Δ_2/Δ_1. It should be noted that in general

$$0 < r = \frac{r_o - [b_o + (v/2)]}{r_o - r_i} < 1 \quad (3.15)$$

Physically, this stipulation infers that the outer web mid-span deflection Δ_2 can neither be negative (positive downwards) nor greater than Δ_1. These conditions can easily be justified from the physical model geometry and loading system. Hence, if $r_o < [b_o + (v/2)]$, there will be no plastic shearing work contribution by the outer web. Also, the angle α will increase to $\pi/2 - \beta$. Figures (3.6b) and (3.6c) depict such cases. On the other hand, if $r_i > (b_o + v/2)$, r will be a maximum and equal to unity (Fig. 3.6a). As a consequence, the plastic hinge line ℓ_4 will reduce to

$$\left(\pi/2 - \gamma - \cos^{-1} \frac{b_o + v/2}{r_i}\right) r_i \qquad (3.16)$$

3.4 Comparison with Shear Beam Experiments

A comparison was made between strengths predicted for the shear beams, P_b, and their experimental counterparts P_{ult} and P_d defined in Chapter 2. These results are presented in Table 3.1 and are graphically displayed in Figures 3.7 and 3.8. It is evident that there is much closer correspondence of the 45° line with P_d values than with P_{ult}. This result is not surprising since the theory excludes strain hardening and membrane force effects which become significant at large inner web deflections. It was found that the trapezoidal mechanism model estimated the beam strength very accurately. The predicted to observed mean strength ratio was 1.00 with a standard deviation of 0.13. However, for three of the specimens having the largest gap distances relative to their size, i.e. 5a, 6a 7a, the strength P_b predicted by the conical mechanism model differed considerably from the experimental limit P_d. The reason may be attributed to the exclusion of bending moment effects in formulating the equation for plastic joint strength. Clearly, such an effect is significant when the gap distance is very much larger than would be contemplated in practice. It may be noted that the trapezoidal model did not exhibit discrepancy of results for large gap specimens. This may be explained by the fact that neither possible contribution of outer webs to shearing resistance nor loss of strength due to bending moments was accounted for in this model. As a result, the two effects seem to have cancelled one another.

A comparison was also made with predictions obtained from an elasto-plastic interaction equation that was developed earlier by Korol and Keen (5). The underlying assumption of that approach was that the webs and flanges would resist certain prescribed proportions of moment, shear and axial force. It was also supposed that all four webs were equally efficient in resisting shear, a statement that was qualified to apply only to square or deep beams. From Table 3.1, it is noted that, for large gap specimens 5a, 6a and 7a, the load P_{int} obtained from the interaction equation provides a better estimate of P_d than does P_b since reduced joint strength due to bending moment is accounted for in that approach. With only one exception, the other specimens possessed smaller gaps, and hence were more in concurrence with simulating K-joint behaviour in normal practice. For these 21 specimens, the conical mechanism approach provided a considerable improvement in correlation with tests. The predicted to observed mean load ratios for both the conical strength model and the interaction equation for these specimens were computed to be 1.04 and 1.15 with standard deviations of 0.10 and 0.28 respectively.

3.5 Application to K-Joints

3.5.1 Basic Modifications to Beam Models

The strength of a double chord K-joint may be directly or indirectly evaluated from the strength of a twin shear beam having similar geometric and physical properties. Thus, if the influence of the chord's axial force in the gap between diagonals is sufficiently small, it is the shearing component of the web member force, $P_w \sin\theta$ (see Figure 3.9) that will precipitate failure. The predicted shear force that occurs in the gap of the twin beam is $P_b/2$. Equating the shear forces yields $P_w = P_b/(2 \sin\theta)$. To account for the reduced strength due to the non-negligible effects of axial force in the chord member, P_w requires modification. Such a reduction may be ascertained by considering the twin beam, having the failure mode previously described, subjected to an axial force of magnitude N + H where N is the chord preload and H is the contribution from a diagonal given by $P_w \cos\theta$. The resulting web member force capacity becomes

$$P_w = P_b'/(2 \sin\theta) \qquad (3.17)$$

where P_b' represents the reduced twin beam capacity. To compute its value, assumptions must be made regarding the distribution of stresses due to N and H. The chord preload N is taken to be uniformly distributed across the section while H is assumed to be distributed over the same region deformed by shearing action. For example, from Figure 3.6(a) which represents the case of a large gap and/or narrow chord, this force component would tend to be transmitted over the entire cross section since the outer webs are effective in resisting shear. On the other hand, the region in Figure 3.6(c) is confined to an inscribed cone occupying a small part of the flange. This reduced area (inner webs and adjacent flange portions) would thus transmit the axial stress flow in the gap. Such a hypothesis is consistent with St. Venant's principle that concentrated forces tend to become uniformly distributed a reasonably short distance beyond the loaded boundary. For the K-joint tests carried out by Korol and Chidiac (1); it was in fact the case 3 mechanism (Figure 3.6) that dominated throughout. Employing the same hypothesis for the trapezoidal mechanism, the force H will be uniformly distributed over the top and bottom flanges and the inner web. The outer web then, would be assumed not to contribute either towards the shearing resistance of the beam, or H, by virtue of the mechanism model adopted in Figure 3.3.

The reduction in web shearing resistance may be determined by linking the shear and normal stresses through the Mises' yield criterion to give

$$\tau' = (\sigma_y/\sqrt{3})\sqrt{1 - f^2} \qquad (3.18)$$

where f is the non dimensional axial stress σ/σ_y. Note that f is composed of the chord preload to axial yield force ratio N/N_y and the term $P_w \cos\theta$ which accounts for H. Thus, the reduced web shearing resistance is

$$V_p' = \tau' h \cdot t_o = V_p \sqrt{1 - f^2} \tag{3.19}$$

The reduction in plastic moment capacity per unit length depends both on the chord axial force and the angle between a hinge line and the longitudinal axis. The plastic moment capacity M_p per unit length is affected to a maximum extent by the axial force if the hinge line is perpendicular to the x-axis (Figure 3.5(c)) but is little influenced when parallel. Consequently the plastic moment capacity per unit length M_p' is given by (12)

$$M_p' = M_p \cdot \left[1 - f^2 \cos^4 \phi\right] \tag{3.20}$$

The modified strength may then be defined by

$$P_b' = P_b - R \tag{3.21}$$

where R is the reduction in strength caused by the axial forces. Hence

$$P_w = (P_b - R)/(2 \sin\theta) \tag{3.22}$$

represents the design equation for double chord K-joints. Because the expression for R will involve P_w, (3.22) must be solved by trial employing a simple iterative procedure.

3.5.2 Trapezoidal Mechanism Model

Referring to Figure 3.1, it is evident that plastic moments at yield lines 1, 2 and 5 will remain unchanged whereas those at 3 and 4 will reduce to

$$M'_p = M_p\left[1 - \frac{f^2}{\left(1 + \frac{s^2}{4b^2}\right)^2}\right] \quad \ldots. \qquad (3.23)$$

The modified strength equation can be written as

$$P'_b = 4M_p\left[\frac{2u + 2s}{b}\right] + 4M'_p\left[\frac{4b}{s} + \frac{s}{b}\right] + 4V'_p \qquad (3.24)$$

Substituting for M_p, M'_p and V'_p and collecting terms, one obtains

$$P'_b = \sigma_y t_o^2 \left[\frac{2u + 3s}{b} + \frac{4b}{s} + \frac{4h}{\sqrt{3}\, t_o}\right] -$$

$$\sigma_y t_o^2\left[\left(\frac{4b}{s} + \frac{s}{b}\right)\left(1 - \frac{f^2}{\left(1 + \frac{s^2}{4b^2}\right)^2}\right) + \frac{4h}{\sqrt{3}\, t_o}\left(1 - \sqrt{1 - f^2}\right)\right]$$

$$\ldots.. \qquad (3.25)$$

Comparing (3.7) and (3.25), it appears that the reduction in strength is given by:

$$R = \sigma_y \cdot t_o^2[(\frac{4b}{s} + \frac{s}{b})\frac{f^2}{(1 + \frac{s^2}{4b^2})^2} +$$

$$\frac{4h}{t_o\sqrt{3}}(1 - \sqrt{1 - f^2})] \qquad (3.26)$$

3.5.3 Conical Mechanism Model

A similar procedure can be followed to calculate the modified strength for the conical mechanism with reference now made to Figure 3.5 for identification of the yield lines involved. In view of Equation 3.20 the reduced moments are:

$$= M_p[1 - f^2\sin^4\phi_j], \; j = 5 \qquad (3.27a)$$

$$= M_p[1 - f^2\cos^4\phi_j], \quad j = 1,4 \qquad (3.27b)$$

$$= M_p \qquad , \quad j = 2,3 \qquad (3.27c)$$

After integrating in accordance with (3.9), it can be shown that the reduction in strength, R, caused by the axial stresses in the flange and web sections is given by

$$R = \frac{8}{r_o - r_i} M_p f^2\{r_o(\frac{3}{4}\alpha + \frac{\sin 4(\alpha + \beta)}{16} - \frac{\sin 4\beta}{16})$$

$$- r_1 \frac{\sin 2\gamma}{2} - \frac{v}{2}\{\cos\beta - \cos\gamma + \frac{\cos^3\gamma}{3} - \frac{\cos^3\beta}{3}$$

$$- \cos(\alpha + \beta) + \frac{\cos^3(\alpha + \beta)}{3}] + b_o[\cos(\alpha + \beta) - \frac{\cos^3(\alpha + \beta)}{3}]\}$$

$$+ 4h\ t_o \frac{\sigma_y}{\sqrt{3}}(1 + r)\{1 - \sqrt{1 - f^2}\} \qquad (3.28)$$

3.6 Comparison of K-Joint Results with Tests

The experimental results of 29 tests performed on four different types of double chord K-joints were reported by Korol and Chidiac (1). Among these, there were twelve joints having separated double chords and diagonals of square HSS. From the diagonal member force-displacement curves of that work, the loads P_d were determined based on the 2% b_o local deflection criterion as described earlier in Section 2.6. To compare the test results with the strength theory just described, a prescription for the gap was needed because the diagonals had not been end cut parallel to each other, but rather conformed to the detail shown in Figure 3.9. Because of bridging action that occurs between diagonals, the stress lines tend to converge at the toes (30). The effective gap will be somewhat larger than the clear space between weldments, s', but less than the centre-to-centre distance of diagonals, with respect to the chord's centreline. A gap distance s of 2c was selected for convenience in computing P_w from Equation 3.22.

The results of predicted strength of the K-joint with experimentally attained values are plotted in Figures 3.10 and 3.11 for the trapezoidal and conical mechanisms. The theoretically obtained strength P_w is observed to be generally slightly lower than the deformation load limit value P_{wd} for both mechanisms. The average difference between corresponding values was computed to be 2% and 6% for the trapezoidal and conical models respectively.

3.7 Variation of Parameters

To assess the influence of varying the geometrical properties on the strength of double chord RHS K-joints, a sensitivity analysis was undertaken using the conical model. Typical strength results of the analysis corresponding to the yield load P_w for K-joints are presented in Figure 3.12. The branch members have been taken as 100 mm squares with 5 mm wall thicknesses and positioned at a 2:1 slope with respect to the chord ($\theta = 63.4°$). The chord preloading force, N, will be assumed to be zero.

Figure 3.12(a) shows the effect of varying the gap distance for different widths of chord. The gap for which the strength P_w is a minimum corresponds to mechanism (b) in Figure 3.6. A larger gap activates the outer webs in shear thus having a positive effect on strength (Figure 3.6(a)). On the other hand, a reduction in the gap causes the bending energy due to large angle changes along the yield lines to become increasingly dominant.

Localizing the mechanism as in Figure 3.6(c) is the cause of no improvement in strength with increasing b_o beyond a certain minimum level that depends on the gaps. This is clearly evident in Figure 3.12(b) by the horizontal strength lines. In contrast, an increasing depth provides consistent benefits in strength since shear resistance is linearly proportional to depth. This attribute is demonstrated in Figure 3.12(c) for varying chord thicknesses. Figure 3.13 demonstrates the effect of chord axial load on joint strength for a particular joint geometry indicated. It is obvious that by varying the geometrical parameters of the joint different paths will evolve; the two limiting points of $N/N_y = 1.0$ and $P_w/P_w^\circ = 1.0$ will however be common for all possible curves. It may be discerned from the illustrated example that chord axial loads should not be ignored if they are in the order of 20% or more of the chord yield load. Finally Figure 3.14 suggests that joint strength increases as the angle between the chord and the diagonal becomes smaller. Such a behaviour can be easily deduced from examining Equation 3.22.

3.8 Discussion

The trapezoidal and conical mechanisms developed in this study have been found to provide a basis for predicting the strength of double chord standard RHS K-joints subjected to high shear forces. The analyses are based on the well known yield line theory of plates and account for localized flange bending of the chord including the effects of chord axial force. Although the analyses have been demonstrated only on K-joints, they are equally applicable to other double chord gap joints of the separated type. . This can be accomplished by appropriately using Equation 3.22 in conjunction with Equations 3.26 or 3.28 that are applicable to the trapezoidal and conical mechanisms respectively.

It may be concluded from both models that the shearing resistance of the connection is primarily dependent upon its chord aspect ratio (h_o/b_o). Both theory and experiments confirm that the joint strength is improved when that ratio is increased. From the conical mechanism model, it is shown that the connection's geometrical properties determine the type of mechanism that is applicable for a given configuration, and this in turn affects the degree to which the outer webs contribute in resisting diagonal member forces. For example, a high depth-to-width ratio (h_o/b_o) and a relatively large gap-to-depth ratio (s/h_o) will ensure full participation by the outer webs. The opposite extremes lead to very localized yielding in the regions surrounding the gap of the inner webs, and thus exclude the outer webs as shear resisting elements.

Predictions of joint strength were compared with experimental strength limits based on a local displacement of 0.01 ($b_o + h_o$) rather than on ultimate values that are associated with unacceptable large deformations. The analytical results show the models to be consistent in providing good agreement both for tests conducted on RHS twin shear beams and on isolated K-joint specimens of square hollow section of a previous study.

The trapezoidal mechanism, besides being simple and easy to use for design purposes, has provided remarkable agreement with experimental results of both shear beams and K-joints. Despite the fact that the outer web's resistance does not enter into the strength expression, the deviation from experimental data is very slight; this is perhaps because at yield load level, the outer web is not yet active in resisting shear. If the model were to be extended for ultimate strength analysis, then it would underestimate the joint's ultimate capacity and empirical factors would have to be introduced to account for outer web shearing resistance (28).

On the other hand, the conical mechanism gave slightly poorer results than the trapezoidal mechanism. However, for other than the large gapped specimen, the agreement was also quite satisfactory. It should be noted that both models do not account for the reduction in strength due to the bending moment acting on the critical section. This bending moment, however, becomes rather insignificant for small gap sizes.

Table (3.1) Double Shear Beam Experimental and Analytical Results

Specimen No.	P_d (KN)	P_{ult} (KN)	P_b^* (KN)	P_b^{**} (kN)	P_{int}^{***} (kN)
1a	280	496	272	285	251
1b	324	571	346	349	290
2a	328	661	304	318	314
2b	378	552	356	362	361
2c	401	628	457	446	379
2d	438	616	505	483	377
3a	375	680	347	359	381
3b	421	727	403	412	461
4a	506	830	571	626	700
4b	567	932	587	602	840
4c	617	1042	669	681	970
4d	801	1113	802	796	1050
8a	901	1450	1027	1107	1325
8b	1081	1661	1099	1116	1645
8c	1050	1622	1119	1111	1657
8d	1184	1618	1383	1301	1750
5a	506	986	550	790	521
5b	644	1157	531	560	628
6a	562	1077	554	828	480
6b	680	1063	541	683	597
6c	668	1110	556	600	672
6d	742	1108	584	689	710
7a	505	943	596	911	463
7b	679	1218	558	800	565

* Predictions from trapezoidal mechanism

** Predictions from conical mechanism

*** Predictions from elasto-plastic interaction equation of Korol and Keen (22)

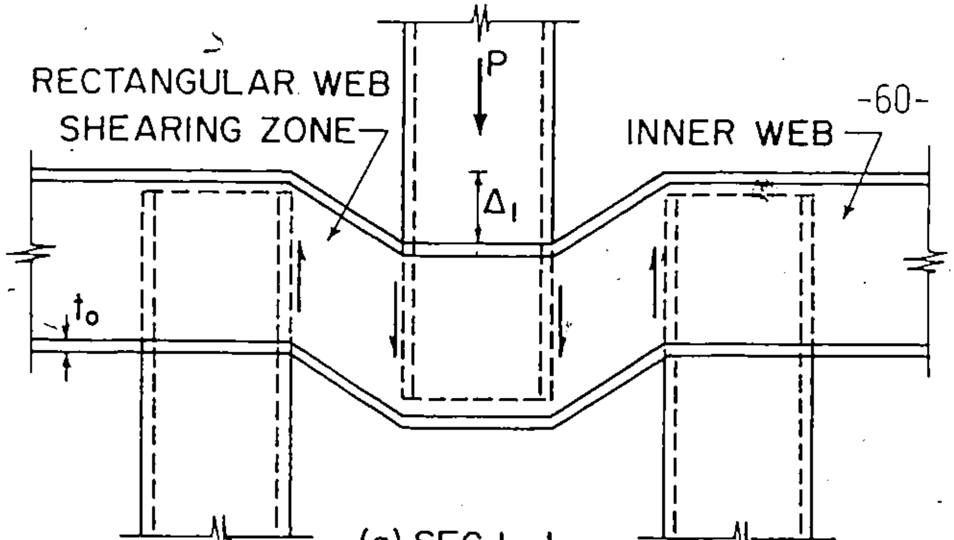
RECTANGULAR WEB SHEARING ZONE
P
Δ_1
INNER WEB
t_o

(a) SEC. 1-1

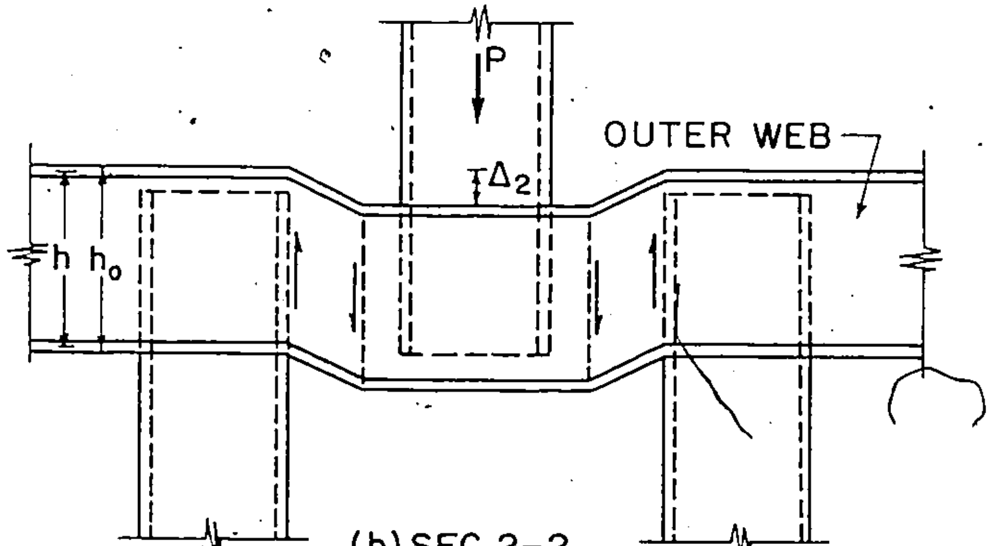
P
Δ_2
OUTER WEB
h
h_o

(b) SEC. 2-2

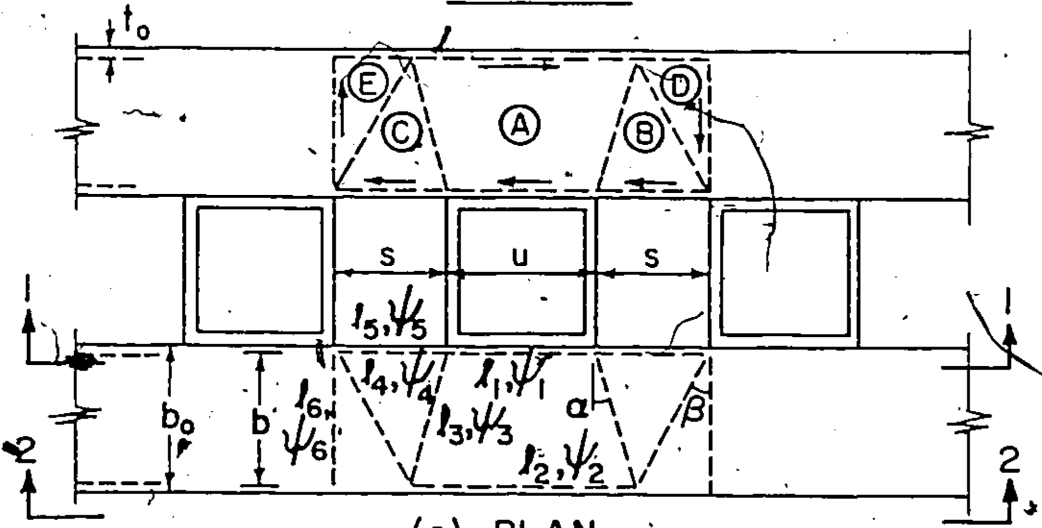
t_o
Ⓔ
Ⓒ
Ⓐ
Ⓑ
Ⓓ
s
u
s
l_5, ψ_5
l_4, ψ_4
l_1, ψ_1
l_6, ψ_6
l_3, ψ_3
l_2, ψ_2
α
β
b_o
b
1
1
2
2

(c) PLAN

FIGURE 3.1 : TRAPEZOIDAL MECHANISM MODEL FOR TWIN SHEAR BEAM

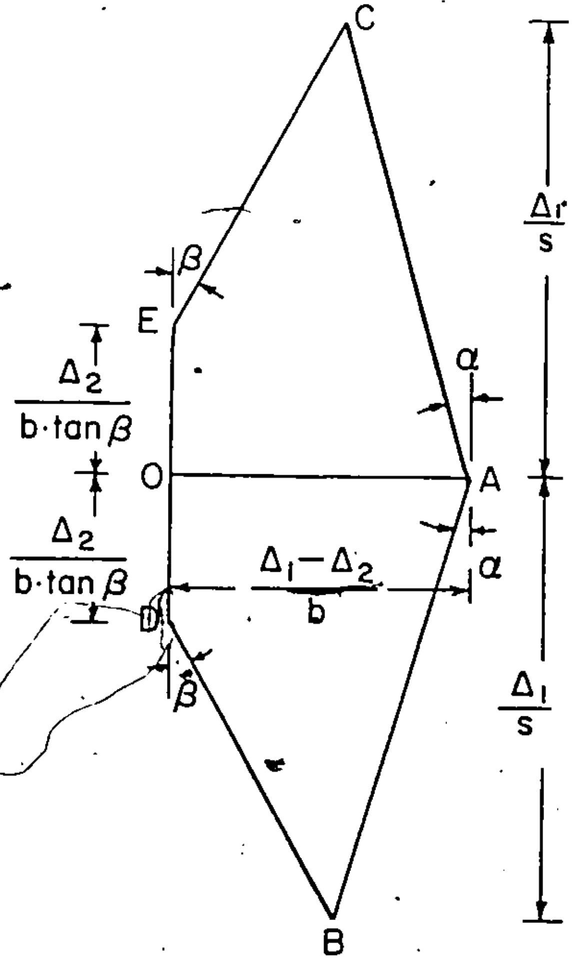
C
E
O
A
D
B
β
β
α
α
$\frac{\Delta_2}{b \cdot \tan\beta}$
$\frac{\Delta_2}{b \cdot \tan\beta}$
$\frac{\Delta_1 - \Delta_2}{b}$
$\frac{\Delta_r}{s}$
$\frac{\Delta_1}{s}$

NOTE: POINTS A, B, C, D AND E REFER TO ZONE A, B, C, D AND E RESPECTIVELY AS SHOWN IN FIGURE 3.1c .

FIGURE 3.2 : HODOGRAPH

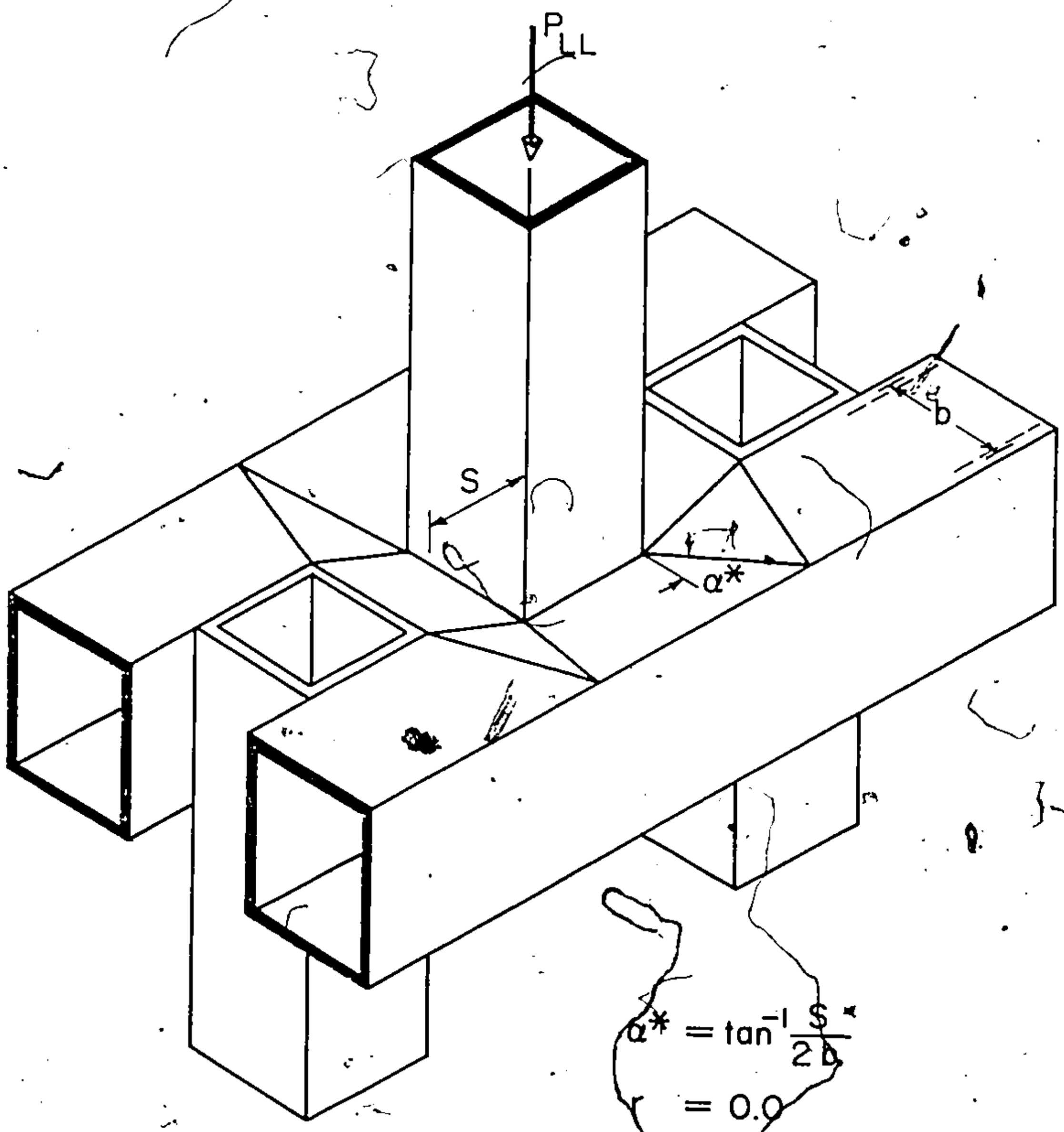
P_{LL}
S
b
α^*
$\alpha^* = \tan^{-1}\frac{S}{2b}$
$r = 0.0$

FIGURE 3.3 : LOWER LIMIT FAILURE MECHANISM

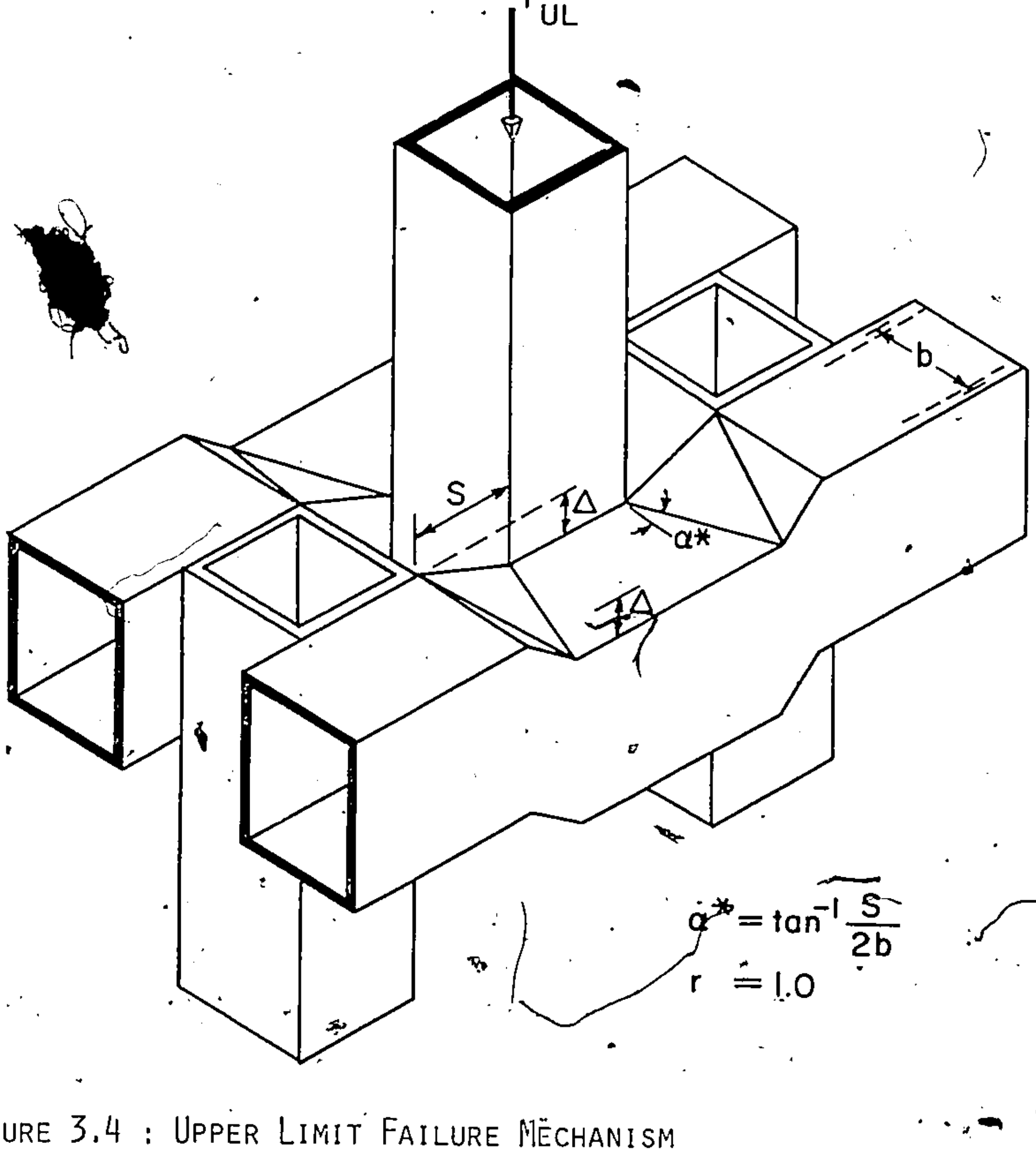
P_{UL}
b
S
Δ
α*
Δ
$\alpha^* = \tan^{-1}\frac{S}{2b}$
$r = 1.0$

FIGURE 3.4 : UPPER LIMIT FAILURE MECHANISM

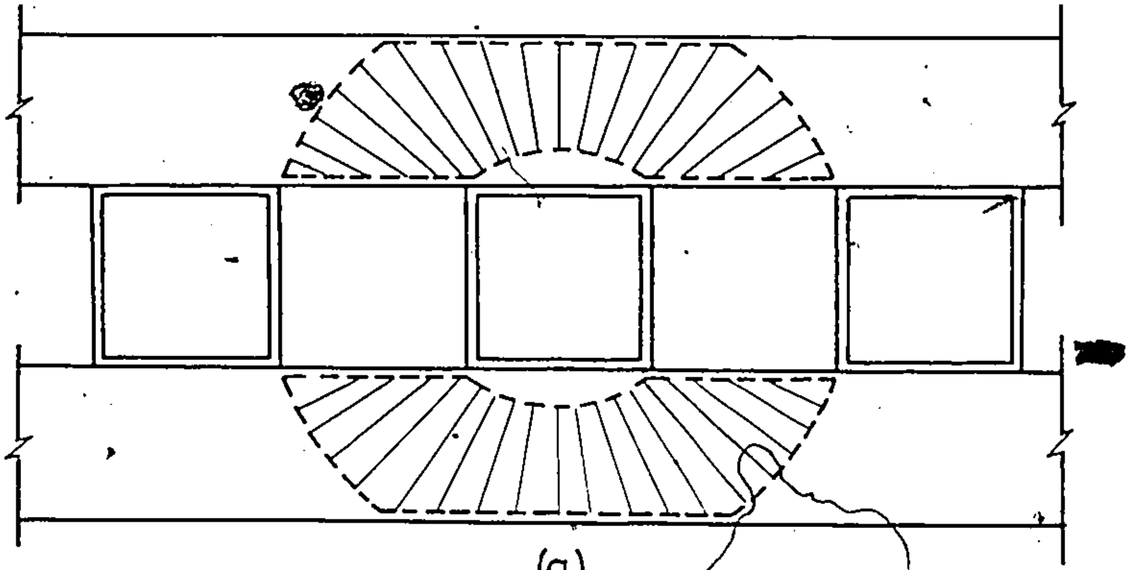

(a)

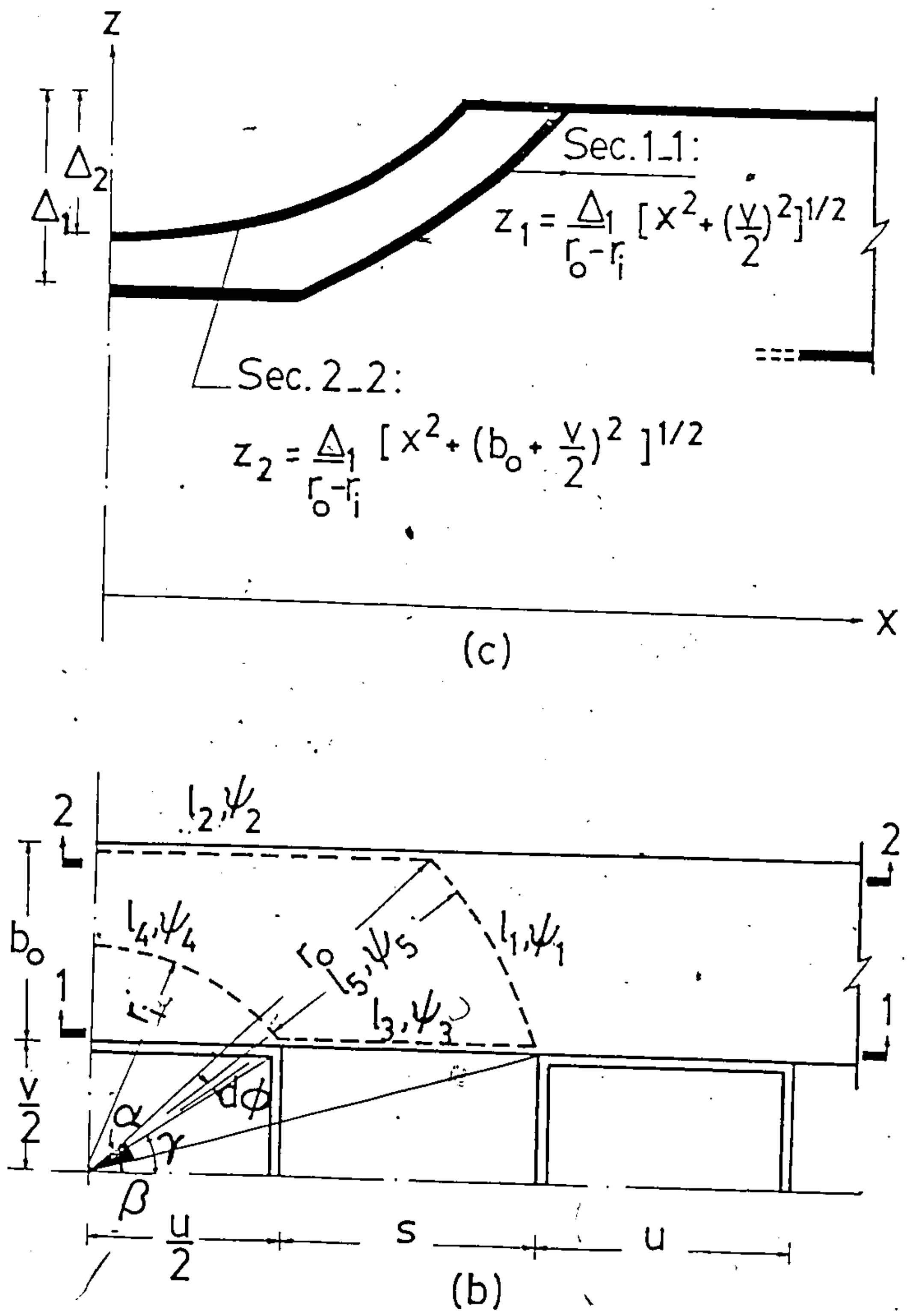
z
Δ2
Δ1
Sec. 1_1:
z1 = Δ1/(ro-ri) [x2+(v/2)2]1/2
Sec. 2_2:
z2 = Δ1/(ro-ri) [x2+(bo+v/2)2]1/2
x
(c)
2
l2,ψ2
2
bo
l4,ψ4
ri
ro
l5,ψ5
l1,ψ1
1
l3,ψ3
1
v/2
dφ
α
γ
β
u/2
s
u
(b)

FIGURE 3.5 : CONICAL MECHANISM MODEL FOR TWIN SHEAR BEAM

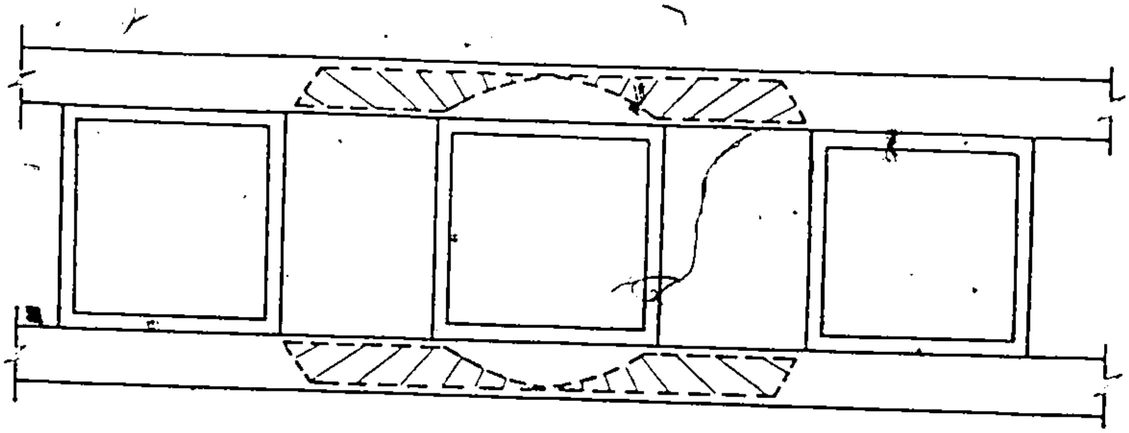

(a) Case 1 : $r_o \quad b_o + v/2$

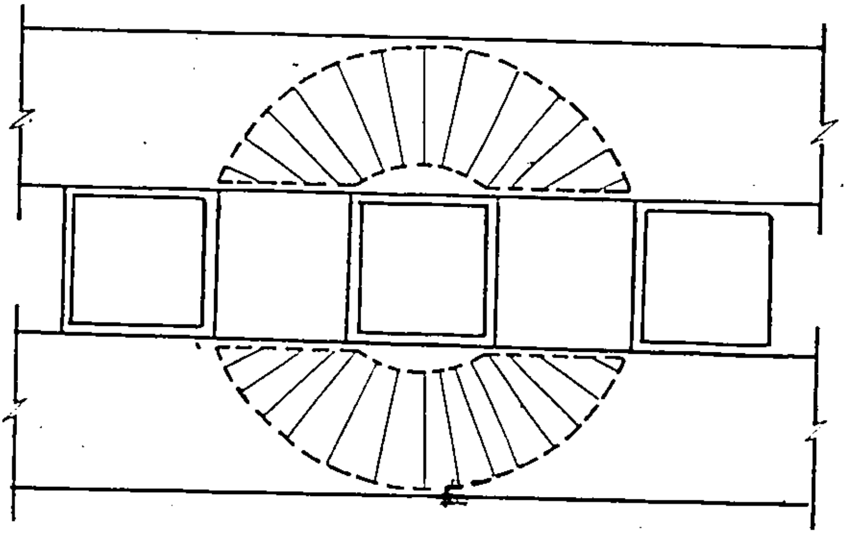

(b) Case 2 : $r_o = b_o + v/2$

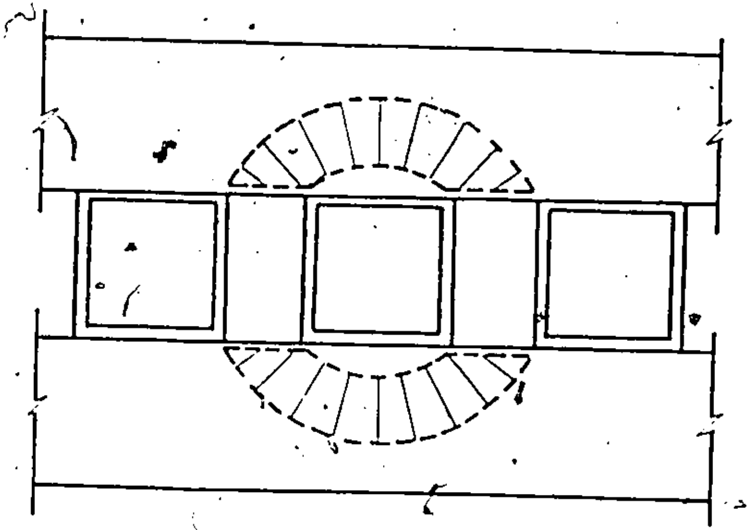

(c) Case 3 : $r_o \quad b_o + v/2$

FIGURE 3.6 : VARIOUS CONICAL MECHANISMS

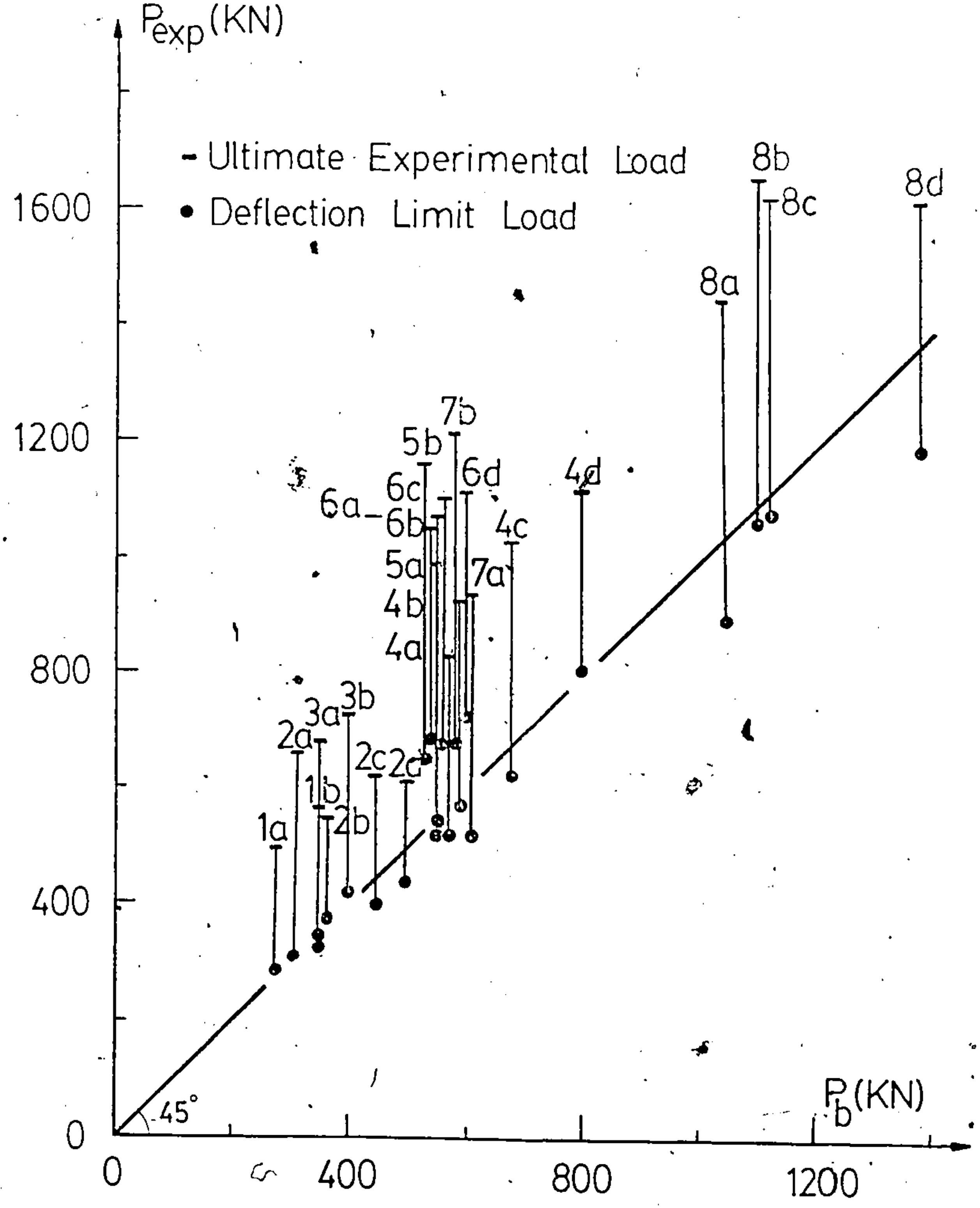

FIGURE 3.7 : COMPARISON OF EXPERIMENTAL AND ANALYTICAL SHEAR BEAM LOADS - TRAPEZOIDAL MECHANISM

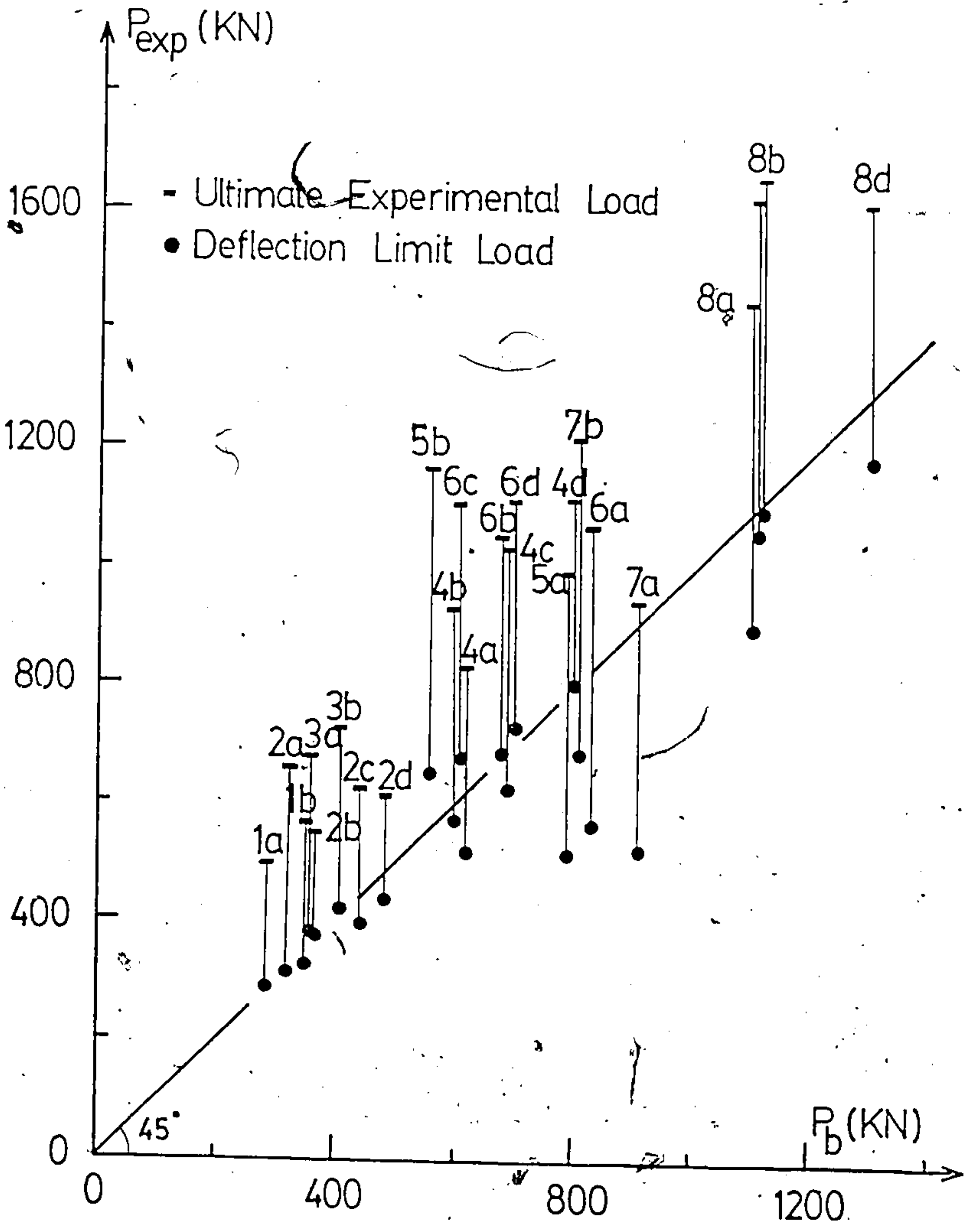

FIGURE 3.8 : COMPARISON OF EXPERIMENTAL AND ANALYTICAL SHEAR BEAM LOADS - CONICAL MECHANISM

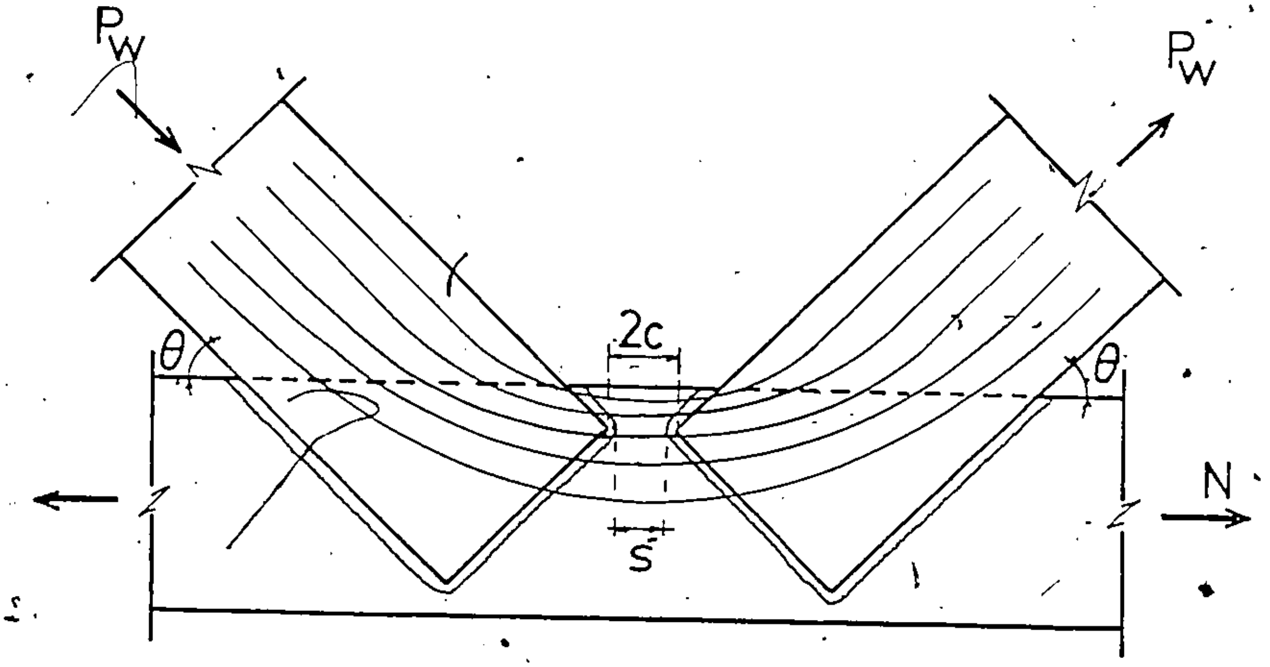
P_W
P_W
2c
θ
θ
s
N

FIGURE 3.9 : FORM OF STRESS LINES DEVELOPED IN A K-JOINT

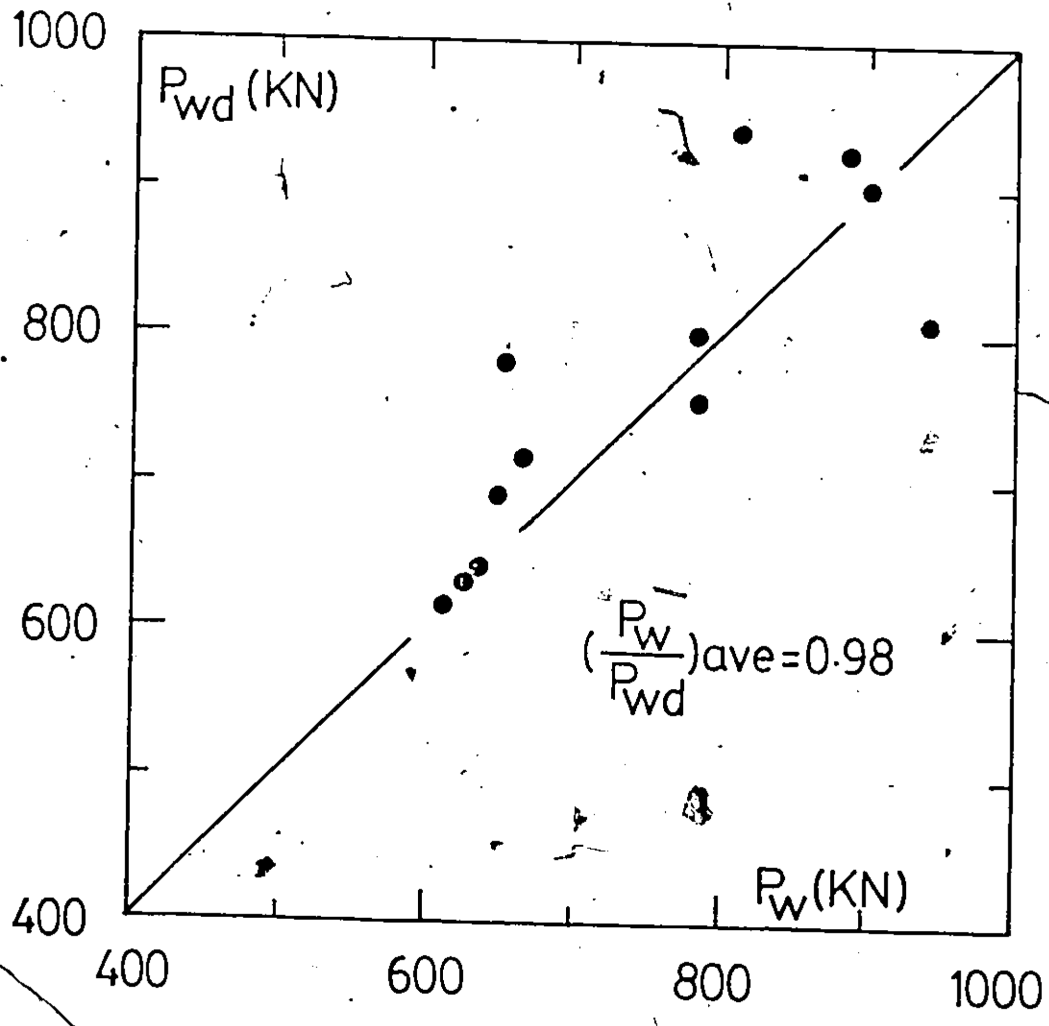

FIGURE 3.10 : CORRELATION BETWEEN TRAPEZOIDAL MODEL AND TEST RESULTS OF K-JOINTS

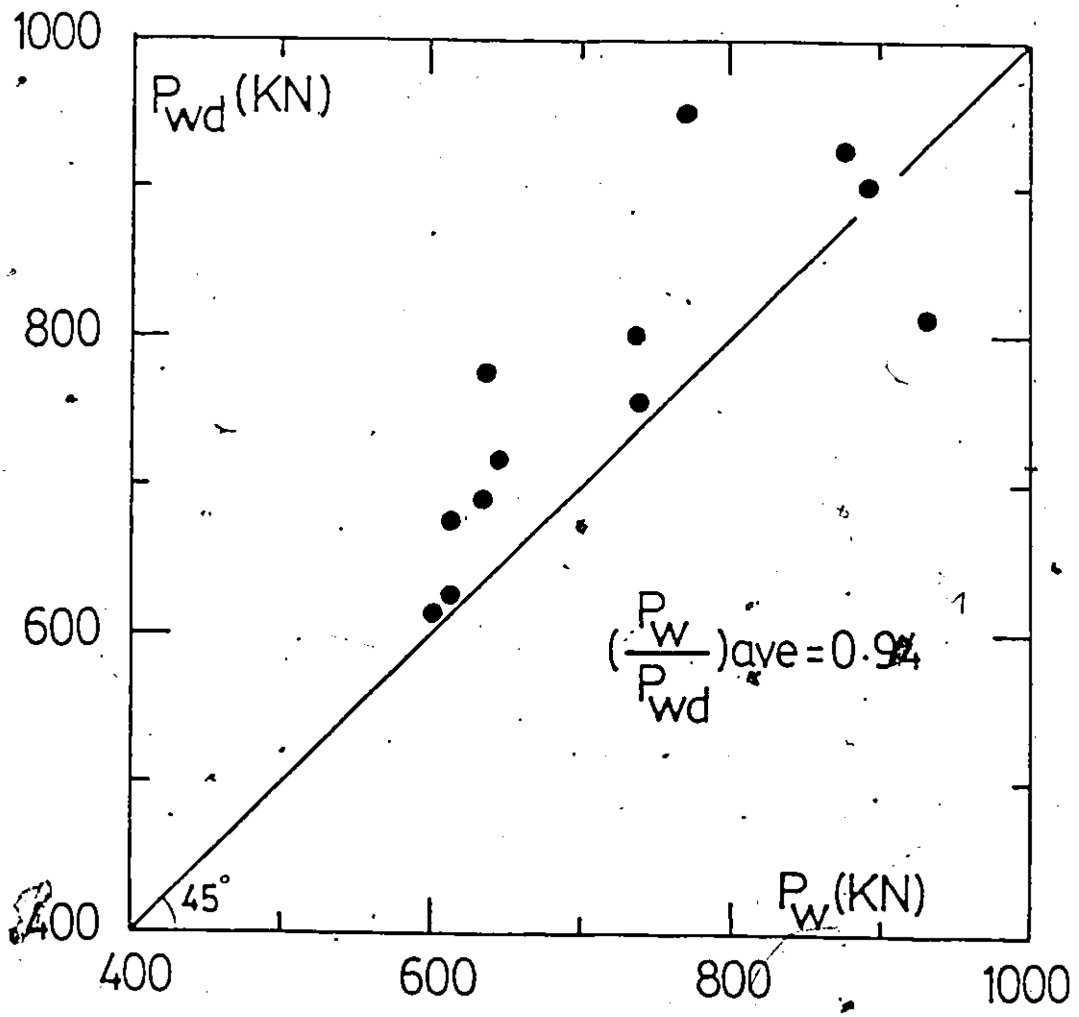

FIGURE 3.11 : CORRELATION BETWEEN CONICAL MODEL AND TEST RESULTS OF K-JOINTS

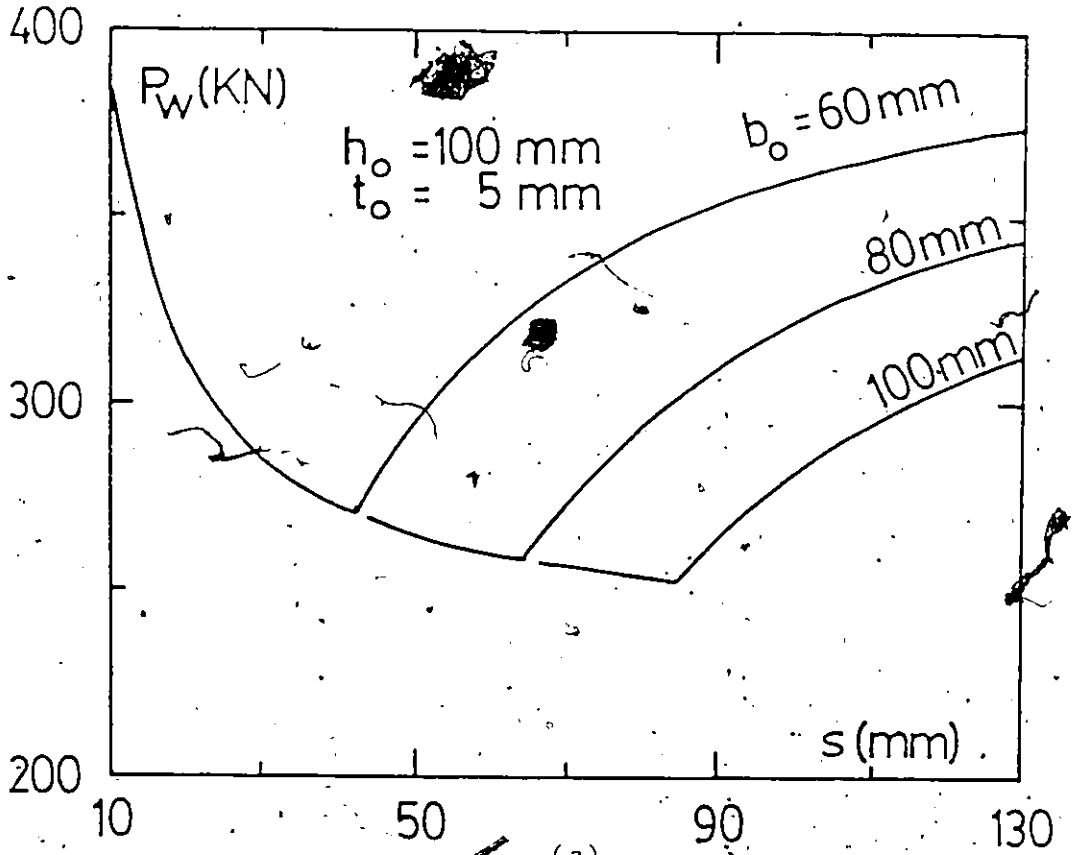

400
300
200
P_W(KN)
h_o =100 mm
t_o = 5 mm
b_o =60 mm
80 mm
100 mm
s (mm)
10
50
90
130

(a)

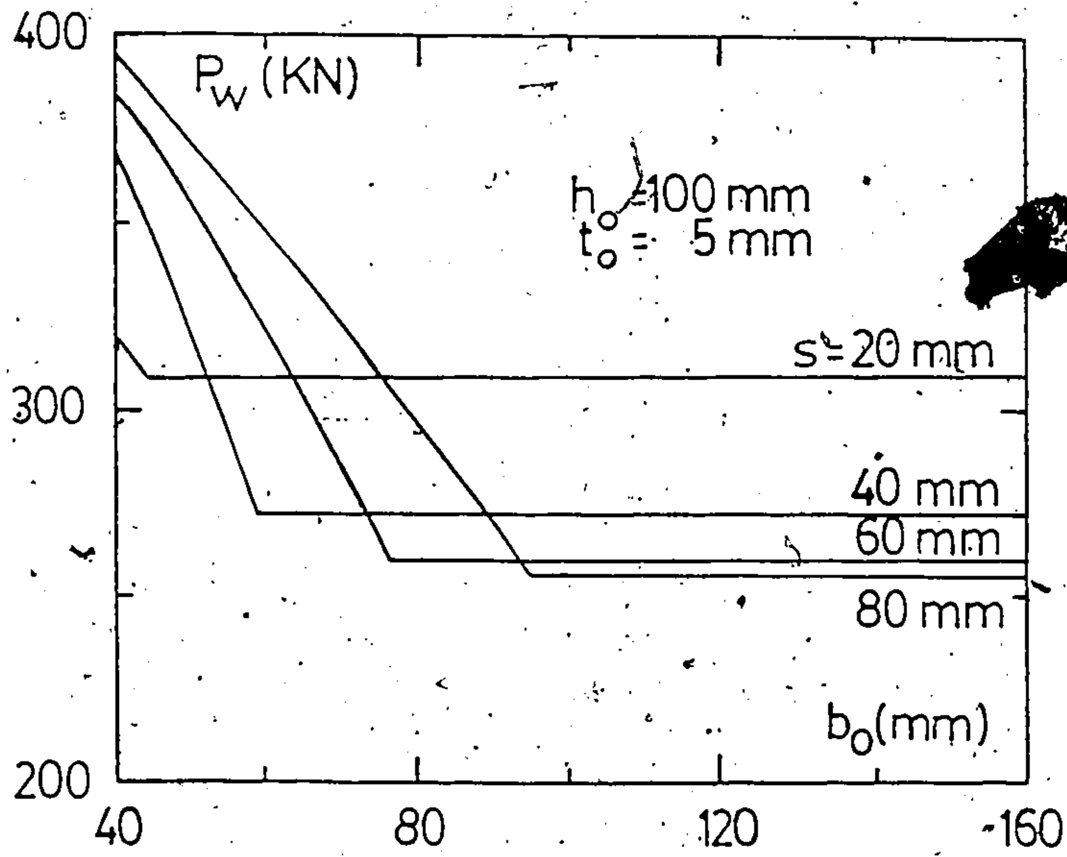

400
300
200
P_W (KN)
h_o =100 mm
t_o = 5 mm
s = 20 mm
40 mm
60 mm
80 mm
b_o(mm)
40
80
120
160

(b)

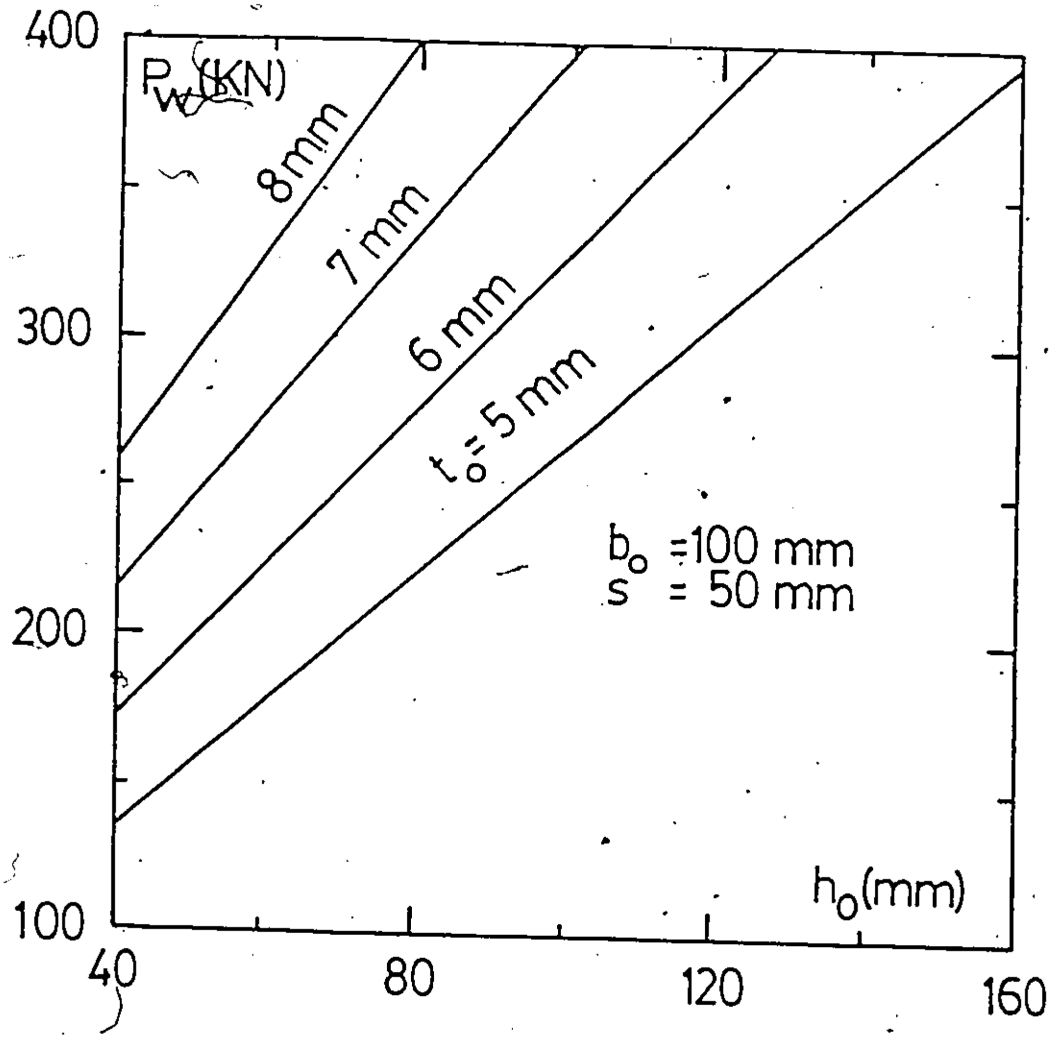

(c)

FIGURE 3.12 : VARIATION OF PARAMETERS FOR RHS DOUBLE CHORD K-JOINT - CONICAL MECHANISM

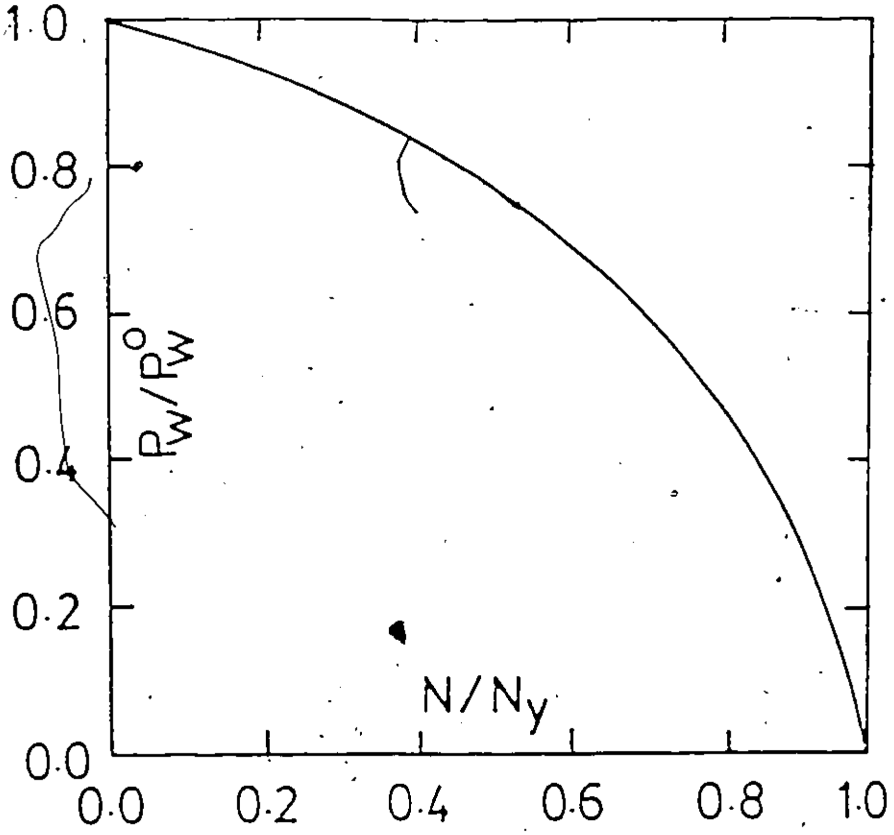

FIGURE 3.13 : INTERACTION BETWEEN K-JOINT STRENGTH AND ITS PRELOAD

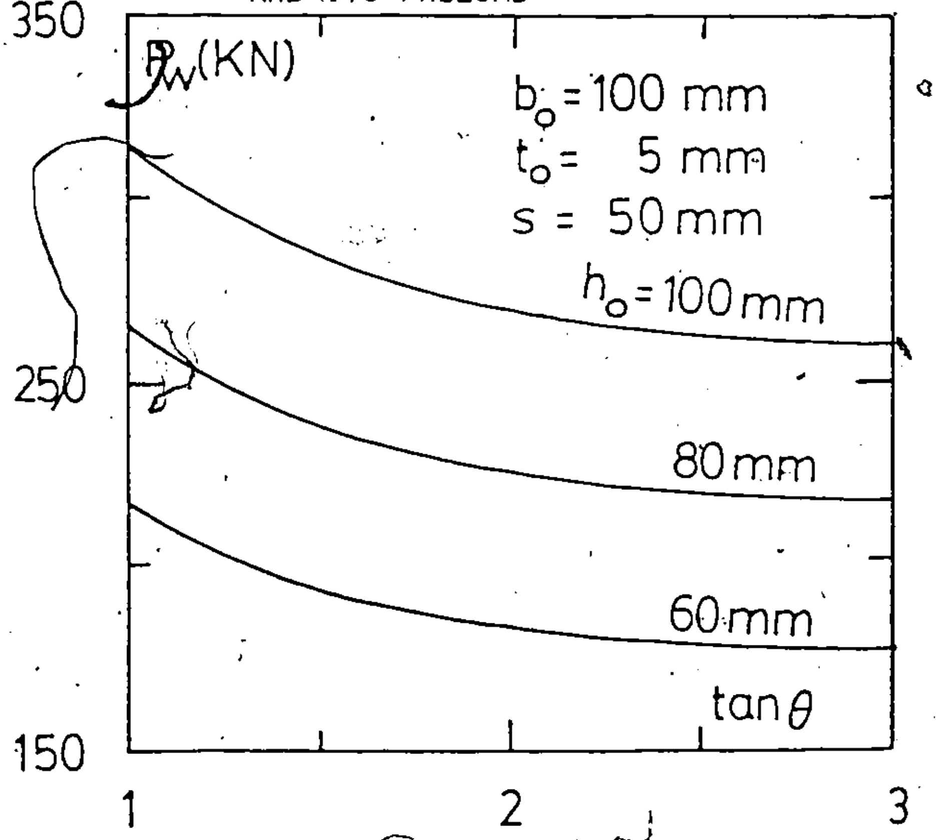

FIGURE 3.14 : EFFECT OF WEB-TO-CHORD MEMBER ANGLE

CHAPTER 4

FINITE ELEMENT MODEL FOR RHS TWIN MEMBER SHEAR BEAM

4.1 Introduction

With the aid of digital computers, the finite element method (FEM) appears to be one of the most powerful tools for analysis of complex structures. The approach is based on subdividing the structure into a number of discrete elements with assumed types of displacement fields. Knowledge of these fields enables the derivation of the elements' stiffness matrices. The solution is then obtained by assembling the stiffness matrices of these elements in such a way that the compatability conditions at element interfaces are satisfied, then solving the system of equations for the unknown displacements. Further details of the basic concepts of the FEM method can be found in references (33) and (34).

In this Chapter, a review of the various numerical models simulating rectangular hollow section (RHS) T and K-joints is first outlined. This is followed by a description of the proposed finite element model for the RHS twin member shear beam. Such a description includes the type of elements employed, discretization and the boundary conditions used. Finally, the idealized stress-strain relationship and the associated properties of the steel used are explained.

4.2 Modelling of RHS Joints-Historical Review

Several studies have been undertaken over the past two decades to model the different RHS connections by numerical methods. The first attempt was made by Redwood (13) in 1965 for elastic analysis of unreinforced T-joints of unequal width. The plate bending of the top flange of the chord member was solved by the finite difference method (FDM). The restraining effect offered by the remainder of the chord section was incorporated through the boundary conditions of the top flange plate in the form of a roller (to prevent vertical deflections) and a rotational spring (to resist rotation) as shown in Figure 4.1(a). In 1979, Korol and Mansour (14) presented a model for haunch reinforced T-joints consisting of square RHS that accounted for both deflections and rotations occurring near the rounded corners of the RHS chord face. This was achieved by introducing translational and rotational flexibilities of the springs shown in Figure 4.1(b). The elastic solution of the top flange plate was then obtained using the FDM. El-Hifnawy (15) and Korol and Mirza (16), then solved the problem by the FEM by discretizing the top flange plate into a number of rectangular nonconforming plate bending elements (12 degress of freedom (DOF) per element). The plate was supported by two coupled edge springs, translational and rotational, whose coefficients were calculated from stiffness analyses of the adjacent U-frames representing the rest of the RHS as indicated in Figure 4.1(c). Each U-frame was made of a series of beam-column elements of unit width with 6 DOF per element. Shehata (10) and Mirza et al. (11) further improved this model and applied it to single chord and back-to-back, double chord T-joints. The in-plane stresses occurring in the top flanges were taken into account by adding plane stress rectangular elements (8 DOF per element), thus permitting a third spring coefficient to be included in the analysis; see Figure 4.1(d). As before, direct stiffness analysis of the U-frame was employed for determining the coupled spring coefficient matrix per unit width of the frame. Recently, Ostrowski (17) and Packer et al (18) introduced geometric nonlinearities into Shehata's model (10) and applied it to single chord K-joints with small branch-to-chord width ratio. In Norway, Strommen (31) used a finite element package called ABAQUS to simulate behaviour of an RHS single chord K-joint. The 8-node combined in-plane-shell rectangular element with 5 DOF per node was selected and the analysis was carried out using elastic-perfectly plastic material properties.

In all of the analyses above, the area of the flange plate inscribed by the branch member was assumed infinitely rigid whether the applied load was punching shear or bending moment. Also, in all but one (31), the chord member webs were assumed not to deflect in their vertical plane with the intention to focus on local joint behaviour alone. While these assumptions well suited T-joint applications, it was pointed out by Ostrowski in his K-joint model that better performance could be achieved if a more flexible inclusion was used. It was also recommended by Packer et al. (18) that the K-joint model be applied to joints for which the branch-to-chord width ratio is less than about 0.8.

It should be noticed that, in general, the trend was always to focus on solving the top flange plate numerically (using FDM or FEM) after separating it from the rest of the chord member section. The influence of the latter was included through a set of uncoupled or coupled edge springs.

4.3 Basic Finite Element Model

It is evident from Figure 4.2(a) that because of the symmetry inherent in the double chord section, only one half of the joint cross section needs to be modelled. Based on the test results described earlier, it is suggested that the inner web plate be modelled by the finite element method and the rest of the chord section be considered to assess the amount of restraint acting along the plate boundaries. As such, the basic model treats the RHS section as composed of a thin plate representing the inner web and a channel grillage representing the top and bottom flanges and the outer web.

In this model, the channel is treated as a substructure; thus in order to obtain the total stiffness matrix of the twin shear beam, it is necessary to do the following.

(1) Formulate the global stiffness matrices of the inner web plate and the channel separately,

(2) Condense the channel into a smaller size matrix (or set of matrices). The influence coefficients of this matrix correspond to the 3 degrees of freedom at every node of the channel-inner web interface as indicated in Figures 4.2(b) and 4.3.

and

(3) Add the stiffness matrices of the inner web plate and the condensed channel according to the compatibility requirement.

This 3-step procedure to compute the total stiffness matrix has certain merits over the classical procedure. While each of the two components of the model (i.e. the plate and the channel) has a considerably large sized stiffness matrix, a common high speed storage in the computer can be allocated because of the nature of substructuring adopted in the model. Indeed, the entire operations of both components can be overlayed, with some bookkeeping scheme, throughout the computational process. Another advantage of this procedure is that it permits analysing each component of the model separately (if desired), thus providing more insight and understanding of the model performance.

Step (2), which involves the estimation of the channel's effect on the inner web plate, is an inherent part of the model. Two methods of analysis, called uncoupled and coupled, are proposed for this purpose.

The uncoupled analysis aims at simulating the channel's resistance by a series of boundary springs located at the top and bottom edges of the inner web plate. Each spring contains 6 coupled DOF that correspond to two translations $\tilde{u}$, $\tilde{v}$ and a rotation $\tilde{\Theta}_z$ at the top and bottom ends of a C-shaped frame (Figure 4.2(b)). Thus, the springs can be expressed as 6 × 6 stiffness matrices, the number of which is equal to the number of C-frames involved. The procedure to compute the spring coefficients is summarized below.

(1) Assemble the global stiffness matrix of the channel grillage.

(2) Referring to Figure 4.3, apply a unit displacement in the direction of DOF k at node j of the ith C-frame while constraining other DOF at nodes j and j + 1 to zero. All other DOF in the system are allowed to "float", i.e. no restraining.

(3) Calculate the holding forces at all 6 DOF of nodes j and j + 1 resulting from such a displacement. These represent the kth column of the ith boundary spring.

(4) Repeat steps (2) and (3) for other DOF at j and j + 1 for the ith C-frame.

(5) Repeat steps (2) to (4) for each C-frame of the grillage. Hence, there is a 6 × 6 coupled spring for every pair of top and bottom boundary nodes.

Because all boundary DOF, other than those at the ith location, are unlocked during the above process, uncoupling evolves; i.e. the 6 DOF of each spring, although coupled among themselves, are not coupled with the rest of the boundary DOF. This technique is analogous to the one proposed by Shehata (10) but with a major difference in that it is carried out on the entire channel grillage as opposed to an individual U-plane frame in his model.

The coupled method of analysis uses the static condensation procedure. The general steps of the method can be outlined as follows.

(1) Formulate the global stiffness matrix of the channel grillage as before.

(2) Condense the channel stiffness matrix in terms of its boundary DOF. Noting that there are 3 DOF per node on the boundary of the grillage, and if there are m C-frames, the resulting matrix $[K_c]$ will be 6m × 6m in size.

(3) Since there are also 6m matching DOF available on the inner web plate top and bottom edges, the matrix $[K_c]$ can therefore be added to the inner web plate stiffness matrix maintaining continuity of the nodal displacements along the interfaces.

(4) The matrix $[K_c]$ is fully populated; its use would result in an extremely large bandwidth of the global system. Neglecting the stiffness coefficients in $[K_c]$ that are sufficiently remote from its diagonal (which are logically very small in magnitude) would help reduce the problem size and improve the model efficiency. The extent to which the bandwidth of $[K_c]$ can be reduced is determined through numerical tests to be presented in Chapter 6.

Both uncoupled and coupled methods are explained in more detail in Chapter 5.

4.4 Inner Web Plate - Discretization and Boundary Conditions

As indicated in Figure 4.4(a), the plate is subdivided into rectangular elements in the X-Y plane. The resulting mesh of elements has dimensions of $(h_o - 3t_o) \times (s + 3h_1/2)$, where h_o is the chord member height, t_o its thickness, s the gap distance and h_1 the branch member depth. The plate is loaded in its plane (X-Y) by a uniformly distributed pressure acting downwards through the branch member. The overlapping part of the branch member is composed of an outstanding leg and a web. The outstanding leg was discretized into plane stress rectangular elements of thickness $(b_1/2)$ and width t_1, where b_1 is the width of the branch member and t_1 its thickness. Bending of these elements out of the X-Y plane was precluded because of the condition of symmetry. The web of the branch member is subdivided into a number of nonconforming plate bending-plane stress elements (20 DOF per element). This resulted in two layers of elements, namely the chord inner web layer and the branch member web layer of thicknesses t_o and t_1 respectively; see Figure 4.4(a). The two layers have different internal nodes and hence different DOF. However, along the boundaries, common nodes are specified for both layers to satisfy the compatibility condition arising from welding the branch member to the chord inner web. As was mentioned in Section 2.2.2, there exists two patterns of welding the support columns to the inner web of the chord member. Accordingly, two different grids are generated in the model. Figures 4.5 and 4.6 illustrate such grids. A roller support was placed along the left bottom boundary of the plate Figure 4.4(b) to replace the reactive stub column. It is worth noting that vertical elastic springs were used in early attempts to simulate the support column. The results obtained were not different from those with roller supports.

It may be noticed that the branch members have been terminated at top and bottom flange levels of the chord member. It was assumed that the removed portions would not play an important role in the twin beam behaviour.

4.5 Top Flange, Bottom Flange and Outer Web

The remaining portion of the RHS section takes the form of a channel as shown in Figure 4.7. This is modelled as a grillage of beam elements both in the longitudinal and transverse directions. The grillage can be envisaged as being constructed from a number of transverse C-shaped plane frames located in (or parallel to) the global Y-Z plane of the inner web (Figure 4.4) and longitudinally connected by beam elements. While beam-column elements (6 DOF per element) are used for the transverse C-frames, combined beam bending-pure shear elements (6 DOF per element) are employed to link the C-frames in the longitudinal direction on all three sides of the channel. The resulting grillage has 4 DOF per node; i.e. two translations $\tilde{u}$ and $\tilde{v}$ in the $\tilde{x}$ and $\tilde{y}$ directions of the channel, and two rotations $\tilde{\Theta}_x$ and $\tilde{Q}_z$ about the $\tilde{x}$ and $\tilde{z}$ axes, respectively. The rotation $\tilde{\Theta}_y$ was assumed to have very little influence on the deformation of the channel. This assumption is based on the experimental observations. For the same reason, the longitudinal axial displacement in the $\tilde{z}$ direction was discarded. As depicted in Figure 4.7, the generalized displacements of beam-column elements are u, w and

Θ. The latter corresponds to $\tilde{\Theta}_z$ in the channel global co-ordinate system. On the other hand, the beam elements running in the $\tilde{z}$ direction have nodal displacements v, w and ϕ. Figure 4.7(b) shows a beam element representing the channel top or bottom flange. Such an element (which will be referred to as the flange element) resists shear due to bending in the $\tilde{y}$-direction (out-of-plane) and pure shear in the $\tilde{x}$-direction (in-plane). The rotation ϕ in this case corresponds to $\tilde{\Theta}_x$. The same element is used to simulate the outer web but rotated by ninety degrees about the $\tilde{z}$ axis as shown in Figure 4.7(c). It should be noticed that ϕ now corresponds to $\tilde{\Theta}_y$ and is therefore set to zero. This element will be referred to as the web element.

Typically, there are 12 beam-column elements per C-frame (Figure 4.8) and 17 beam element in $\tilde{z}$ direction joining every pair of C-frames (Figure 4.9). The web elements in $\tilde{z}$ direction at the tips of the channel have a depth of t_o each. Implicit in this assumption is that the depth of the inner web plate that is effective in pure shear is $(h_o - t_o)$. This is consistent with the strength analysis presented earlier in Chapter 3. The widths of all elements of the grillage are simply taken as the centre-to-centre distance between the nodes. The number and locations of the centre lines of transverse C-frames vary according to the anticipated stress levels and the type of stiffness analysis performed on the channel and as such they will be defined later.

4.6 Modelling of Material Properties

The material properties play an important role in the behaviour of the joint assembly. As such, it is important to identify these properties with reasonable accuracy. In RHS joints, the material used is structural steel which, fortunately, exhibits to a great extent, consistent behaviour. Research has been done previously to develop approximate uniaxial stress-strain relationships; a review of the subject is not intended in this study. For structural steel, a tri-linear stress-strain relation is considered to be sufficiently accurate for most applications (32). Initially, the material is elastic with the stress-strain relation a straight line having a slope E (Young's Modulus). This is followed by a plastic plateau which is a horizontal line extending from the point of elastic limit strain ε_y to the strain ε_{st} beyond which strain hardening begins. The third line, then, represents material strain hardening with a slope of E_{st}.

If one attempts to further simplify the tri-linear behaviour to a bilinear one, then only values of the yield stress and the tangent modulus E_T are to be specified. From the uniaxial test results undertaken on the RHS twin shear beam coupons, such values were selected for a "best fit" to the actual stress-strain curve. The "bi-linear" yield stress values and the associated tangent moduli are listed in Table 4.1 for each of the 24 specimens tested.

For K-joint tests, full stress-strain curve data was not available and hence bilinear yield stress values could not be determined. For steels used in the manufacturing of HSS, it is evident from Table 4.1 that the measured yield stress (0.2% offset method) and the bilinear yield value differ by no more than about 10%. As this difference is not excessive, the reported yield stress values (2) were used for modelling joint behaviour using the finite element method. For other than comparing with experimental results, a yield stress of 350 Mpa was employed throughout.

To account for two dimensional plate action, the usual assumption of material isotropy is made. The material is also assumed to follow the Von Mises yield criterion and the associated plastic flow rule.

Table 4.1 Material Properties of Twin Beam Specimens

Specimen	Measured Yield Stress (MPa)	Bilinear Yield Stress (MPa)	E_T/E
1a	338	372	0.025
1b	343	377	0.025
2a	335	369	0.025
2b	334	367	0.025
2c	325	363	0.025
2d	319	378	0.025
3a	337	371	0.025
3b	349	384	0.025
4a	367	373	0.010
4b	365	371	0.010
4c	391	399	0.010
4d	402	408	0.015
8a	413	420	0.015
8b	424	431	0.010
8c	392	395	0.015
8d	400	408	0.015
5a	343	377	0.025
5b	333	366	0.025
6a	338	372	0.025
6b	337	371	0.025
6c	336	368	0.025
6d	333	360	0.025
7a	351	386	0.025
7b	341	375	0.025

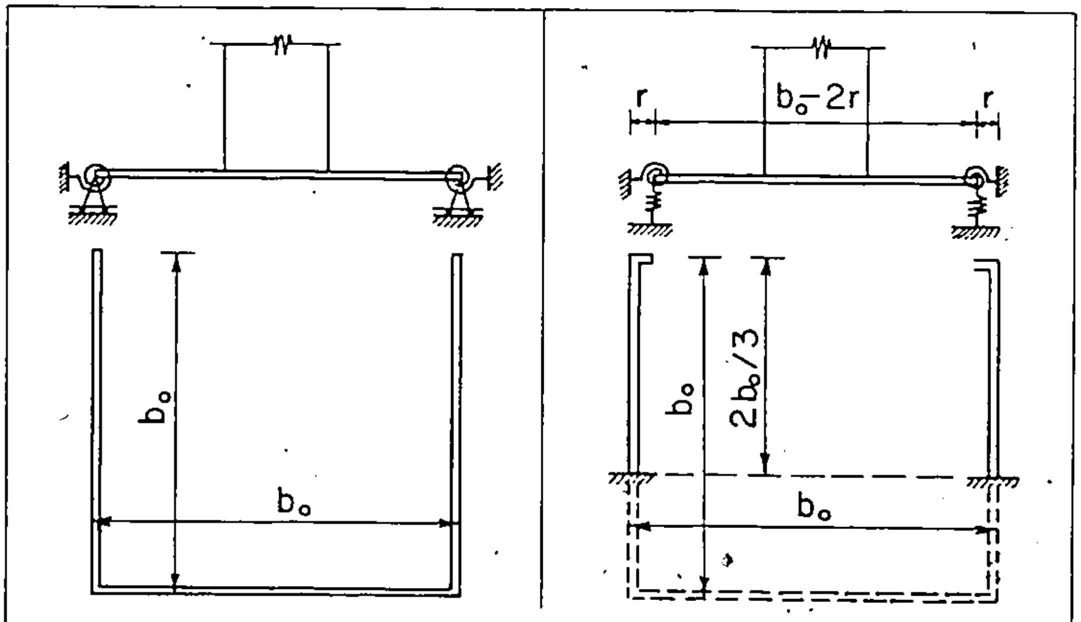
r
$b_o - 2r$
r
b_o
b_o
b_o
$2b_o/3$
b_o

(a) REDWOOD (1965) (b) KOROL and MANSOUR (1979)

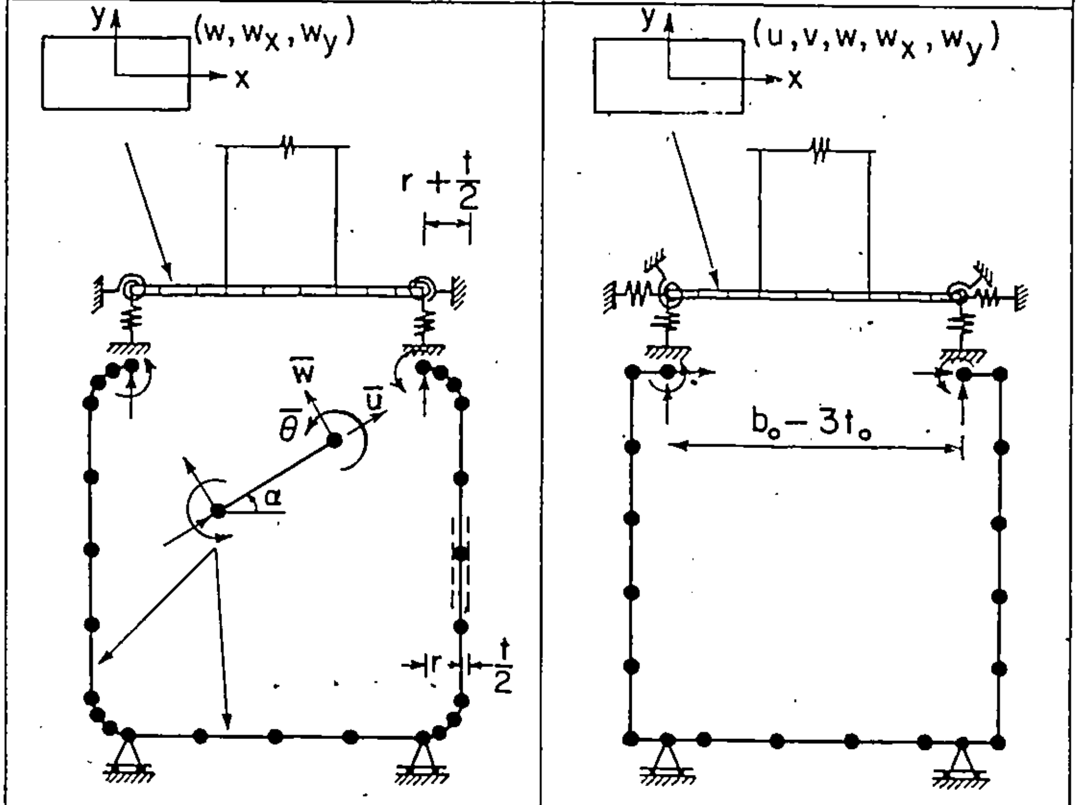
y
(w, w_x, w_y)
x
$r + \frac{t}{2}$
$\overline{w}$
$\overline{\theta}$
$\overline{u}$
α
r
$\frac{t}{2}$
y
(u, v, w, w_x, w_y)
x
$b_o - 3t_o$

(c) KOROL and MIRZA (1982) (d) MIRZA et al (1982)

FIGURE 4.1 : VARIOUS MODELS OF RHS T-JOINTS

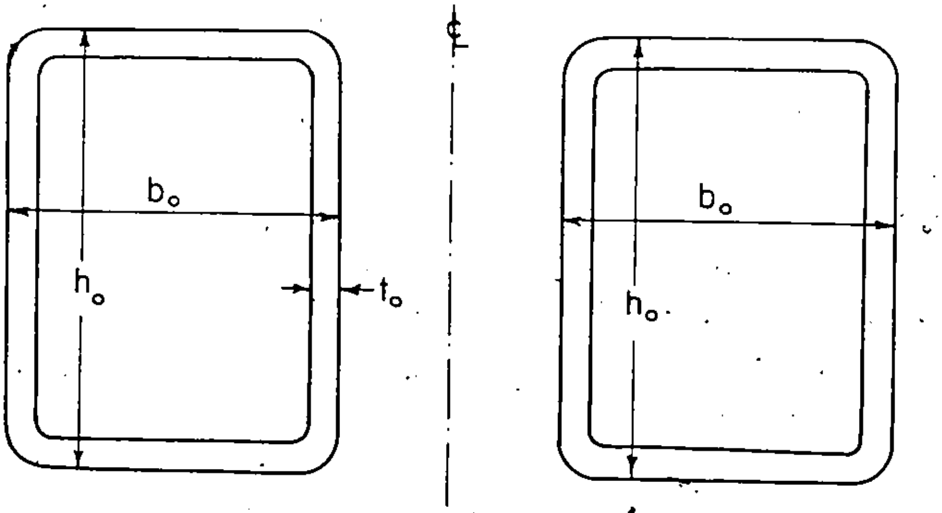

℄
b_o
b_o
h_o
h_o
t_o

(a) SEPARATED DOUBLE CHORD SECTION.

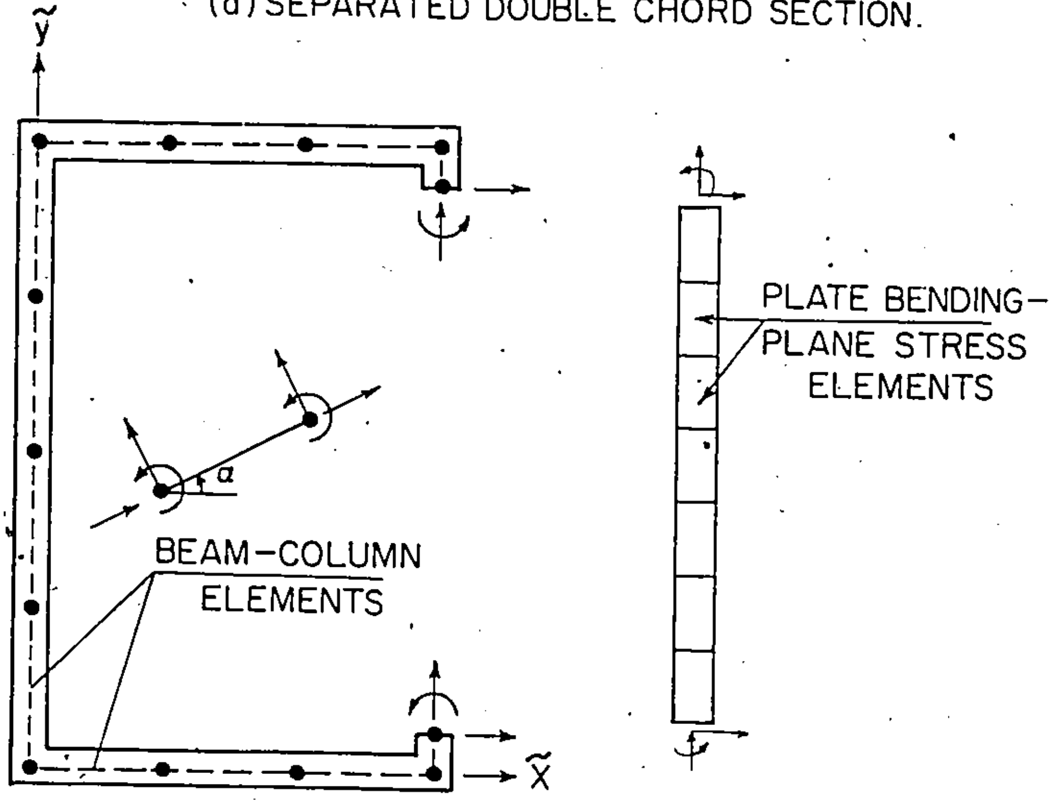

$\tilde{y}$
$\tilde{x}$
α
BEAM-COLUMN ELEMENTS
PLATE BENDING-PLANE STRESS ELEMENTS

(b) BASIC FINITE ELEMENT MODEL.

FIGURE 4.2 : MODELLING OF TWIN SHEAR BEAM

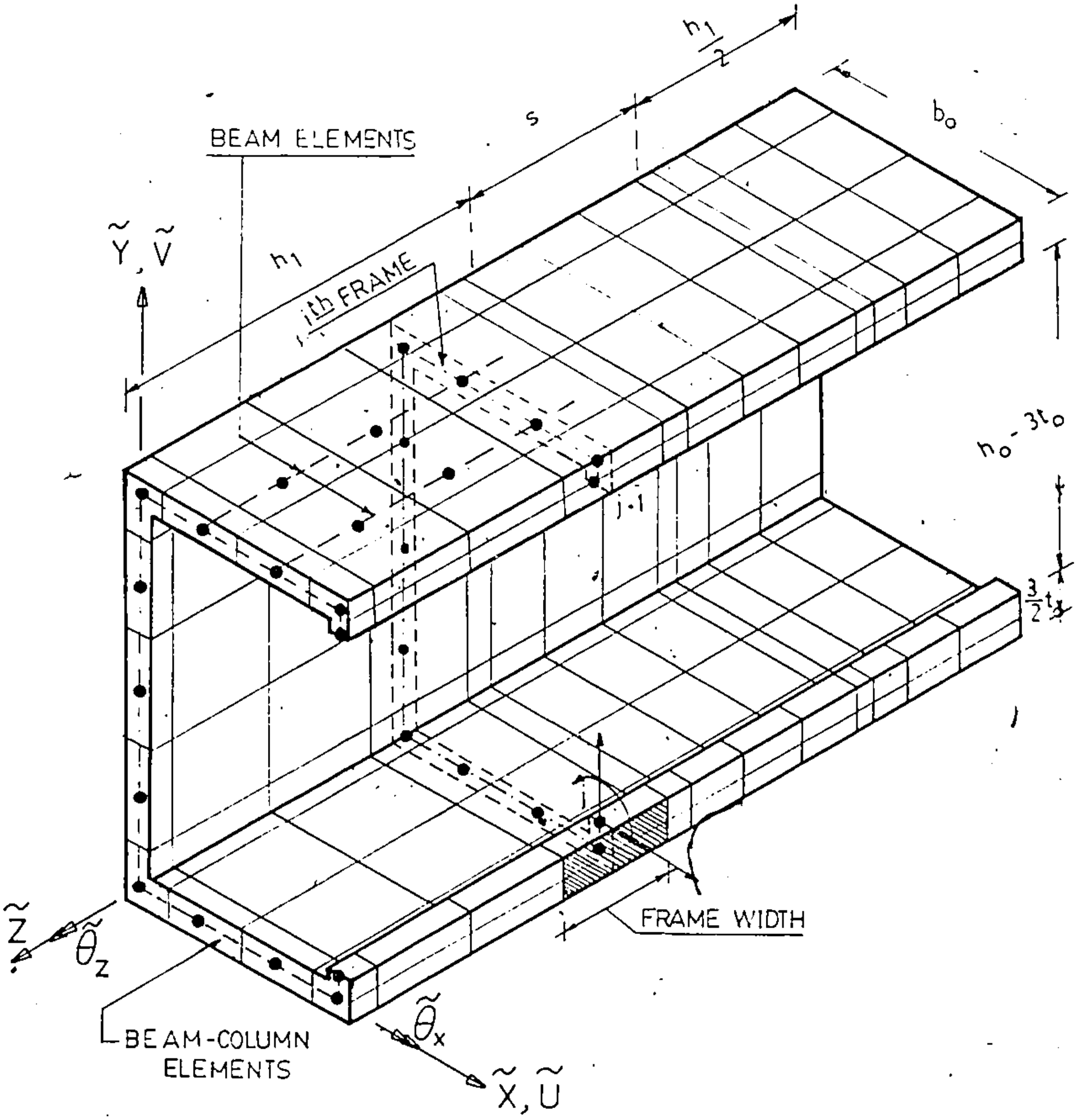
BEAM ELEMENTS
$\tilde{Y}, \tilde{V}$
h_1
$\frac{h_1}{2}$
s
b_o
ith FRAME
$h_o - 3t_o$
j-1
j
$\frac{3}{2}t_o$
FRAME WIDTH
$\tilde{Z}$
$\tilde{\theta}_z$
$\tilde{\theta}_x$
BEAM-COLUMN ELEMENTS
$\tilde{X}, \tilde{U}$

FIGURE 4.3 : CHANNEL GRILLAGE OF BEAM ELEMENTS

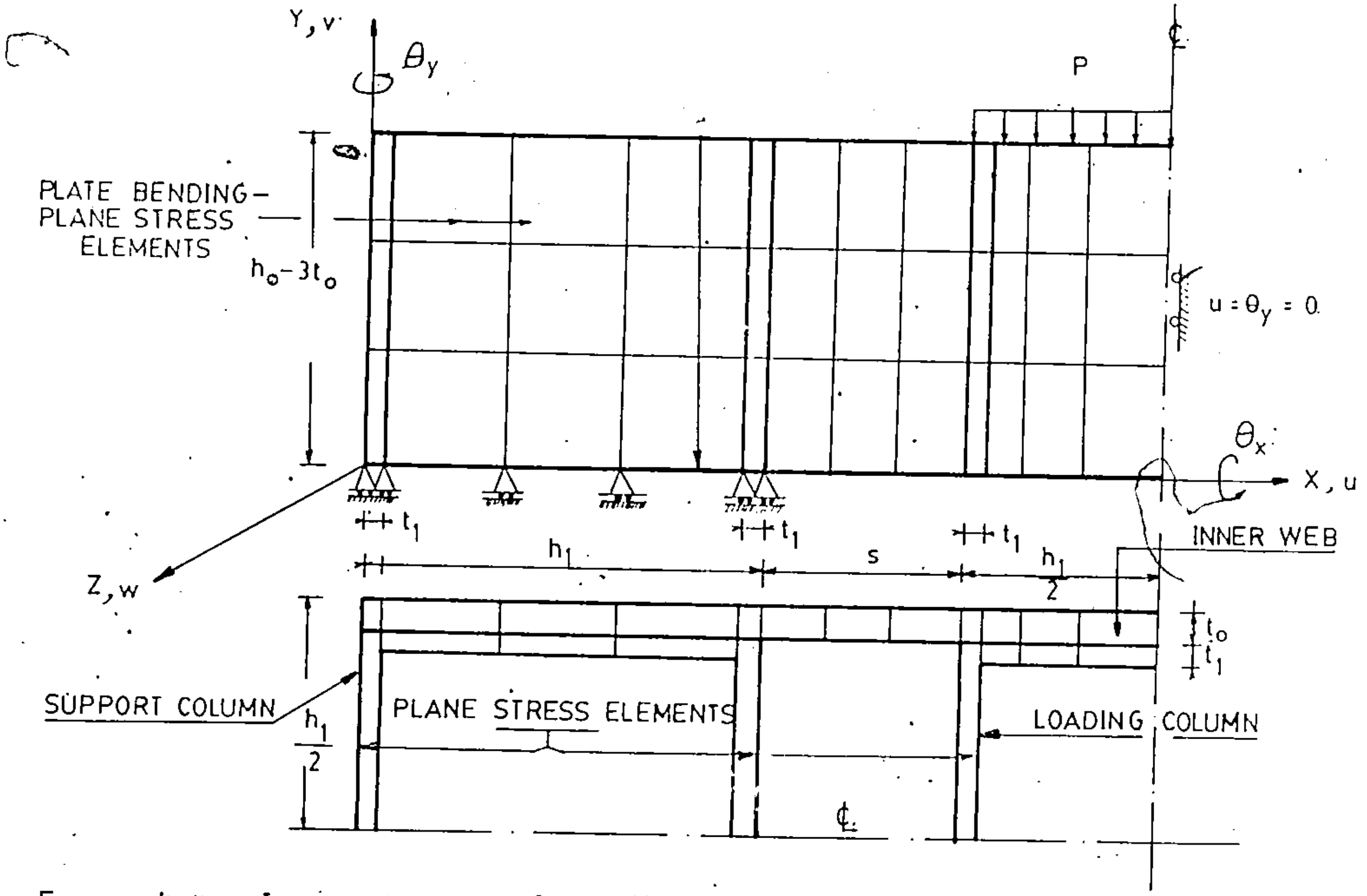
Y, v
θ_y
P
℄
PLATE BENDING-
PLANE STRESS
ELEMENTS
$h_o - 3t_o$
$u = \theta_y = 0$
θ_x
X, u
Z, w
t_1
t_1
t_1
h_1
s
$\frac{h_1}{2}$
INNER WEB
t_o
t_1
SUPPORT COLUMN
$\frac{h_1}{2}$
PLANE STRESS ELEMENTS
LOADING COLUMN
℄

Figure 4.4 : Idealization of Inner Web Plate and Overlapping Branch Members

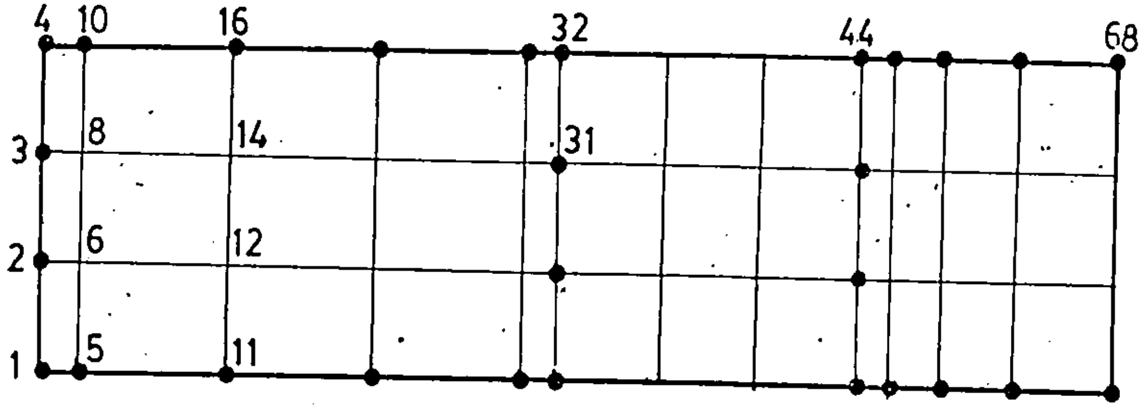
4
10
16
32
44
68
3
8
14
31
2
6
12
1
5
11

(a) Inner Web

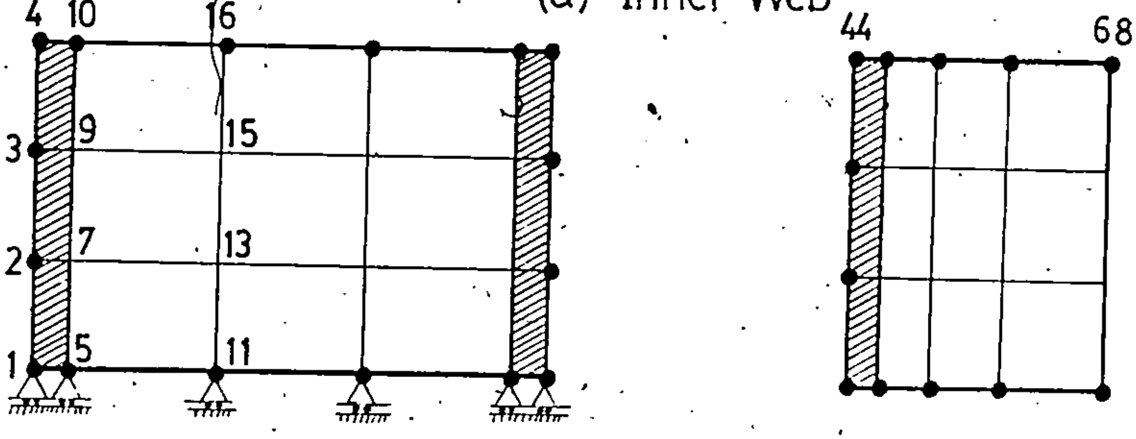
4
10
16
3
9
15
2
7
13
1
5
11
44
68

(b) Support Column

(c) Load Column

FIGURE 4.5 : GRID FOR a AND b TYPE OF TWIN BEAM SPECIMENS

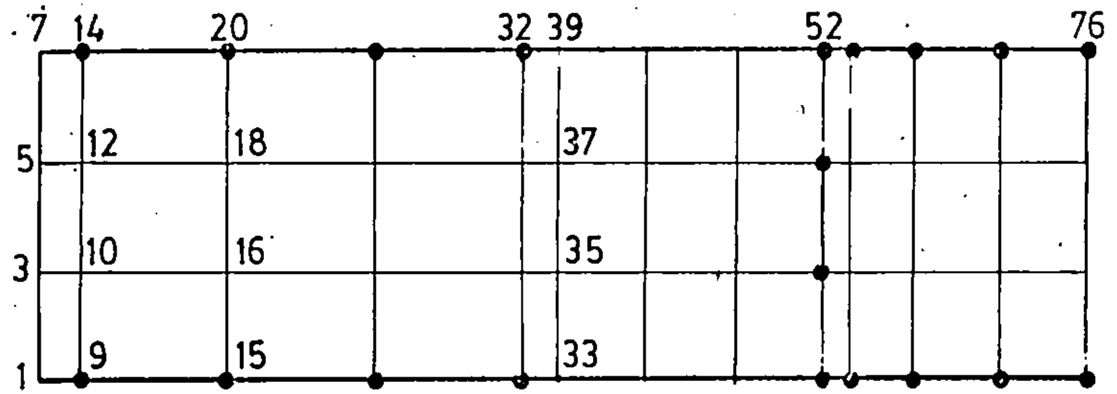
7
14
20
32
39
52
76
5
12
18
37
3
10
16
35
1
9
15
33

(a) Inner Web

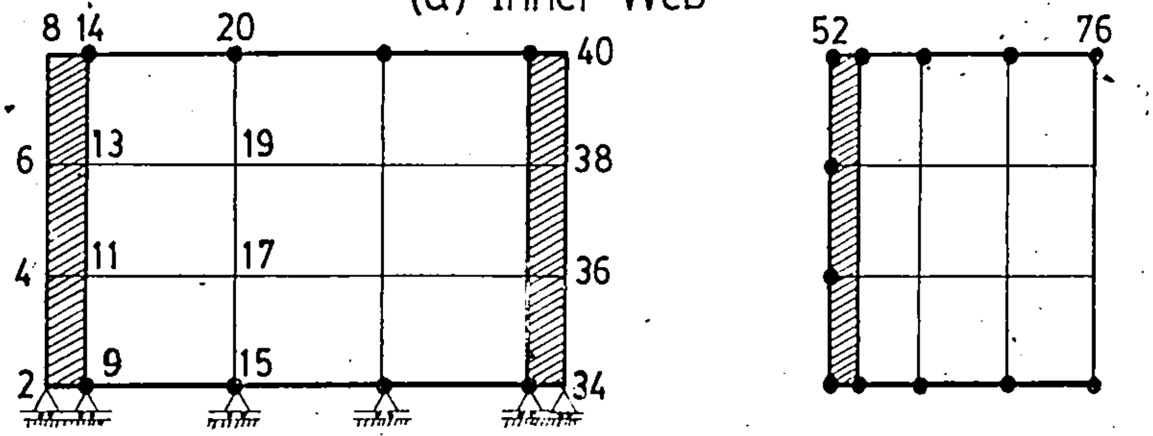
8
14
20
40
6
13
19
38
4
11
17
36
2
9
15
34
52
76

(b) Support Column

(c) Load Column

FIGURE 4.6 : GRID FOR c AND d TYPE OF TWIN BEAM SPECIMENS

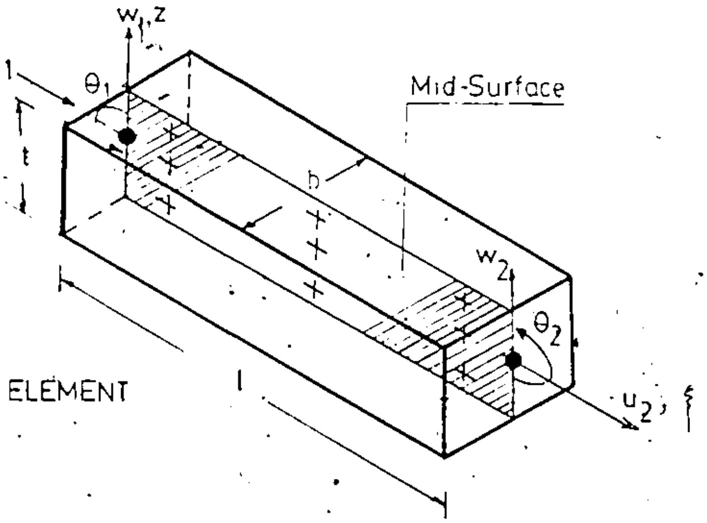
w1, z
u1
θ1
t
Mid-Surface
b
w2
θ2
l
u2, ξ

(a) BEAM-COLUMN ELEMENT

(b) SHEAR BEAM ELEMENT
IN FLANGE

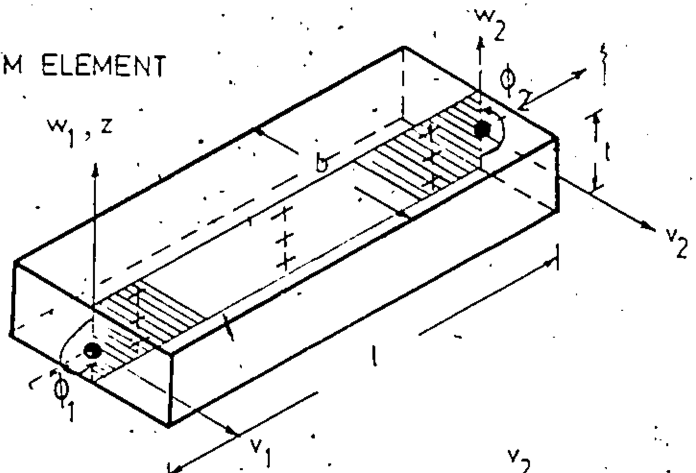
w2
ϕ2
ξ
t
w1, z
b
v2
l
ϕ1
v1

(c) SHEAR BEAM ELEMENT
IN WEB

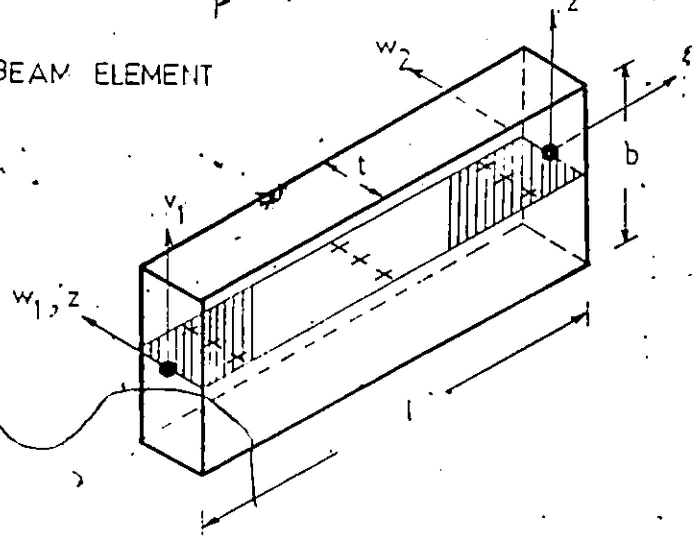
v2
w2
ξ
t
b
v1
w1, z
l

FIGURE 4.7 : BEAM ELEMENTS EMPLOYED IN THE CHANNEL GRILLAGE

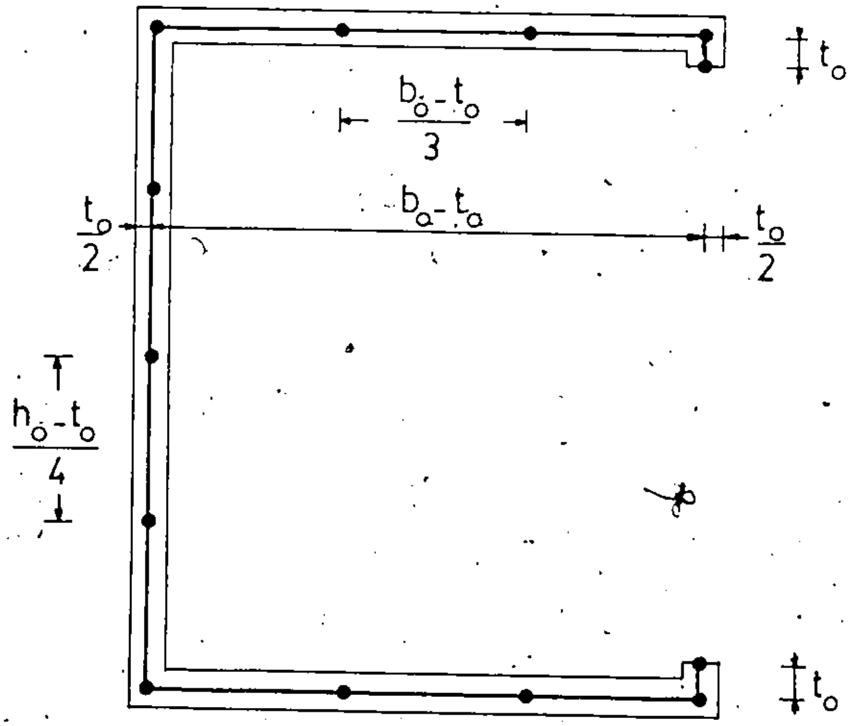

t_o
$\frac{b_o - t_o}{3}$
$\frac{t_o}{2}$
$b_o - t_o$
$\frac{t_o}{2}$
$\frac{h_o - t_o}{4}$
t_o

FIGURE 4.8 : DISCRETIZATION OF C-FRAME INTO BEAM-COLUMN ELEMENTS

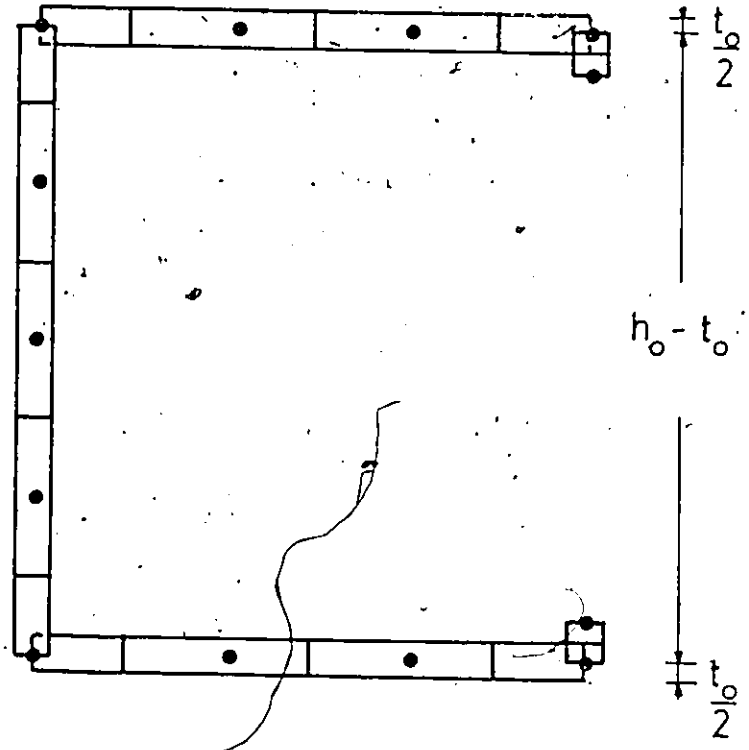

$\frac{t_o}{2}$
$h_o - t_o$
$\frac{t_o}{2}$

FIGURE 4.9 : TYPICAL DISTRIBUTION OF BEAM ELEMENTS IN $\tilde{z}$ DIRECTION

CHAPTER 5

FINITE ELEMENT FORMULATION AND NONLINEAR ANALYSIS

5.1 Equilibrium Equation

In finite element modelling, it is essential to establish the discrete equations of equilibrium and identify the unknown parameters for which these equations should be solved. Since the displacement finite element method is adopted in this study, (Section 4.1), these parameters are the system nodal displacements. The equations of static equilibrium for an element can be derived through a minimization of the total potential energy for linear problems or by using the principle of virtual work for the nonlinear problems (33, 34). For the eth finite element which has a volume V and subjected to a set of forces, it can be shown that either approach leads to:

$$\{P^e\} = [K^e]\ \{\delta^e\} \tag{5.1}$$

where $$[K^e] = \int_V [B]^T[D]\ [B]dV \tag{5.2}$$

is the element stiffness matrix which is a function of its strain matrix [B] and elasticity matrix [D]. $\{P^e\}$ is the load vector due to the applied loads to the element. Equation 5.1, for each element, can be assembled for the overall equilibrium of the discretized structure. Thus

$$\underset{n\times 1}{\{P\}} = \underset{n\times n}{[K_T]}\ \underset{n\times 1}{\{\delta\}} \qquad (5.3)$$

represents n simultaneous equations that correspond to n DOF of the structure to be analysed. The first task in this Chapter is therefore centred on the formulation of individual stiffness matrices of the elements proposed in Chapter 4 for the twin shear beam model. This leads to the formation of the global stiffness matrices $[K_W]$ and $[K_{CH}]$ of the inner web plate and the channel, respectively. It is then required to incorporate the stiffening effect of the channel into the inner web stiffness matrix $[K_W]$ to obtain the total stiffness matrix $[K_T]$. Two methods of analysis, namely uncoupled and coupled, and mentioned earlier, are presented for this purpose. A quantitative assessment of the resulting uncoupled and coupled FEM models will be made subsequently in Chapter 6. Owing to the presence of material non-linearities, incremental stress-strain relation must be furnished beyond the elastic limit. As such, an elasto-plastic analysis that is based on the Von Mises yield criterion and the Prandtl-Reuss plastic flow rule is used. Also, the equations of equilibrium 5.3 are developed in incremental form and the Newton-Raphson iterative method (34) is employed to arrive at the equilibrium at the end of each load increment. A detailed description of the method and the adopted procedure in the nonlinear range is also presented.

5.2 Finite Element Formulation

5.2.1 Inner Web Plate

The 12 DOF nonconforming plate bending element and the 8 DOF plane stress element have been employed to form a plate element for the inner web. Both elements are well documented in the literature (32, 34). For completeness, however, their basic features will be highlighted below.

The out-of-plane displacement, w, of the plate bending element is assumed as

$$\begin{aligned} w &= a_1 + a_2 x + a_3 y + a_4 x^2 + a_5 xy + a_6 y^2 \\ &\quad a_7 x^3 + a_8 x^2 y + a_9 xy^2 + a_{10} y^3 + a_{11} xy^3 + a_{12} x^3 y \end{aligned} \tag{5.4}$$

Since there are 12 DOF for the rectangular, plate bending element with four corner nodes (w, Θ_x, Θ_y at each node), Equation 5.4 can be solved for the unknowns a_1 to a_{12} in terms of the nodal DOF. Thus, w can be expressed as:

$$w = \underset{1\times 12}{[N_b]} \{\delta_b\} = \sum_{i=1}^{12} N_{bi} \delta_{bi} \tag{5.5}$$

where $\{\delta_b\}^T = \langle w_1 \Theta_{x_1} \Theta_{y_1} \cdots w_4 \Theta_{x_4} \Theta_{y_4} \rangle.$ (5.6)

The shape functions $[N_b]$ are listed in Appendix A.1. The rotations Θ_x and Θ_y can be obtained by differentiating (5.5) with respect to y and x, respectively, i.e.

$$\Theta_x = \frac{\partial w}{\partial y} \text{ and } \Theta_y = -\frac{\partial w}{\partial x}. \tag{5.7}$$

The generalized displacement fields for in-plane displacements u and v are assumed to be bilinear, i.e.

$$u = b_1 + b_2 x + b_3 xy + b_4 y \tag{5.8}$$

$$v = c_1 + c_2 x + c_3 xy + c_4 y. \tag{5.9}$$

The coefficients in (5.8) and (5.9) can easily be calculated in terms of the corner nodal DOF (u_i, v_i). Hence

$$u = \underset{1\times4}{[N_p]} \{u\} = \sum_{i=1}^{4} N_{p_i} u_i \tag{5.10}$$

$$v = \underset{1\times4}{[N_p]} \{v\} = \sum_{i=1}^{4} N_{p_i} v_i \tag{5.11}$$

where $\{u\}^T = \langle u_1 u_2 u_3 u_4 \rangle$ (5.12) and $\quad \{v\}^T = \langle v_1 v_2 v_3 v_4 \rangle$ (5.13)

and the shape functions $[N_p]$ are given in Appendix A.2.

Equations 5.5, 5.10 and 5.11 can be condensed into the following matrix form.

$$\begin{Bmatrix} u \\ v \\ w \end{Bmatrix} = \underset{3\times 20}{[N]} \; \underset{20\times 1}{\{\delta^e\}} \qquad (5.14)$$

$$\{\delta^e\}^T = \langle u_1 v_1 w_1 \Theta_{x_1} \Theta_{y_1} \ldots \Theta_{y_4} \rangle \qquad (5.15)$$

which contains the twenty DOF of the rectangular plate element. The shape functions matrix [N] has the following form.

$$\underset{3\times 20}{[N]} = \left[\begin{array}{cccccccccc} N_{p1} & 0 & 0 & 0 & 0 & N_{p2} & 0 & 0 & 0 & 0 \\ 0 & N_{p1} & 0 & 0 & 0 & 0 & N_{p2} & 0 & 0 & 0 \\ 0 & & N_{b1} & N_{b2} & N_{b3} & 0 & 0 & N_{b4} & N_{b5} & N_{b6} \end{array} \right.$$

$$\left. \begin{array}{cccccccccc} N_{p3} & 0 & 0 & 0 & 0 & N_{p4} & & 0 & 0 & 0 \\ 0 & N_{p3} & 0 & 0 & 0 & 0 & N_{p4} & 0 & 0 & 0 \\ 0 & 0 & N_{b7} & N_{b8} & N_{b9} & 0 & 0 & N_{b10} & N_{b11} & N_{b12} \end{array} \right] \qquad (5.16)$$

The strains at any point in the element are determined from

$$\{\varepsilon\} = \begin{Bmatrix} \varepsilon_{xx} \\ \varepsilon_{yy} \\ \gamma_{xy} \end{Bmatrix} = \begin{bmatrix} \frac{\partial}{\partial x} & & -z\,\frac{\partial^2}{\partial x^2} \\ 0 & \frac{\partial}{\partial y} & -z\,\frac{\partial^2}{\partial y^2} \\ \frac{\partial}{\partial y} & \frac{\partial}{\partial x} & -2z\,\frac{\partial^2}{\partial x \partial y} \end{bmatrix} \begin{Bmatrix} u \\ v \\ w \end{Bmatrix} . \qquad (5.17)$$

Denoting the differential operator matrix on the right hand side of (5.17) as [L] and substituting (5.14) for u, v and w, one obtains

$$\underset{3\times1}{\{\varepsilon\}} = \underset{3\times3}{[L]}\ \underset{3\times20}{[N]}\ \{\delta^e\} = \underset{3\times20}{[B]}\ \underset{20\times1}{\{\delta^e\}} \qquad (5.18)$$

where [B] is the element strain matrix. The stiffness matrix of the plate element can now be computed from Equation 5.2 in which [D] is the plane elasticity matrix and is given by

$$[D] = \frac{E}{1-\nu^2} \begin{bmatrix} 1 & \nu & 0 \\ \nu & 1 & 0 \\ 0 & 0 & \frac{1-\nu}{2} \end{bmatrix} . \qquad (5.19)$$

Beyond the elastic limit, the matrix [D] is variable with the stress level at a point within the element and is known as the compliance matrix. As such, 27 integration points within an element were used for the calculation of [D] in the elasto-plastic range; see Figure 5.1. Locations of points and the associated weight factors are determined from Gauss Quadrature Tables (34). In its discretized form, Equation 5.2 is written as

$$\underset{20\times 20}{[K^e]} = \frac{a}{2} \cdot \frac{b}{2} \cdot \frac{t}{2} \sum_{i=1}^{3} \sum_{j=1}^{3} \sum_{k=1}^{3} \omega_i \omega_j \omega_k \underset{20\times 3}{[B(\zeta_i,\ \eta_j,\ z_k)]^T}$$

$$\underset{3\times 3}{[D]_{ijk}} \cdot \underset{3\times 20}{[B(\zeta_i,\ \eta_j,\ z_k)]}. \tag{5.20}$$

The locations of the integration points are

$$\{\zeta\}^T = \{\eta^T\} = \langle 0.5 - \sqrt{0.15},\ 0.5,\ 0.5 + \sqrt{0.15} \rangle \tag{5.21}$$

$$\{z\}^T = \langle -\ t\ \sqrt{0.15},\ 0.0,\ t\ \sqrt{0.15} \rangle \tag{5.22}$$

and the corresponding weight factors are

$$\{\omega\}^T = \langle 5/9\ \ 8/9\ \ 5/9 \rangle. \tag{5.23}$$

The stresses in the elastic range at any point in the element are determined from

$$\{\sigma\} = \begin{bmatrix} \sigma_{xx} \\ \sigma_{yy} \\ \sigma_{xy} \end{bmatrix} = \underset{3\times 3}{[D]}\ \underset{3\times 1}{\{\varepsilon\}} \tag{5.24}$$

where [D] is defined in (5.9). In the elasto-plastic range, stress increments are calculated from

$$\{\Delta\sigma\} = [D_{ep}]\ \{\Delta\varepsilon\} \qquad (5.25)$$

in which $[D_{ep}]$ is the compliance matrix which will be defined in Section 5.4. It should be noted that the strain matrix [B] at an integration point (ξ_i, η_j, z_k) is constant throughout the analysis since the geometric nonlinearities are not included. The [B] matrix is therefore computed only once at each of the 27 sampling points of an element in the beginning of the computational procedure and stored.

5.2.2 Top and Bottom Flanges and Outer Web

The 6 DOF beam-column element has been used to model the transverse C-shaped frames of the remaining portion of the RHS section. The element is capable of resisting normal stresses resulting from axial deformations $\hat{u}$ as well as bending deformations $\hat{w}$ and $\hat{\theta}$. The axial displacement field is linear whereas the bending displacement field $\hat{w}$ is cubic. Hence the element strain matrix <B> is given by

$$\underset{1\times 6}{\langle B\rangle} = \langle \frac{-1}{\ell}, \frac{6z}{\ell^2}(1-2\xi), \frac{2z}{\ell}(2-3\xi), \frac{1}{\ell}, \frac{-6z}{\ell^2}(1-2\xi),$$

$$\frac{2z}{\ell}(1-3\xi)\rangle \qquad (5.26)$$

and the corresponding element DOF are

$$\{\delta^e\}^T = \langle \hat{u}_1 \hat{w}_1 \hat{\theta}_1 \hat{u}_2 \hat{w}_2 \hat{\theta}_2 \rangle \qquad (5.27)$$

For numerical evaluation of the element stiffness matrix, 9 integration points are selected as shown in Fig. 5.2. The locations z and ξ are identical to those of the plate element defined in Equations 5.21 and 5.22, respectively. Thus, the element stiffness matrix can be computed from

$$\underset{6\times 6}{[K^e]} = b \cdot \frac{\ell}{2} \cdot \frac{t}{2} \sum_{i=1}^{3} \sum_{j=1}^{3} \omega_i \omega_j \underset{6\times 1}{[B(\xi_i, z_j)]^T} \cdot \frac{E}{1-\nu^2} \cdot \underset{6\times 1}{[B(\xi_i, Z_j)]} \tag{5.28}$$

It may be observed that [D] matrix has been replaced by $E/(1-\nu^2)$ in the beam element. The term $1-\nu^2$ has been used to account for plate action occurring in the channel grillage. The weight factors are the same as given in (5.23).

In the longitudinal direction of the channel, the beam bending element with DOF $\hat{w}$, $\hat{\theta}$ is combined with the inplane, pure shearing element with DOF $\hat{v}$. This element then offers resistance to out-of-plane deformation by bending and to in-plane deformation by pure shear. Therefore the strain matrix for this element, for discretizing the flange, is 2×6 and is given by:

$$\underset{2\times 6}{[B]} = \begin{bmatrix} \frac{6z}{\ell^2}(1-2\xi), & \frac{2z}{\ell}(2-3\xi), & 0, & \frac{-6z}{\ell^2}(1-2\xi), & \frac{2z}{\ell}(1-\xi), & 0 \\ 0, & 0, & \frac{-1}{\ell}, & 0, & 0, & \frac{1}{\ell} \end{bmatrix} \tag{5.29}$$

and the element nodal displacements are

$$\{\delta^e\}^T = \langle \hat{w}_1 \hat{\Theta}_1 \hat{v}_1 \hat{w}_2 \hat{\Theta}_2 \hat{v}_2 \rangle .$$

As described in Section 4.5, the elements discretizing the outer webs of the C-frames have only 4 DOF which are

$$\{\delta^e\}^T = \langle \hat{w}_1 \hat{v}_1 \hat{w}_2 \hat{v}_2 \rangle$$

and their strain matrix is 2×4 as listed below.

$$\underset{2\times 4}{[B]} = \begin{bmatrix} \frac{6z}{\ell^2}(1-2\xi), & 0, & -\frac{6z}{\ell^2}(1-2\xi), & 0 \\ 0 & , \frac{-1}{\ell}, & 0 & , \frac{1}{\ell} \end{bmatrix} \tag{5.30}$$

Employing 9 integration points as before and noting that the plane elasticity matrix for the flange or the web element is

$$\underset{2\times 2}{[D]} = \frac{E}{1-\nu^2} \begin{bmatrix} 1 & 0 \\ 0 & \frac{1-\nu}{2} \end{bmatrix} , \tag{5.31}$$

the element stiffness matrix can be easily computed. Hence,

$$[K^e] = b \cdot \frac{\ell}{2} \cdot \frac{t}{2} \cdot \sum_{i=1}^{3} \sum_{j=1}^{3} \omega_i \omega_j \, [B(\xi_i, Z_j)]^T [D_{ij}] \, [B(\xi_i, Z_j)] \tag{5.32}$$

To illustrate the strain and stress calculations in the channel grillage, consider for example the stresses occurring in the flange.

σ_x = normal stress computed from beam-column element.

σ_z = normal stress computed from beam bending-shear element.

σ_{xz} = shear stress computed from beam bending-shear element.

The axial strain at any point in the beam-column element is evaluated from

$$\varepsilon_x = \underset{1\times 6}{\langle B\rangle} \; \underset{6\times 1}{\{\delta^e\}} \; . \tag{5.33}$$

Consequently, the normal stress is

$$\sigma_x = \frac{E}{1-\nu^2} \cdot \varepsilon_x . \tag{5.34}$$

The axial and shear strains of beam bending-shear element are determined from

$$\underset{2\times 1}{\left\{ \begin{matrix} \varepsilon_z \\ \gamma_{xz} \end{matrix} \right\}} = \underset{2\times 6}{[B]} \; \underset{6\times 1}{\{\delta^e\}} \; . \tag{5.35}$$

Hence,

$$\begin{Bmatrix}\sigma_z\\ \tau_{xz}\end{Bmatrix} = [D]_{2\times 2} \begin{Bmatrix}\varepsilon_z\\ \gamma_{xz}\end{Bmatrix} \qquad (5.36)$$

are the corresponding normal and shear stresses.

In the elasto-plastic range, the above relations (5.33) to (5.36) hold true for calculation of strain and stress increments. For the latter, the following criterion is also checked. If the affective stress $\bar{\sigma}$ at a point exceeds the uniaxial yield stress of the material σ_y, the modulus of elasticity E is replaced by the tangent modulus E_T defined in Section 4.6. From the Von Mises yield criterion, the effective stress, $\bar{\sigma}$ at a point in the grillage is computed from

$$\bar{\sigma} = \sqrt{\sigma_x^2 - \sigma_x\sigma_z + \sigma_z^2 + 3\,\tau_{xz}^2} \qquad (5.37)$$

5.3 Stiffness Analysis of the Channel Frame

5.3.1 Feasible Strategies

It is conceivable that the top and bottom flange and the outer web of the RHS double chord section offer a considerable restraint to deformation of the inner web. It is therefore important to include such a restraint in the FEM model. However, before a method of analysis is suggested, the following should be considered.

1. The inner web grid has 5 DOF per node $(u, v, w, \Theta_x, \Theta_y)$ while the channel grillage has 4 DOF per node $(\tilde{u}, \tilde{v}, \tilde{\Theta}_x, \tilde{\Theta}_z$ in Figure 5.3). At the common nodes on the inner web plate-channel boundaries, there are only 3 DOF that match; i.e. $(v, w, \Theta_x$ vs $\tilde{v}, \tilde{u}, \tilde{\Theta}_z)$. The fourth DOF $\tilde{\Theta}_x$, is locked by virtue of the web elements used at the channel's tips (Figure 4.9).
2. The global stiffness matrix of the inner web plate is banded due to the node numbering and a banded solution routine is therefore employed in the computer model to solve the equations of equilibrium. Thus, it is desired to keep the problem band width minimum, after augmenting the plate with the channel, to allow the best efficiency for solution.

With the above considerations in mind, two approaches are described below. These are the uncoupled and coupled models mentioned in Section 4.3. The merits and disadvantages of each approach will be discussed accordingly.

5.3.2 Uncoupled Model

In this model, it is assumed that the influence of the channel frame is transmitted to the plate by sets of boundary springs. Each set contains six coupled springs located at the top and bottom boundaries of the plate; three springs at each. These are in the directions of DOF v, w and Θ_x, of the inner web plate two translational and one rotational at each boundary. The 6 × 6 coupled spring coefficient matrices are determined from a stiffness analysis of the channel frame. This was described earlier in Section 4.3. The resulting matrix for each C-frame takes the following form.

$$[k_{sp}] = \begin{bmatrix} \underset{3\times3}{[k_{bb}]} & \underset{3\times3}{[k_{bt}]} \\ \underset{3\times3}{[k_{tb}]} & \underset{3\times3}{[k_{tt}]} \end{bmatrix} \tag{3.38}$$

The submatrices $[k_{bb}]$ and $[k_{tt}]$ represent the holding forces necessary to maintain unit displacements, one at a time, in the directions $\hat{u}$, $\hat{v}$, and $\hat{\theta}_z$ at the bottom and top of the channel, respectively. Also, the submatrix $[k_{bt}]$ represents the forces required at the bottom due to a unit displacement imposed along a DOF at the top of the channel and vice versa for $[k_{tb}]$. From Figure 5.4, it can be seen that each pair of plate elements at the top and bottom boundaries (elements T and B respectively) are attached to a C-shaped frame whose centreline is located mid-way of the plate element length. Thus, in order to determine the nodal stiffness contributions from $[K_{sp}]$ it is first divided by the plate length to obtain the uniform spring properties per unit length $[K^*_{sp}]$.

The matrix $[K^*_{sp}]$ can now be regarded as a set of coupled springs imposed along the top and bottom edges of the inner web in the directions v, w and θ_x. The strain energy stored in these springs is given by

$$U_b = \frac{1}{2}\int_a \{\delta^*\}^T[K^*_{sp}]\ \{\delta^*\}dx$$

where $\{\delta^*\}^T = \langle v^b w^b \Theta^b_x v^t w^t \Theta^t_x\rangle$ is the vector of the generalized displacement fields of the plate elements T and B in Figure 5.4. Since the displacement field can always be expressed in terms of the nodal displacements using the shape functions, one can write $\{\delta^*\} = [N^*]\{\delta^{*e}\}$. The relation between $[N^*]$ and the shape functions of the plate elements T and B is explained in Appendix A.3. Hence,

$$U_b = \frac{1}{2}\ \{\delta^{*e}\}^T \int_a \{N^*\}^T[K^*_{sp}]\ [N^*]dx\ \{\delta^{*e}\}. \qquad (5.39)$$

But

$$U_b = 1/2\ \{\delta^{*e}\}^T[K_b]\ \{\delta^{*e}\} \qquad (5.40)$$

in which $[K_b]$ is the stiffness matrix of the boundary spring element. Comparing (5.39) and (5.40)

$$\underset{40\times40}{[K_b]} = \int_a \underset{40\times6}{[N^*]^T}\underset{6\times6}{[K^*_{sp}]}\ \underset{6\times40}{[N^*]}dx. \qquad (5.41)$$

The above equation has been previously presented in detail (10). For easier assembling of the boundary element stiffness matrix $[K_b]$, the dimension 40 arises from maintaining all twenty DOF per element T and B in Figure 5.4. Equation 5.3 can now be solved for the unknown nodal displacements of the inner web noting that

$$[K_T] = [K_w] + \sum_{j=1}^{m} [K_b]_j, \quad m = \text{total no. of boundary spring elements} \qquad (5.42a)$$

Knowing the displacements, the strains and stresses in the plate elements can be computed from Equations 5.18 and 5.24, respectively. For the strain and stress calculations in the channel portion, the following procedure is followed.

1. Extract the top and bottom boundary displacements of the plate from its global displacement vector.
2. Since each C-shaped frame is located midway through the boundary plate element (Figure 5.4), use the average of the two adjacent boundary nodal displacements for the channel tip nodes j and j + 1 in Figure 5.3.
3. Repeat step 2 for all of the channel tip nodes to obtain the vector $\{C\}$ containing the channel's tip displacements.
4. Compute the equivalent load vector $\{P_{CH}\}$ resulting from imposing the constraint vector $\{C\}$ on the channel boundary while locking all other degrees of freedom in the system.
5. Knowing the global stiffness matrix $[K_{CH}]$, solve for the displacements in the entire grillage.
6. Calculate strains and stresses in the grillage using the appropriate of Equations 5.33 to 5.36 depending on the type of element as under consideration.

5.3.3 Coupled Model

As described earlier, this approach utilizes the concept of static condensation to obtain the influence of the channel frame on the inner web plate. By condensing the channel frame matrix $[K_{CH}]$ in terms of its boundary nodal displacements, a smaller size matrix (6m × 6m) results; where 2m is the total number of boundary nodes with three DOF per boundary node and m is the number of C-frames. The efficiency of this method is dependent upon the node numbering of the channel grillage. Two methods, with different node numbering systems, have been implemented and are presented below. While, of course, identical results were obtained, the primary objective at this point was to compare the computational efficiency of the two methods and to opt for the one possessing economy. In the following presentations, the centrelines of C-frames align with the plate element edges, i.e. the channel boundary nodes coincide with the inner web plate boundary nodes.

In the first method, the node numbering illustrated in Figure 5.5a is considered. It is seen that C-shaped frames are numbered in an alternating sequential manner. The advantage of this type of numbering is that the global stiffness matrix has a uniform bandwidth; (Figure 5.5b). Typically, for 13 node per C-frame, the half bandwidth is 50 excluding the diagonal. The procedure to obtain the condensed matrix is summarized as follows.

1. Formulate the global stiffness matrix of the channel $[K_{CH}]$.
2. Impose a unit displacement in the direction of a DOF on the

boundary while locking all other boundary DOF.

3. Calculate the equivalent load vector $\{P_{CH}\}$ necessary to maintain such a discpacement and modify the stiffness matrix accordingly to $[K^*_{CH}]$.
4. Solve $\{P_{CH}\} = [K^*_{CH}]\ \{\delta\}$ for the displacement $\{\delta\}$ and hence compute the end forces acting in directions of all 6m DOF on the boundary. These forces represent the i^{th} column of the required matrix, albeit, very small away from the nodal DOF under consideration.
5. Repeat steps 2 to 4 for all 6m DOF of the channel boundary.

The resulting matrix $[K_C]$ is 6m × 6m in size and is fully populated.

Considering Figure 5.6a, the boundary nodes are numbered first. These are followed by the internal nodes of the C-frames which are numbered sequentially. This numbering scheme, which is used in the second method, allows partitioning of the channel's global stiffness matrix in the following manner.

$$\underset{47m\times47m}{[K_{CH}]} = \begin{bmatrix} \underset{6m\times6m}{[K_{bb}]} & \underset{46m\times41m}{[K_{bi}]} \\ \\ \underset{41m\times6m}{[K_{ib}]} & \underset{41m\times41m}{[K_{ii}]} \end{bmatrix} \qquad (5.43)$$

where for a typical of 13 nodes per frame, 4 DOF per node on the flange and 3 DOF on the web, there exists a total of 47 DOF per C-frame; thence

47m DOF for the channel grillage. The subscripts bb and ii denote the boundary and internal DOF, respectively. The matrix $[K_{CH}]$ in Equation 5.43 has a very common form; its structure is sketched in Figure 5.6(b); and it is easy to see that by applying the static condensation to suppress the internal DOF, one obtains (33)

$$\underset{6m\times 6m}{[K_C]} = \underset{6m\times 6m}{[K_{bb}]} - \underset{6m\times 41m}{[K_{bi}]} \; \underset{41m\times 41m}{[K_{ii}]^{-1}} \underset{41m\times 41m}{[K_{ib}]} \tag{5.44}$$

in which $[K_C]$ represents the condensed stiffness matrix of the channel in terms of its 2m boundary nodes. The matrix $[K_C]$ is identical to that derived previously. While the two methods just described are equally valid, the first one is distinguished by its apparent simplicity and storage economy. Unfortunately, the execution time required to implement this method is inevitably high. The stiffness matrix $[K_{CH}]$ must be modified and decomposed 6m number of times. The difficulty with the second method stems from its very large sized matrix $[K_{bi}]$. This problem was treated by writing an algorithm to store only the active columns of $[K_{bi}]$ which are shown by the hatched boxes in Figure 5.6c. With this provision made, the second method appeared to outperform the first one both in storage and time. Equation 5.42(a) can now be written for the coupled model as

$$[K_T] = [K_W] + [K_C] \tag{5.42b}$$

to obtain the total stiffness matrix of the twin beam. It may be observed that when $[K_C]$ is added to $[K_W]$ to obtain the total stiffness matrix, the bandwidth of the latter would greatly increase. As such, the solution would require extremely large computer storage and the model becomes insufficient. Clearly, this problem stems from the fact that the matrix $[K_C]$ is fully populated; i.e. there exists complete coupling among all of its 6m DOF. Therefore, if one assumes that the influence coefficients of $[K_C]$ that are remote from the diagonal can be neglected, the matrix $[K_C]$ would tend to take a banded shape and consequently the problem bandwidth can be reduced. Physically, it is implied in this assumption that although a unit displacement at a boundary joint at the i^{th} C-frame can cause forces to develop at all boundary nodes, such forces will diminish gradually away from the node considered and become small enough to be ignored at node locations that are n or more C-frames away from the displaced node; i.e.

$$k_{cij} \cong 0 \quad \text{if} \quad |i - j| > 6n$$

where the appropriate number of lines n can only be determined from numerical tests. Such number represents the extent of effective coupling between boundary nodes to be accounted for in $[K_C]$ and should be large enough to preserve the overriding condition of equilibrium. To avoid this assumption, an alternative solution routine will be presented subsequently in Chapter 7, which will permit full utilization of $[K_C]$ in the total stiffness matrix.

Substituting Equation 5.42(b) into Equation 5.3 and after solving for the nodal displacements, the strains and stresses in the inner web can be computed. The procedure in the channel is summarized below.

1. Extract the top and bottom boundary displacements of the inner web plate from its global displacement vector and store in $\{\delta_{bb}\}$. The size of this array is 6m and contains the boundary displacements $\tilde{u}$, $\tilde{v}$ and $\tilde{\Theta}_z$.
2. Solve for the channel interior displacements $\{\delta_{ii}\}$ as follows

$$\underset{41m\times 1}{\{\delta_{ii}\}} = - \underset{41m\times 41m}{[K_{ii}]^{-1}} \underset{41m\times 6m}{[K_{ib}]} \underset{6m\times 1}{\{\delta_{bb}\}} \tag{5.45}$$

3. Use $\{\delta_{bb}\}$ and $\{\delta_{ii}\}$ to calculate strains and stresses at every sampling point in the grillage using Equations 5.33 to 5.36.

5.4 Plasticity Relations for Elasto-Plastic Analysis

5.4.1 Introduction

The plastic behaviour of a material is distinguished from that of an elastic material by the fact that, for the former, strains are not uniquely defined for a given state of stress. In fact it can be shown that completely different strains exist for the same state of stress (35) which infers that plastic strains are dependent on the loading history of the material. It is for this reason that an incremental stress-strain relation must be established. As will be seen, such a relation, in its simplest form, is analogous to Hooke's Law for elastic materials with the difference that the plane elasticity matrix [D] is replaced by the elasto-plastic "compliance" matrix $[D_{ep}]$. The derivation of the elasto-plastic matrix was first presented by Yameda et al (36) and Zeinkiewicz et al (37). In this section the Prandtl-Reuss flow rule and the Von Mises yield criterion are employed to arrive at the explicit form of the compliance matrix.

5.4.2 Elasto-Plastic Compliance Matrix

The basic plastic flow rule states that plastic-strain increments can be expressed as (35)

$$\{d\varepsilon p\} = \lambda \left\{\frac{\partial F}{\partial \sigma}\right\} \qquad (5.46)$$

where λ is a proportionality factor and F is the yield function. The latter can be defined as

$$F = F(\sigma_1, \sigma_2, \ldots, K) = F(\sigma, K) = 0 \qquad (5.47)$$

in which K is a parameter representing material hardening. Differentiating (5.47) gives

$$dF = \frac{\partial F}{\partial \sigma_1} \cdot d\sigma_1 + \frac{\partial F}{\partial \sigma_2} \cdot d\sigma_2 + \ldots \frac{\partial F}{\partial K} \cdot dK = 0.$$

Defining $A = -\partial F/\partial K \cdot dK/\lambda$, the above equation becomes

$$\left\{\frac{\partial F}{\partial \sigma}\right\}^T \{d\sigma\} = A\lambda. \tag{5.48}$$

A stress increment $\{d\sigma\}$ can be calculated as

$$\{d\sigma\} = [D]\ \{d\varepsilon_e\}$$

where $\{d\varepsilon_e\}$ is the elastic strain increment. Since the total strain increment $\{d\varepsilon\}$ is the sum of plastic and elastic strain increments, one can write

$$\{d\sigma\} = [D]\ \{d\varepsilon\} - [D]\ \{d\varepsilon_p\}. \tag{5.49}$$

Premultiplying by $\{\partial F/\partial\sigma\}^T$ and substituting for $\{d\varepsilon_p\}$,

$$\left\{\frac{\partial F}{\partial \sigma}\right\}^T \{d\sigma\} = \left\{\frac{\partial F}{\partial \sigma}\right\}^T [D]\ \{d\varepsilon\} - \left\{\frac{\partial F}{\partial \sigma}\right\}^T [D]\lambda \cdot \left\{\frac{\partial F}{\partial \sigma}\right\} \tag{5.50}$$

Comparing (5.48) and (5.50), it can be seen that the left hand sides of the two equations are identical. As such, a value of λ can be obtained as

$$\lambda = \frac{\left\{\frac{\partial F}{\partial \sigma}\right\}^T [D]\ \{d\varepsilon\}}{A + \left\{\frac{\partial F}{\partial \sigma}\right\}^T [D]\ \left\{\frac{\partial F}{\partial \sigma}\right\}}. \tag{5.51}$$

Substituting [illegible] value into (5.50) after removing the premultiplier, one obtains the required incremental stress-strain relation as follows

$$\{d\sigma\} = [D_{ep}]\ \{d\varepsilon\} \tag{5.52}$$

where $[D_{ep}]$ is (37)

$$[D_{ep}] = [D] - [D]\ \{\frac{\partial F}{\partial \sigma}\}\ \{\frac{\partial F}{\partial \sigma}\}^T [D]\ [A + \{\frac{\partial F}{\partial \sigma}\}^T [D]\ \{\frac{\partial F}{\partial \sigma}\}]^{-1} . \tag{5.53}$$

It is now desired to apply this result to the particular problem at hand. Since we have a plane stress problem, only σ_x, σ_y and σ_{xy} are the stresses present. From the Von Mises yield criterion, we have:

$$F = (\sigma_x 2 + \sigma_y 2 - \sigma_x \sigma_y + 3\sigma_{xy} 2)^{1/2} - \bar{\sigma}(K) = 0. \tag{5.54}$$

Hence,

$$\{\frac{\partial F}{\partial \sigma}\}^T = < \frac{3\sigma^1_x}{2\bar{\sigma}}\ \frac{3\sigma^1_y}{2\bar{\sigma}}\ \frac{3\sigma_{xy}}{\bar{\sigma}} > \tag{5.55}$$

where $\sigma^1_x = \sigma_x - \frac{1}{3}(\sigma_x + \sigma_y)$, etc., are the deviatoric stresses. From the Prandtl-Reuss plastic flow rule (35)

$$\{d\varepsilon_p\} = d\overline{\varepsilon_p}\ \{\frac{\partial F}{\partial \sigma}\}. \tag{5.56}$$

It follows from the comparison of equations (5.46) and (5.56) that

$$\lambda = \overline{d\varepsilon_p} \qquad (5.57)$$

where $\overline{d\varepsilon_p}$ is the effective plastic strain increment. Substituting this result into the definition of A yields

$$A = \frac{d\bar{\sigma}}{\overline{d\varepsilon_p}} \qquad (5.58)$$

Since $\overline{d\varepsilon} = \overline{d\varepsilon_e} + \overline{d\varepsilon_p}$, (5.59)

or

$$\frac{d\bar{\sigma}}{E_T} = \frac{d\bar{\sigma}}{E} + \overline{d\varepsilon_p}$$

then

$$A = \frac{d\bar{\sigma}}{d\bar{\varepsilon}_p} = \frac{E \cdot E_T}{E - E_T} \qquad (5.60)$$

for a bilinear material behaviour with modulii E and E_T in the elastic and plastic ranges, respectively. Thus, the information needed to compute the compliance matrix is now available (Equations (5.55) and (5.60)). Substituting these into (5.53), one obtains the explicit form of the compliance matrix. This is

$$[D_{ep}] = \begin{bmatrix} \left(\frac{E}{1-\nu^2} - \frac{s_1^2}{S}\right) & & \text{symm} \\ \left(\frac{\nu E}{1-\nu^2} - \frac{s_1 s_2}{S}\right) & \left(\frac{E}{1-\nu^2} - \frac{s_2^2}{S}\right) & \\ \left(- \frac{s_1 s_3}{S}\right) & \left(- \frac{s_2 s_3}{S}\right) & \left(\frac{E}{2(1+\nu)} - \frac{s_3^2}{S}\right) \end{bmatrix} \quad (5.61)$$

where

$$S = \frac{4}{9} A\sigma^2 + s_1\sigma_x^1 + s_2\sigma_y^1 + 2S_3\sigma_{xy}, \quad (5.62)$$

$$S_1 = \frac{E}{1-\nu^2} (\sigma_x^1 + \nu\sigma_y^1),$$

$$S_2 = \frac{E}{1-\nu^2} (\sigma_y^1 + \nu\sigma_x^1),$$

and $S_3 = \frac{E}{(1+\nu)} \sigma_{xy}$.

It is worth noting that for elastic-perfectly plastic material where $E_T = 0$, only the term involving A will drop out but S remains nonzero. Thus the compliance matrix above is valid for both the perfectly plastic and the strain hardening materials.

5.5 Nonlinear Finite Element Analysis

5.5.1 Newton-Raphson Method

Nonlinear analysis involves establishing the finite element equilibrium equations through virtual work for each load increment. These are then solved for the incremental displacements, strains and stresses. Since the displacement finite element method is used, the principle of virtual displacement has been employed to express equilibrium. The discretized equations of equilibrium after the n^{th} load increment can be expressed in the following form (34).

$$\{\Psi(\delta_n)\} = \int_V [B]^T\{\sigma_n\}dV - \{R_n\} = 0. \tag{5.63}$$

The vector $\{R_n\}$ represents the consistent load vector due to surface tractions (uniformly distributed stress over the branch member parameter). For incremental load analysis. Equation 5.63 takes the following form

$$\int_V [B]^T\{\Delta\sigma_n\}dV - \{\Delta R_n\} = 0. \tag{5.64}$$

Obviously. Equation 5.64 is not satisfied exactly after peforming a limited number of iterations and there are undesired residual forces present. In order to minimize these residual forces and prevent drifting of the solution, the Newton Raphson method is employed and iterations are carried out within each load increment. Hence, during the n^{th}

load increment and the m^{th} iteration, the residual forces are computed in the following manner.

$$\{\Psi_n^m\} = \int_V [B]^T \{\sigma_n^m\} dV - \{R_n\}. \qquad (5.65)$$

The iterative Newton-Raphson equation can be written as

$$\{\Psi_n^{m+1}\} = \{\Psi_n^m\} + [K_T(\underline{\sigma}_n^m)] \; \{\Delta\delta_n^m\} = \{0\} \qquad (5.66)$$

where the tangential stiffness matrix $[K_T(\underline{\sigma}_n^m)]$ has been computed by assembling the individual stiffness matrices of all elements. It is important to note that an individual stiffness matrix is computed through numerical integration by using twenty-seven integration points for the state of stress $\underline{\sigma}_n^m$. Proper $[D_n^m]$, elastic or elasto-plastic matrix, is used depending on the stress level and the tangent modulus at each integration point. It may very well happen that within the same element some integration points can be within the elastic range and others past the proportional limit. The residual load vector in Equation 5.65 which can be controlled by specifying a certain tolerance, is added to the next load increment $\{\Delta R_n\}$ at the beginning of m iterations. This prevents drifting of the solution.

✓

The incremental displacements are computed as

$$\{\Delta\delta_n^m\} = - [K_T(\underline{\sigma}_n^m)]^{-1} \{\Psi_n^m\} \qquad (5.67)$$

and the incremental total strains and stresses at any point within an element are given by

$$\{\Delta\varepsilon^m_{ne}\} = [B]\ \{\Delta\delta^m_{ne}\} \tag{5.68}$$

$$\{\Delta\sigma^m_{ne}\} = [D^m_n]\ \{\Delta\varepsilon^m_{ne}\} \tag{5.69}$$

where $\{\Delta\delta^m_{ne}\}$, $\{\Delta\varepsilon^m_{ne}\}$ and $\{\Delta\sigma^m_{ne}\}$ are the element, incremental nodal displacements, strains and stresses at any given point, respectively.

The strain matrix [B] and the updated elastic or elasto-plastic matrix $[D^m_n]$ are functions of space (i.e., x, y and z or ξ, η and $\hat{z}$) and must be evaluated at the point where the strain and the stress increments are required to be computed. The updated element stiffness matrix $[k^e_T(\underline{\sigma}^m)]$ is evaluated by using Equation 5.20 and $[D^m_n]$, the elastic or elasto-plastic compliance matrix determined for stress level $\underline{\sigma}^m_n$. The Newton-Raphson iterative scheme above is illustrated graphically in Figure 5.7 for a single degree of freedom system. However, it is equally applicable to a multi-degree of freedom system.

5.5.2 Algorithm for Computer Model

A description of the steps followed in the finite element computer program is presented here.

Suppose that at a load level $\{R_n\}$, the displacement vector $\{\delta_n^0\}$ and the stiffness matrix $[k_T(\underline{\sigma}_n^0)]$ of the system are known. Apply the next load increment $\{\Delta R_n\}$ which brings the load level up to $\{R_{n+1}\}$. The resulting displacement increment $\{\Delta\delta_n\}$ is computed in the following manner.

(1) After the Newton-R[illegible]hson iterative procedure has converged (within the specified tolerance) for the $(n-1)^{th}$ load increment after m iterations, assume that the residual forces are given by $\{\Psi_{n-1}^m\}$ according to Equation (5.65). The displacement increment due to the first iteration for the n^{th} load increment can be computed from the following equation:

$$[k_T[(\underline{\sigma}_n^0)] \; \{\Delta\delta_n^0\} = - \{\Psi_{n-1}^m\} + \{\Delta R_n\} = - \{\Psi_n^0\} + \{\Delta R_n\}$$

where $\{\Psi_n^0\} = \{\Psi_{n-1}^m\}$ and $\{\Delta R_n\}$ is the $(n)^{th}$ load increment.

(2) The displacement vector is updated in the following manner.

$$\{\delta_n^1\} = \{\delta_n^0\} + \{\Delta\delta_n^0\}.$$

(3) In the inner web plate, do the following for each plate element:

(i) Extract the element incremental nodal displacements $\{\Delta\delta^0_{ne}\}$ from $\{\Delta\delta^0_n\}$ just computed.

(ii) At each integration point (ξ_i, η_i, z_i), calculate the incremental strains via Equation 5.68

$$\{\Delta\varepsilon^0_n\}_i = [B(\xi_i, \eta_i, z_i)]\ \{\Delta\delta^0_{ne}\}$$

- calculate the incremental stresses via Equation 5.69

$$\{\Delta\sigma^0_n\}_i = [D^0_n]_i\{\Delta\varepsilon^0_n\}_i$$

where the elasto-plastic compliance matrix $[D^0_n]_i$ is determined for the stress levels (σ^0_n) at point i with local coordinates (ξ_i, η_i, z_i);

- update the stresses at each integration point;

$$\{\sigma^1_{n+1}\}_i = \{\sigma^0_n\}_i + \{\Delta\sigma^0_n\}_i$$

- check for the compliance matrix.

$$[D^1_n]_i = [D_{e\ell}]_i \quad \text{if} \quad \bar{\sigma}_i < \sigma_y$$

$$[D_n^1]_i = [D_{ep}]_i \quad \text{if} \quad \bar{\sigma}_i > \sigma_y$$

where $\bar{\sigma}_i$ is the effective stress at point i defined in Equation 5.54.

(iii) If $\bar{\sigma}_i > \sigma_y$ at one or more integration points, update the element stiffness matrix $[K^e]$ using Equation 5.20.

(iv) Calculate the internal forces for each element.

$$[F_{ne}^1] = \int_{V_e} [B]^T \{\sigma_n^1\} dV.$$

Steps (i) to (iv) are repeated for all plate elements in the inner web. Meanwhile, the global stiffness matrix $[K_w(\sigma_n^1)]$ and the internal force vector $\{F_w\}_n^1$ are assembled.

(5) For the channel - Uncoupled Model, follow the six steps outlined in Section 5.3.2 to obtain the incremental strains and stresses at every point in the grillage.

For the channel - Coupled Model, the 3-step procedure described at the end of Section 5.3.3 is carried out.

In addition, the following calculations must be made for each beam element:

(i) Update stress level to $\{\sigma^1_{n+1}\}$ at every sampling point;

(ii) Check for yielding at each point by comparing the effective stress $\bar{\sigma}$, Equation 5.37, with the yield stress σ_y. As such,

$$\text{if } \bar{\sigma} > \sigma_y \qquad E^1_n = E_T, \text{ and}$$
$$\text{if } \bar{\sigma} < \sigma_y \qquad E^1_n = E.$$

(ii) Update the element stiffness matrix using the appropriate of Equations 5.28 and 5.32.

The updated global stiffness matrix $[K_{CH}(\underline{\sigma}^1_n)]$ is then formulated. Employing the Uncoupled Model or the Coupled Model, the boundary spring element stiffness matrices $[K_b(\underline{\sigma}^1_n)]$ or the condensed boundary matrix $[K_c(\underline{\sigma}^1_n)]$ are computed using Equation 5.42(a) or Equation 5.42(b), respectively. The associated internal resistance of the channel $\{F_{Ch}\}^1_n$ is calculated from

$$\{F_{CH}\}^1_n = \sum_{i=1}^{m} [K_b(\underline{\sigma}^1_n)] \cdot \{\bar{\delta}^{e*}\}^1_n \qquad \text{for uncoupled model}$$

or,

$$\{F_{CH}\}_n^1 = [K_C(\sigma_n^1)]\ \{\delta_{bb}\}_n^1 \qquad \text{for coupled model}$$

(5) Assemble the global tangential stiffness matrix $[K_T(\underline{\sigma}_n^1)]$ using Equation 5.42 or 5.45 for the uncoupled or coupled model, respectively. Also, add $\{F_W^1\}_n^1$ and $\{F_{CH}\}_n^1$ to obtain the total internal resistance $\{F_T\}_n^1$. The residual forces are now computed as

$$\{\Psi_n^2\} = \{F_T\}_n^1 - \{R_n\}.$$

(6) Solve the following equation to determine the next incremental displacement vector.

$$[K_T(\underline{\sigma}_n^1)]\ \{\Delta\delta_n^2\} = -\{\Psi_n^2\}$$

(7) Repeat steps (2) to (6) until two consecutive determinants of the global stiffness matrix are within the specified percentage tolerance ϵ_D which is calculated in the following manner.

$$\epsilon_D = 100 \times \frac{\text{Det } [K_T(\underline{\sigma}_n^m)] - \text{Det } [K_T(\underline{\sigma}_n^{m-1})]}{\text{Det } [K_T(\underline{\sigma}_n^{m-1})]}$$

(8) If the percentage tolerance is within the prescribed value,

apply the next load increment and repeat steps (1) to (7).

The iterative procedure outlined above is commenced by formulating the system elastic stiffness matrix and applying an arbitrary magnitude of the loads. The system is then solved for displacements, strains and stresses. The elastic limit is determined by scaling the applied loads such that $\bar{\sigma}$ at the most stressed point in the model is equal to the yield limit σ_y. The same scaling factor is applied to the calculated displacements, strains and stresses. Additional loads are then applied in increments as a percentage of the initial yield load until stiffness of the joint reduces significantly in comparison with its initial value where stiffness is defined as the slope of the P-Δ diagram.

The computer algorithm outlined in this section requires a complete re-analysis of the system for every iteration since the Newton Raphson method has been employed. However, it allows application of the loads in relatively large increments. Furthermore, the method converges in about two to three iterations for each load increment. For equal load increments, the number of iterations required for convergence starts increasing rather quickly as the P-Δ curve becomes flatter and the stiffness diminishes rapidly. This is usually a signal to decrease the load increments in this range to help reduce the number of iterations.

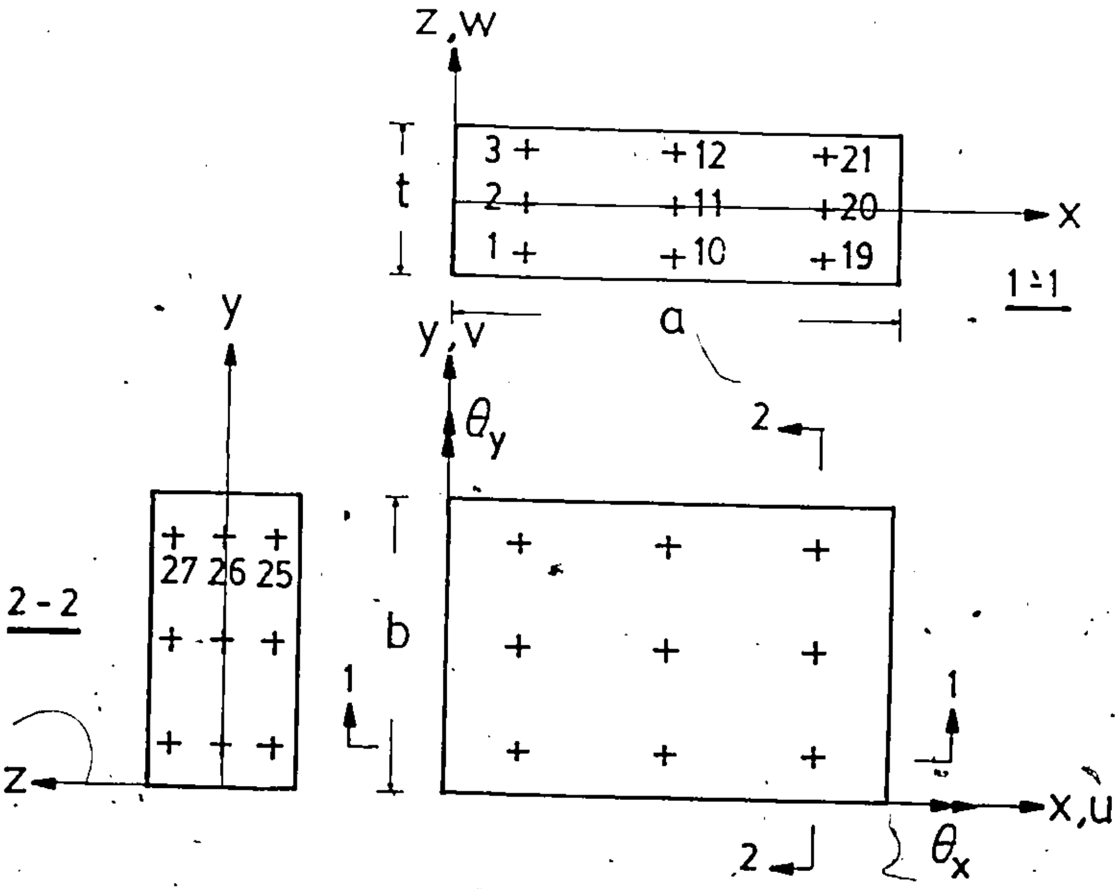
z,w
3
12
21
2
11
20
1
10
19
t
x
1-1
a
y,v
θy
2
y
27
26
25
2-2
b
1
z
x,u
θx
2

FIGURE 5.1 : RECTANGULAR PLATE ELEMENT

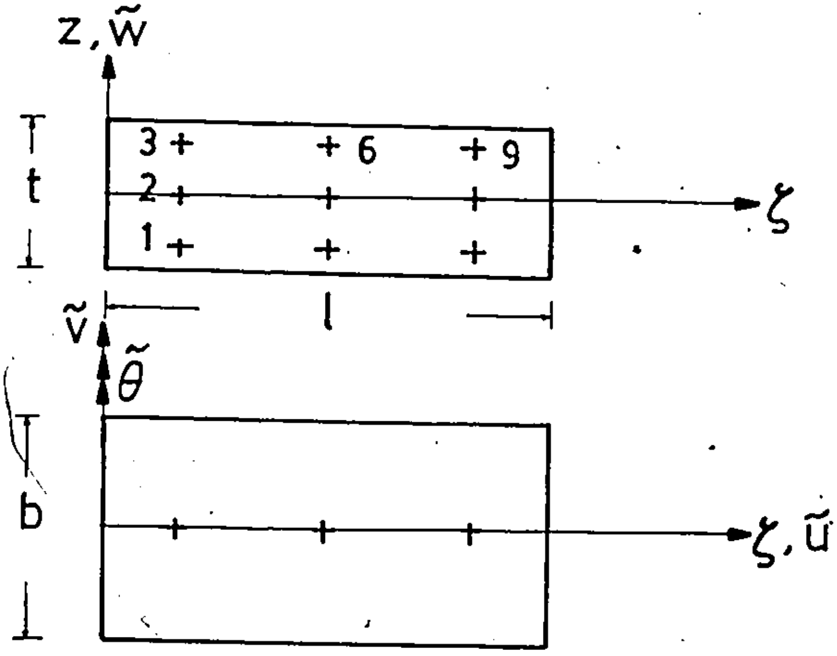
z,w̃
3
6
9
2
1
t
ζ
l
ṽ
θ̃
b
ζ,ũ

FIGURE 5.2 : BEAM ELEMENT

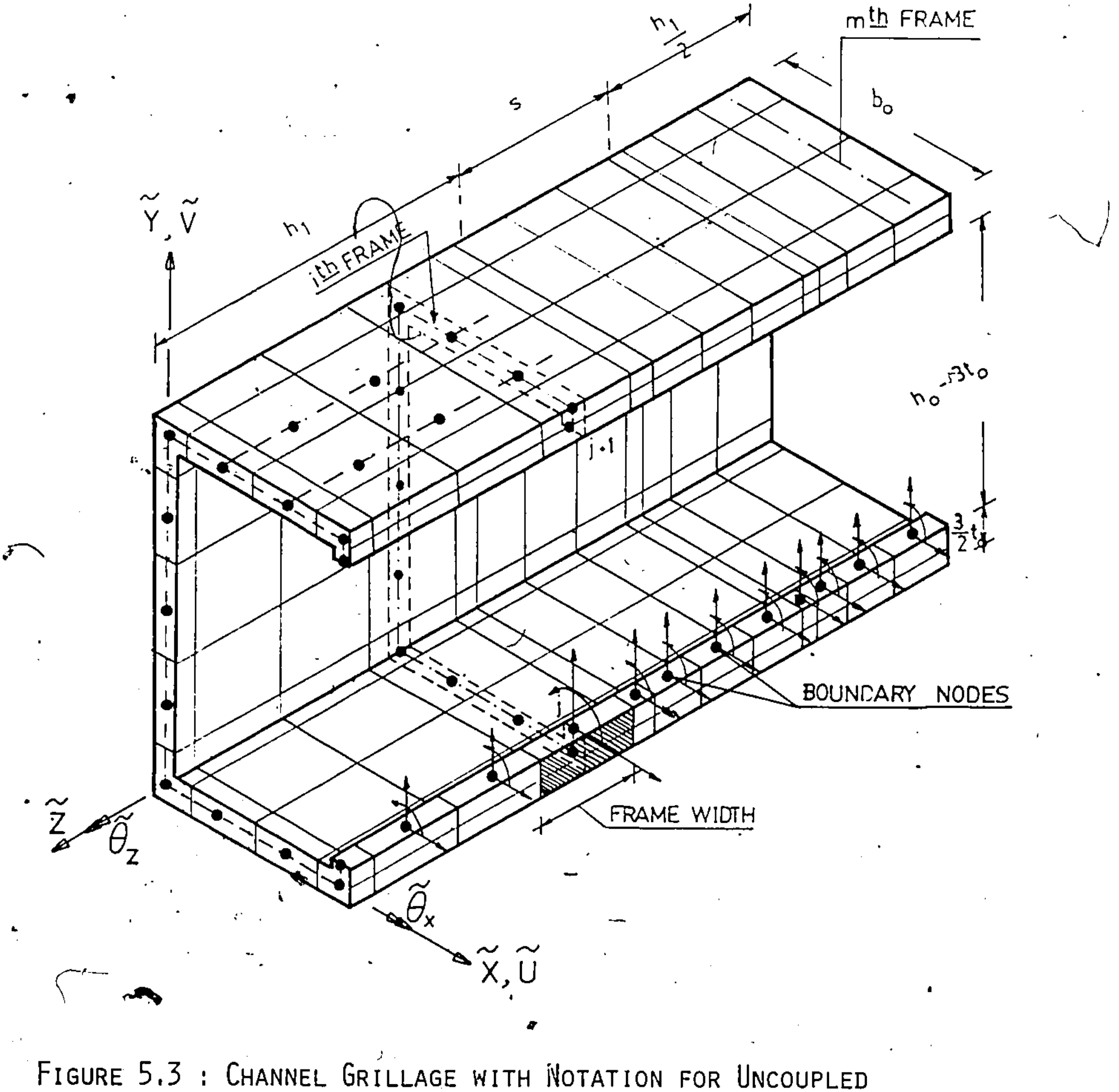
mth FRAME
$\frac{h_1}{2}$
s
b_o
h_1
ith FRAME
$\tilde{Y}, \tilde{V}$
$h_o - \frac{3}{2}t_o$
j+1
j
$\frac{3}{2}t_o$
BOUNDARY NODES
FRAME WIDTH
$\tilde{Z}$
$\tilde{\theta}_z$
$\tilde{\theta}_x$
$\tilde{X}, \tilde{U}$

FIGURE 5.3 : CHANNEL GRILLAGE WITH NOTATION FOR UNCOUPLED ANALYSIS

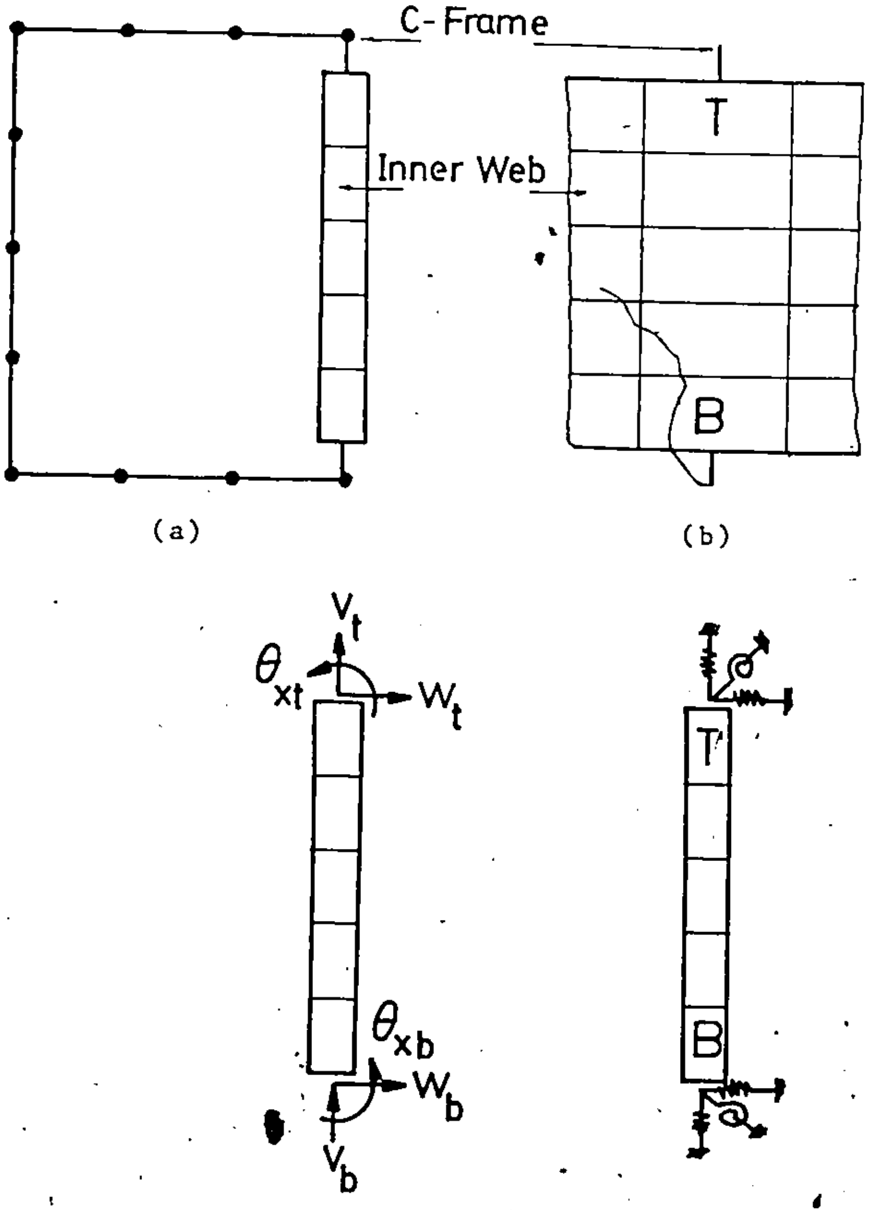
C-Frame
Inner Web
T
B
V_t
θ_{xt}
W_t
θ_{xb}
W_b
V_b
T
B

(a) (b)

(c) (d)

FIGURE 5.4 : BOUNDARY SPRING ELEMENT

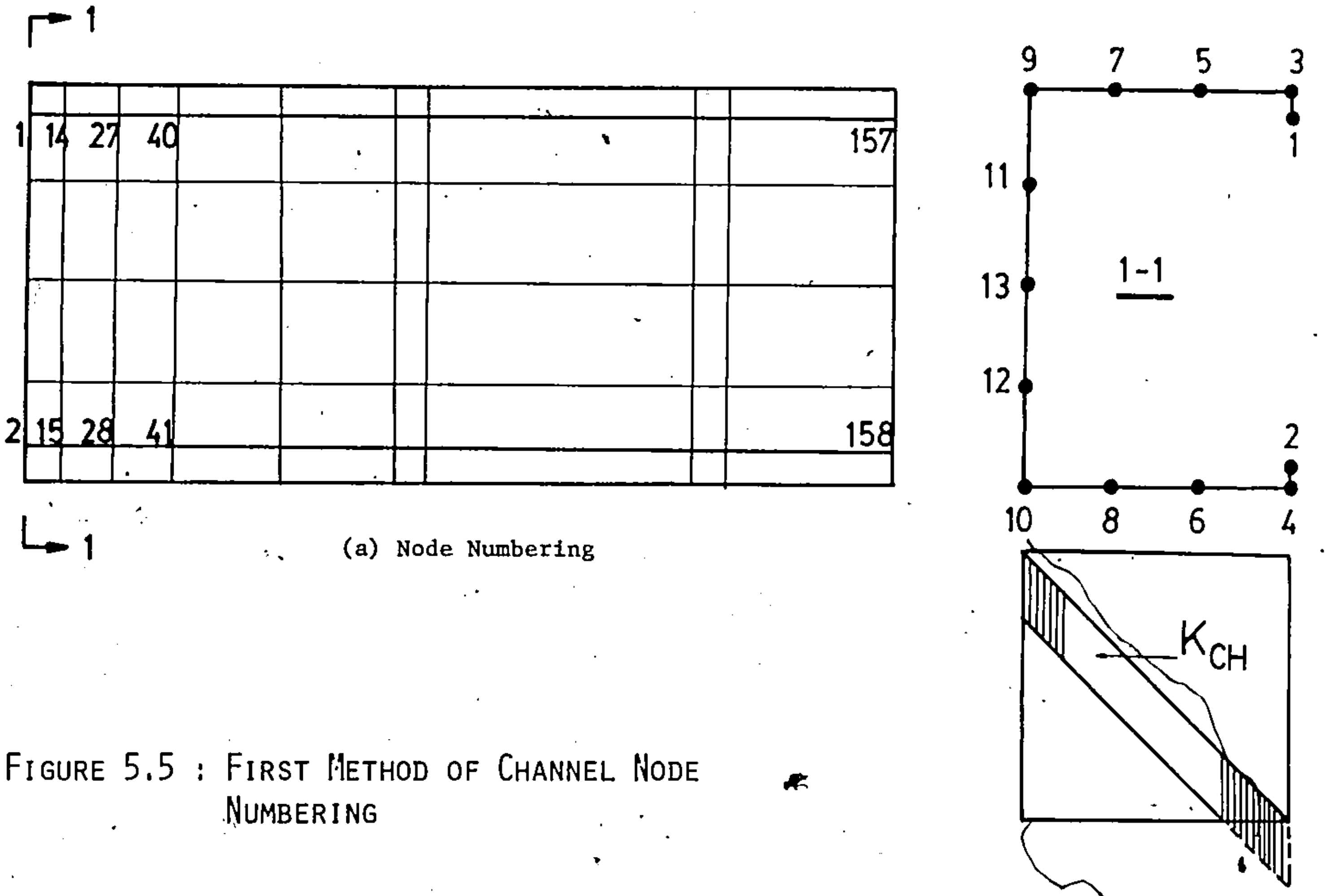
1
1
1
14
27
40
157
2
15
28
41
158
9
7
5
3
1
11
13
12
1-1
2
10
8
6
4
K_{CH}

(a) Node Numbering

(b) Stiffness Matrix

FIGURE 5.5 : FIRST METHOD OF CHANNEL NODE NUMBERING

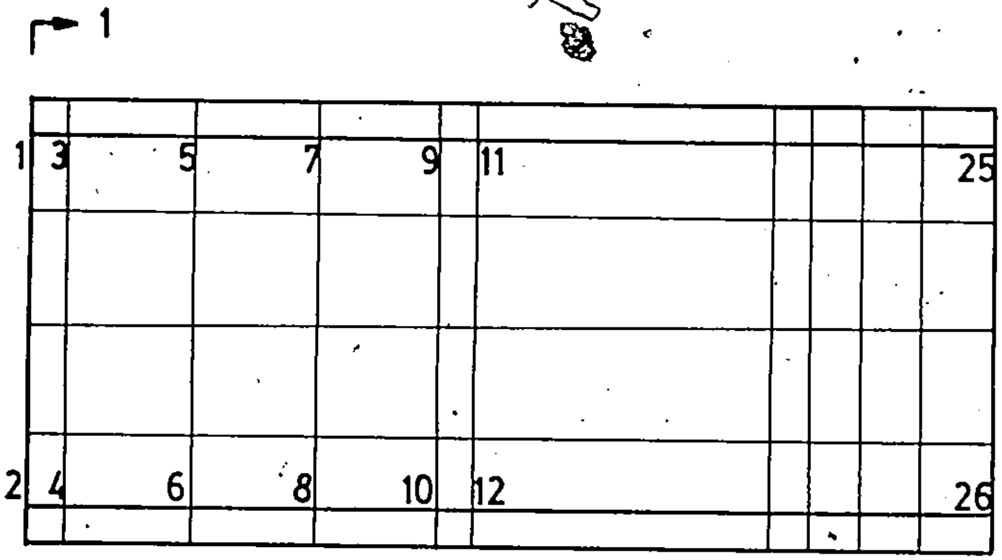
1
1
1
2
3
4
5
6
7
8
9
10
11
12
25
26

(a) Node Numbering

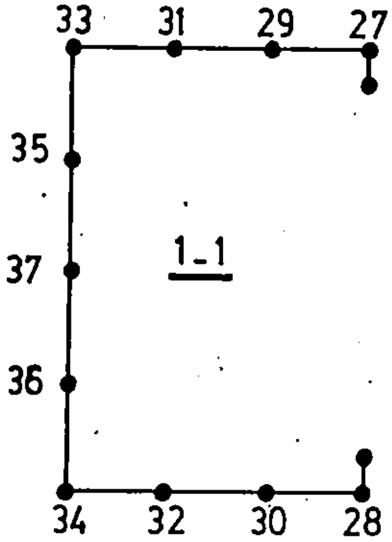
33
31
29
27
35
37
36
34
32
30
28
1-1

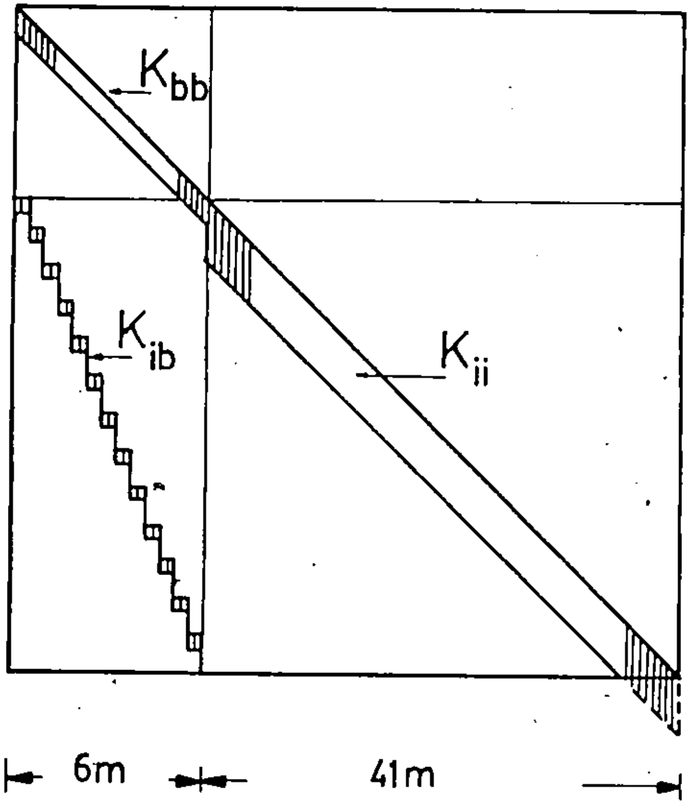
K_bb
K_ib
K_ii
6m
41m

(b) Global Stiffness Matrix

FIGURE 5.6 : SECOND METHOD OF CHANNEL NODE NUMBERING

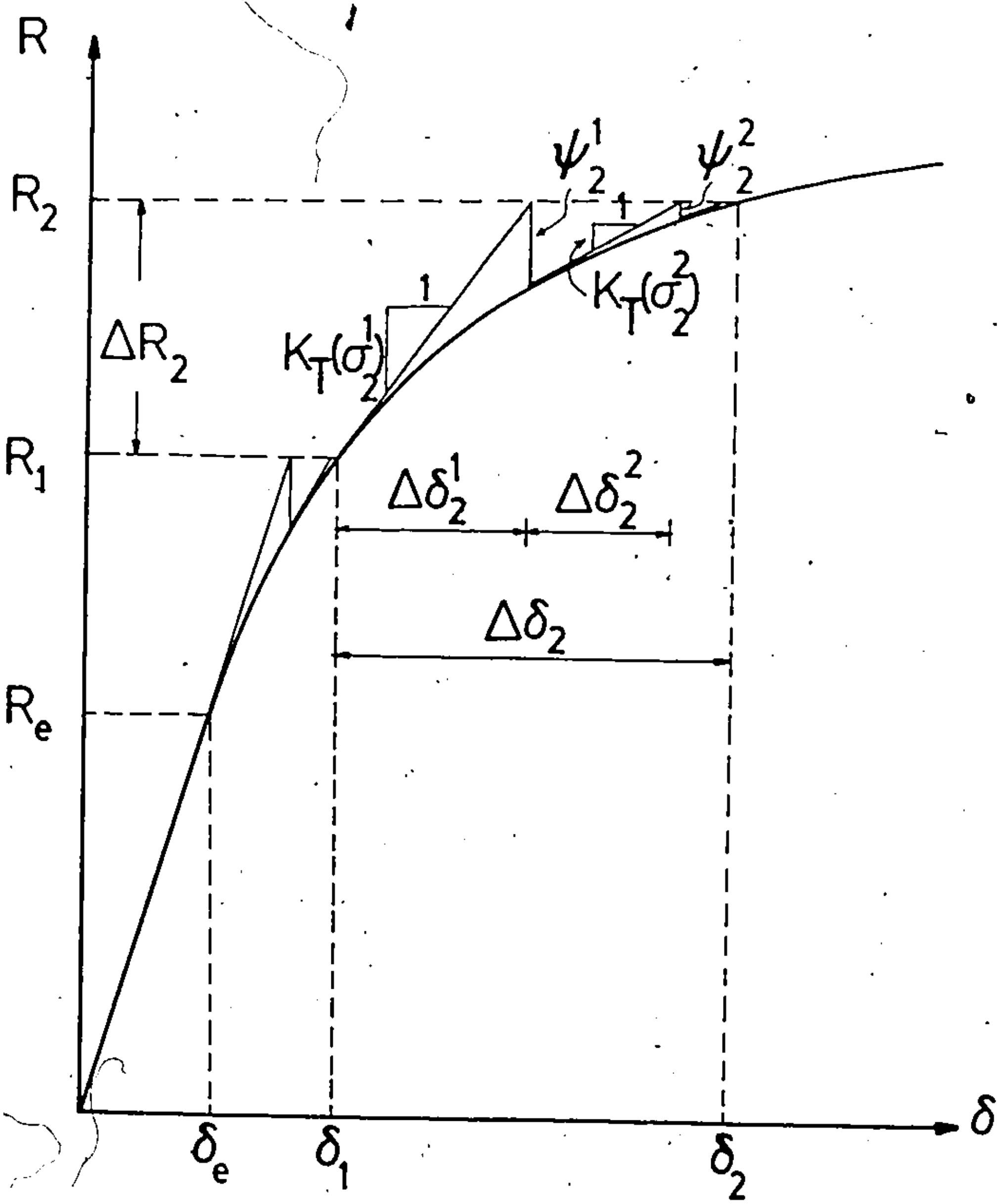
R
R₂
ΔR₂
R₁
Rₑ
ψ_2^1
ψ_2^2
1
1
$K_T(\sigma_2^1)$
$K_T(\sigma_2^2)$
$\Delta\delta_2^1$
$\Delta\delta_2^2$
$\Delta\delta_2$
δ
δ_e
δ_1
δ_2

FIGURE 5.7 : NEWTON - RAPHSON ITERATIVE METHOD

CHAPTER 6

MODEL VERIFICATION AND SENSITIVITY ANALYSIS

6.1 Introduction

The response of the uncoupled and coupled finite element models presented in Chapters 4 and 5 are the subject of investigation in this Chapter. Of importance was to establish the degree to which coupling of the longitudinal effects (which is accounted for in the coupled model only) along the inner web plate's top and bottom boundaries can influence the strength and stiffness characteristics of the twin shear beam. The investigation was carried out through numerical examples covering a wide range of chord member and gap dimensions. Secondly, verification of the FEM model is presented. For such verification, modelling was extended to the twenty-four twin shear beam specimens tested and reported earlier (Chapter 2). Theoretical and experimental load-deflection paths are compared, thus providing a basis for evaluating the adequacy of the finite element model.

Also to be considered in this Chapter is a sensitivity analysis of the FEM model. The coupled twin beam model was selected for this purpose. The effects of changing the geometry of the chord and web members, and the gap distance were investigated using a three-level parametric study. Of interest, as well, is the influence of the tangent modulus on the post-elastic behaviour. Numerical results of predicted test specimen behaviour are assimilated into groups and are expressed in terms of load-deflection plots to reveal properties of the model.

Finally, the spread of plastic zones under incrementally increasing load is graphically illustrated for two typical twin beams.

6.2 Comparison Between Uncoupled and Coupled Finite Element Twin Shear Beam Models

From a theoretical viewpoint, it is known that the coupled model is superior to the uncoupled one in providing a more accurate response of the channel's resistance, particularly in shear. The economy in computer time and storage inherent in the uncoupled model, however, makes it worthwhile to compare the performances of the two models to see whether the difference in their responses is of any practical significance. Three idealized twin shear beams (shallow, square and deep) were selected to assess the performances of the uncoupled and coupled finite element models for a practical range of depth to width ratio. Geometric properties of these beams are indicated in Figure 6.1. Employing these properties and the mesh of elements shown in Figure 4.5 for a and b type beams, the two models were run under the same boundary conditions. Before using the coupled model, it was necessary to determine the parameter "n" which denotes the degree of coupling considered in the matrix $[K_c]$ derived in Equation 5.41. It is known, a priori, that complete coupling is achieved when n is a maximum and is equal to the number of boundary nodes on one side of the inner web plate minus one. However, this was not practically feasible as it required extremely large storage on the computer. Rather, elastic test runs of the model were made for a typical beam using n=2,3,4,5,6 and 7. From a comparison of the results it was found that the behaviour gradually stabilized until it became identical both for n=6 and 7. A value of n=7 was thus selected for the analysis to follow in subsequent work of this Chapter.

The twin beams were theoretically loaded well into the plastic range. Each run was terminated when the midspan deflection attained a value of 1% $(h_0 + b_0)$ as proposed in Section 2.6. Predicted behaviour is represented by the load-deflection diagrams of Figure 6.1. From these results, it is observed that:

(1) The coupled model generally predicted a stiffer response in and beyond the elastic range.

(2) The difference in strength between the two models constantly increased with deflection and becomes more pronounced in the elasto-plastic range.

(3) The slope of the P-Δ curve of the coupled model at the limiting deflection is considerably steeper than that of the uncoupled model indicative of the capability of sustaining more loads at larger deflections.

The coupling of the degrees of freedom at the channel-inner web plate interface in the longitudinal direction appears then to have a sizable effect on the overall behaviour of the model. It is therefore concluded that the coupled model is more appropriate than the uncoupled one in simulating the twin shear beam and consequently separated double chord joints.

6.3 Verification

The coupled finite element model had to then be verified using the experimental results of the twin shear beams reported in Chapter 2. Firstly however, it was essential to test the rectangular plate element employed in the inner web plate model. While well documented in the literature, it was necessary to perform some simple checks to ensure that the present computer program was operating correctly. The out-of-plane action of the nonconforming plate bending element was previously checked by Shehata (10) who used an example given by Stanton et al. (45) for a simply supported square plate with uniformly distributed load. Comparisons of results in the elastic, as well as in the elasto-plastic, range showed good agreement.

The in-plane action simulated by the eight DOF plane stress rectangular element is checked herein. This element was tested both in the elastic and elasto-plastic ranges in applications of gravity loaded beams having span-to-depth ratios of 4:1 and 6:1. Another test was conducted on a deep shear panel (2:1) subject to in-plane edge loading.

The first test (1V), which was limited to the elastic range, was done on a cantilever beam loaded at its free end by a parabolically distributed traction to simulate a concentrated load. The deflection at point c was compared with the "exact solution" derived from a closed form of elasticity solution (38). The ratio of computed to exact deflection was found to be 0.951 for a 4 × 16 mesh of elements. The second test (2V) was done on a cantilever beam with a higher span-to-depth ratio of 6:1 in order to ensure that the behaviour would be governed solely by bending. As can be seen from Figure 6.2(a), the beam was subjected to uniformly distributed pressure. Employing a 4 × 24 grid of elements and elastic-perfectly plastic material, the beam was subjected to simulated loading into the plastic range until no further convergence was achieved after 10 iterations of the Newton Raphson method for a load increment of 2% of the elastic limit load. From the computed normal stresses of the sampling points of elements adjacent to the clamped end, the bending moment M acting on the support section could thus be evaluated. The ratio of M/M_p is plotted against the tip deflection in Figure 6.2(b). It was found that the finite element solution provided as much as 99% of the plastic moment capacity M_p. As expected, yielding of the cantilever beam commenced simultaneously at the top and bottom fibres at the support, then progressed through the depth and the length, making a symmetrical pattern about the longitudinal centreline. The distribution of the plastic regions in the beam at the point of failure is traced in Figure 6.2(c).

Verification test No. 3V comprised a deep shear panel with an aspect ratio of 2:1. The primary objective of this test was to induce a situation where shearing action governs the behaviour and hence to check the element's capability of developing the full plastic shearing resistance of the section. The panel was subjected to a uniformly distributed load applied along its edge as shown in Figure 6.3(a) and was subdivided into 32 elements using a 4 × 8 grid. For an elastic-perfectly plastic material, the maximum shearing load sustained by the panel was only 86.7% of the plastic shearing force V_p -indicative of a lower bound solution. Results are demonstrated in Figure 6.3(b). The apparent bilinear behaviour of the load-deflection plot is due to the abrupt failure of the panel which resulted from simultaneous yielding of the twelve elements in the middle of the panel as shown in Figure 6.3(c).

For the verification of the FEM model against the twin shear beam experiments, the material properties defined in Section 4.6 were used. The discretized inner web plate for a and b type beams is presented in Figure 6.4. (Those for c and d types were previously shown in Figure 4.5). Each twin beam analysed consumed twenty to forty load increments of variable size beyond the elastic limit level in order to arrive at the prescribed deformation limit determined in accordance with the deflection criterion proposed in Section 2.6. To provide the basis for proper comparison between theoretical and experimental results, the deflection values from the test specimens were modified slightly in order to conform with the assumption of the roller support underneath the reactive stub column. Experimental and theoretical load-deflection curves are presented in Figures 6.5, 6.6 and 6.7 for shallow, square and deep twin beams respectively. The Δ values in these figures represent the relative deflection occurring in the gap, rather than the midspan deflection minus the nominal contraction of support columns. It will be observed that while very good agreement was obtained for some twin beams such as 6d, 7a and 8c, poor agreement was observed for others, such as

1a, 2c and 4c. Computed values of elastic stiffness C_e^* and deflection limit load P_b^* are plotted for the beam versus their experimental counterparts in Figures 6.8 and 6.9. It is evident from both plots that the theoretical results exhibit a reasonable scatter around their experimental counterparts.

In Chapter 2, it was observed that the elastic stiffness generally increased with reduced gap size. This was not observed to be the case for specimen 4c. In calculating the relative deflection occurring in the gap from the dial gauge readings at the supporting stubs, the results of specimens 2c and 2d exhibited the same unexpected behaviour. Their elastic stiffnesses calculated from relative deflection were lower than those of 2a and 2b which possess larger gaps. It is possible that this is due to experimental errors as theoretical prediction indicates that reducing the gap increases the elastic stiffness which is expected. It follows that the P-Δ curve is flattened and the strength at the deflection limit was less than it should have been. Consequently, it was deemed that the results of these three specimens ought to be excluded from an assessment of the model's validity. In light of the demonstrated results, these observations are made.

(1) Except for three twin beams (2c, 2d and 4c), the predicted elastic stiffness is in good agreement with the measured value. The mean ratio of computed to experimental elastic stiffness is 0.97 for the remaining 21 specimens.

(2) Theoretical deflection limit loads for a and b type speci-

mens are lower than their experimental counterparts with an average agreement of 0.81. Higher correlation is obtained for c and type specimens where the mean value of predicted to observed loads is increased to 0.99 at the limiting deflection. Overall, the theoretical model correlates with experiments at an average of 0.87.

As the inner web continues to distort in its plane, a field of membrane tensile stresses develops along a line making a maximum of 45° with the horizontal towards the longer diagonal of the distorted web (46). This action, which is due to a change in geometry of the web is known as the "diagonal tension field". The extent to which tension fields can grow in the inner web under large displacements depends on its width-to-depth ratio and its boundary conditions. The width-to-depth ratio determines which sides of the web are supposed to serve as anchors for a tension stress field. When this ratio is small, as is the case for all twin beams tested in this study, the tensile stress flow would tend to bridge the vertical sides. As such, the development of tension field stresses in the twin shear beams will depend primarily on the amount of anchorage offered by the vertical boundaries of the inner web.

In the theoretical model, tension fields are not accounted for since the model is based on small deformation theory. Twin beam specimens of a and b type were completely welded to their branch members and as such the development of membrane stresses was enhanced. It is for this reason that the theoretically analysed twin beams of a and b type exhibited somewhat premature loss of strength and stiffness. It is surmised that the lack of weldment along the supported side of the inner web in c and d type specimens played a role in retarding the effective growth of membrane tensile stresses; it would be expected therefore that theoretical and experimental results would thus be in better agreement as in fact they were (see Figures 6.6(c), (d), (g), (h) and 6.7(e) and (f)).

6.4 Sensitivity Analysis

All the parameters h_o, b_o, t_o, s, h_1, b_1, t_1 and E_T were candidates for a sensitivity analysis of the FEM coupled model. No attempt was made initially to consolidate the number. This was done intentionally with the primary objective of revealing the effect of each parameter separately. With the exception of E_T, the selected parameters completely describe the geometry of the twin shear beam. A total of 17 hypothetical twin shear beams, designated TB1,TB2,...,TB17, and having the data shown in Table 6.1 were analysed. The postulated beams were classified into nine groupings, the first of which contained only TB1. Each of the other groupings consisted of two twin shear beams for which a certain parameter was assigned upper and lower limit values. Mid values of all eight parameters investigated were established for TB1. In this way, only a single parameter need be varied without interference from other parameters. With TB1 as a bench mark, there existed therefore three typical results for each parameter for which the groupings are denoted in Table 6.1.

It was assumed that all beams were welded to their stub columns along the perimeters of contact; i.e. the case for a and b type physical specimens illustrated in Figure 2.2(a). A consistent grid for the inner web plate having four rows and twelve columns of elements, three of which were in the gap spacing, was used throughout the sensitivity tests. This element representation is sketched in Figure 6.4. The channel grillage was generated to conform with the beam element distribution depicted in Figures 4.8 and 4.9.

The beams were presumed to be loaded incrementally until well into their plastic range. The elastic limit load was determined from application of an arbitrary uniform pressure to the upper stub column and computations were made for the resulting stresses at every sampling point in both the inner web mesh and the channel grillage. That point possessing maximum effective stress was identified after which a factor was used to attain the yield value. The associated factored pressure would then define the elastic limit load P_e. Twenty or more variable sized load increments (5 to 20% of P_e) were then applied beyond the elastic limit load. The permissible tolerance for the convergence of solution in the nonlinear range was preset to 1%.

Load-midspan deflection curves for the twin shear beams from the finite element analyses are plotted in eight groups; each of which represents a variation of a single parameter. These are displayed in Figures 6.10 to 6.17. Somewhat smoother P-Δ curves would have resulted had smaller load increments been used, however, not without increased computer costs. In order to maintain consistency, a common legend was used in all plots. The curve corresponding to the parameter's central level value is denoted by a solid line. Results of lower and upper level values are expressed by dashed and solid-dotted lines respectively. In view of these results it is observed that:

(1) There is a pronounced benefit both in strength and stiffness for increasing the chord depth h_0 and chord thickness t_0 (Figures 6.10 and 6.12).

(2) The change in the chord member width has virtually no influence on the performance of the twin shear beam except where it is very small. In this case (b_0 = 50 mm), the P-Δ curve was slightly elevated in the post-elastic range.

(3) The strength and stiffness characteristics were noticeably weakened for enlarged gap size. The load-deflection curve corresponding to the smallest gap in Figure 6.13 maintained the highest slope throughout the range of loading applied.

(4) Except for varying h_1, the geometry of the branch members has only a minor influence on the behaviour of the twin shear beam; (Figures 6.15 and 6.16). Comparing the three load-deflection plots traced in Figure 6.14, it is observed that the value of h_1 = 50 mm provided a response slightly higher than h_1 = 100 mm in the elastic range but thenceforth somewhat weaker. On the other hand, when h_1 took on its 150 mm value, the P-Δ curve initially had a relatively lower slope indicating a reduced elastic stiffness but eventually joined the curve of h_1 = 100 mm. As the results concerning h_1 were rather inconclusive, two additional

beams TB18 and TB19 (Table 6.2) having h_1 = 200 and 250 mm were analysed. Figure 6.18 presents the results of TB1, TB10, TB11, TB18 and TB19 representing five different values of h_1. It becomes evident that the larger the value of h_1 the smaller is the elastic stiffness of the beam. It is also observed that the group of load-deflection curves are almost parallel in the plastic range which implies equal stiffness. The differences in resistance for large Δ is within 10% throughout the post elastic range.

(5) As expected, a variation in E_T had no influence on behaviour up to the elastic limit load (Figure 6.17). Beyond this level, the increase in the tangent modulus was accompanied by gains in both strength and stiffness.

Based on these observations, it is evident from the model that the parameters h_o, t_o and s play the greatest role in the performance of the twin shear beam both in the elastic and the post-elastic ranges. This is to be expected since it is these parameters that define the web geometry of a double chord gap joint and offer the major source of resistance by shearing action (Chapter 2). By increasing the web dimensions (h_o and t_o), an improved behaviour is therefore achieved. Also, a smaller gap distance results in a higher elastic stiffness since the stiffness of a shear beam may simply be expressed by $\frac{GA}{s}$ where s is its span. A higher stiffness is observed to extend to the elasto-plastic range since only portions of the web have yielded for the cases plotted in Figure 6.13. The reason there is an increase in strength for reduced gap size is the subsequent reduction of bending moment acting on the critical section.

There is an apparent insignificance of the chord member width b_o on the model's behaviour. A plausible explanation for this response is that when the gap is small (which is the case in all tests conducted), major flange deformations tend to be localized around the loaded member regardless of how wide is the chord member. As regards h_1, a high value reflects a larger overall span (or centre-to-centre eccentricity in the case of double chord joints). This would invariably lead to reduced elastic stiffness. The post-elastic strength attained may vary only within 10% depending on the chosen value of h_1.

It is of interest to examine the effect of weldment type on the behaviour of the twin beam. While all beams analysed were of the a and b type, an additional beam TB20 that is welded to its support member according to the c and d pattern was also analysed, i.e. the weldment was presumed to exist along one side of the inner web plate only. The geometric properties of TB20 are given in Table 6.2 and are identical to TB1, thus enabling a comparison of performance to be made between the two. Such comparison is graphically illustrated in Figure 6.19. It is evident that there exists substantial benefits in both strength and stiffness when complete welding along the supported side of the gap is employed.

To provide a better understanding of the resistance offered by the channel and the inner web segments of the RHS, an assessment was made of the amount of restraint offered by the channel portion. For this purpose the twin beam TB21 (Table 6.2) identical in geometry to TB1 but without the channel part was analysed. A comparison between the two is shown in Figure 6.20. It was found that TB21 could not sustain further loads beyond the last point identified in the figure. At that point a load increment of 0.05 P_e was applied but no convergence was reached after 10 iterations. From the numerical results, it appears that the channel portion is responsible for 4.8% of the total elastic stiffness and 9.3% of the strength when TB21 failed by shear. However, TB1 continued to sustain greater loads at larger deflections implying that the channel provides an increasing contribution to the strength of the twin beam. It is worth noting that this test could not be performed without the substructuring method employed in the model. Such a method permits optional elimination of the channel and analysis of the inner web alone.

Figure 6.21 presents the progression of plastic regions in the inner webs of two representative twin beam specimens 5a and 7a. As can be seen from the figure, yielding commenced at the bottom corner of the gap zone near the roller support. This was a result of a combination of high normal and shear stresses. The other three corners of the gap spacing yielded soon afterwards at a higher load level. As the load was further incremented plasticity spread and occupied virtually the whole gap spacing.

Table 6.1: Test Data for Sensitivity Analysis

Beam	h_o	b_o	t_o	s	h_1	b_1	t_1	E_T/E	Parameter Varied
TB1	100	100	6	15	100	100	5	0.025	None
TB2	50	100	6	15	100	100	5	0.025	h_o
TB3	150	100	6	15	100	100	5	0.025	h_o
TB4	100	50	6	15	100	100	5	0.025	b_o
TB5	100	150	6	15	100	100	5	0.025	b_o
TB6	100	100	4	15	100	100	5	0.025	t_o
TB7	100	100	8	15	100	100	5	0.025	t_o
TB8	100	100	6	10	100	100	5	0.025	s
TB9	100	100	6	20	100	100	5	0.025	s
TB10	100	100	6	15	50	100	5	0.025	h_1
TB11	100	100	6	15	150	100	5	0.025	h_1
TB12	100	100	6	15	100	50	5	0.025	b_1
TB13	100	100	6	15	100	150	5	0.025	b_1
TB14	100	100	6	15	100	100	3.5	0.025	t_1
TB15	100	100	6	15	100	100	6.5	0.025	t_1
TB16	100	100	6	15	100	100	5	0.00	E_T
TB17	100	100	6	15	100	100	5	0.05	E_T

Note: All dimensions in mm.

Table 6.2: Additional Test Data for Sensitivity Analysis

Beam	h_o	b_o	t_o	s	h_1	b_1	t_1	E_T/E	Parameter Varied
TB18	100	100	6	15	200	100	5	0.025	h_1
TB19	100	100	6	15	250	100	5	0.025	h_1
TB20	100	100	6	15	100	100	5	0.025	a&b type of weld
TB21	100	100	6	15	100	100	5	0.025	Inner web Plate only

Note: All dimensions in mm.

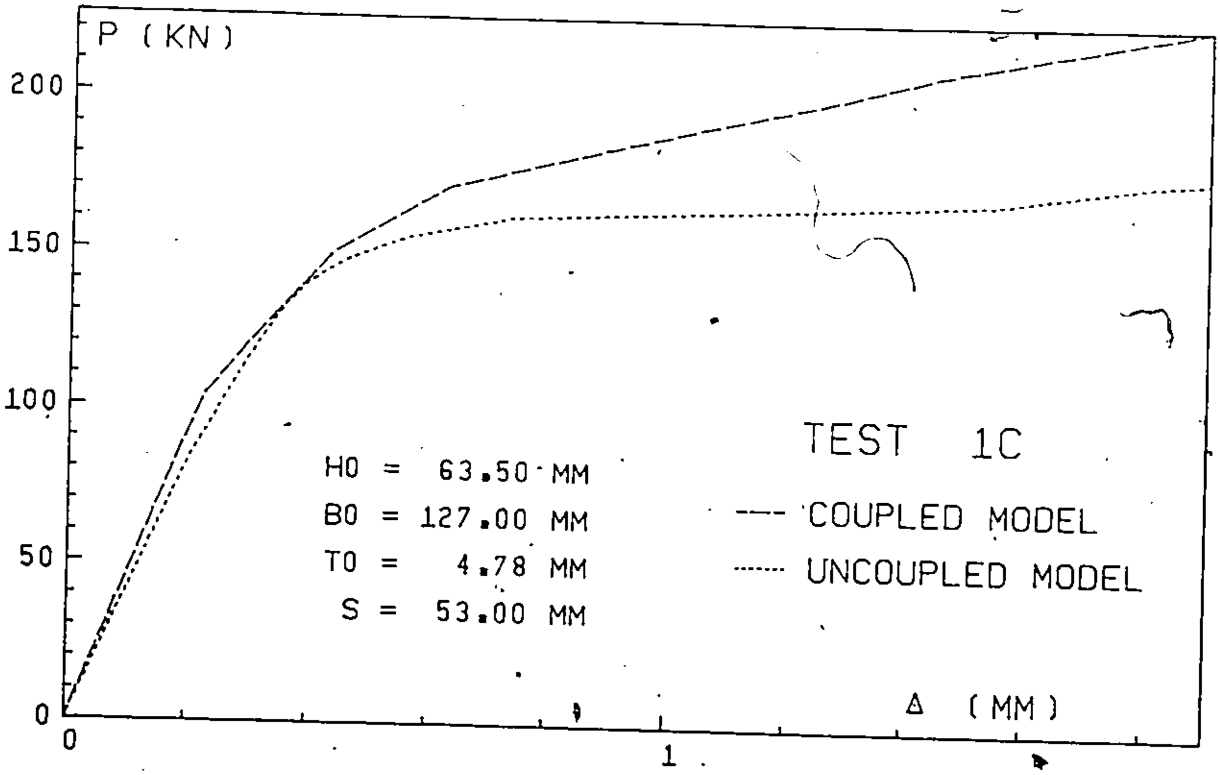
P (KN)
200
150
100
50
0
0
1
Δ (MM)
H0 = 63.50 MM
B0 = 127.00 MM
T0 = 4.78 MM
S = 53.00 MM
TEST 1C
COUPLED MODEL
UNCOUPLED MODEL

(a)

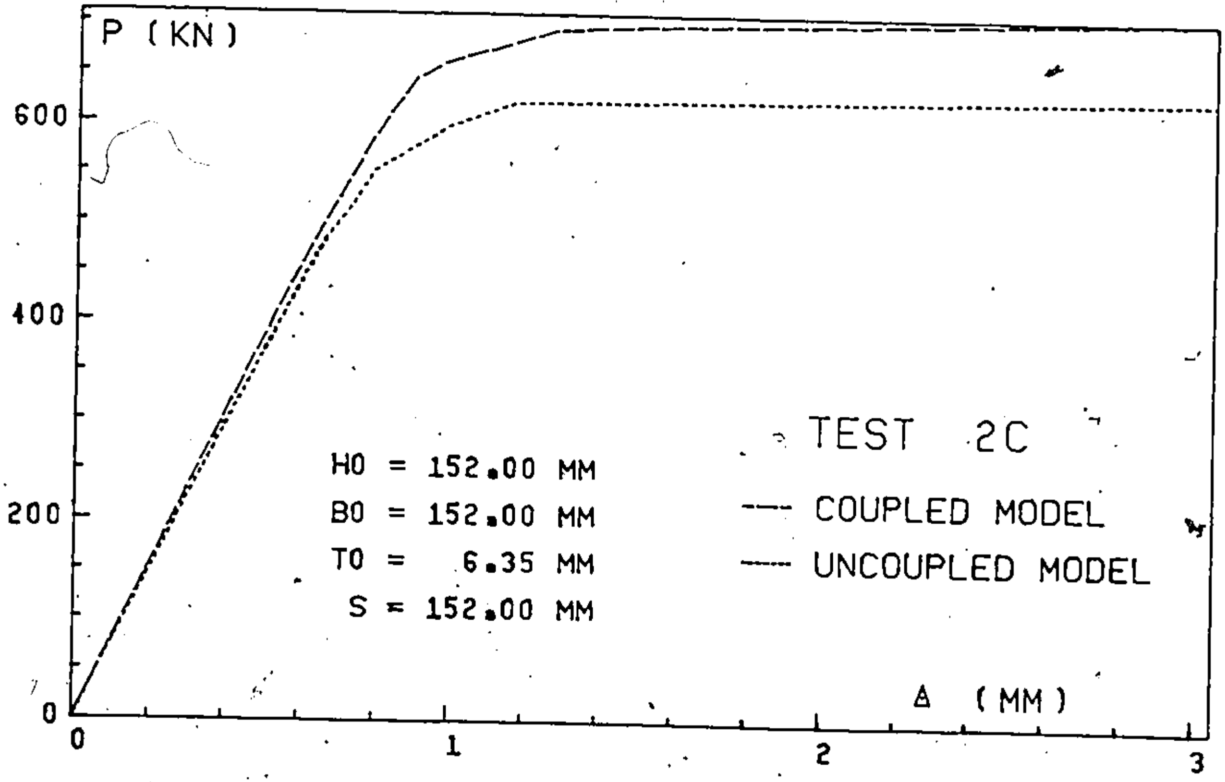
P (KN)
600
400
200
0
0
1
2
3
Δ (MM)
H0 = 152.00 MM
B0 = 152.00 MM
T0 = 6.35 MM
S = 152.00 MM
TEST 2C
COUPLED MODEL
UNCOUPLED MODEL

(b)

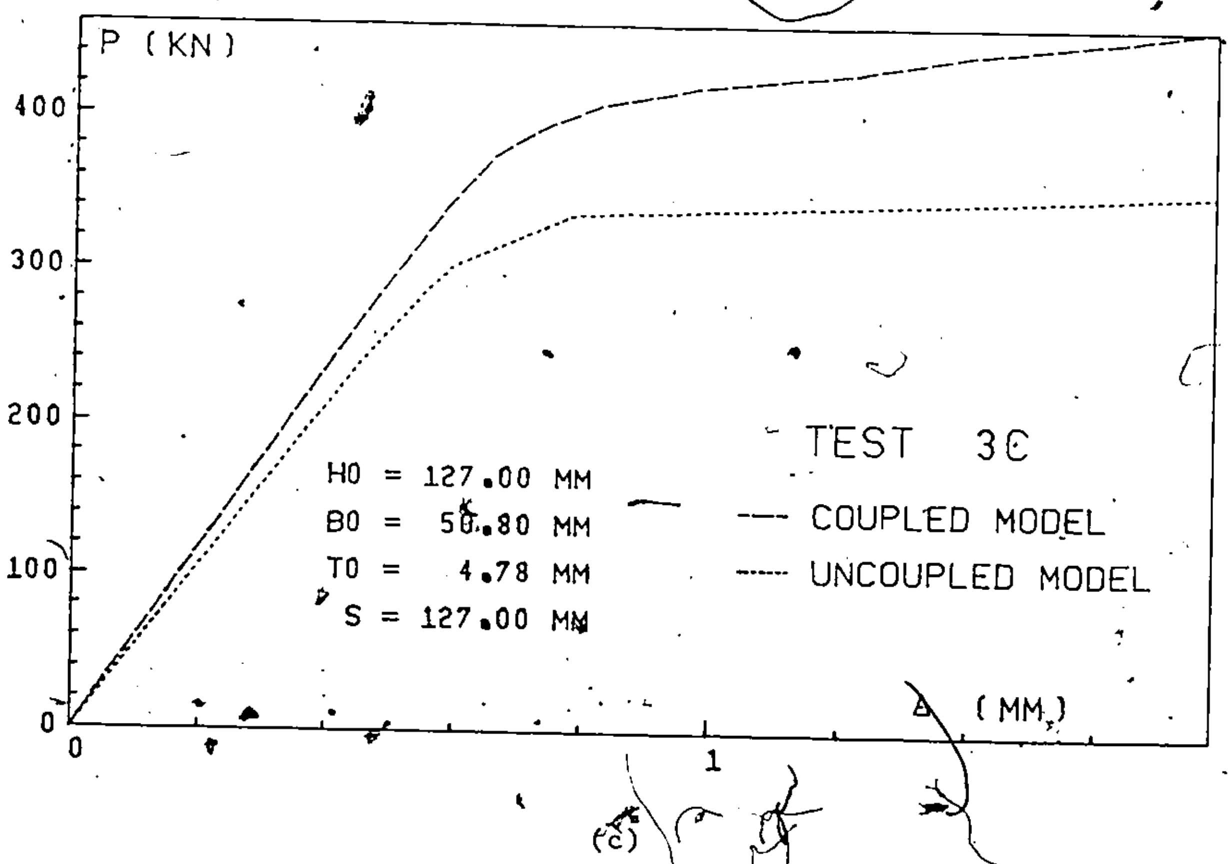

FIGURE 6.1 : COMPARISON OF PERFORMANCE BETWEEN COUPLED AND UNCOUPLED MODELS

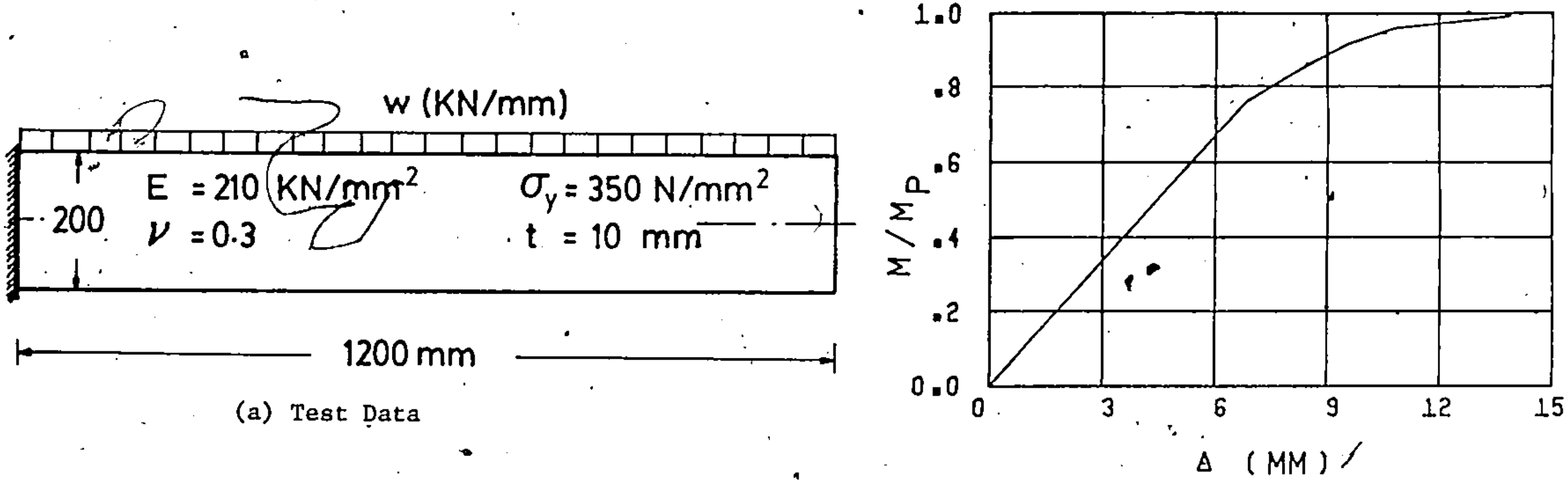

(a) Test Data

(b) Results

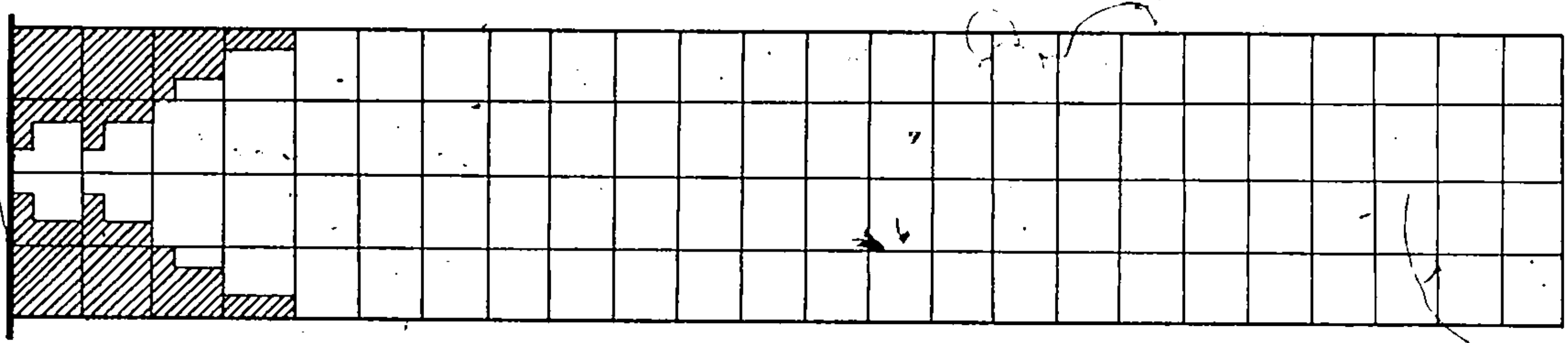

(c) Distribution of Plastic Regions at Failure

FIGURE 6.2 : DATA AND RESULTS OF TEST 2V

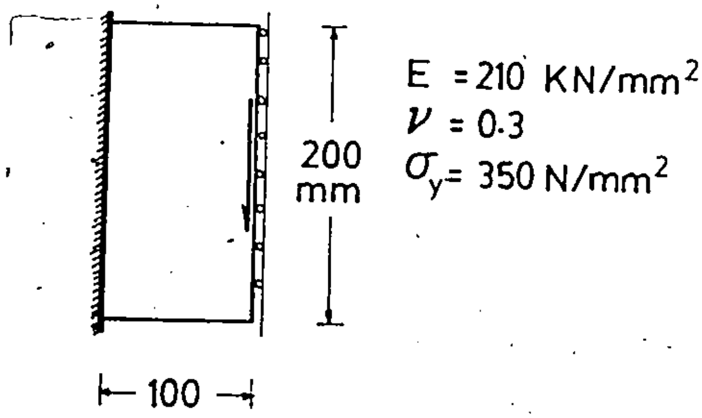
E = 210 KN/mm^2
ν = 0.3
σ_y= 350 N/mm^2
200 mm
100

(a) Data

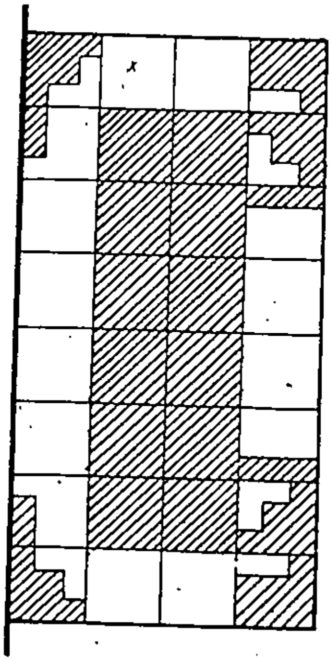

(c) Distribution of Plastic Regions at Failure

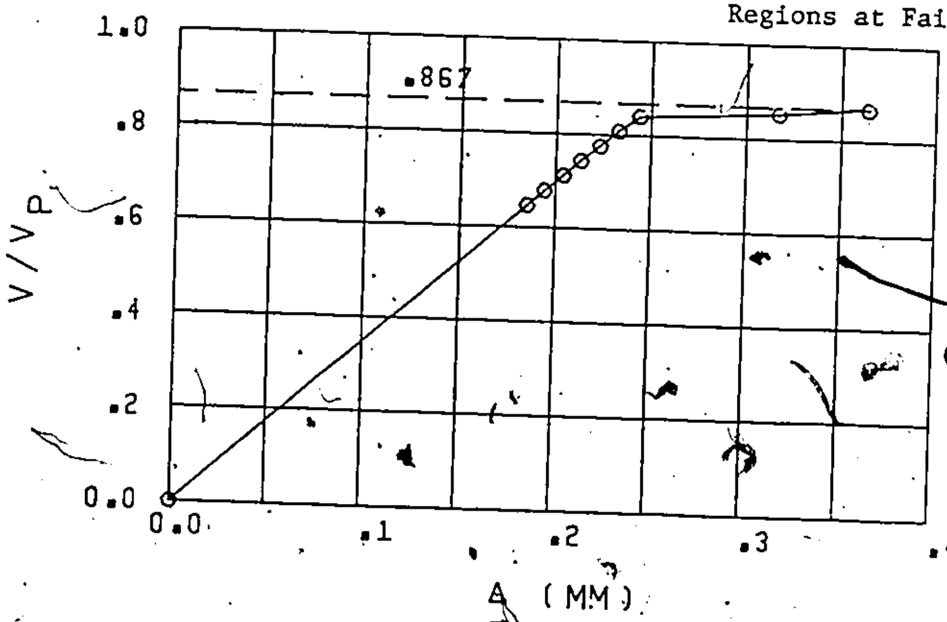

(b) Results

FIGURE 6.3 : DATA AND RESULTS OF TEST 3V

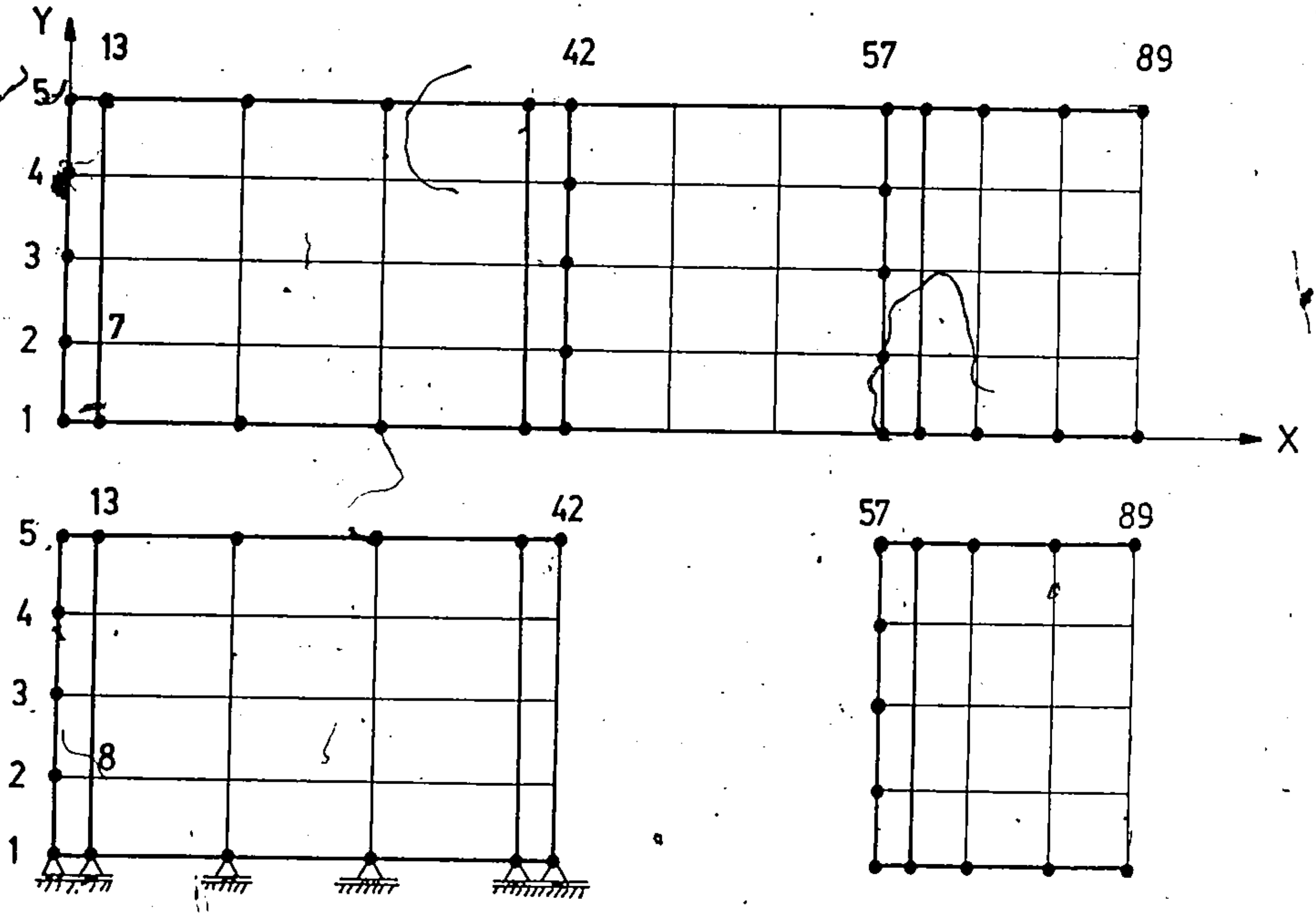
Y
13
42
57
89
5
4
3
2
1
7
X
13
42
5
4
3
2
1
8
57
89

FIGURE 6.4 : TYPICAL FINITE ELEMENT GRID USED FOR SENSITIVITY ANALYSIS

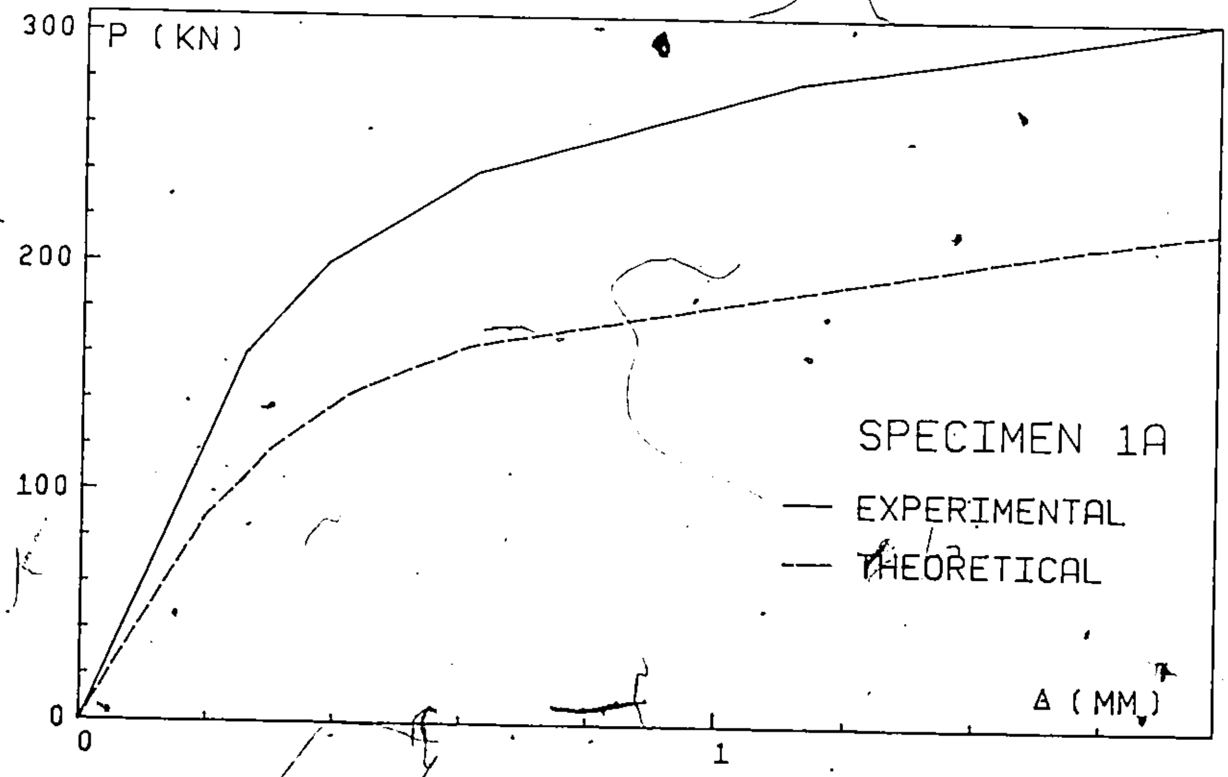
P (KN)
300
200
100
0
0
1
Δ (MM)
SPECIMEN 1A
EXPERIMENTAL
THEORETICAL

(a)

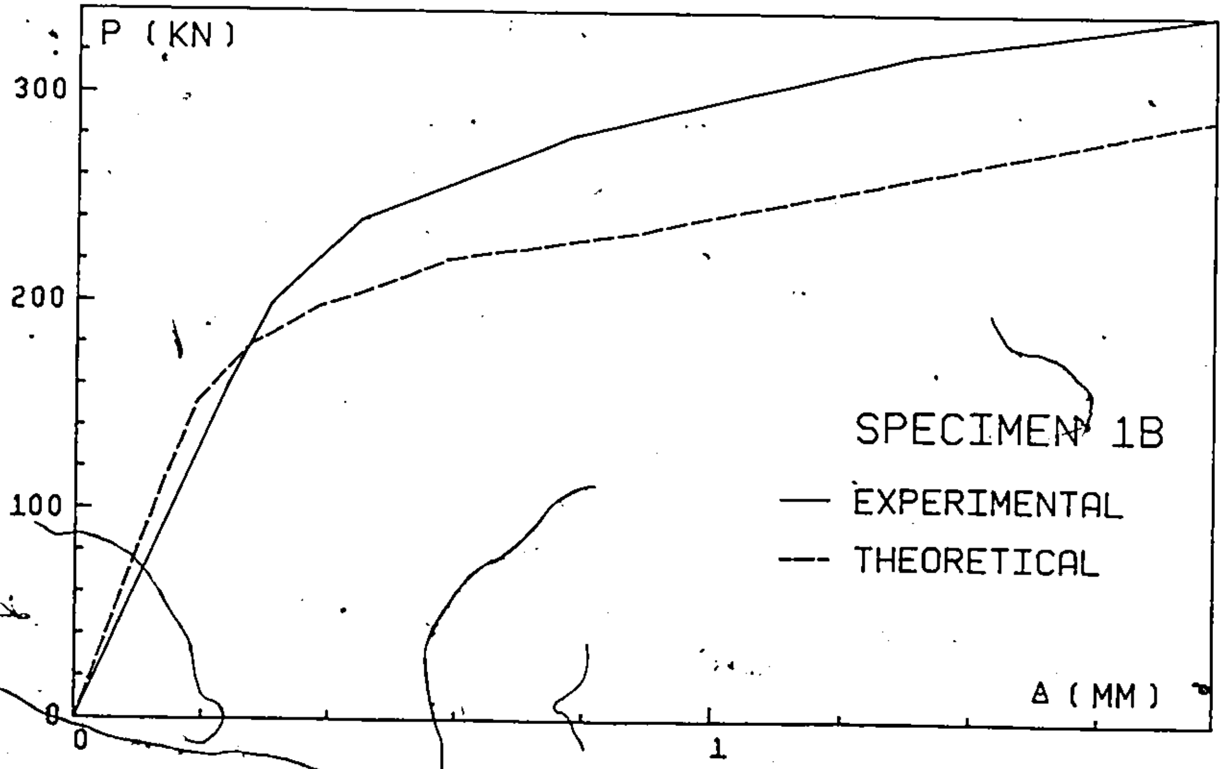
P (KN)
300
200
100
0
0
1
Δ (MM)
SPECIMEN 1B
EXPERIMENTAL
THEORETICAL

(b)

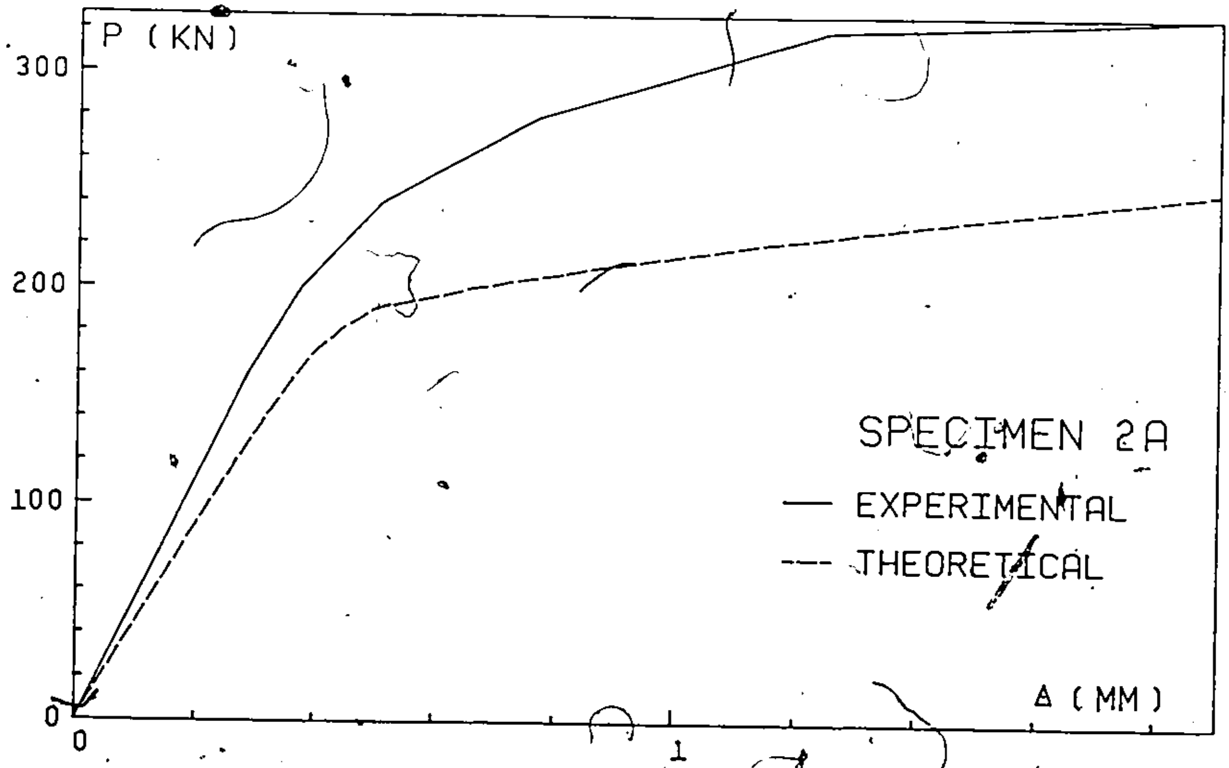
P (KN)
300
200
100
0
0
1
Δ (MM)
SPECIMEN 2A
EXPERIMENTAL
THEORETICAL

(c)

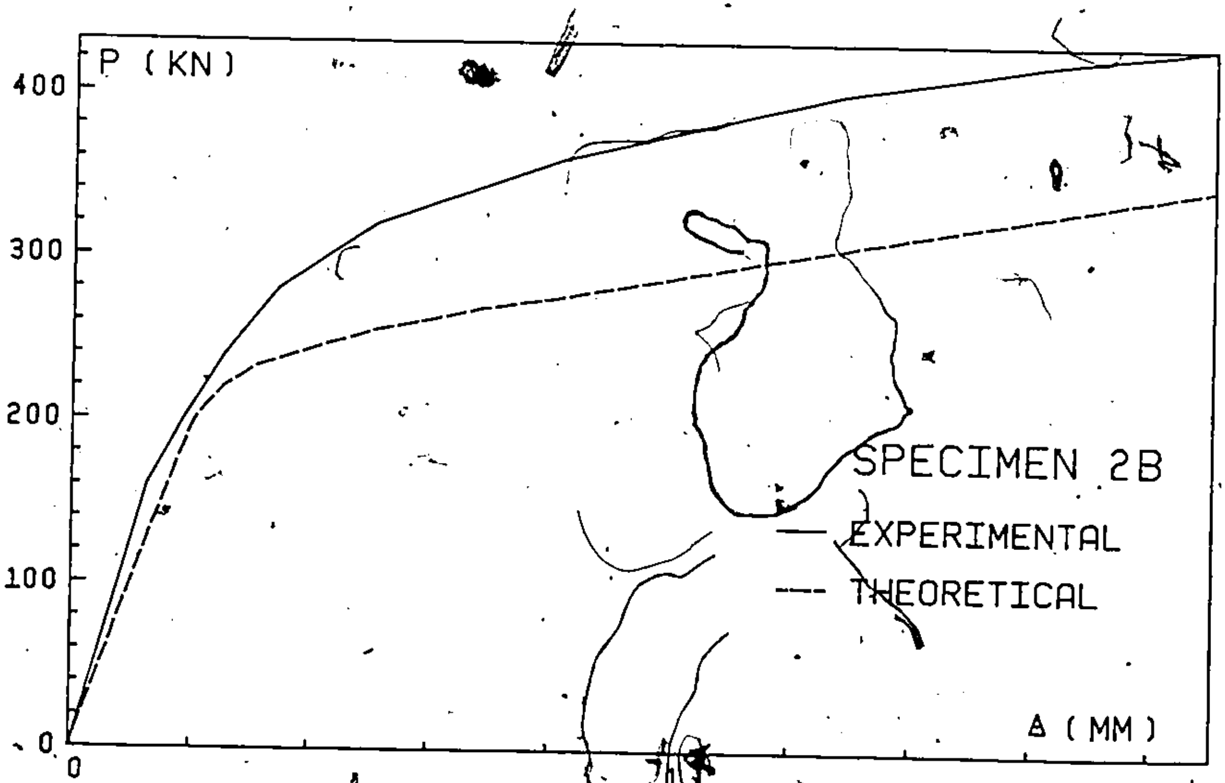
P (KN)
400
300
200
100
0
0
1
Δ (MM)
SPECIMEN 2B
EXPERIMENTAL
THEORETICAL

(d)

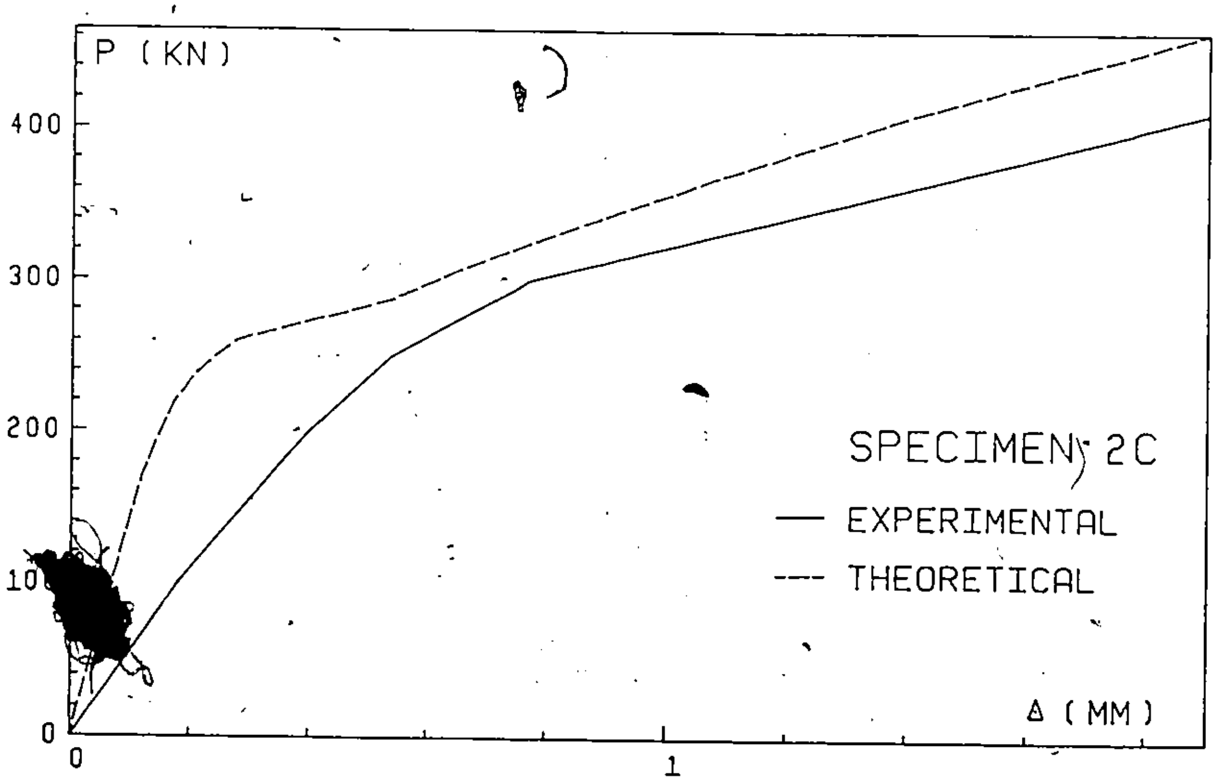
P (KN)
400
300
200
100
0
0
1
Δ (MM)
SPECIMEN 2C
EXPERIMENTAL
THEORETICAL

(e)

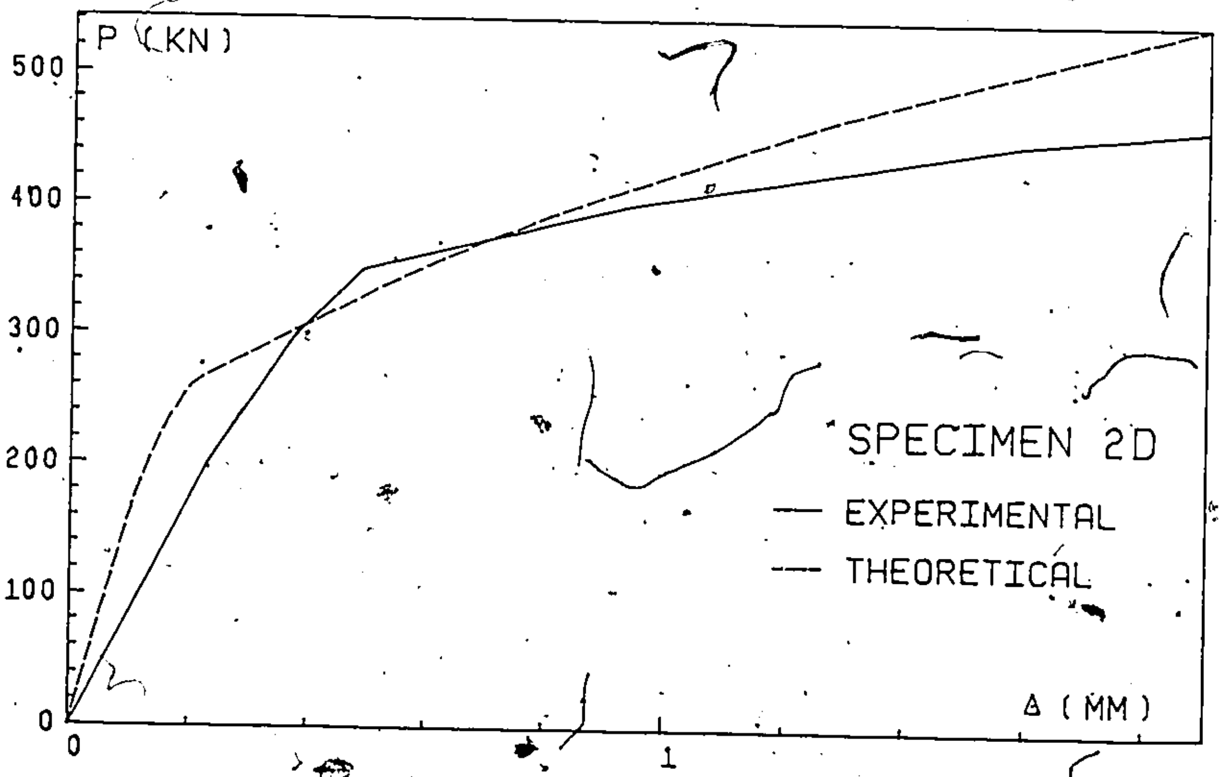
P (KN)
500
400
300
200
100
0
0
1
Δ (MM)
SPECIMEN 2D
EXPERIMENTAL
THEORETICAL

(f)

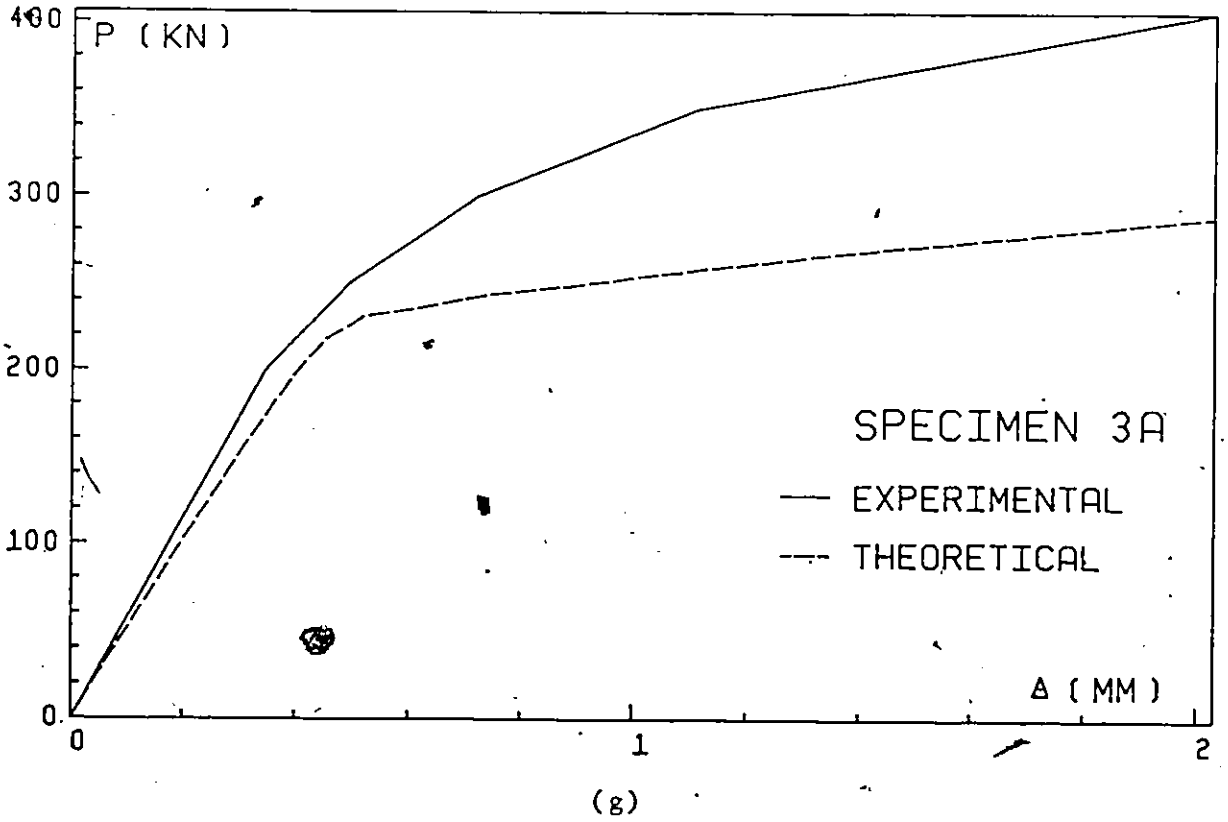

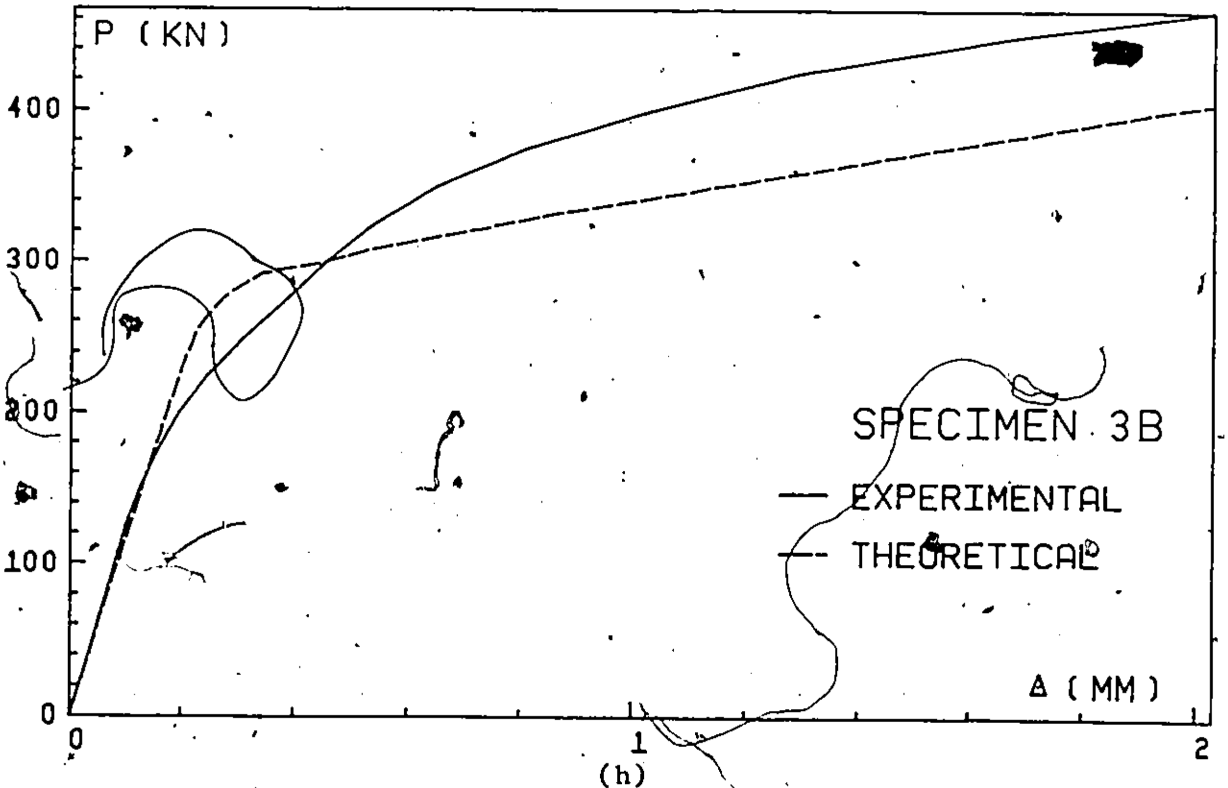

FIGURE 6.5 : COMPARISON OF THEORETICAL AND EXPERIMENTAL P-RELATIONSHIPS FOR SHALLOW BEAMS (GROUP I)

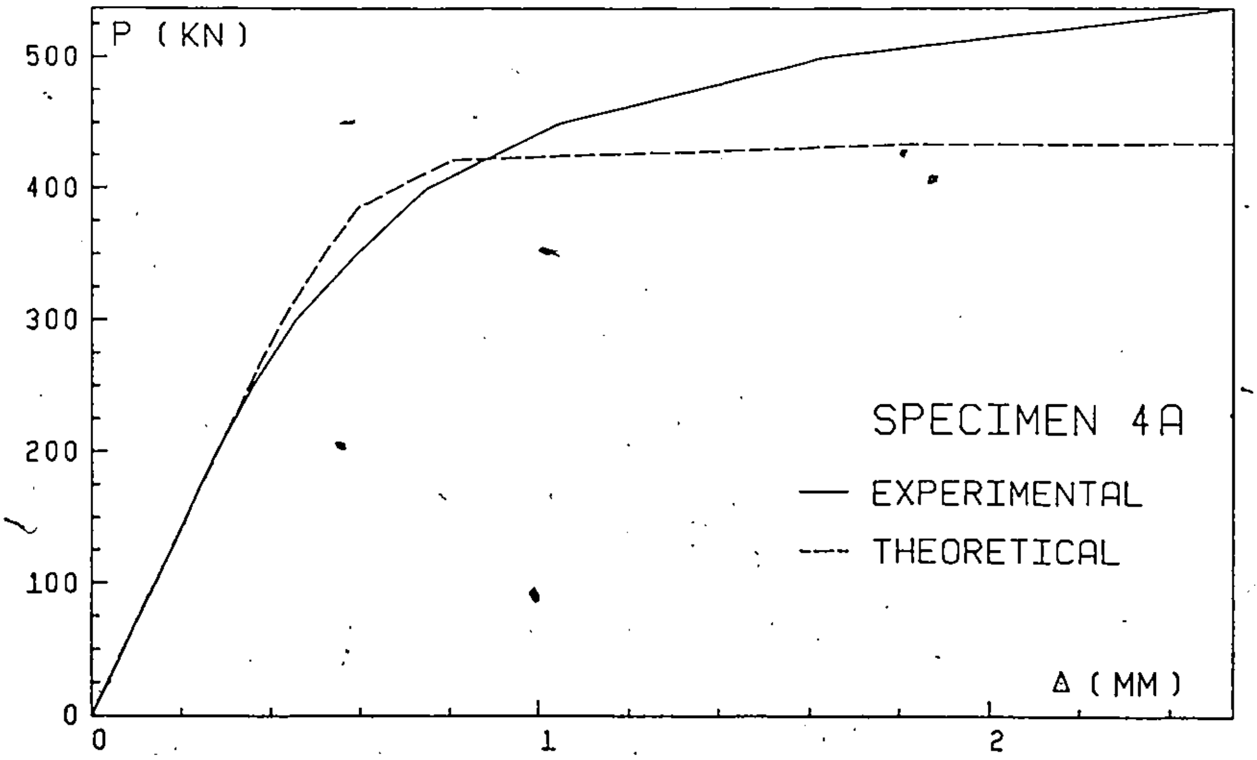
P (KN)
500
400
300
200
100
0
0
1
2
Δ (MM)
SPECIMEN 4A
EXPERIMENTAL
THEORETICAL

(a)

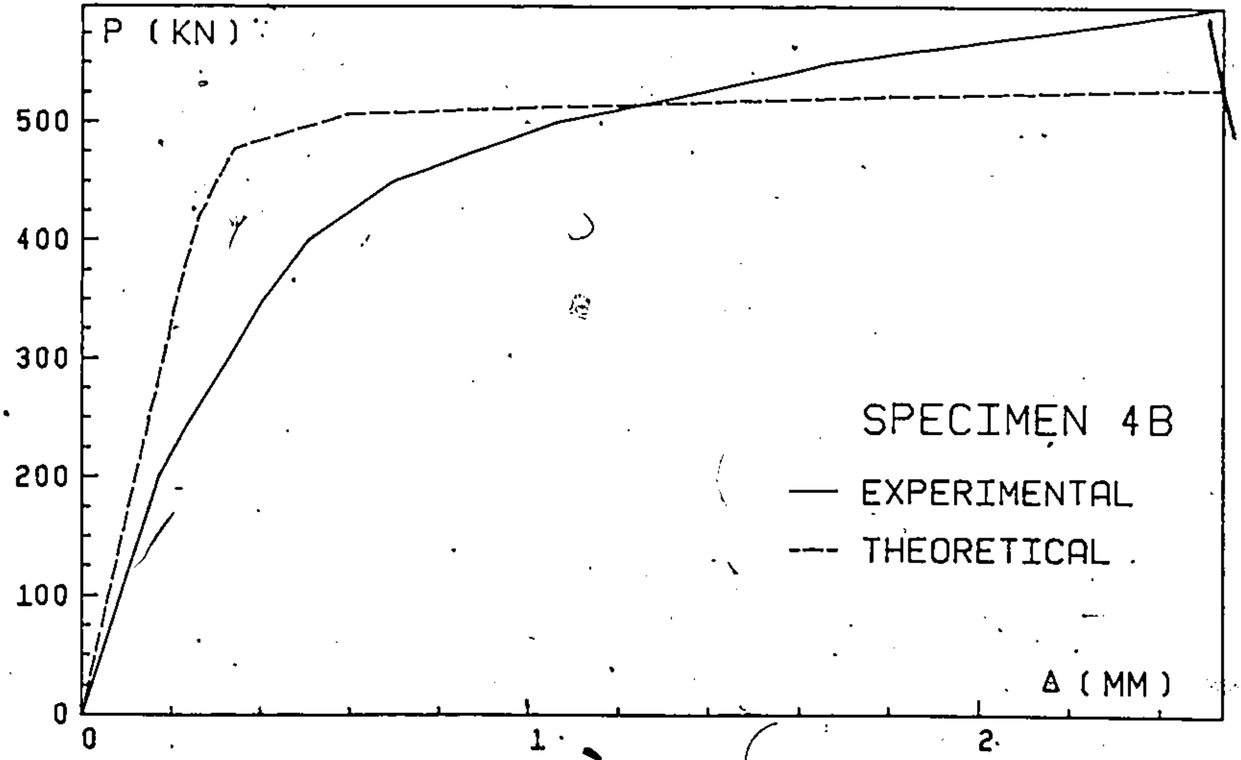
P (KN)
500
400
300
200
100
0
0
1
2
Δ (MM)
SPECIMEN 4B
EXPERIMENTAL
THEORETICAL

(b)

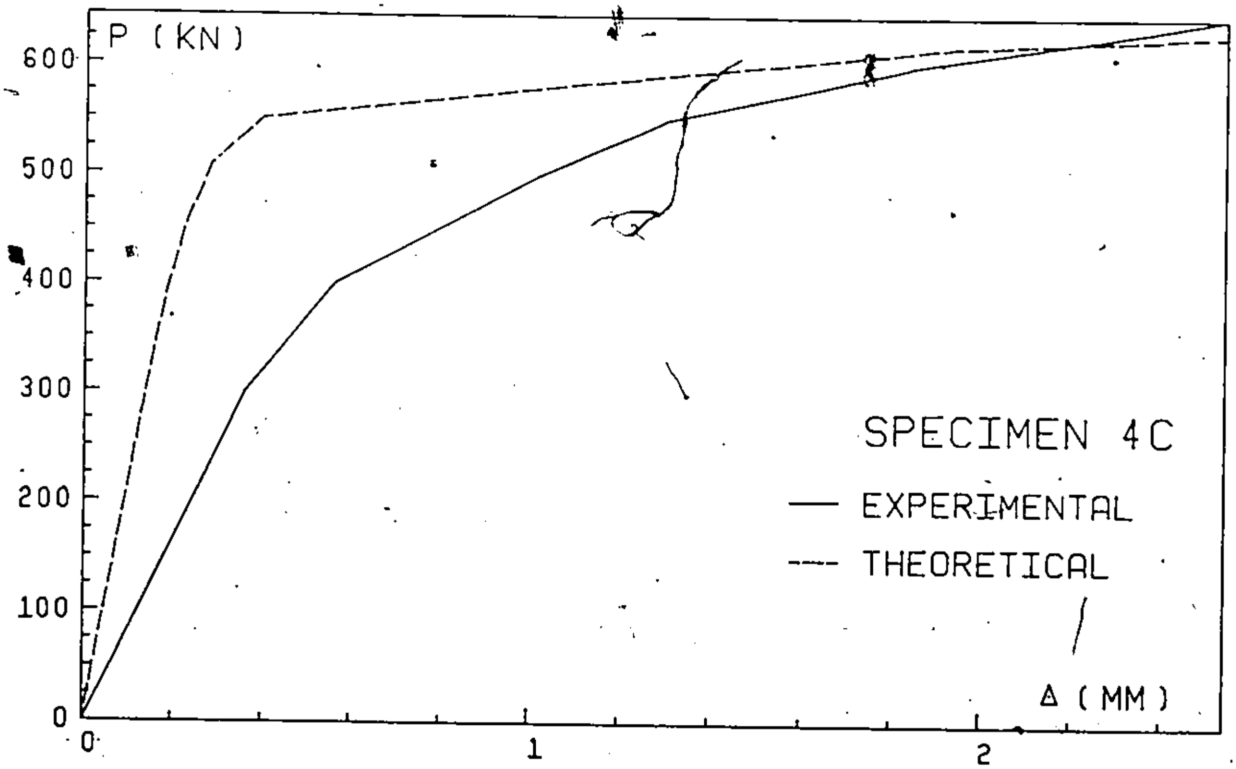
P (KN)
600
500
400
300
200
100
0
0
1
2
Δ (MM)
SPECIMEN 4C
EXPERIMENTAL
THEORETICAL

(c)

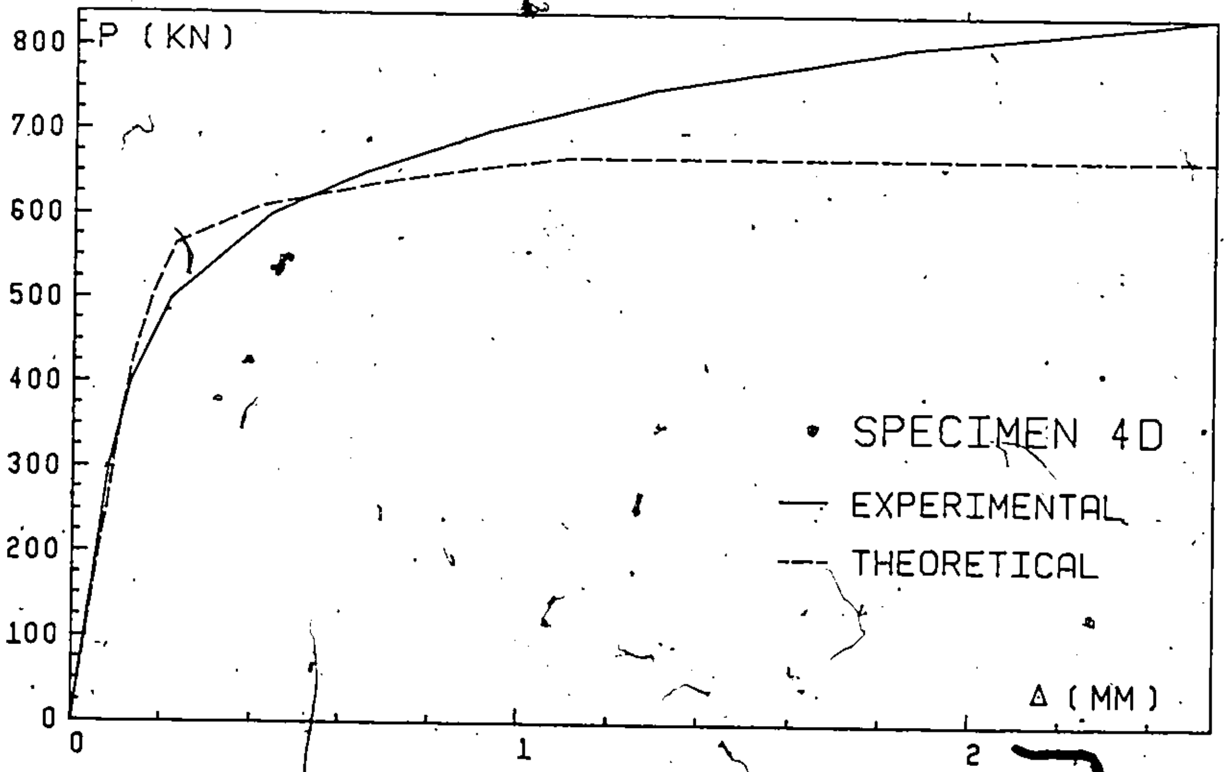
P (KN)
800
700
600
500
400
300
200
100
0
0
1
2
Δ (MM)
SPECIMEN 4D
EXPERIMENTAL
THEORETICAL

(d)

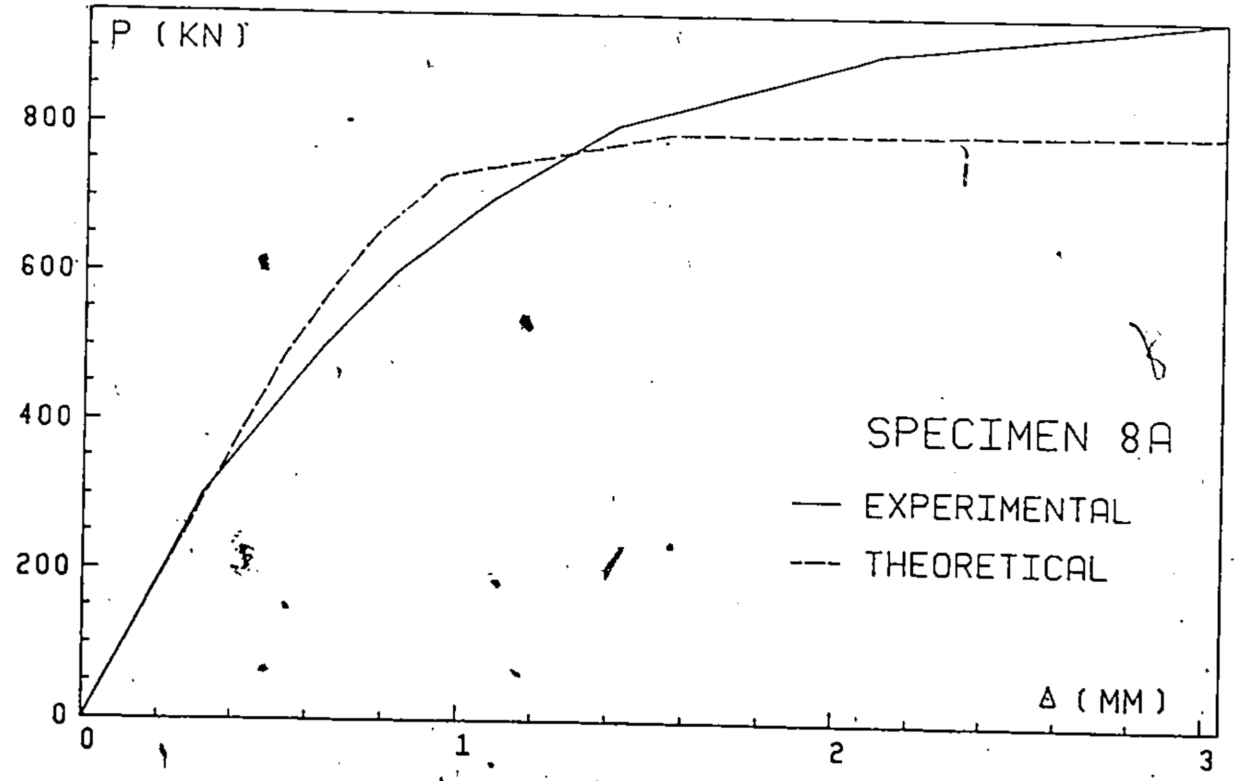
P (KN)
800
600
400
200
0
0
1
2
3
Δ (MM)
SPECIMEN 8A
EXPERIMENTAL
THEORETICAL

(e)

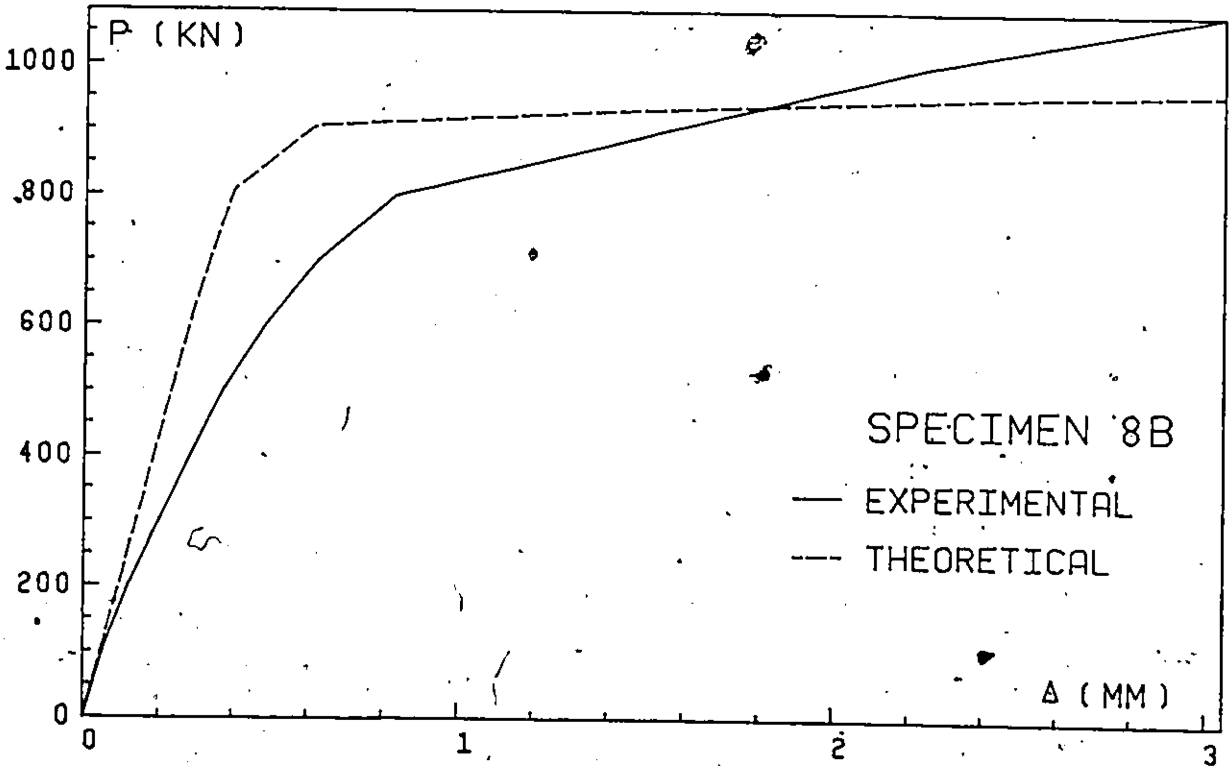
P (KN)
1000
800
600
400
200
0
0
1
2
3
Δ (MM)
SPECIMEN 8B
EXPERIMENTAL
THEORETICAL

(f)

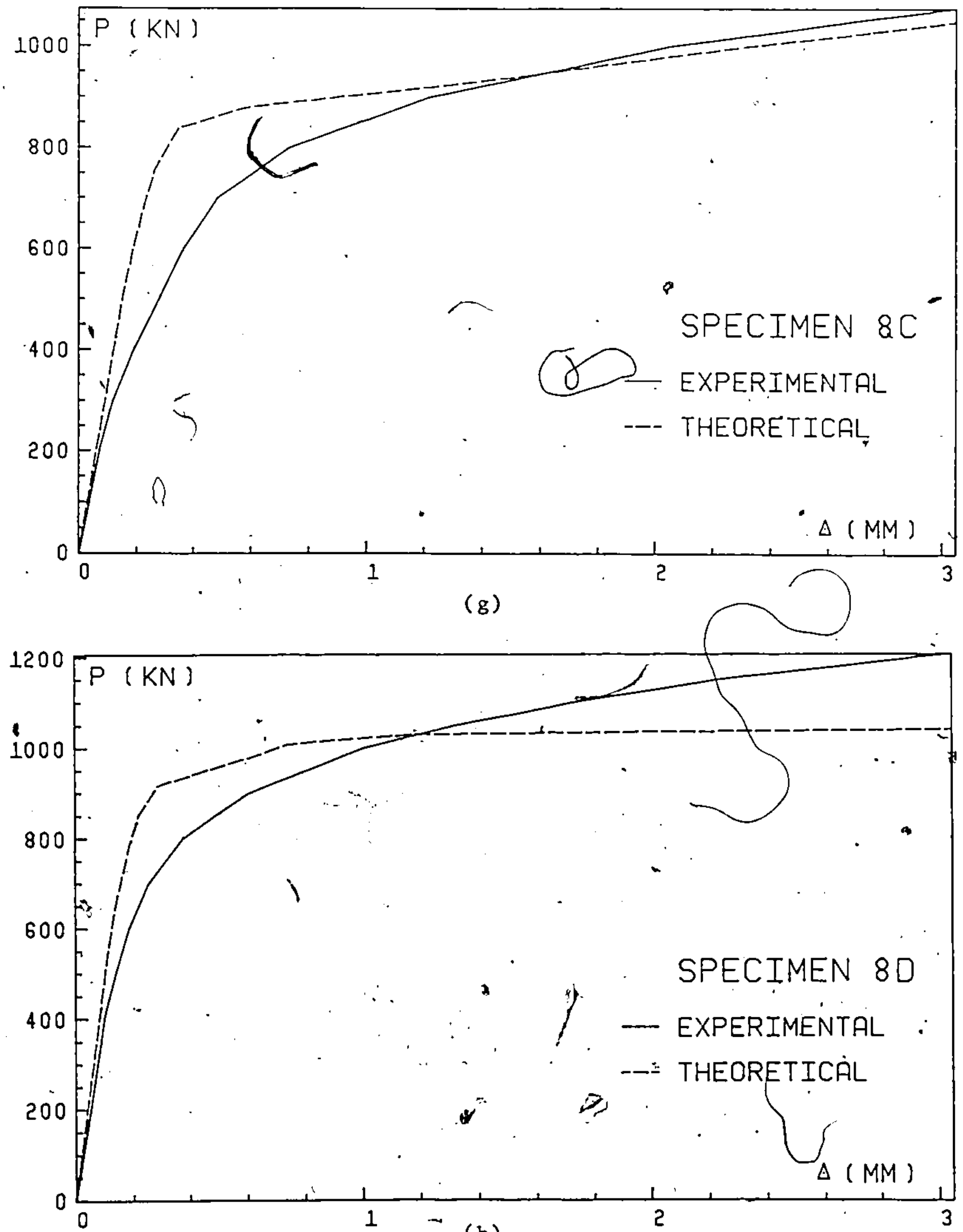

(g)

(h)

FIGURE 6.6 : COMPARISON OF THEORETICAL AND EXPERIMENTAL P-
RELATIONSHIPS FOR SQUARES (GROUP II)

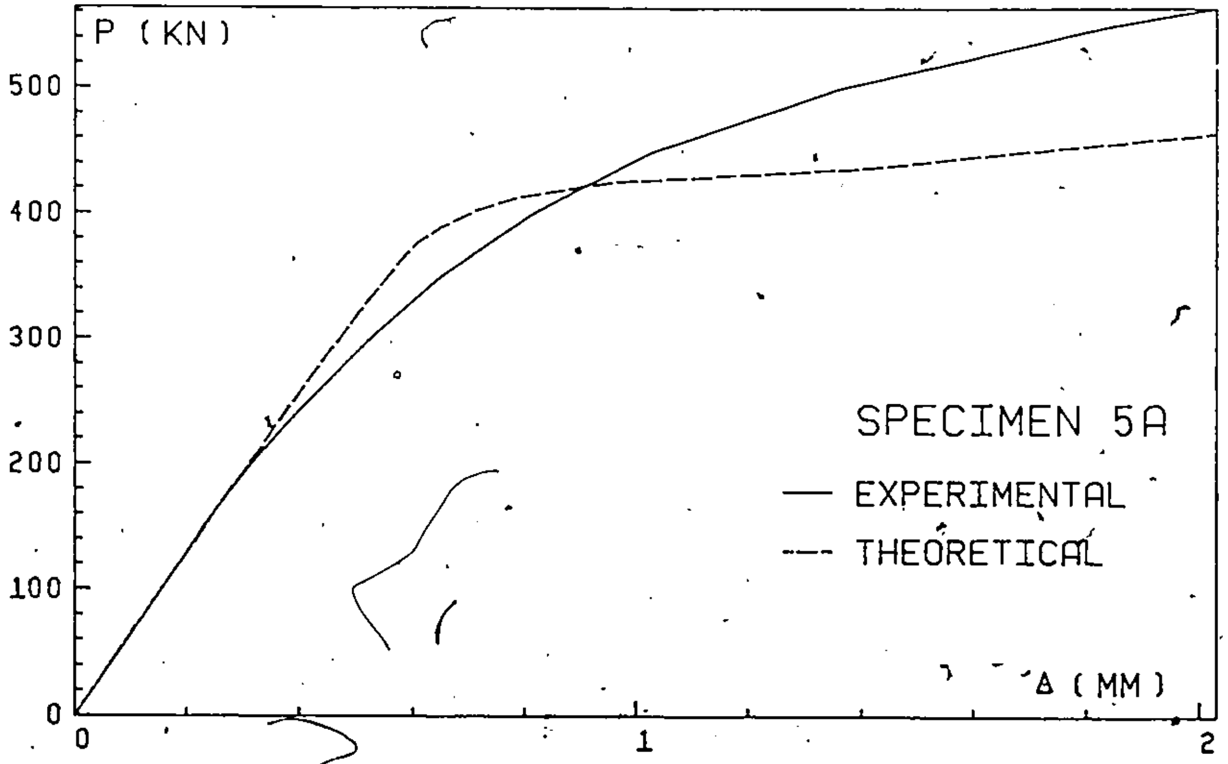
P (KN)
500
400
300
200
100
0
0
1
2
Δ (MM)
SPECIMEN 5A
EXPERIMENTAL
THEORETICAL

(a)

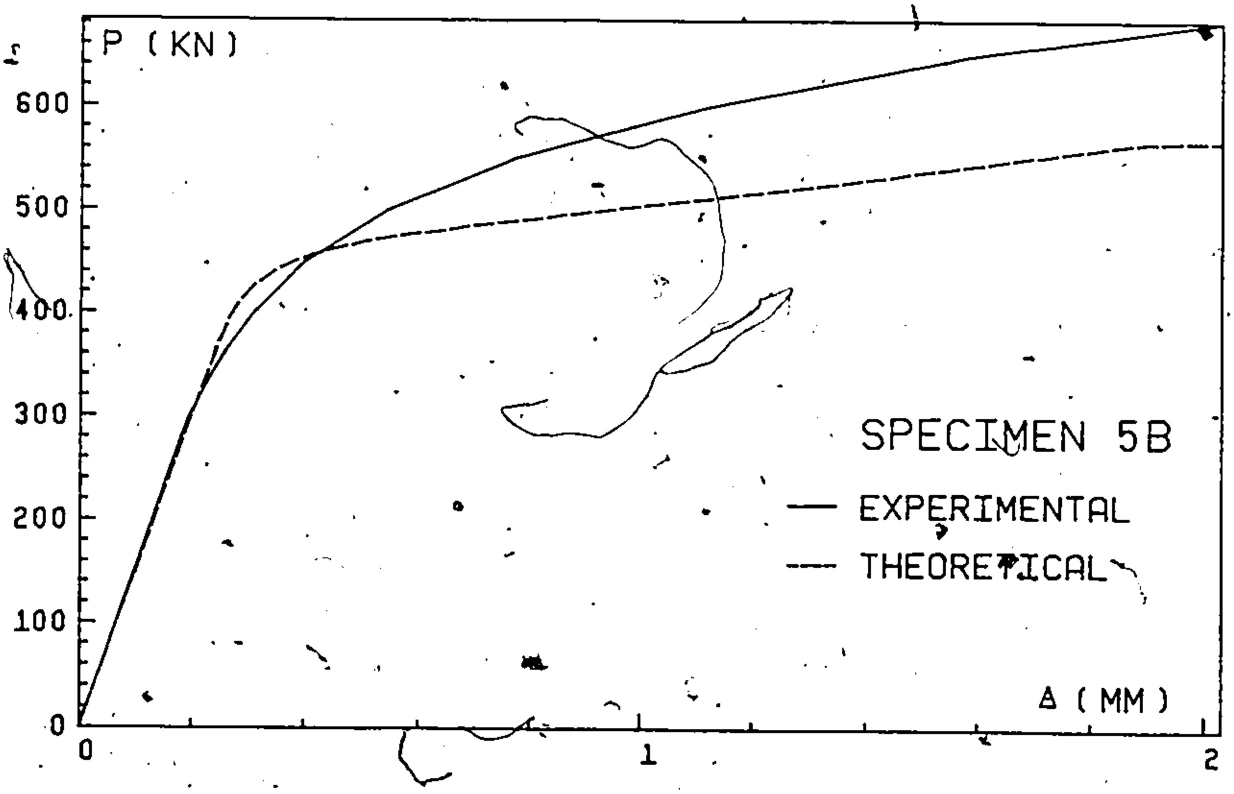
P (KN)
600
500
400
300
200
100
0
0
1
2
Δ (MM)
SPECIMEN 5B
EXPERIMENTAL
THEORETICAL

(b)

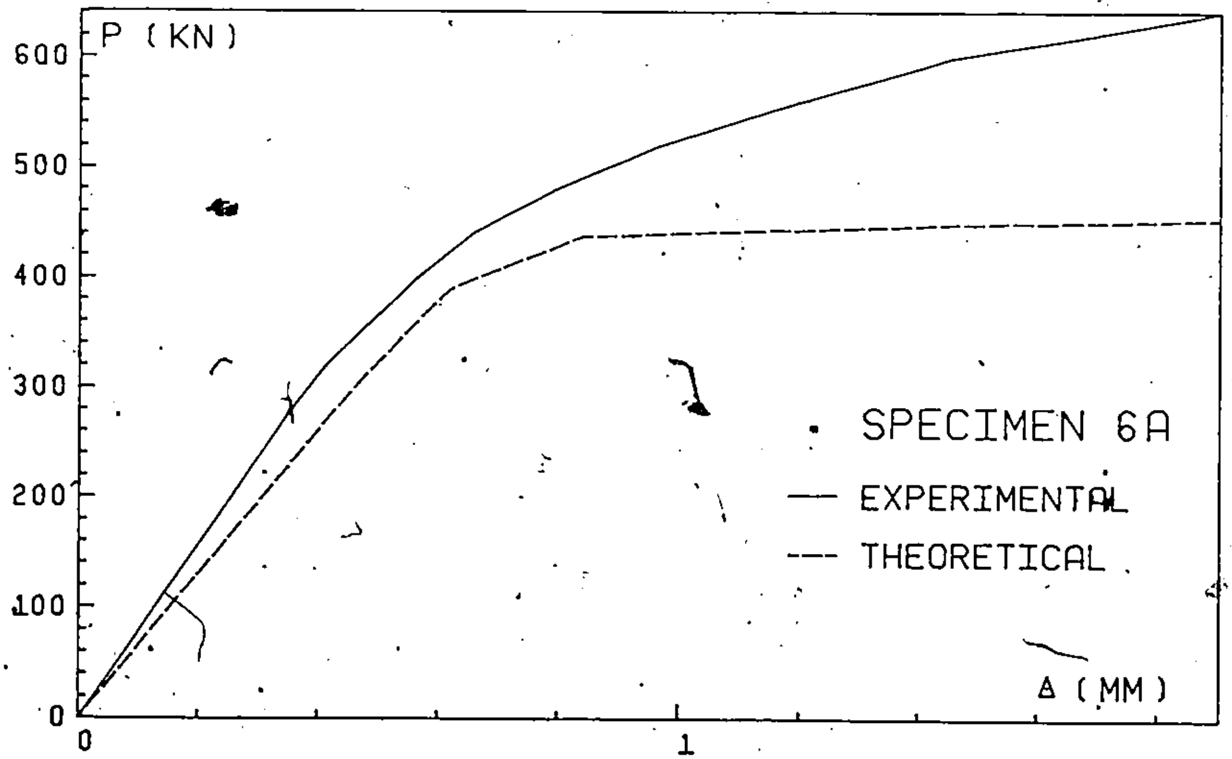
P (KN)
600
500
400
300
200
100
0
0
1
Δ (MM)
SPECIMEN 6A
EXPERIMENTAL
THEORETICAL

(c)

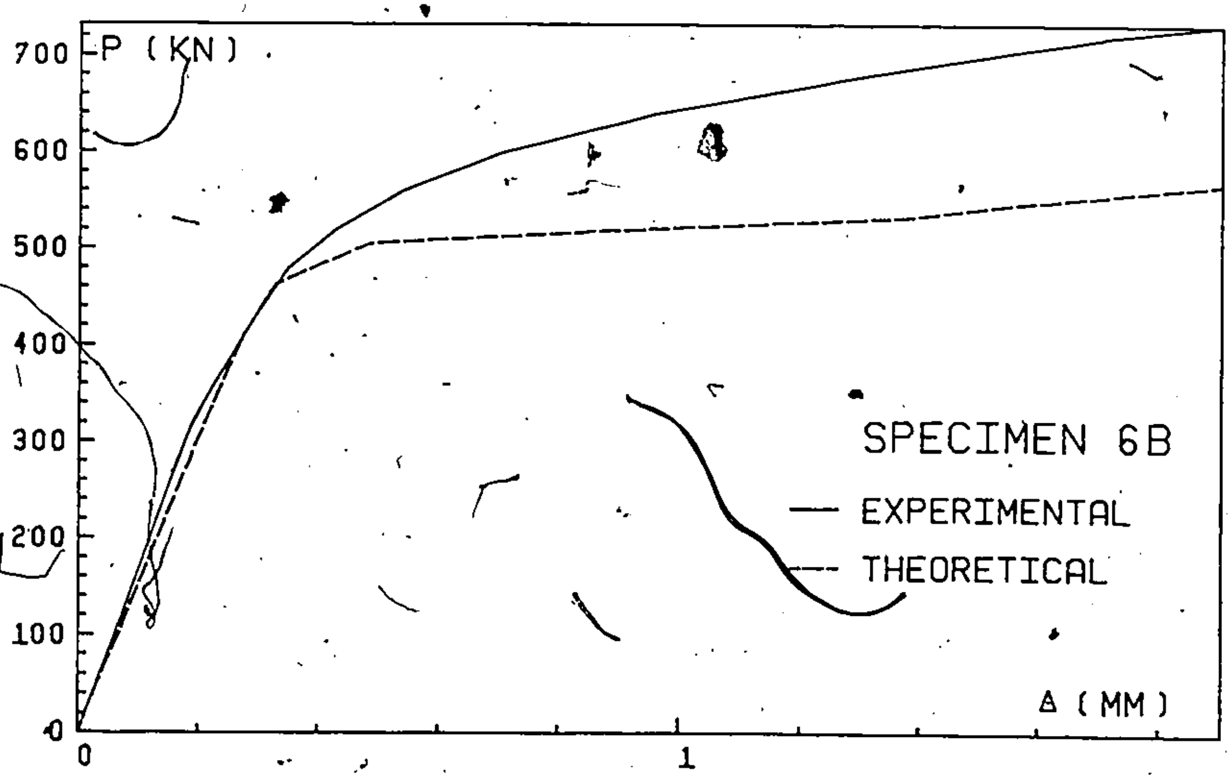
P (KN)
700
600
500
400
300
200
100
0
0
1
Δ (MM)
SPECIMEN 6B
EXPERIMENTAL
THEORETICAL

(d)

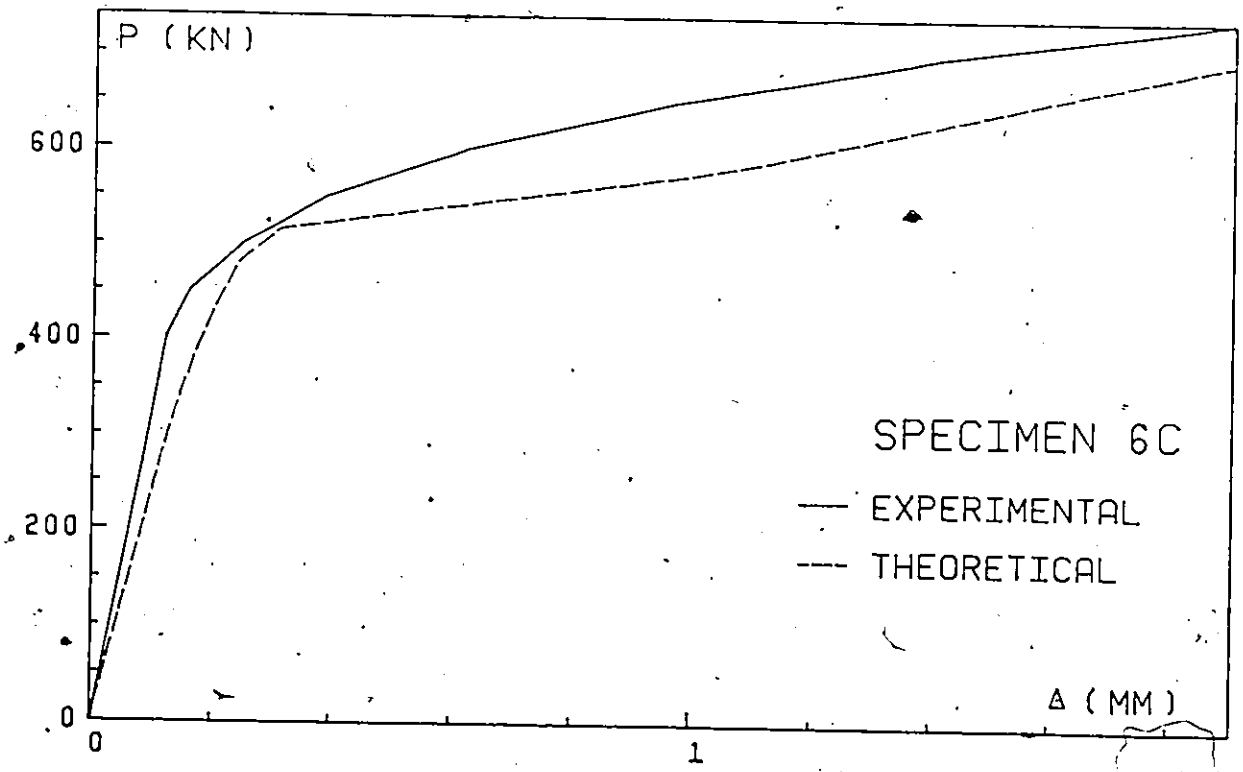
P (KN)
600
400
200
0
0
1
Δ (MM)
SPECIMEN 6C
EXPERIMENTAL
THEORETICAL

(e)

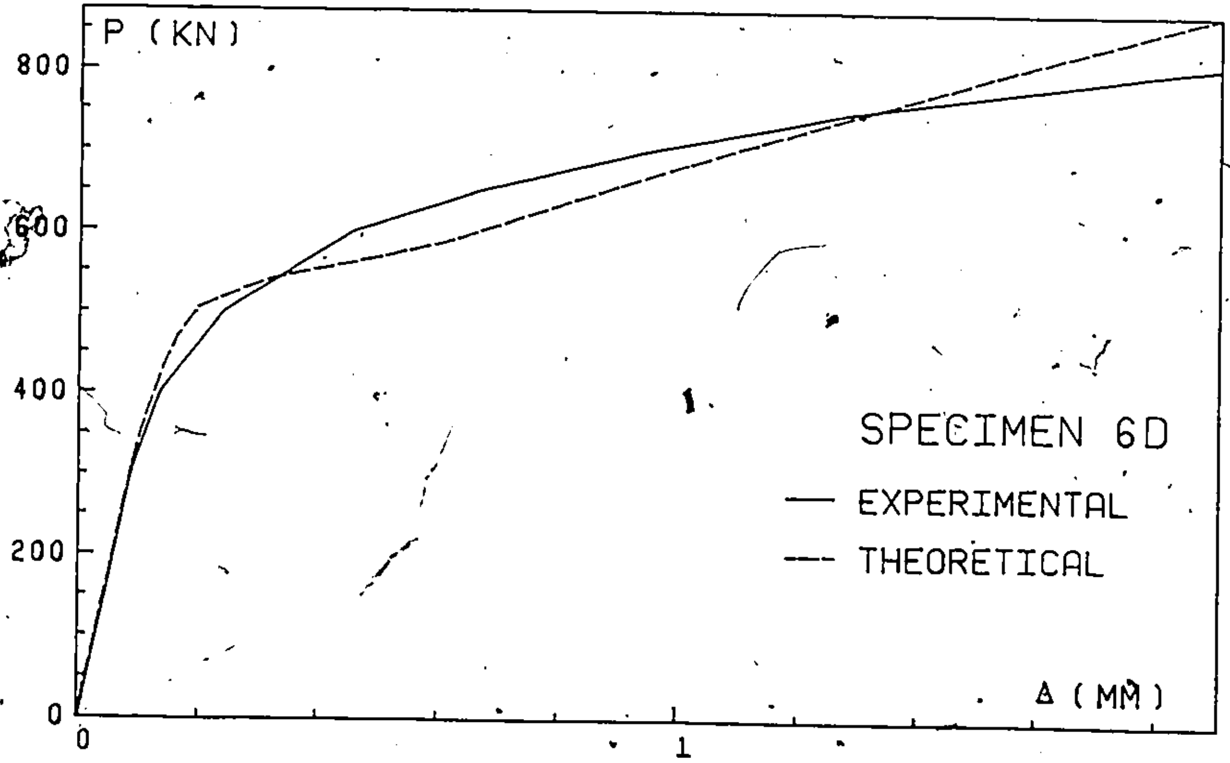
P (KN)
800
600
400
200
0
0
1
Δ (MM)
SPECIMEN 6D
EXPERIMENTAL
THEORETICAL

(f)

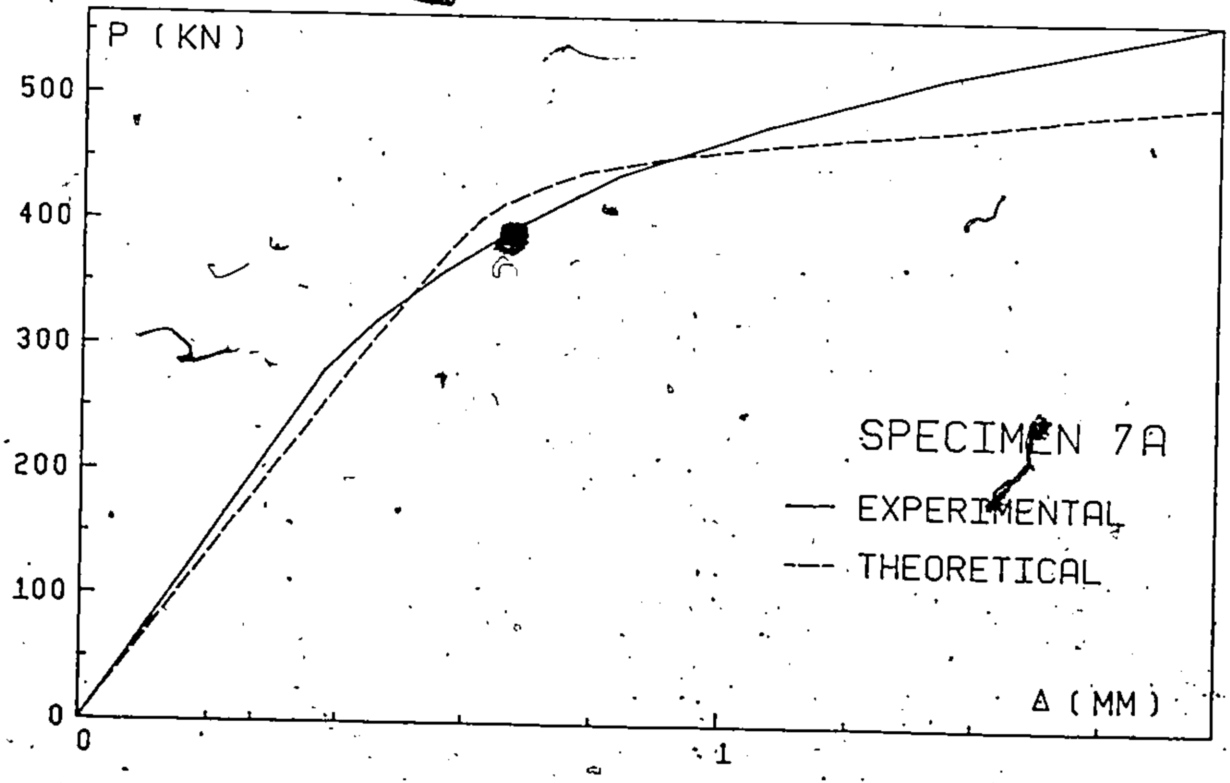

(g)

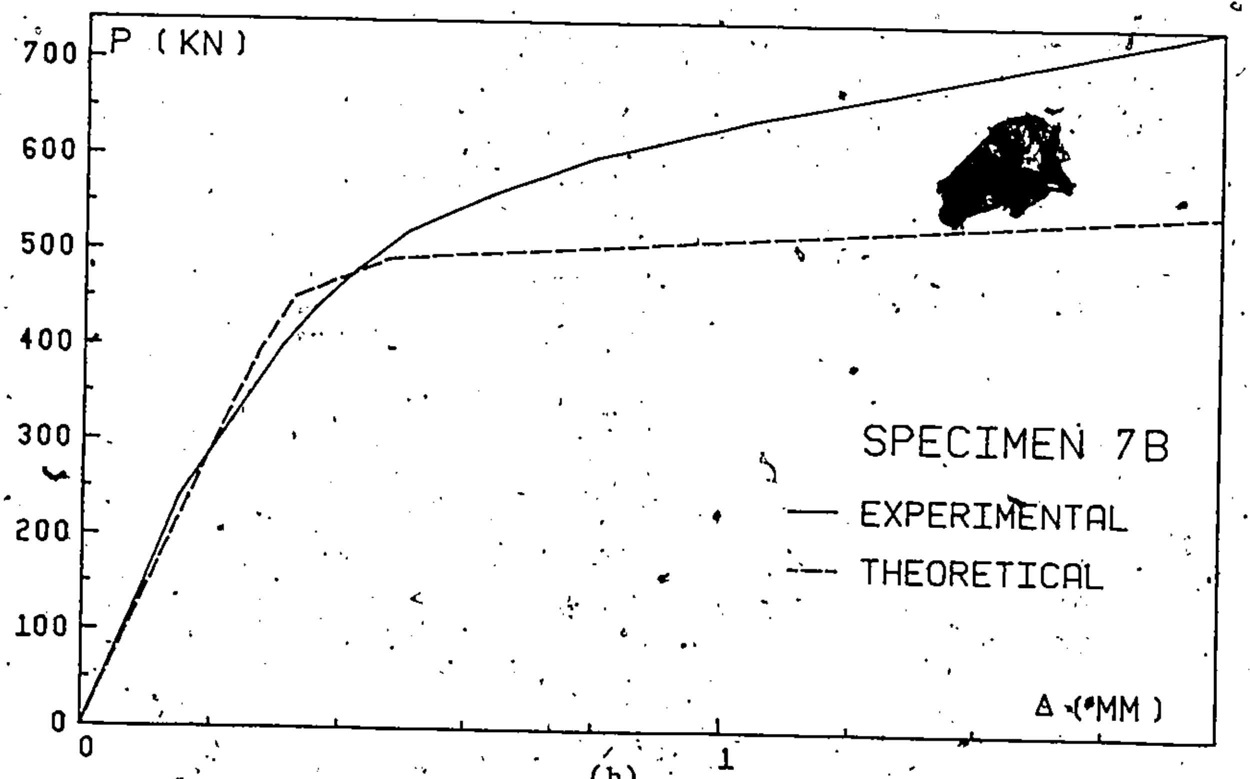

(h)

FIGURE 6.7 : COMPARISON OF THEORETICAL AND EXPERIMENTAL P-Δ RELATIONSHIPS FOR DEEP BEAMS (GROUP III)

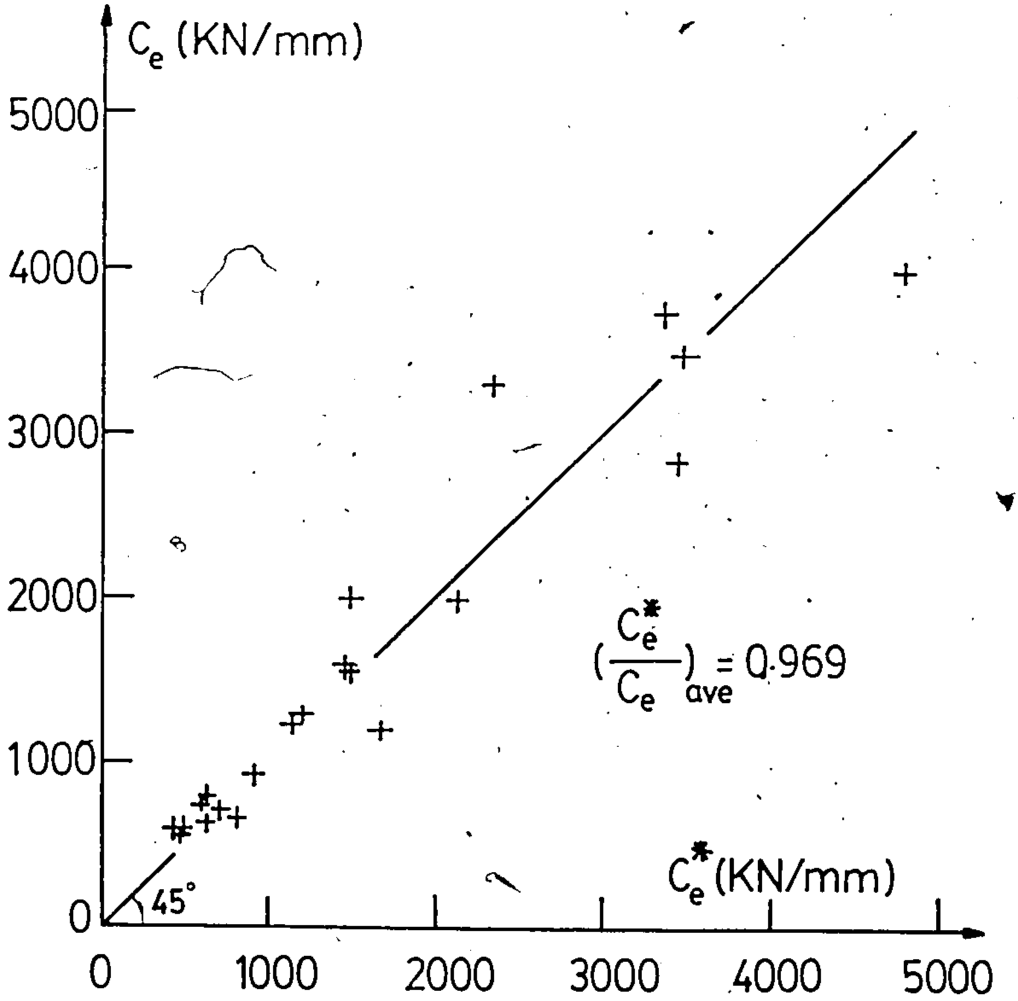

FIGURE 6.8 : CORRELATION BETWEEN EXPERIMENT AND FINITE ELEMENT PREDICTION OF TWIN BEAM ELASTIC STIFFNESSES

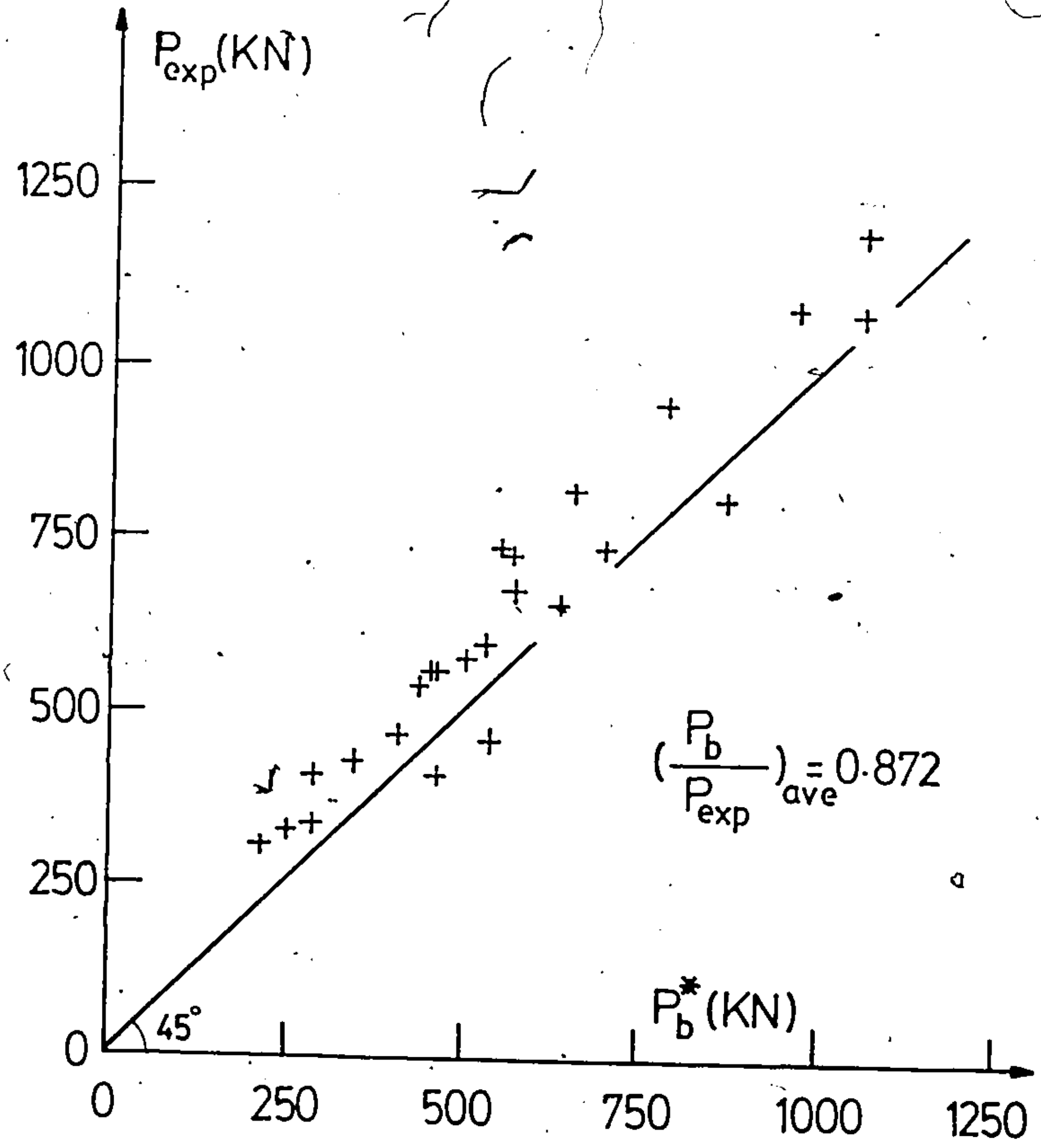

FIGURE 6.9 : CORRELATION BETWEEN EXPERIMENT AND FINITE ELEMENT PREDICTION OF TWIN BEAM LOADS

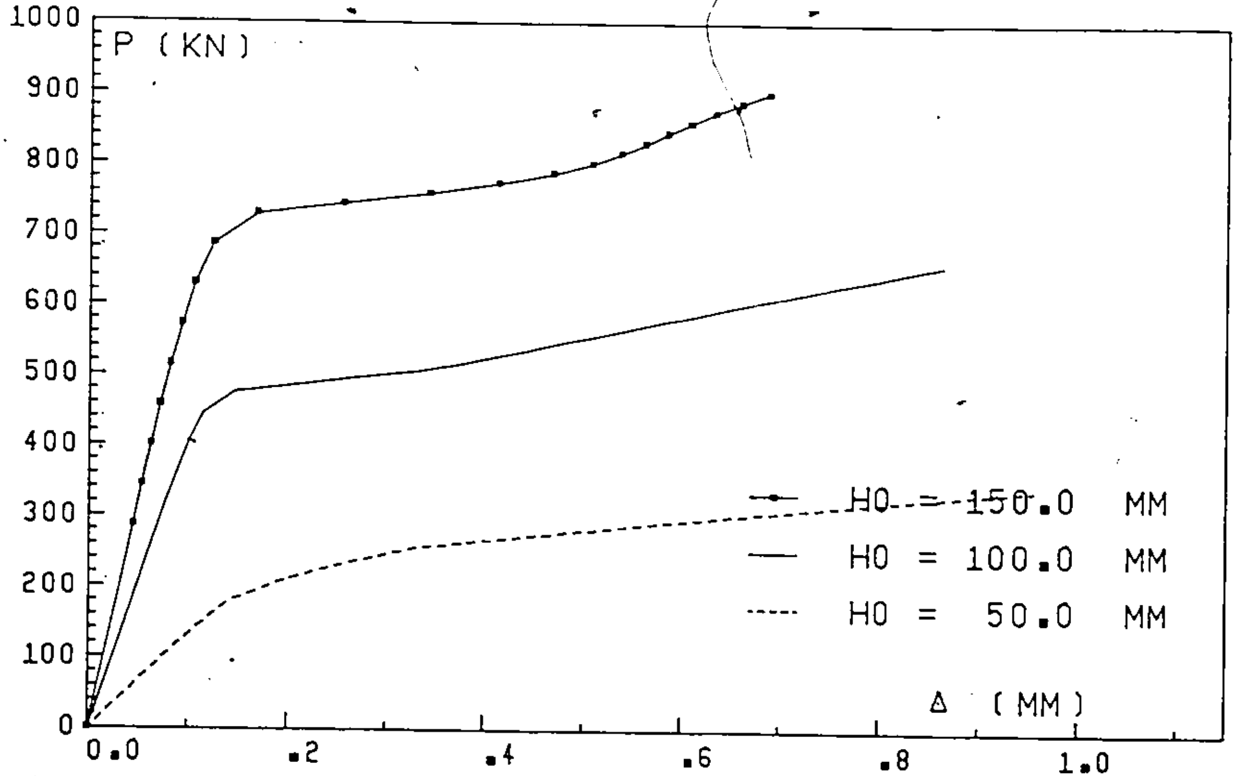

FIGURE 6.10 : VARIATION OF BEAM DEPTH

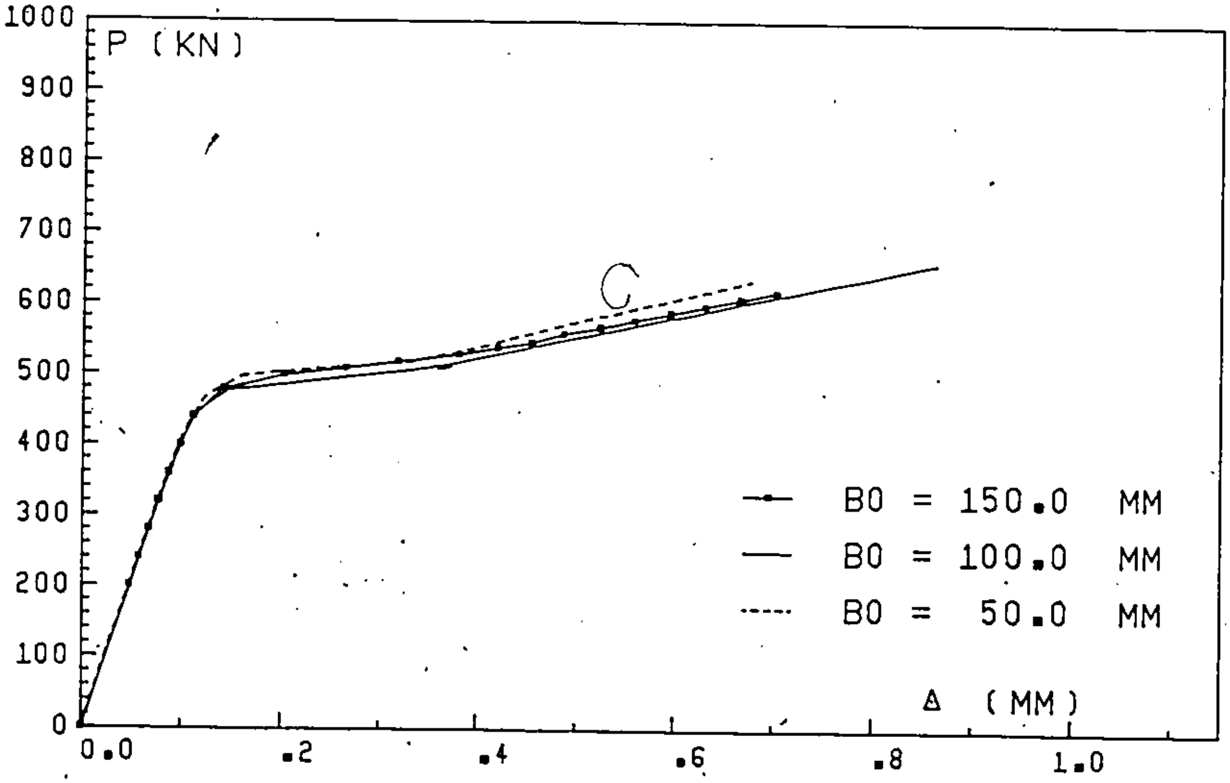

FIGURE 6.11 : VARIATION OF BEAM MEMBER WIDTH

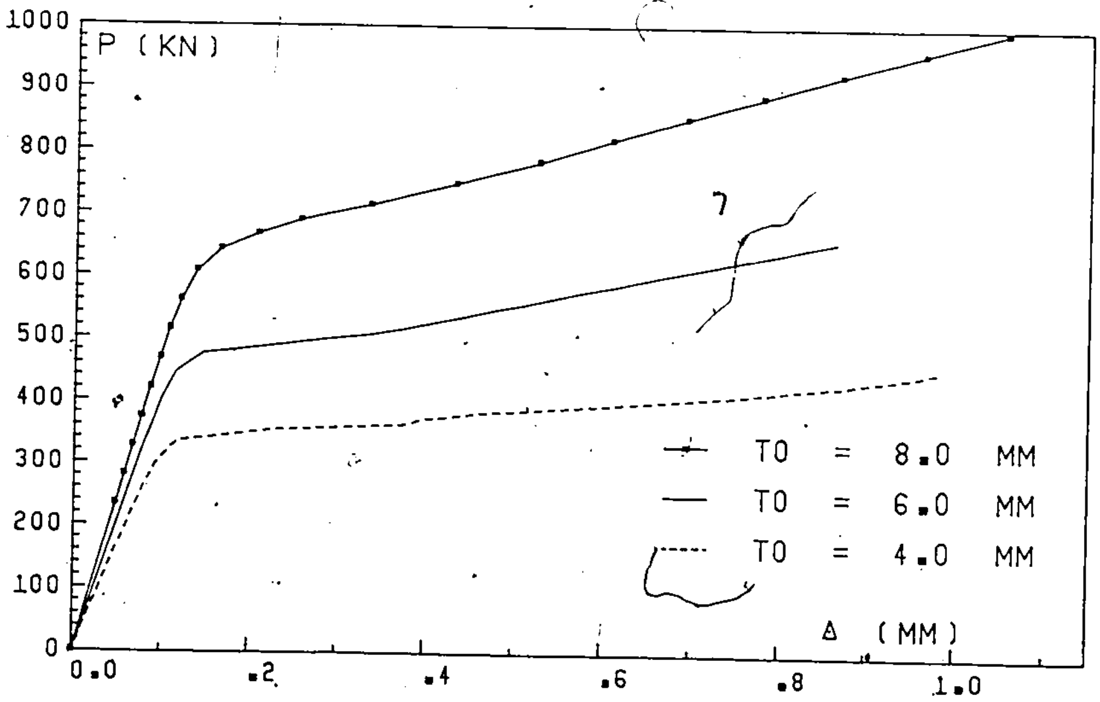

FIGURE 6.12 : VARIATION OF BEAM THICKNESS

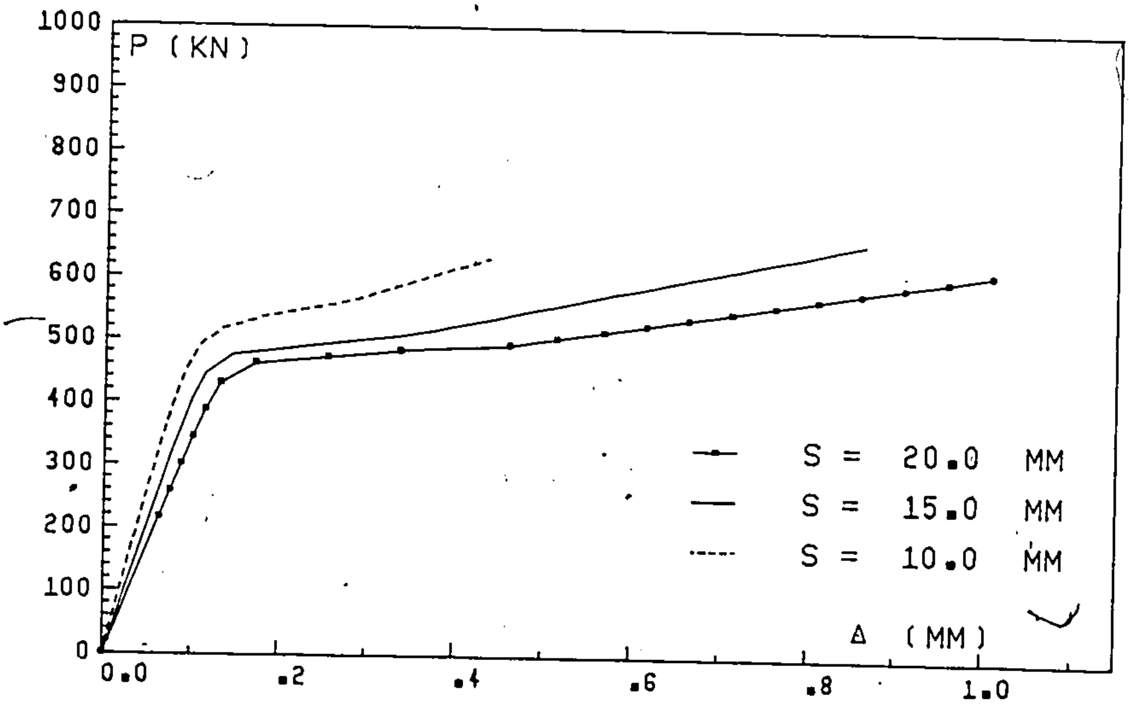

FIGURE 6.13 : VARIATION OF GAP DISTANCE

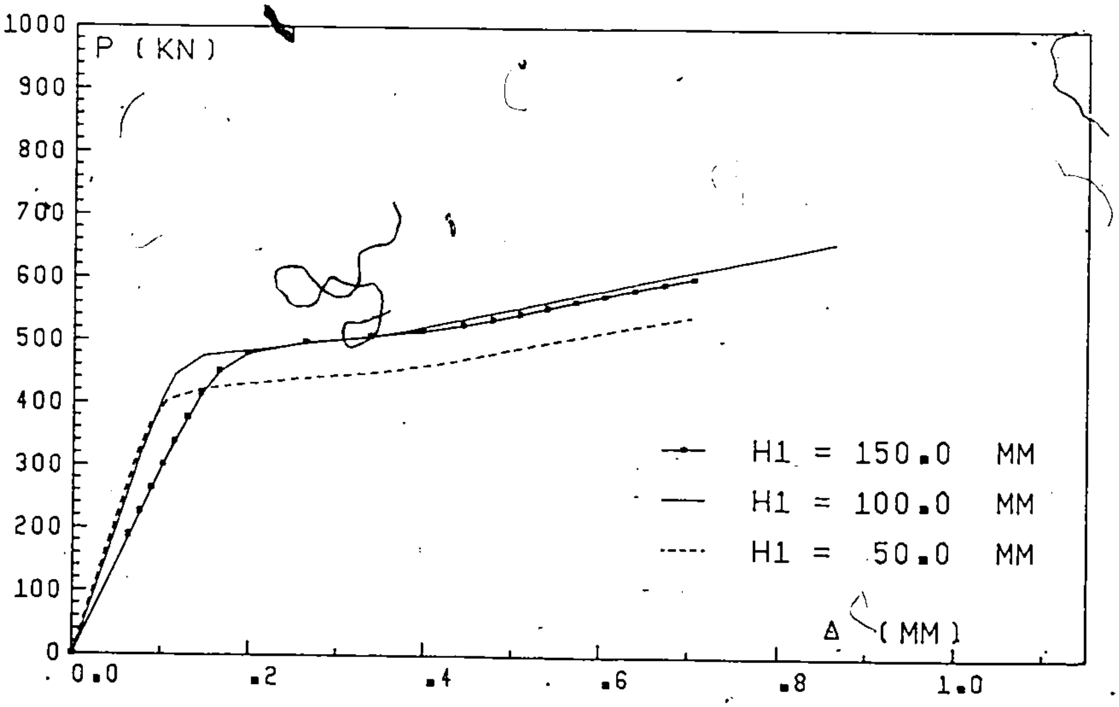

FIGURE 6.14 : VARIATION OF VERTICAL MEMBER DEPTH

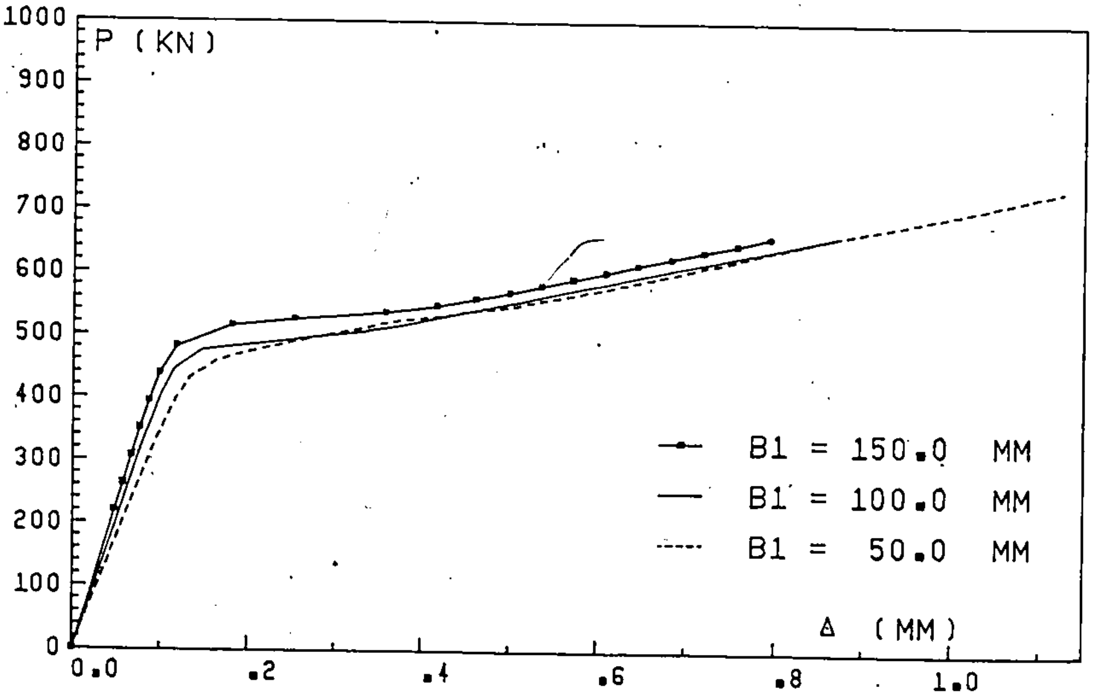

FIGURE 6.15 : VARIATION OF VERTICAL MEMBER WIDTH

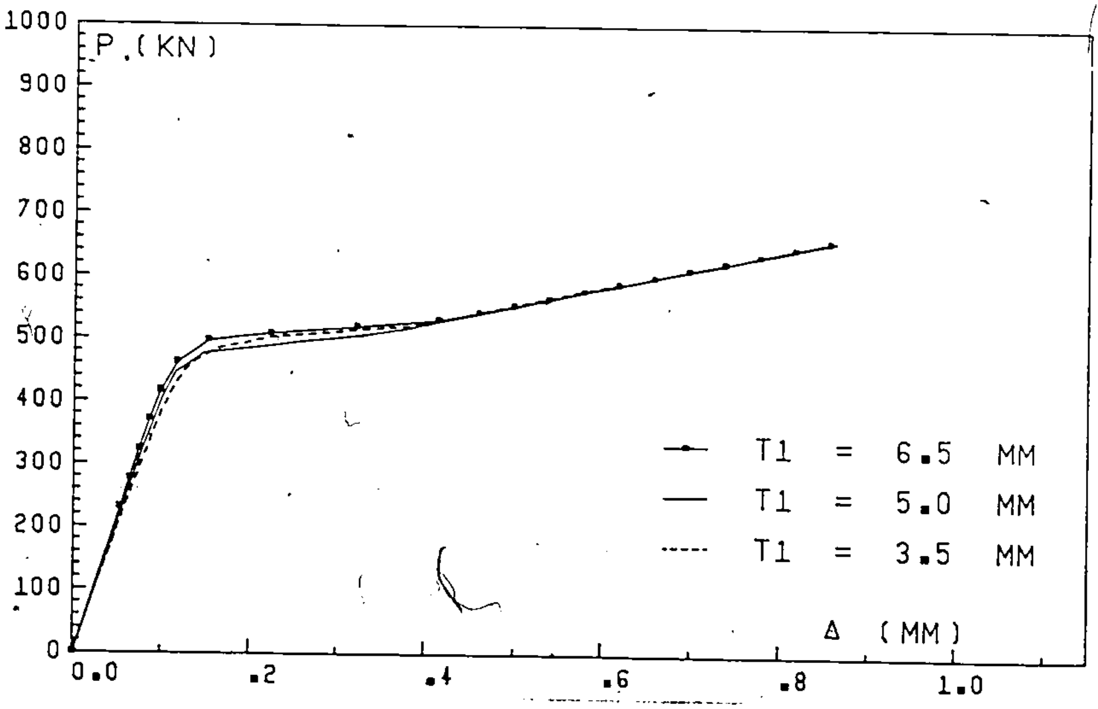

FIGURE 6.16 : VARIATION OF VERTICAL MEMBER THICKNESS

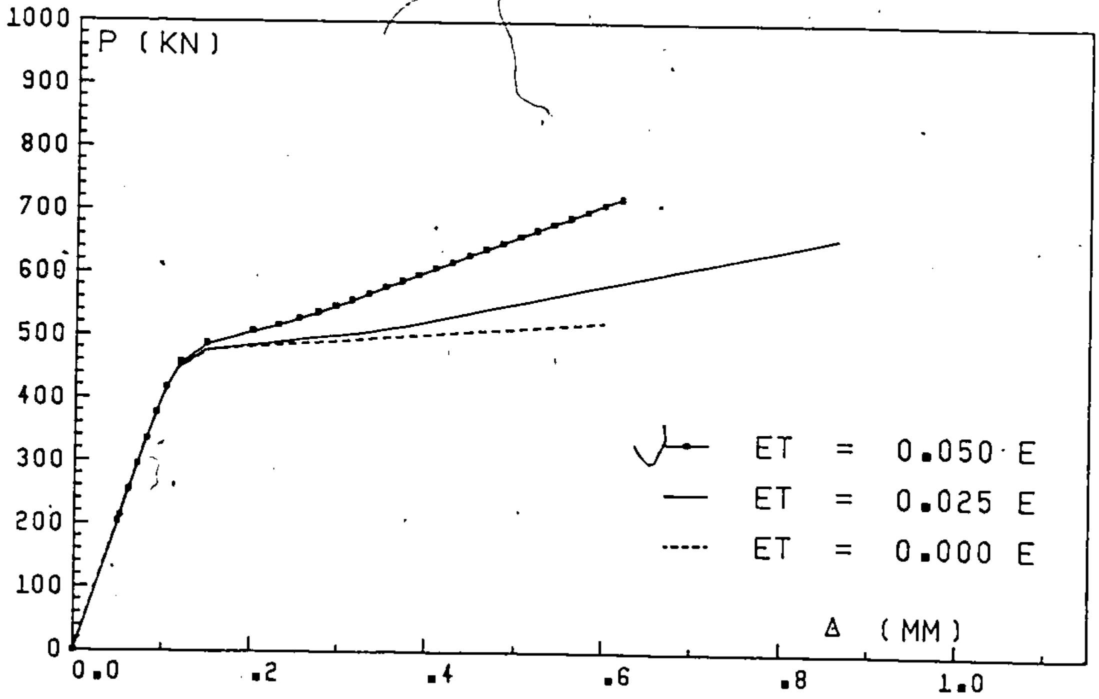

FIGURE 6.17 : VARIATION OF TANGENT MODULUS

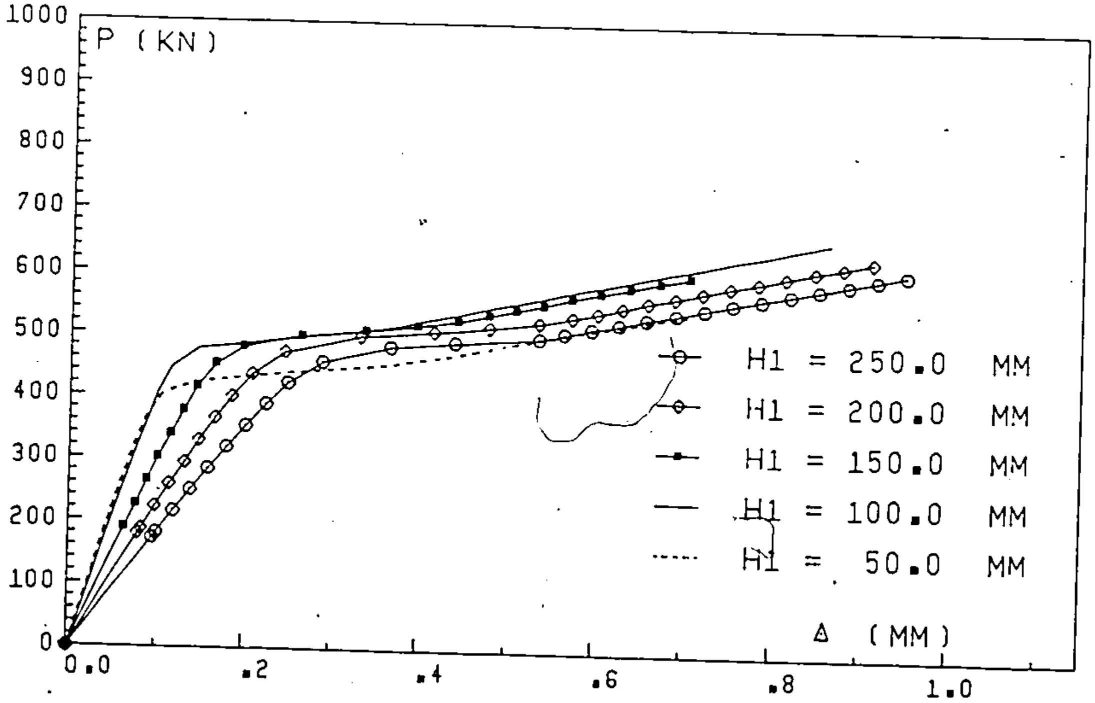

FIGURE 6.18 : WIDER RANGE OF VARIATION OF VERTICAL MEMBER DEPTH

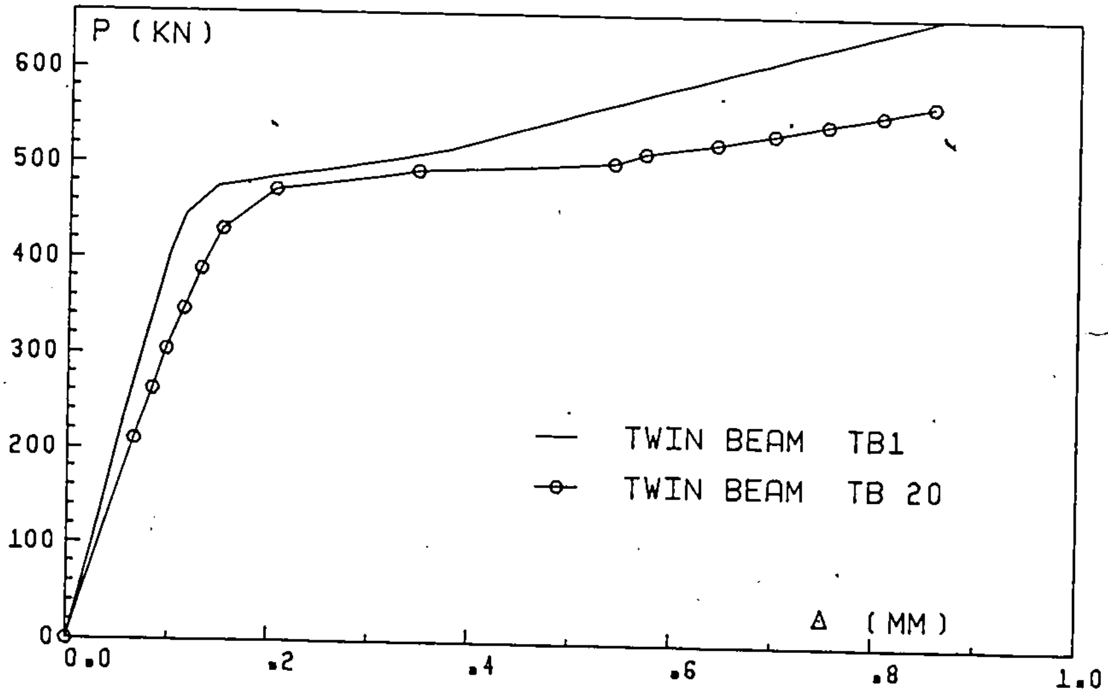

FIGURE 6.19 : INFLUENCE OF THE WELDMENT TYPE ON THE BEHAVIOUR OF TWIN SHEAR BEAM

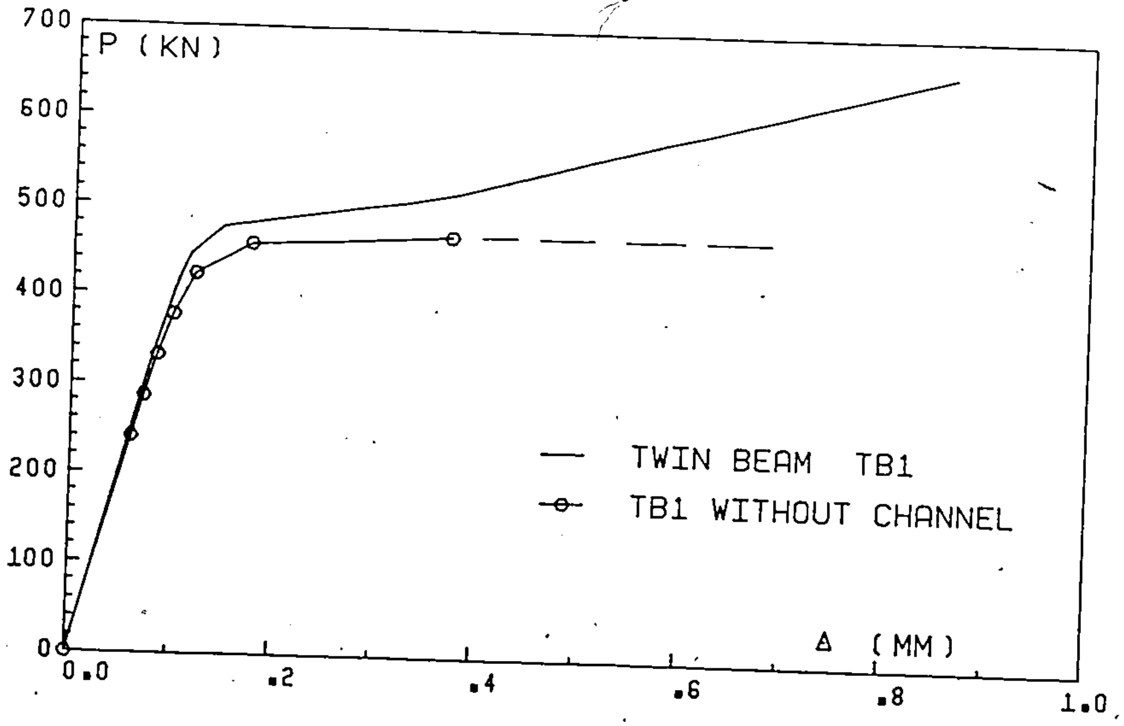

FIGURE 6.20 : STIFFENING EFFECT OF THE CHANNEL PORTION OF THE RHS CHORD MEMBER

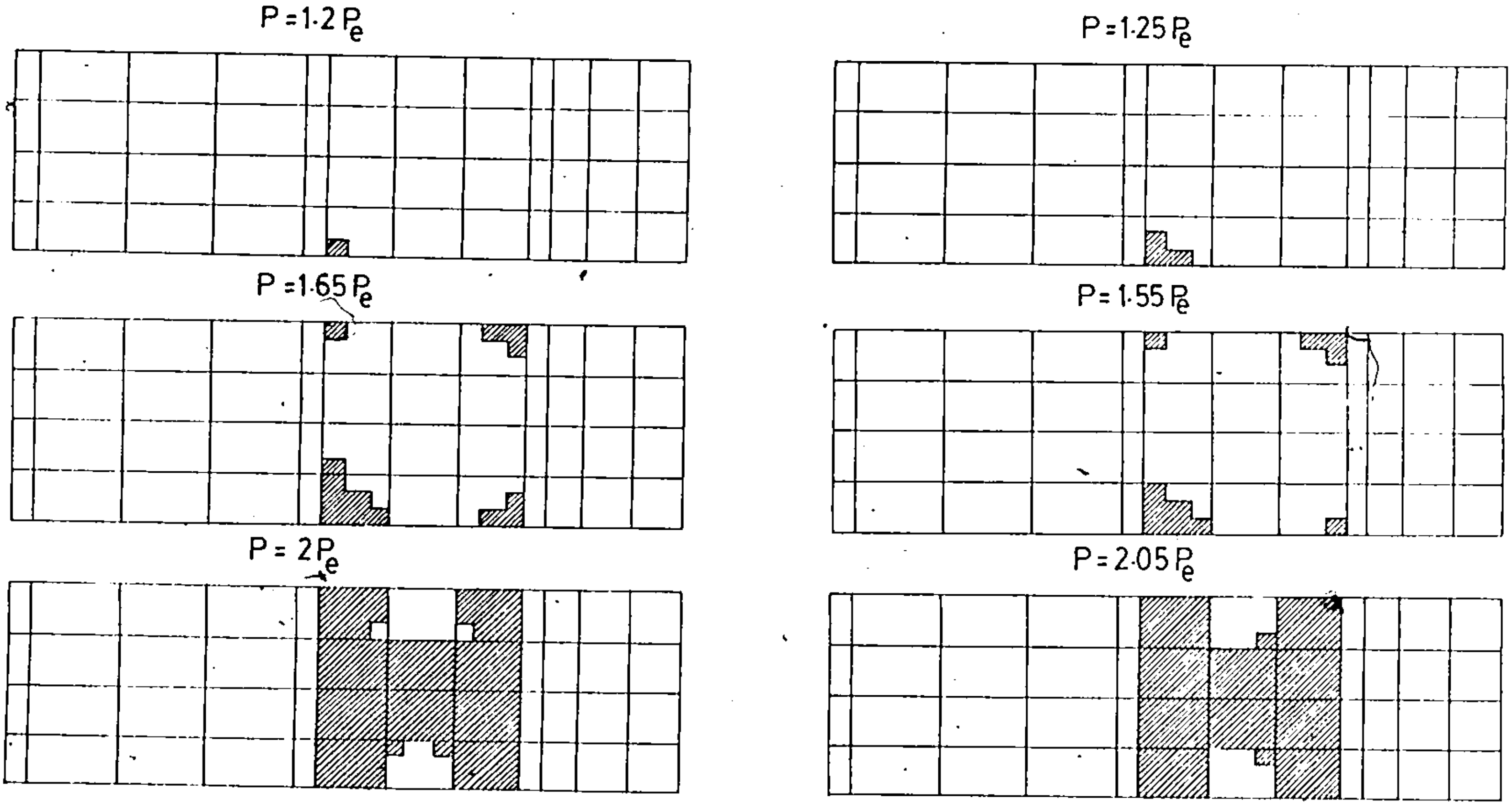
P = 1·2 P_e
P = 1·65 P_e
P = 2 P_e
P = 1·25 P_e
P = 1·55 P_e
P = 2·05 P_e

(a) Specimen 5a

(b) Specimen 7a

FIGURE 6.21 : PROGRESSION OF YIELD ZONES IN THE INNER WEB PLATE

CHAPTER 7

EXTENSION OF TWIN BEAM FINITE ELEMENT MODEL TO SEPARATED DOUBLE CHORD JOINTS

7.1 Introduction

A general finite element program for separated double chord joints is presented in this Chapter. The model called "Elasto-Plastic Analysis of RHS Connections" (EPAC-RHS) is capable of analysing N, K or T-joint configurations with the branch members sandwiched between the chords. Owing to the similarity between twin member shear beams and separated double chord gap joints, the new model is an extension of the twin shear beam FEM model. The concept of subdividing the RHS chord member into a plate and a channel representing the inner web and the remainder of the RHS is retained. Of the two methods of analysis presented earlier for condensing the channel, only the coupled one is included in the present model EPAC-RHS. There are, however, some changes to be invoked into the new model in order to account for different joint geometry and the problem size. Such changes are described in detail in this Chapter.

Because of the unsymmetric response of an N or K joint, there exists only one plane of symmetry, i.e. the vertical plane along the longitudinal axis of the joint. Therefore, half of the joint needs to be modelled and, consequently, the storage required on the computer increases significantly. To circumvent this problem, the active column solution technique developed by Bathe (40) replaced the banded solution routine in the new computer model. The technique, which is commonly known as the skyline, permits assembling and decomposing a matrix with variable bandwidths (or rather column heights). Hence, the method is particularly economical when the global stiffness matrix of a structure is not uniformly banded. Such is the case with RHS joint models cited in this study since the boundary degrees of freedom of the inner web plate are coupled. Not only is the skyline method economical, it also permits full inclusion of the matrix $[K_C]$ in the global stiffness matrix of the joint. In the twin beam model, the stiffness coefficients of $[K_C]$ that are remote from its diagonal were neglected in an effort to reduce the bandwidth of $[K_T]$ (Section 5.3.3). Such an assumption is not needed in the present model.

In truss joint assemblies, nonrectangular regions invariably exist and discretization of the inner web plate using rectangular subdivisions is just not possible. To overcome this difficulty, triangular elements are introduced. The nonconforming plate bending and the constant strain triangular elements have been combined to form a triangular plate element for the inner web or the branch member as the need may be. The formulation of the combined element is outlined in Section 7.3.

Constant as well as proportional loading types can be simulated in EPAC-RHS. This provision has been made in the new model to permit the application of chord axial preloads, as a prescribed load, while proportioning the applied load on the diagonal. The search procedure for the elastic limit load is different from before (Section 5.5.2) and is summarized in Section 7.4.

Finally, it was decided to include the modified Newton Raphson method for the nonlinear part of the analysis with an option of using either the original Newton Raphson, which is explained in Section 5.5.1 or the modified method to be described in Section 7.4.

7.2 Special Considerations

Figure 7.1 presents a typical configuration of a separated double chord K-joint. In finite element simulation of this joint using EPAC-RHS, the following points should be considered.

1. The inner web plate and the branch members are represented by separate layers of elements. Common nodes are specified along the boundaries of the branch members welded to the inner web.
2. Outstanding webs of the branch members are modelled as plane stress elements.
3. Top and bottom boundary nodes of the inner web plate must remain aligned vertically. This is a prerequisite for proper attachment of the channel grillage of beam elements to the inner web.

The first two considerations were addressed earlier in the twin beam model. The stringent requirement of aligning the boundary nodes, although not readily established as was the case for the twin beam, can be accommodated by properly using the triangular plate elements. The discretized inner web plate and the branch members are shown in Figure 7.2.

7.3 Triangular Plate Element

To be consistent with the existing rectangular plate element, the nine DOF nonconforming plate bending triangular element derived by Bazeley et al (41) has been employed. In addition, the constant strain triangle with 6 DOF (34) has been combined with the bending element. Thus, the combined triangular element has 15 DOF with 5 at each node, i.e., u, v, w, $\Theta_x = \frac{-\partial w}{\partial y}$ and $\Theta_y = \frac{\partial w}{\partial x}$.

In the derivation of the nonconforming plate bending element, Bazeley et al (41) assumed that the lateral displacement w at any point in the element is made up of a rigid body translation w^r and a displacement due to curvature w^b. Thus

$$w = w^r + w^b \tag{7.1}$$

where

$$w^r = a_1L_1 + a_2L_2 + a_3L_3 \tag{7.2}$$

is a linear function of the area coordinates L_1, L_2 and L_3 representing the strain free translation and

$$\begin{aligned} w_b = {} & a_4(L_2^2L_1 + \frac{1}{2}L_1L_2L_3) + a_5(L_2^2L_3 + \frac{1}{2}L_1L_2L_3) + \\ & a_6(L_3^2L_2 + \frac{1}{2}L_1L_2L_3) + a_7(L_3^2L_1 + \frac{1}{2}L_1L_2L_3) + \\ & a_8(L_1^2L_3 + \frac{1}{2}L_1L_2L_3) + a_9(L_1^2L_2 + \frac{1}{2}L_1L_2L_3) \end{aligned} \tag{7.3}$$

is the lateral displacement function due to bending. Thus, it is possible to solve for the unknowns a_1 to a_9, and hence obtain the element shape functions. There are nine nodal displacements available which are given by

$$\{\delta_1\}^T = \langle w_1\Theta_{x1}\Theta_{y1}w_2\Theta_{x2}\Theta_{y2}w_3\Theta_{x3}\Theta_{y3}\rangle . \tag{7.4}$$

The explicit form of the resulting shape functions is listed in Appendix B. It is readily seen that $a_1 = w_1$, $a_2 = w_2$ and $a_3 = w_3$ from direct substitution in Equation 7.2. It follows that w^b must be a function of the bending components of the six rotations of the element which are

$$\{\Theta^b\}^T = \langle \Theta^b_{x_1}\ \Theta^b_{y_1}\ \Theta^b_{x_2}\ \Theta^b_{y_2}\ \Theta^b_{x_3}\ \Theta^b_{y_3} \rangle \tag{7.5}$$

where

$$\Theta^b_{x_i} = \Theta_{x_i} + \frac{\partial w^r}{\partial y} \tag{7.6a}$$

and

$$\Theta^b_{y_i} = \Theta_{y_i} - \frac{\partial w^r}{\partial x}. \tag{7.6b}$$

Equation 7.6 can be used to relate the bending slopes $\{\Theta^b\}$ to the element nodal displacement $\{\delta_1\}$. Hence

$$\underset{6\times1}{\{\Theta^b\}} = \underset{6\times9}{[T]}\ \underset{9\times1}{\{\delta_1\}}. \tag{7.7}$$

The transformation matrix [T] is given in Appendix B.2. The form of the element strain matrix [B] was reported by Cheung et al. (42). Having performed the necessary differentiation of the shape functions w.r.t. x and y, they showed that the strain matrix is given by

$$\underset{3\times9}{[B]} = \frac{z}{8\Delta^3}\ \underset{3\times7}{[A]}\ \underset{7\times6}{[\bar{B}]}\ \underset{6\times9}{[T]} \tag{7.8}$$

where Δ is the area of the triangle and [A] is a function of x and y and is given by:

$$[A] = \begin{bmatrix} -2 & 0 & 0 & -6x & -2y & 0 & 0 \\ 0 & 0 & -2 & 0 & 0 & -2x & 6y \\ 0 & 2 & 0 & 0 & 4x & 4y & 0 \end{bmatrix}. \qquad (7.9)$$

The matrix $[\bar{B}]$ is rather lengthy and is therefore given in Appendix B.3.

The assumed fields for the in-plane displacements are (34)

$$u = u_1L_1 + u_2L_2 + u_3L_3 \qquad (7.10)$$

$$v = v_1L_1 + v_2L_2 + v_3L_3 \qquad (7.11)$$

which are linear in both x and y. The strain within the element can be calculated from

$$\underset{3\times1}{\{\varepsilon\}} = \begin{bmatrix} \frac{\partial}{\partial x} & 0 \\ 0 & \frac{\partial}{\partial y} \\ \frac{\partial}{\partial y} & \frac{\partial}{\partial x} \end{bmatrix} \begin{Bmatrix} u \\ v \end{Bmatrix} = [L]\ [N_2]\ \{\delta_2\} \qquad (7.12)$$

i.e. $[B_2] = [L]\ [N_2]$ (7.13)

is the strain matrix for in-plane displacements where

$$\{\delta_2\}^T = \langle u_1 v_1 u_2 v_2 u_3 v_3 \rangle \qquad (7.14)$$

and

$$[N_2] = \begin{bmatrix} L_1 & 0 & L_2 & 0 & L_3 & 0 \\ 0 & L_1 & 0 & L_2 & 0 & L_3 \end{bmatrix}. \qquad (7.15)$$

Since the assumed fields are linear, the strain and hence the stress is constant within the element. Combining the matrices $[B_1]$ and $[B_2]$ in a similar manner to the one described for the rectangular element, the total strain matrix, which is 3 × 15, can be obtained; its columns correspond to the following degrees of freedom.

$$\{\delta^e\}^T = \langle u_1 v_1 w_1 \theta_{x_1} \theta_{y_1} \; \cdots\cdots \; \theta_{y_3} \rangle. \qquad (7.16)$$

Twenty-one integration points within the element were selected for strain and stress computations and for evaluation of the element stiffness matrix by means of numerical integration. Locations of integration points through the element thickness and the associated weight factors are identical to those reported earlier for the rectangular element. The positions of the seven points selected over the element area and their weight factors are determined from Hammer's Table (34) for triangular element with area co-ordinates and are shown in Figure 7.3. The plate element stiffness matrix can now be computed as

$$\underset{(15\times15)}{[K^e]} = \Delta \cdot \frac{t}{2} \sum_{i=1}^{3} \sum_{j=1}^{7} \omega_i \omega_j \underset{(15\times3)}{[B(L_{1j}, L_{2j}, z_i)]^T} \underset{(3\times3)}{[D]}$$

$$[\underset{(3\times15)}{B}(L_{1j},\ L_{2j},\ z_i)]. \tag{7.17}$$

The weight factors ω_i and the corresponding z coordinates have been defined earlier in Equations 5.22 and 5.21, respectively. The [D] matrix is given by Equation 5.18 in the elastic range and Equation 5.60 for the elasto-plastic range. Also,

$$\{L_{1j}\}^T = \langle\tfrac{1}{3},\ \alpha_1,\ \beta_1,\ \beta_1,\ \alpha_2,\ \beta_2,\ \beta_2\rangle$$

$$\{L_{2j}\}^T = \langle\tfrac{1}{3},\ \beta_1,\ \alpha_1,\ \beta_1,\ \beta_2,\ \alpha_2,\ \beta_2\rangle \tag{7.18}$$

with $\alpha_1 = 0.05971,58717$

$\beta_1 = 0.47014,20641$

$\alpha_2 = 0.79742,69853$

$\beta_2 = 0.10128,65073$

and

$$\{\omega_j\}^T = \langle\omega_1,\ \omega_2,\ \omega_2,\ \omega_2,\ \omega_3,\ \omega_3,\ \omega_3\rangle \tag{7.19}$$

with $\omega_1 = 0.22500,00000$

$\omega_2 = 0.13239,41527$

$\omega_3 = 0.12593,91805.$

It may be worth noting that the area coordinate L_{3j} at any point j is redundant once L_{1j} and L_{2j} are determined because $\sum_{n=1}^{3} L_{nj} = 1$.

Verification tests reported in Section 6.3 for the rectangular element were repeated for the triangular element and showed equally good results. For test 1V, the computed to exact deflection ratio at point c for a 4 × 16 division mesh containing 128 elements was 0.854, which is in close agreement with the 0.859 reported in reference (39). This compares with 0.951 for the rectangular element for which some difference is to be expected since the rectangular elements are more flexible in view of their bilinear displacement field. The elasto-plastic test 2V yielded almost identical results, albeit with slight difference in final yield pattern due to the fact that the CST element yield wholly (constant stress state). The data for test 3V shown in Figure 6.4(a) was used to check the elasto-plastic performance of the CST element in a shear predominant situation. This was a case of deep shear panel having an aspect ratio of 2:1 and subjected to simulated edge loading. The maximum shearing force by the panel was found to be 0.862 of the plastic shearing force of the section (with the result for the rectangular element being 0.867).

In addition, the triangular plate bending element was also checked using 21 integration points having the locations defined earlier. The elastic response of the element was successfully tested against the exact solutions of a thin square plate subjected to a variety of loads and boundary conditions (34). As is evident from the results listed in Table 7.1, both convergence and accuracy were good.

Load-deflection curves and yield zone progression for tests 2V and 3V are not being presented as they are similar to those for the rectangular element.

7.4 Chord/Web member Preload

Joint failure is normally induced by high magnitude forces acting on the joint, such as punching shear or bending moment. It is well known that in real truss systems, there also exist significant forces that can influence the joint performance. For example, N and K joints usually collapse under increased web member forces while their chords are subjected to small axial forces. On the other hand, critically loaded Vierendeel T-joints normally experience high branch bending moment when the chord transmits relatively small axial forces e.g. simply supported trusses. These normal forces are termed preloads since during joint testing such forces are often applied prior to the incrementing of the major force component. Preloads have been allowed in the new model. As such, the search for the elastic limit load requires some additional steps in the analysis than usual. The approach is conceptually simple and is summarized as follows.

1. Store the load vectors due to prescribed preload and arbitrary web member load separately in $\{P_p\}$ and $\{P_w\}$.
2. Compute the displacements due to each of the two loads and store these separately.
3. Calculate the corresponding strains and hence the effective

stresses $\bar{\sigma}_p^{ij}$ and $\bar{\sigma}_w^{ij}$ due to preload and web member load, respectively.

4. The elastic limit load factor "μ" at a point can be found from the expression

$$\sigma_y = \bar{\sigma}_p^{ij} + \mu\, \bar{\sigma}_w^{ij} \tag{7.20}$$

where i varies from 1 to the number of sampling points of the j^th element, and j varies from 1 to the total number of elements in the joint. The minimum value of "μ" (μ_{min}) is the required elastic limit load factor.

5. The total elastic limit load $\{P_{te}\}$ is then given by

$$\{P_{te}\} = \{P_p\} + \mu_{min}\,\{P_w\} = \{P_p\} + \{P_{we}\}. \tag{7.21}$$

The nonlinear analysis is commenced noting that load increments should be taken as fractions of the web member elastic limit load $\{P_{we}\}$ and not $\{P_{te}\}$.

Chord member preloads were simulated in the computer model by a set of nodal forces acting at the vertical boundary of the inner web plate. This was not possible for the channel, unfortunately, since there is not a degree of freedom in the longitudinal direction of the grillage. Alternatively, preloads were simulated by a "preset" uniformly distributed normal stress acting at all integration points of the beam bending elements of flange and web type (Section 4).

7.5 Solution Technique for Nonlinear Analysis

The iterative Newton Raphson method was previously employed in the nonlinear analysis of the twin beam model to search for the equilibrium position at the end of every load increment. In the present model, the modified Newton Raphson method (34) was also included to provide the opportunity of comparing computer costs from the two methods. Originally, the global stiffness matrix was updated after each iteration until equilibrium was attained. The latter was based on a comparison of determinant values of "current" and "previous" iterations. In the modified method, the global stiffness matrix is kept constant throughout the load increment and is only updated at the end of the load increment. Naturally, the solution in this case takes more iterations to converge to the equilibrium configuration. However, the global stiffness matrix is decomposed only once at the beginning of the load increment. As such it may be difficult to predict the efficiency of each method without experimentation.

Testing the convergence based on a comparison of the determinant value is, of course, not valid since ~~the~~ stiffness matrix remains unchanged. Alternatively, Bathé and Cimento (43) proposed three convergence criteria based on displacement, out-of-balance force and incremental internal energy considerations. From their experience, it appeared that a displacement convergence criterion can sometimes be ill behaved. They also cautioned about inconsistencies of units that may arise when calculating the norm of the out-of-balance force vector.

Such a vector may contain forces and moments. Hence, it was deemed most suitable to adopt their third convergence criterion which recommends computing the increment in internal energy during each iteration ΔW^i and comparing it with the initial work done by the residual (out-of-balance) forces on the initial displacement increments ΔW^o. Thus, the iteration is terminated when

$$\frac{\Delta W^i}{\Delta W^o} < \varepsilon_E$$

or $$\frac{\{\Delta\delta^i\}^T\{\Delta R_r^i\}}{\{\Delta\delta^o\}\{\Delta R^o\}} < \varepsilon_E \qquad (7.22)$$

where $\{\Delta\delta^o\}$ is the first approximation of displacement increments when the full load increment $\{\Delta R^o\}$ has been applied; $\{\Delta\delta^i\}$ and $\{\Delta R_r^i\}$ are the subsequent displacement increment and the corresponding residual force vectors. The value of the tolerance ε_E employed in EPAC-RHS was 0.005.

Numerical results of typical K-joint models indicated that the Newton Raphson method always provided a more economical solution. It may be worth remarking that several methods to accelerate the convergence of the modified Newton Raphson method have been presented in the literature such as the Aitken accelerator (44) and the BFGS method (43). Implementation of these schemes was not however attempted in the present model since the performance of the Newton Raphson method was believed to be satisfactory.

7.6 Comparison with Previous Experiments on K-Joints

Twelve separated double chord K-joint specimens were tested by Korol and Chidiac (1,2). These comprised 3 groups that had web-to-chord member slopes of 2:1, 2:1 and 1:1. The centre-to-centre gap distance between diagonals measured 178 mm, 108 mm and 90 mm for the three groups with other dimensions provided in Table 7.2. Chord preload and yield stress data were previously given in Table 3.2.

The joint behaviour was characterized in terms of a load-deflection plot in which the load was the simulated axial force of the diagonal member and the deflection was the relative displacement in Y-direction between two points on the diagonal centre lines. These are points A and B marked by heavy dots in Figure 7.1. The discreticized inner web plates and the mated branch members for groups 1, 2 and 3 are shown in Figures 7.4, 7.5 and 7.6, respectively.

Using the model EPAC-RHS, analytical joint models were subjected to similar chord preloading and incremental loading beyond their proportional limit load until the relative displacement reached the prescribed limit of 1% $(h_0 + b_0)$ (Section 2.6). Experimental load-deflection curves obtained from reference (2) have been plotted with the corresponding results from EPAC-RHS in Figures 7.7, 7.8 and 7.9 for the three groups. It is obvious that very good correlation between theoretical and experimental elastic stiffnesses exist. In the post-elastic range, the finite element solution exhibited a more rapid deterioration than experiment. However, very good agreement was obtained for some joints such as S2P46T and S1P26T. It should be pointed out that the proper σ_y and E_T for best fit with bilinear behaviour could not be evaluated for the K-joints due to lack of information. Instead, the reported yield stresses and a value of $E_T = 0.025$ E were employed. Clearly, had E_T or σ_y been higher, a better agreement would have resulted in the post-elastic range without affecting the elastic response.

In order to maximize the benefit from the finite element results, joint models S2P76C and S2P46C were compared to evaluate the effect of changing the joint eccentricity (or gap distance). As was concluded earlier for the twin beam model, there are substantial gains in both strength and stiffness for a decrease in eccentricity from 178mm (S2P76C) to 108mm (S2P46C); this is evident from Figure 7.10(a). A similar comment can be made in relation to the performances of S2P74C and S2P44C which are illustrated in Figure 7.10(b). The latter possesses considerably higher strength properties than the former.

To investigate the influence of the chord axial preload, load-deflection curves of S2P76C, S2P74C and S2P72C were traced in Figure 7.11. Such joints, while identical in geometry, were subjected to simulated compressive chord prestresses of 0.085 σ_y, 0.165 σ_y and 0.235 σ_y, respectively. As can be seen from Figure 7.10, it was not until the preload ratio was 0.235 when a sizeable decline in behaviour could be observed. Similar observation was made earlier in Section 3.7 from a consideration of the interaction diagram constructed by the conical mechanism model (Figure 3.13).

7.7 Discussion

The finite element model EPAC-RHS developed in this study has been found to provide a means for predicting the behaviour of double chord RHS joints of the separated type. With the introduction of triangular plate elements and the algorithm for allowing preloads, a realistic simulation of such joints can be made. Substantial savings on computer time and storage can also be achieved by employing the skyline technique and the dynamic storage scheme (40). While only demonstrated on K-joints in this Chapter, EPAC-RHS is also capable of analysing the behaviour of other RHS connections of the separated type. This can be accomplished without difficulty with the aid of the User's Information Manual for EPAC-RHS (47).

From the demonstrated results, it may be concluded that the finite element model predicts the joint elastic response with reasonable accuracy. On the other hand, conservative estimates of joint strength were found for localized relative displacement of 1% ($h_o + b_o$). This was perhaps due to an underestimation of the yield stress or tangent modulus values used.

It may be noted that the locked-in-stresses that develop due to weldments were not included in the analysis. However, the stiffening effect of the weld material itself was also discarded from the simulated joints. It was assumed that these effects would tend to cancel each other. However, the relative magnitudes of their effects are unknown as these aspects were beyond the scope of this work.

Table 7.1 Computed Central Deflection of a Square Plate for Several Meshes Using Triangular Plate Bending Element - 21 Integration Points

Mesh whole plate	Simply Supported UDL(a)	 Point Load(b)	Clamped UDL(a)	 Point Load(b)
4 × 4	.00458203	.01367346	.00136291	.00653056
6 × 6	.00433830	.01279051	.00135117	.00630664
8 × 8	.00423687	.01240747	.00132527	.00611835
16 × 16	.00412268	.01192449	.00128758	.00582943
Exact(*)	.004062	.01160	.00126	.00560

(*) Extracted from Ref. (34).

Note: Central Deflection $= a\left(\frac{qL^4}{D}\right)$ .. for uniformly distributed load q

$= b\left(\frac{PL^2}{D}\right)$ .. for a concentrated load P at the centre.

Table 7.2 Dimensions of Separated Double Chord K-Joints (Ref. 2)

Group	Specimen	ℓ_c (mm)	ℓ_w (mm)	ℓ_c (mm)
1	S2P76C S2P76C* S2P74C S2P72C S2P74T S2P72T	1168.5	1219	178
2	S2P46C S2P44C S2P46T	1168.5	1194	108
3	S1P26C S1P26C* S1P26T	1168.5	1181	45

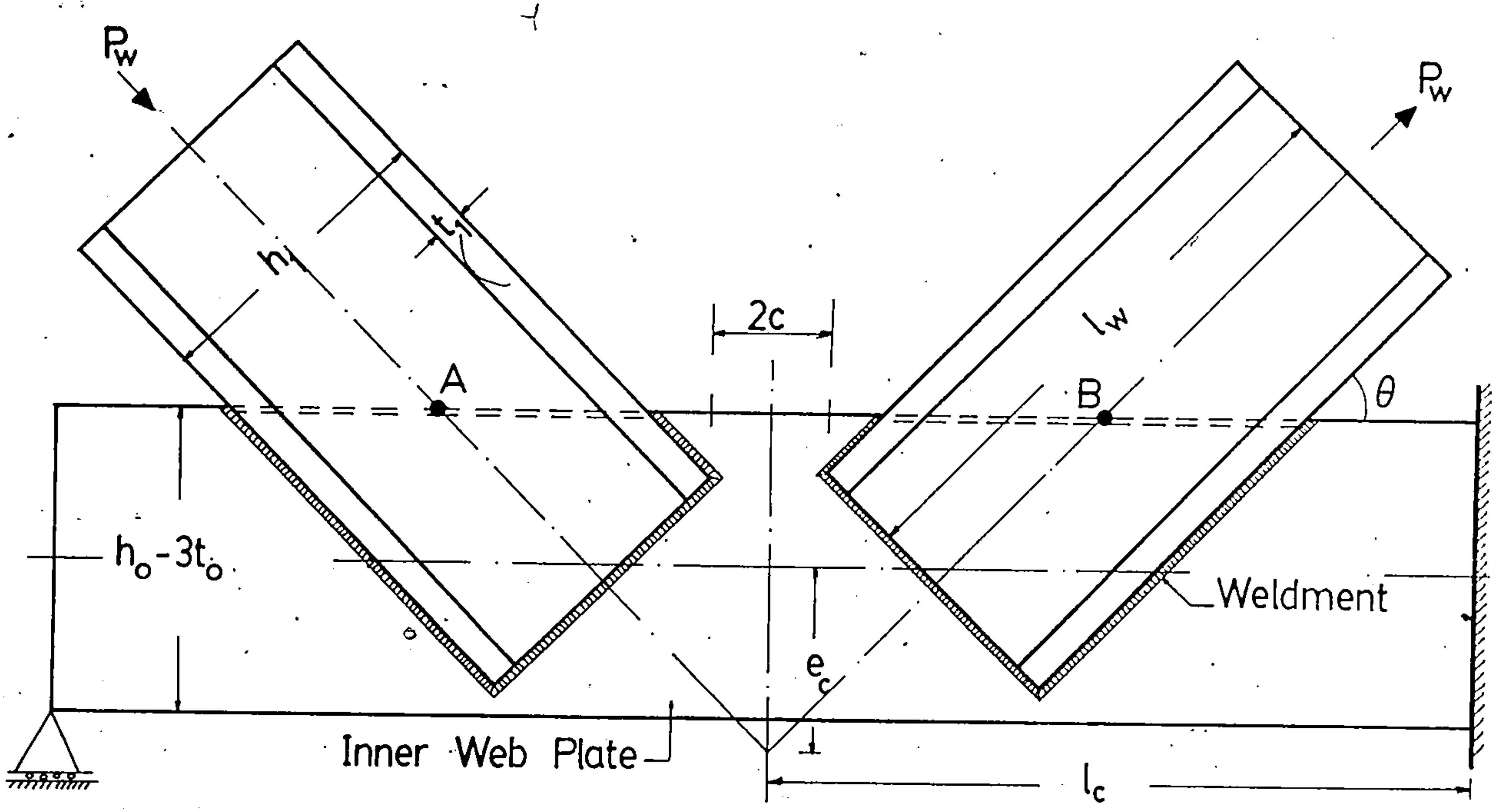
P_w
P_w
h_1
t_1
l_w
2c
A
B
θ
h_o-3t_o
Weldment
e_c
Inner Web Plate
l_c

FIGURE 7.1 : LONGITUDINAL SECTION IN A SEPARATED DOUBLE CHORD K-JOINT

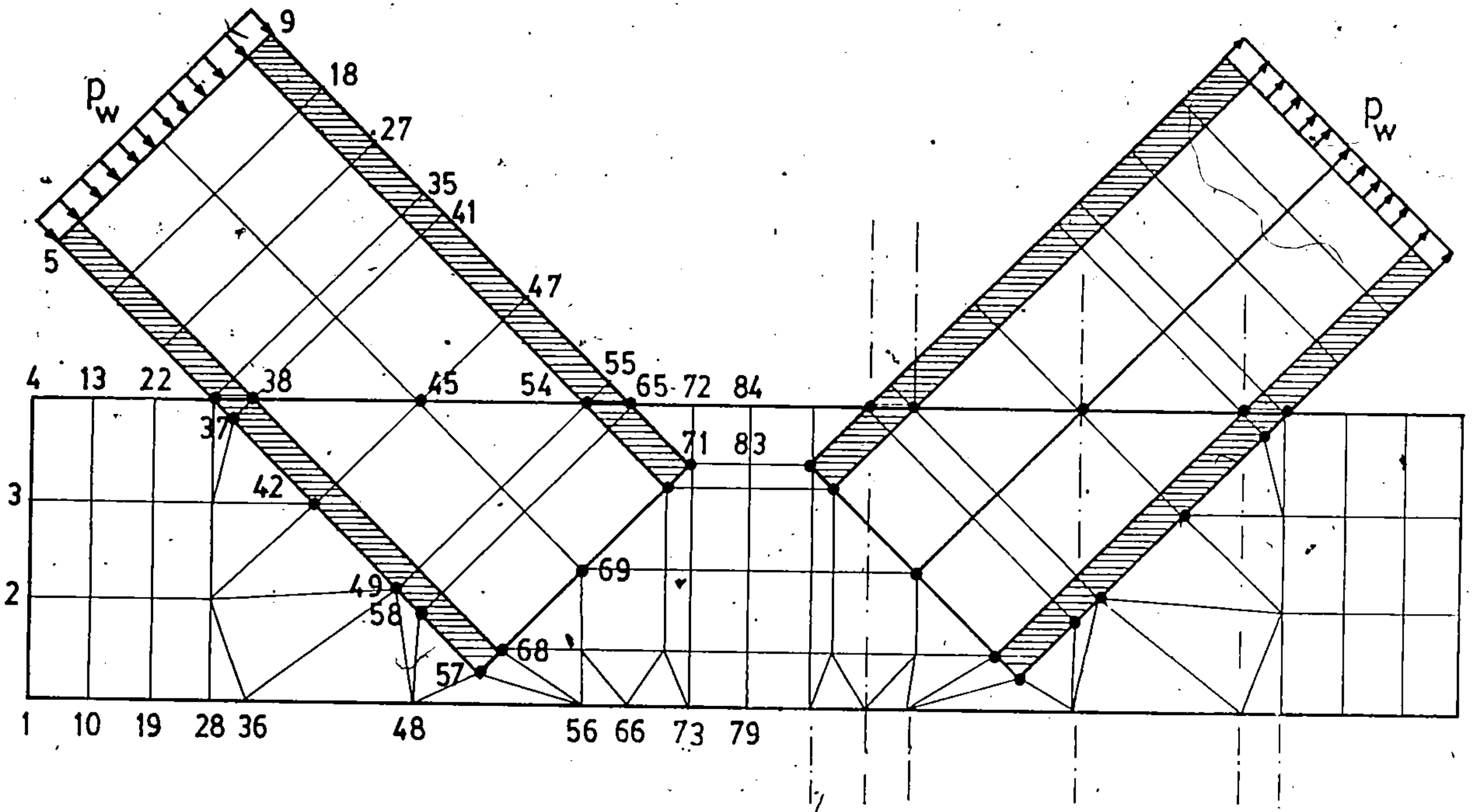
P_w
P_w
9
18
27
35
41
47
55
5
4
13
22
38
45
54
65
72
84
37
71
83
3
42
69
2
49
58
68
57
1
10
19
28
36
48
56
66
73
79

FIGURE 7.2 : IDEALIZATION OF INNER WEB PLATE AND OVERLAPPING BRANCH MEMBERS OF A K-JOINT

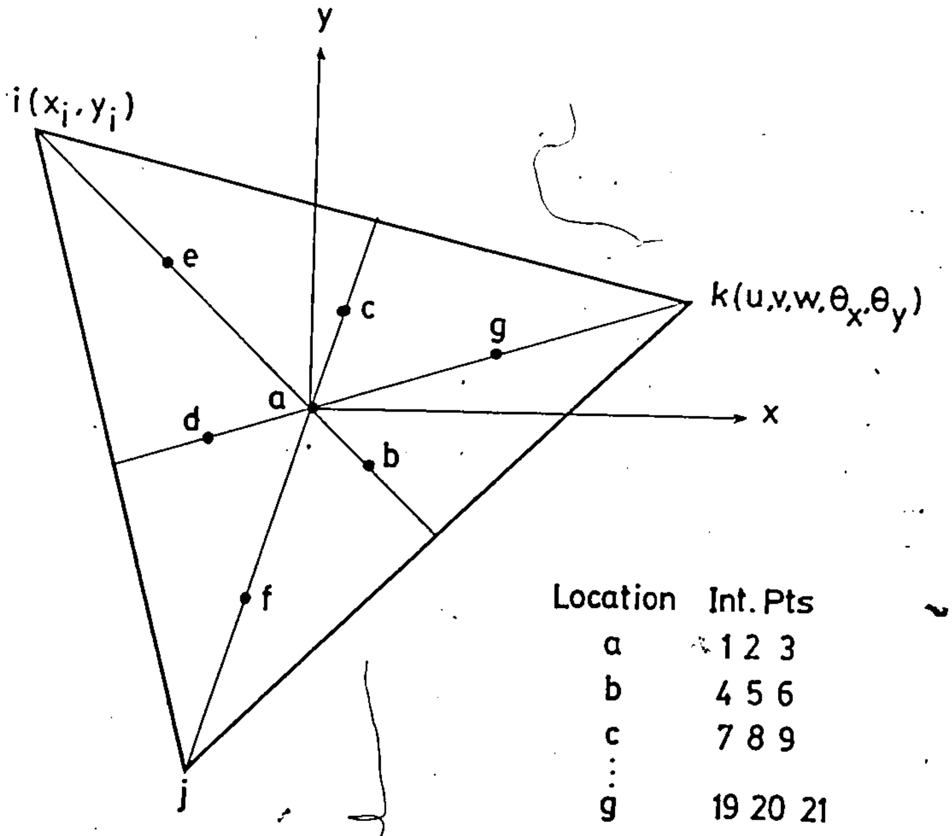
y
$i(x_i, y_i)$
e
c
$k(u,v,w,\theta_x,\theta_y)$
g
a
d
x
b
f
j

Location	Int. Pts
a	1 2 3
b	4 5 6
c	7 8 9
⋮	
g	19 20 21

FIGURE 7.3 : TRIANGULAR PLATE ELEMENT

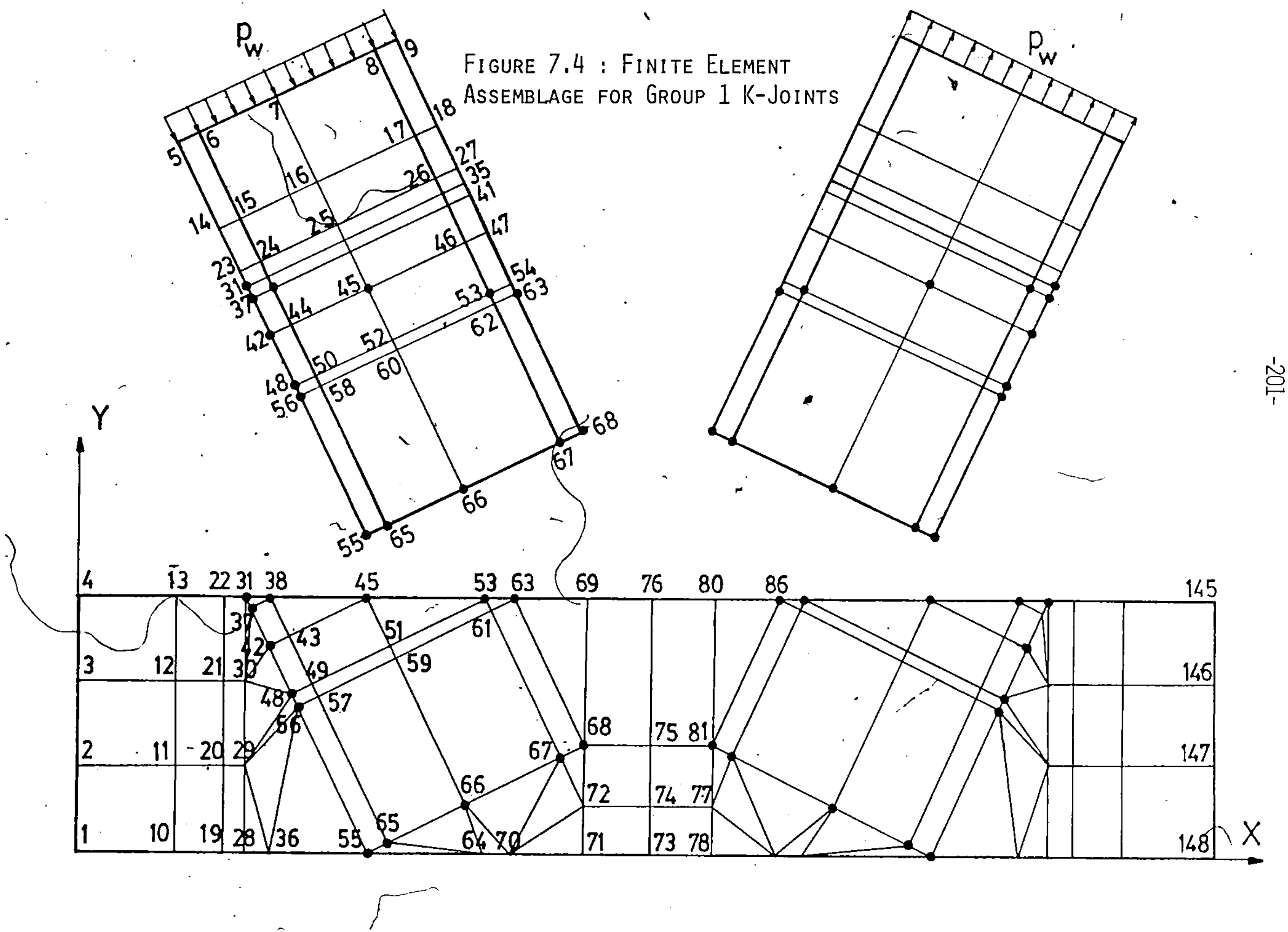
P_w
5
6
7
8
9
14
15
16
17
18
23
24
25
26
27
31
35
37
41
42
44
45
46
47
48
50
52
53
54
56
58
60
62
63
55
65
66
67
68
P_w
Y
X
4
13
22
31
38
45
53
63
69
76
80
86
145
3
12
21
30
37
42
43
51
61
59
49
48
57
56
146
2
11
20
29
68
75
81
67
66
147
1
10
19
28
36
55
65
64
70
72
71
74
73
77
78
148

FIGURE 7.4 : FINITE ELEMENT ASSEMBLAGE FOR GROUP 1 K-JOINTS

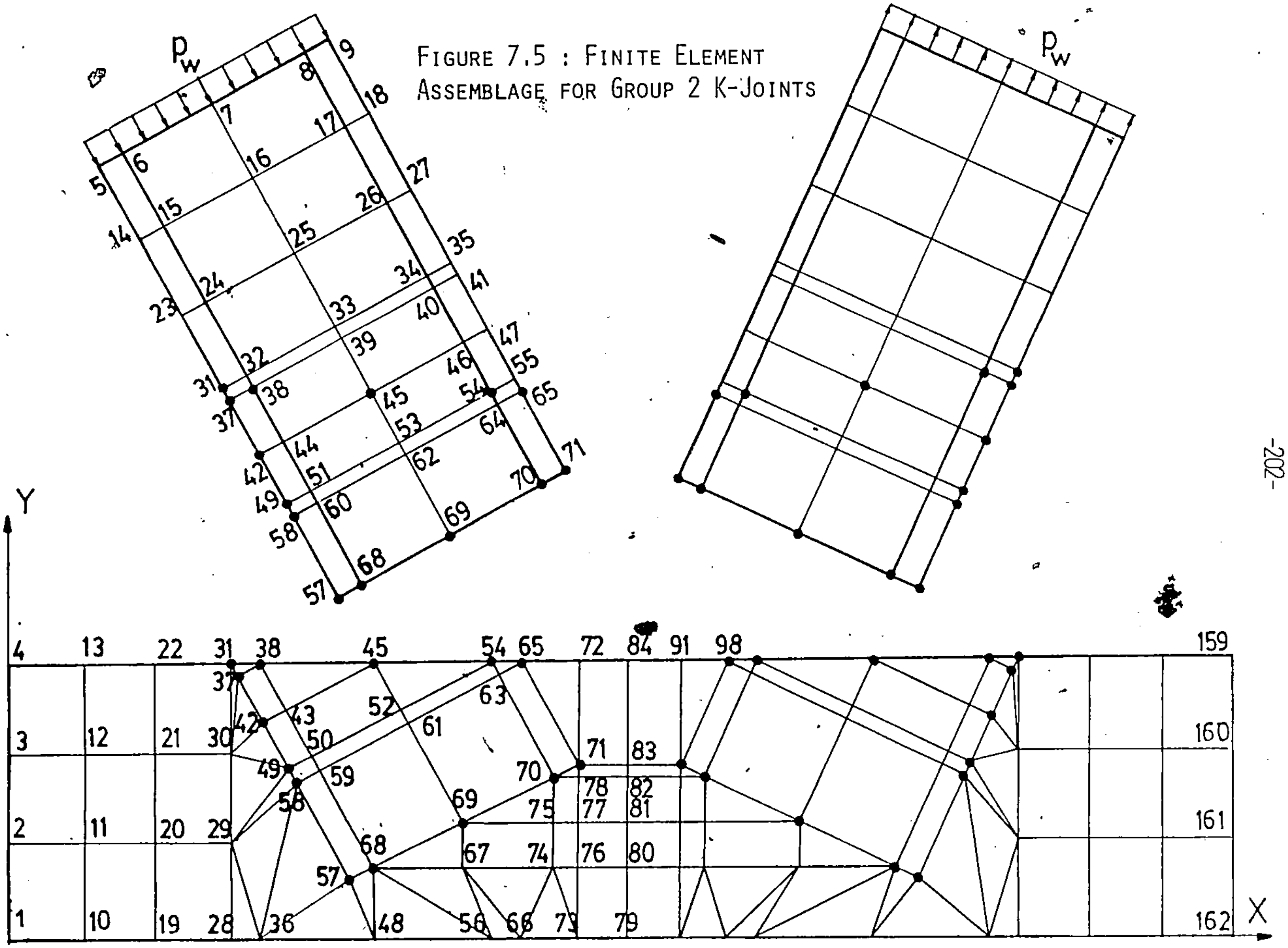
P_w
P_w
1
2
3
4
5
6
7
8
9
10
11
12
13
14
15
16
17
18
19
20
21
22
23
24
25
26
27
28
29
30
31
32
33
34
35
36
37
38
39
40
41
42
43
44
45
46
47
48
49
50
51
52
53
54
55
56
57
58
59
60
61
62
63
64
65
66
67
68
69
70
71
72
73
74
75
76
77
78
79
80
81
82
83
84
91
98
159
160
161
162
X
Y

FIGURE 7.5 : FINITE ELEMENT ASSEMBLAGE FOR GROUP 2 K-JOINTS

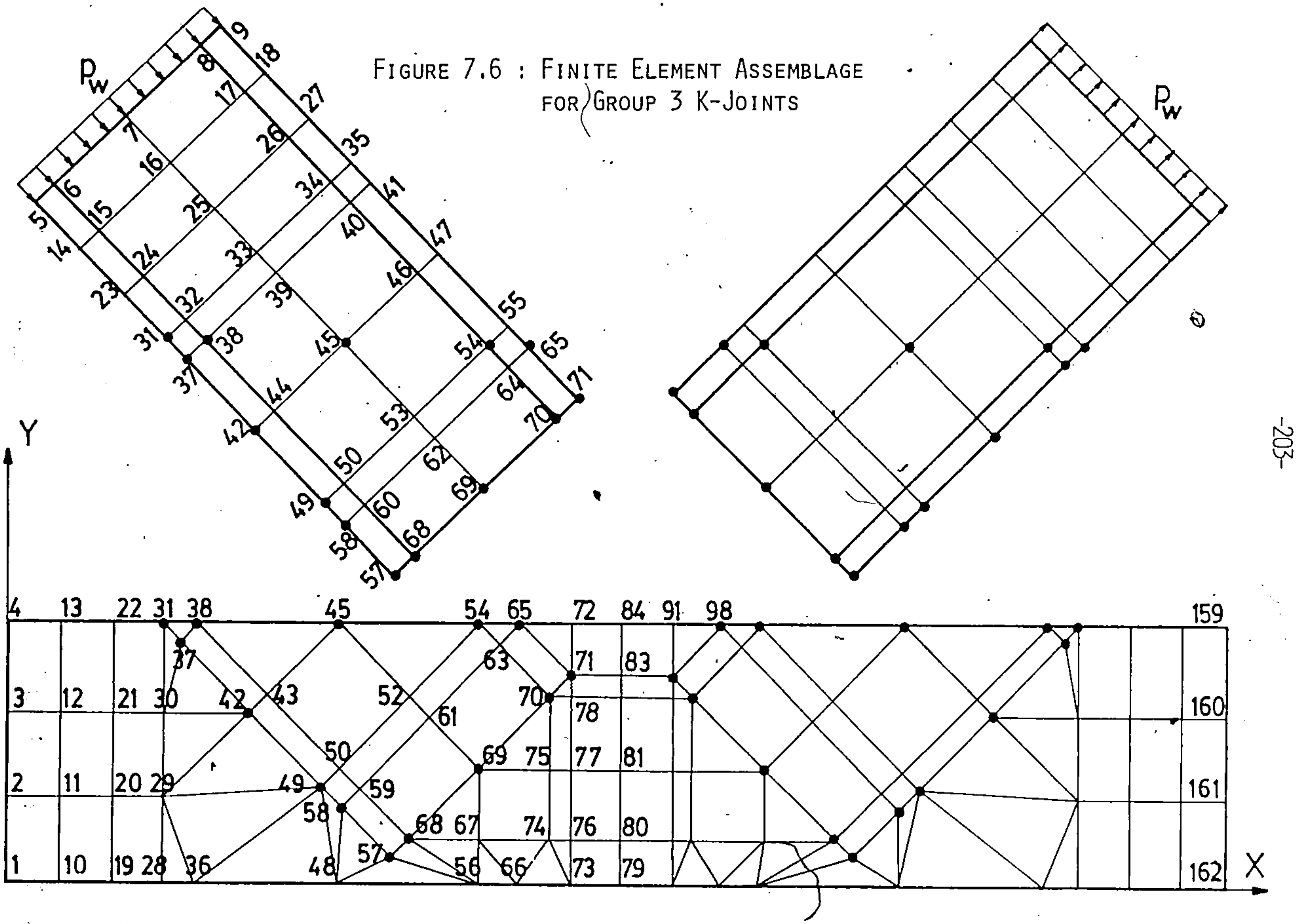
P_w
5 6 7 8 9
14 15 16 17 18
23 24 25 26 27
31 32 33 34 35
37 38 39 40 41
42 44 45 46 47
49 50 53 54 55
58 60 62 64 65
57 68 69 70 71
P_w
Y
X
4 13 22 31 38 45 54 65 72 84 91 98 159
37 63 71 83
3 12 21 30 42 43 52 61 70 78 160
50 69 75 77 81
2 11 20 29 49 59 161
58 68 67 74 76 80
1 10 19 28 36 48 57 56 66 73 79 162

FIGURE 7.6 : FINITE ELEMENT ASSEMBLAGE FOR GROUP 3 K-JOINTS

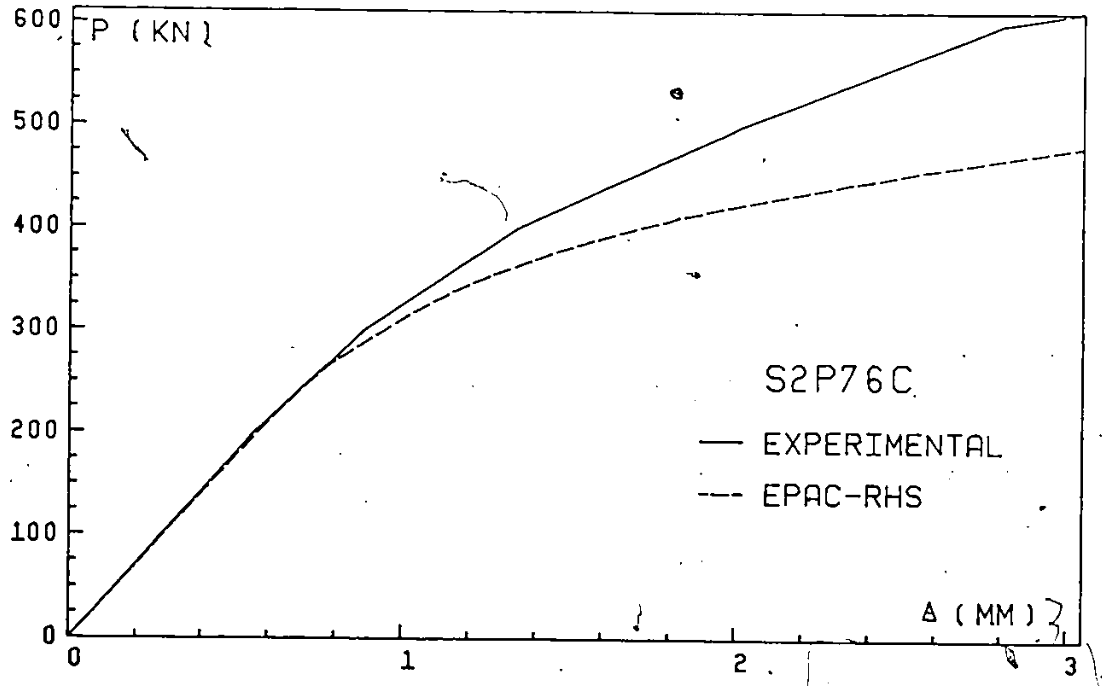
P (KN)
600
500
400
300
200
100
0
Δ (MM)
0
1
2
3
S2P76C
EXPERIMENTAL
EPAC-RHS

(a)

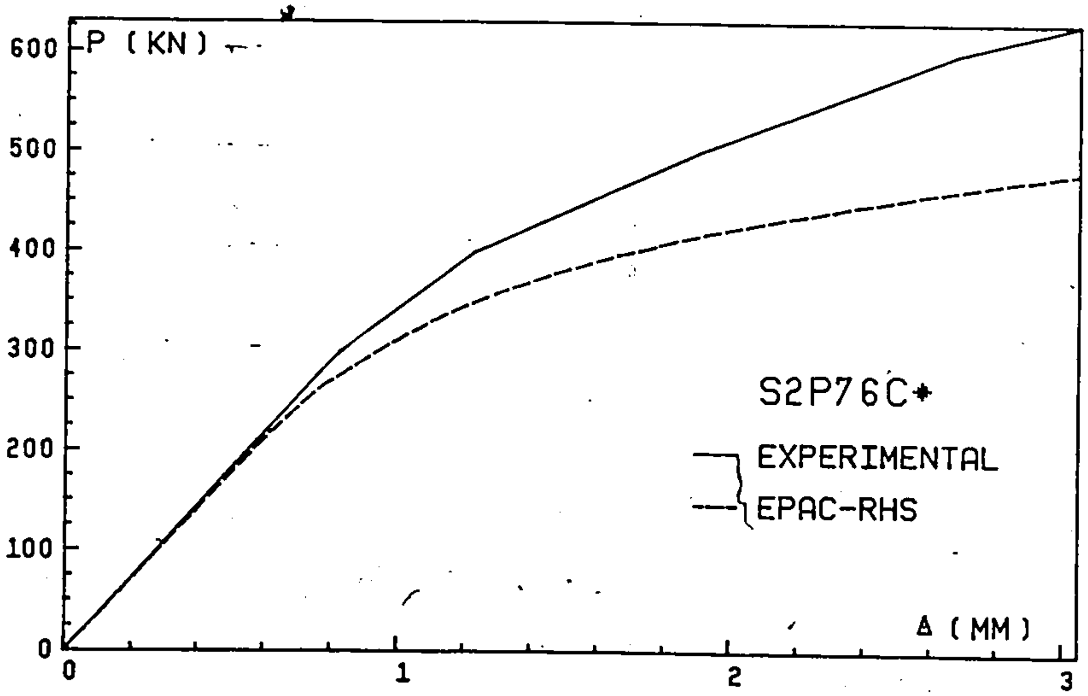
P (KN)
600
500
400
300
200
100
0
Δ (MM)
0
1
2
3
S2P76C*
EXPERIMENTAL
EPAC-RHS

(b)

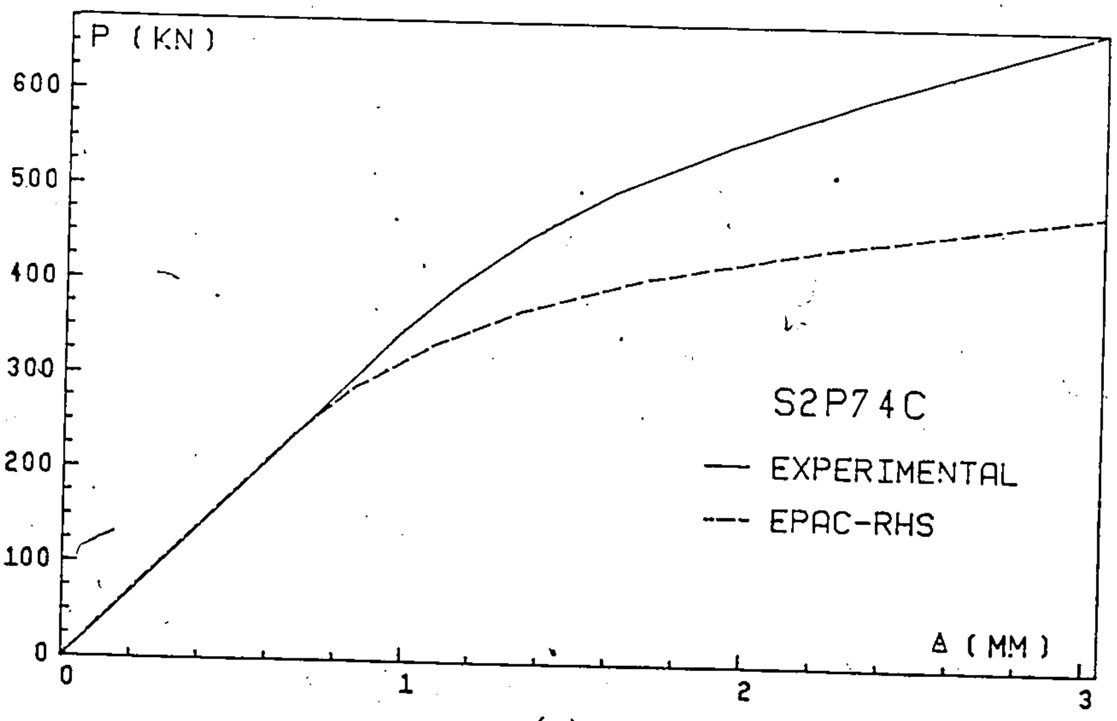
P (KN)
600
500
400
300
200
100
0
0
1
2
3
Δ (MM)
S2P74C
EXPERIMENTAL
EPAC-RHS

(c)

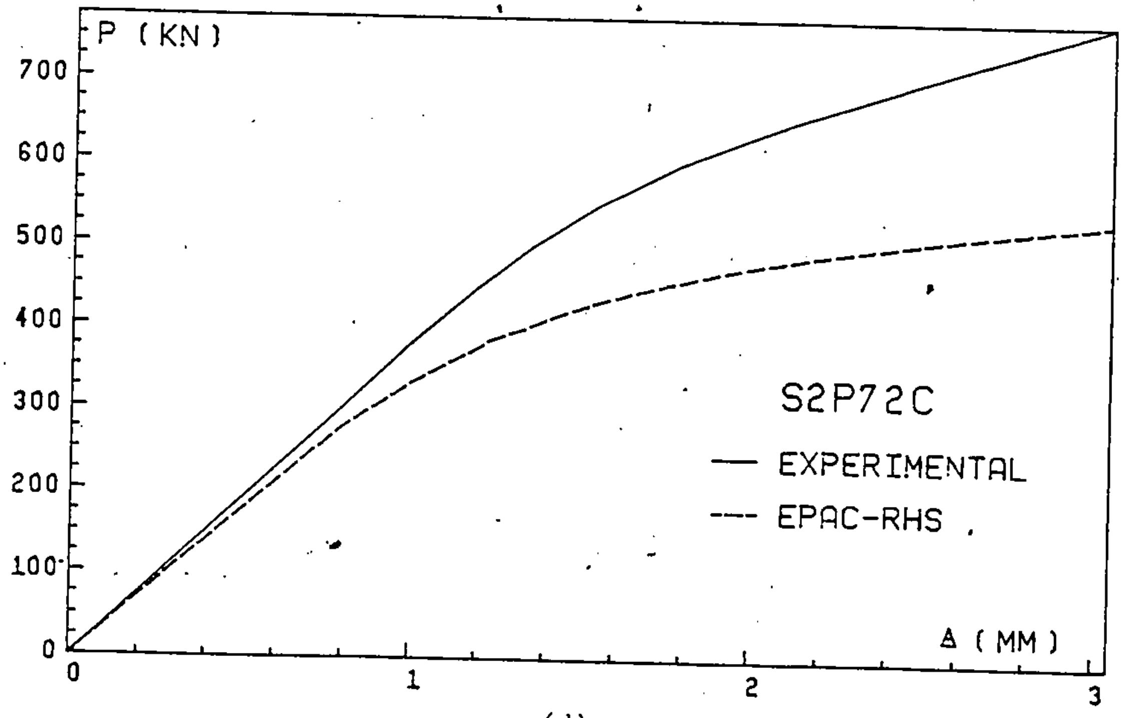
P (KN)
700
600
500
400
300
200
100
0
0
1
2
3
Δ (MM)
S2P72C
EXPERIMENTAL
EPAC-RHS

(d)

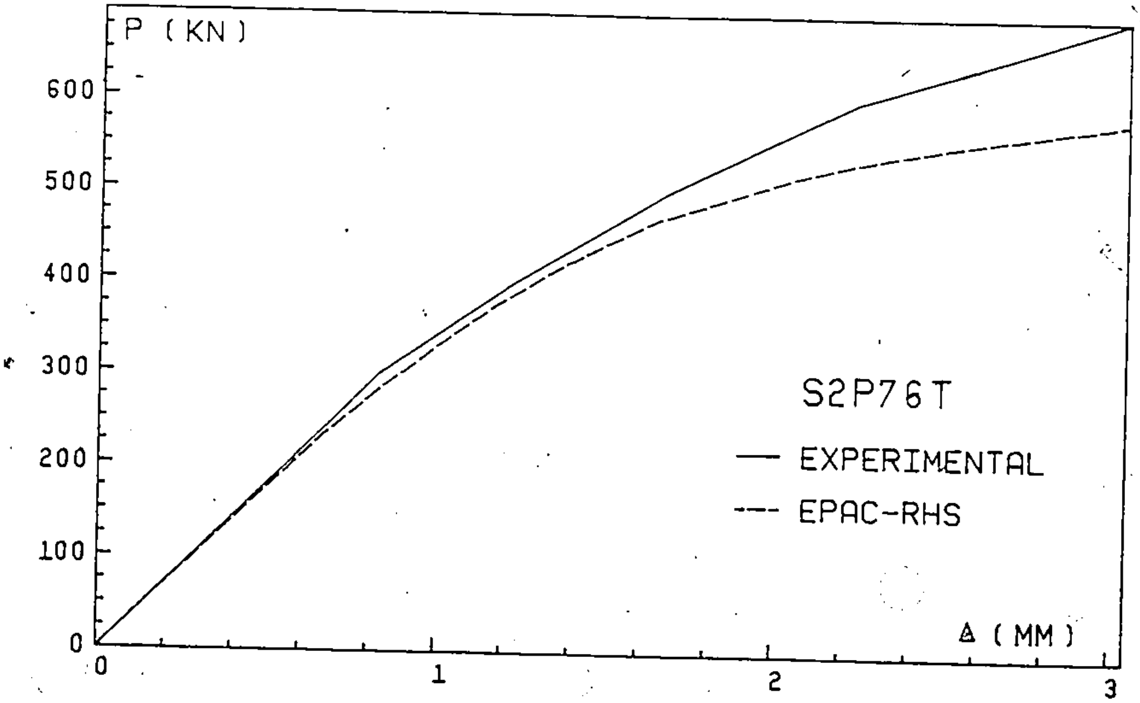

(e)

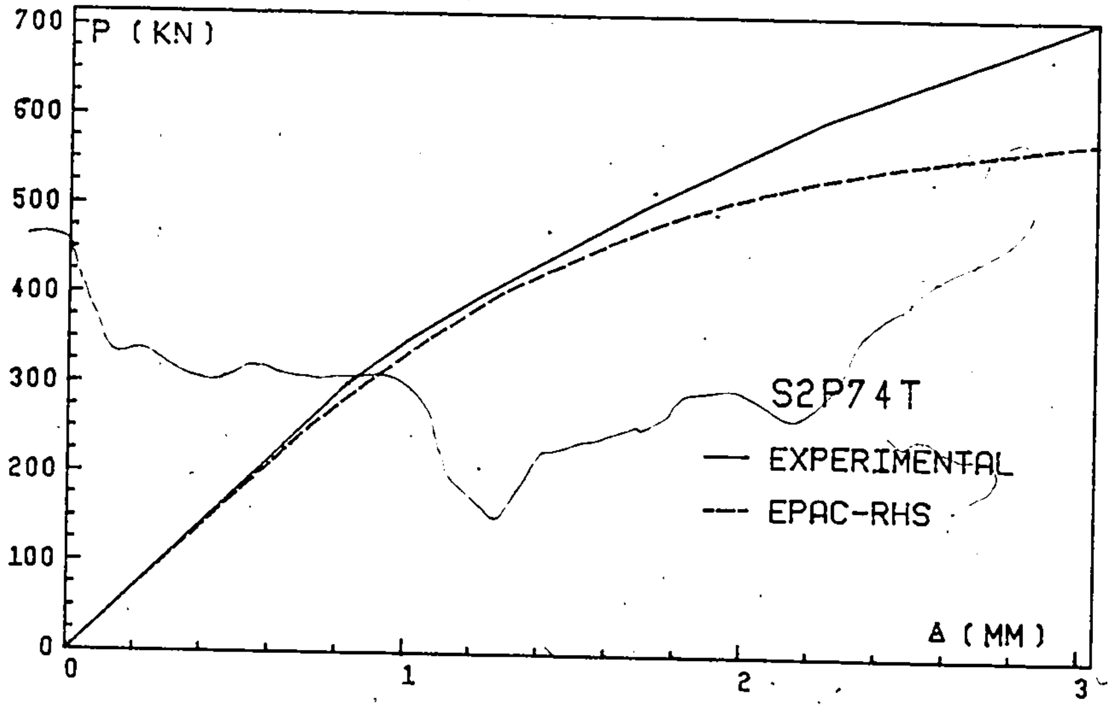

(f)

Figure 7.7 : Comparison of Experiments and EPAC-RHS Model for Group 1 K-Joints

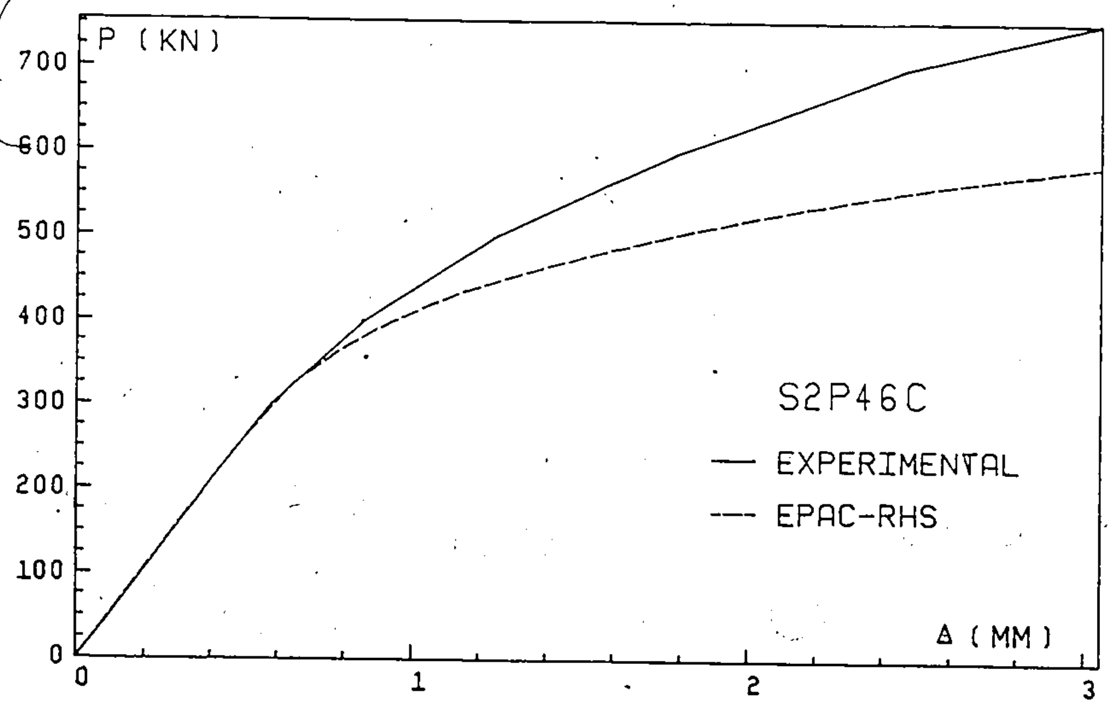
P (KN)
700
600
500
400
300
200
100
0
0
1
2
3
Δ (MM)
S2P46C
EXPERIMENTAL
EPAC-RHS

(a)

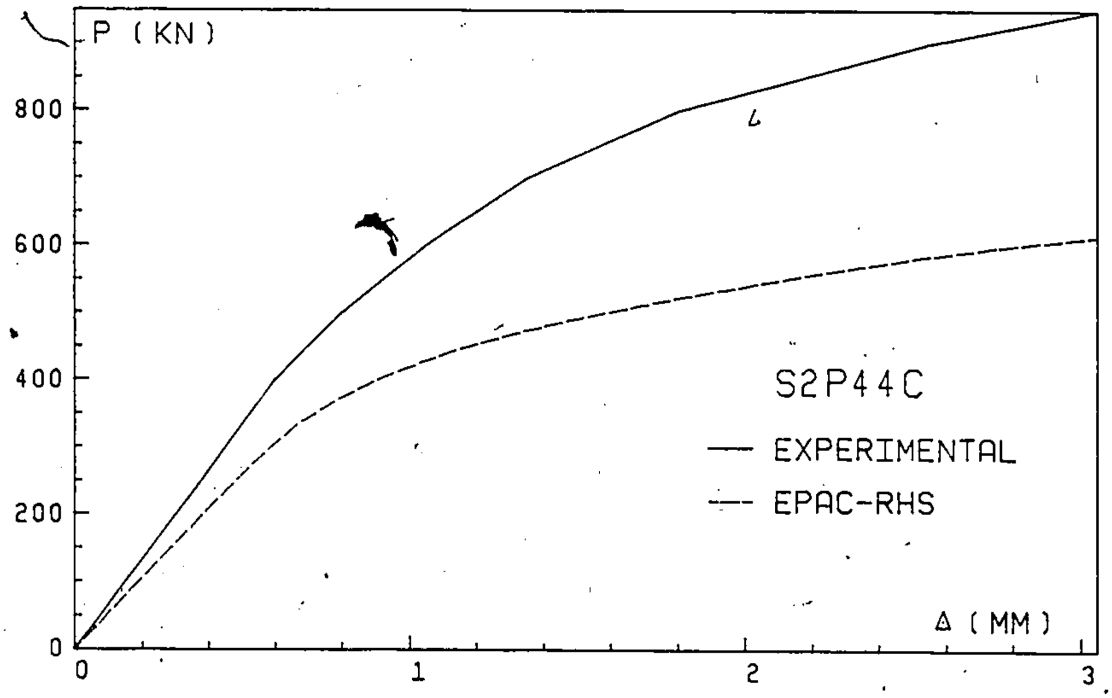
P (KN)
800
600
400
200
0
0
1
2
3
Δ (MM)
S2P44C
EXPERIMENTAL
EPAC-RHS

(b)

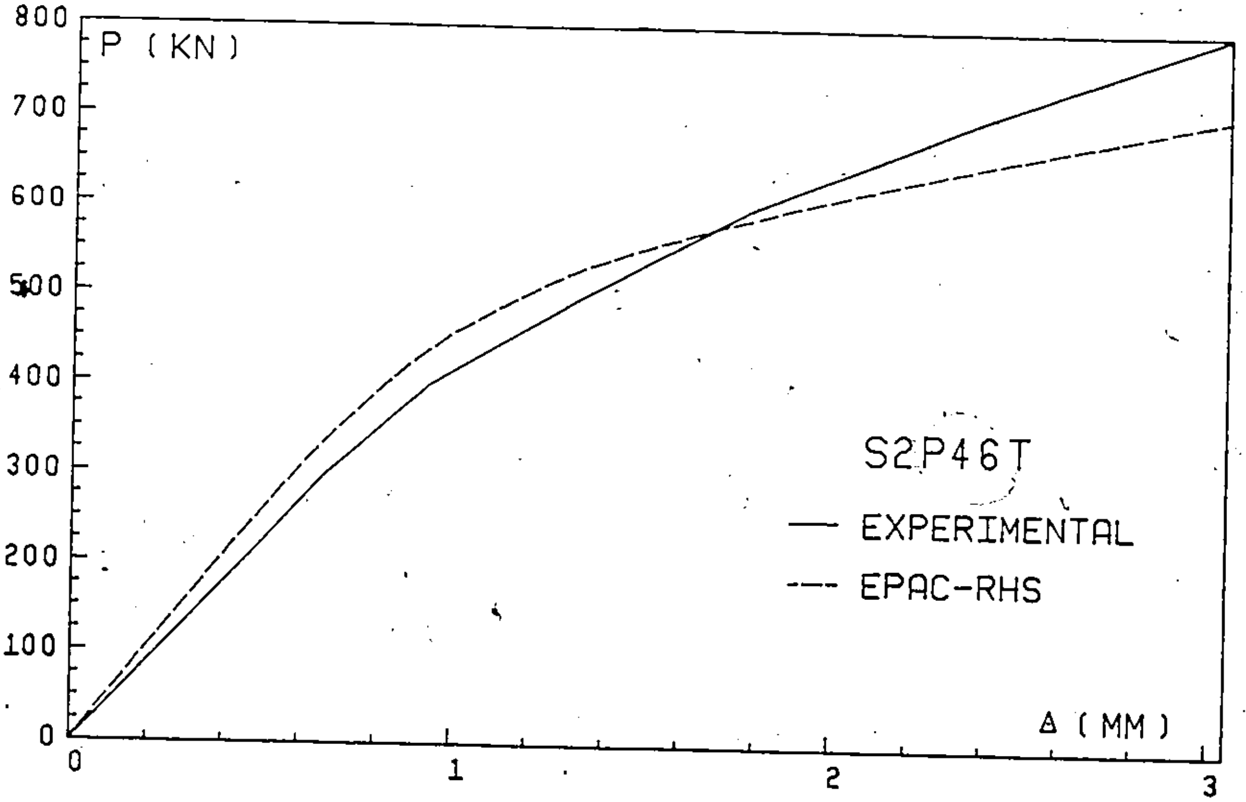

(c)

FIGURE 7.8 : COMPARISON OF EXPERIMENTS AND EPAC-RHS MODEL FOR GROUP 2 K-JOINTS

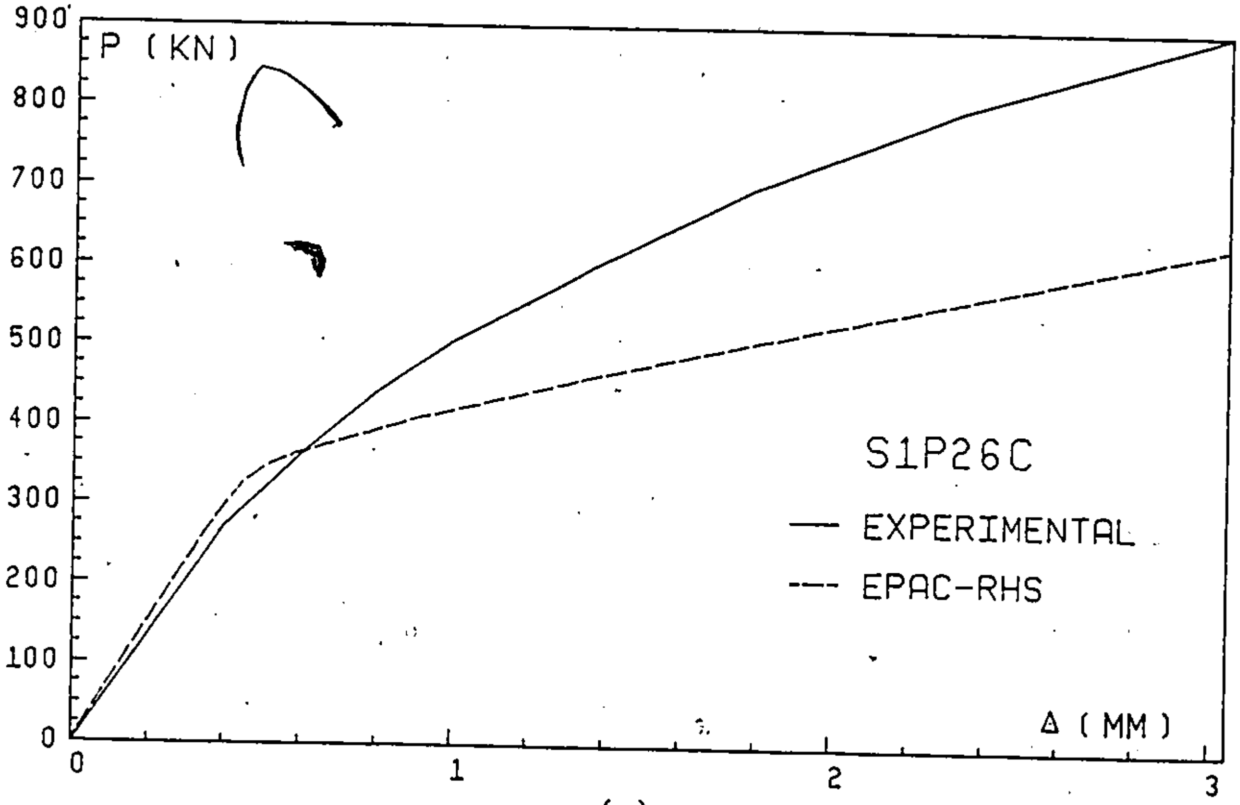

(a)

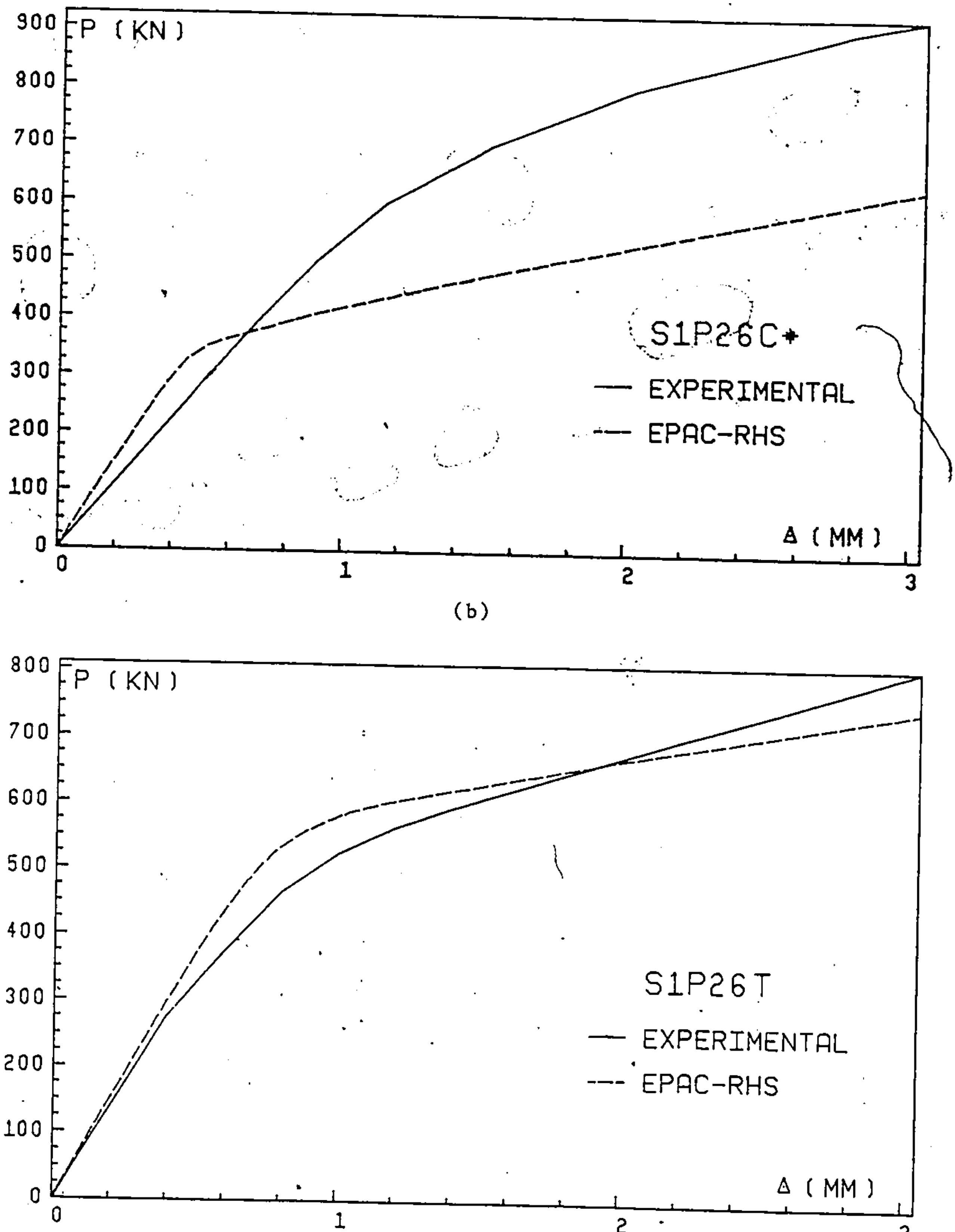

(b)

(c)

FIGURE 7.9 : COMPARISON OF EXPERIMENTS AND EPAC-RHS MODEL FOR GROUP 3 K-JOINTS

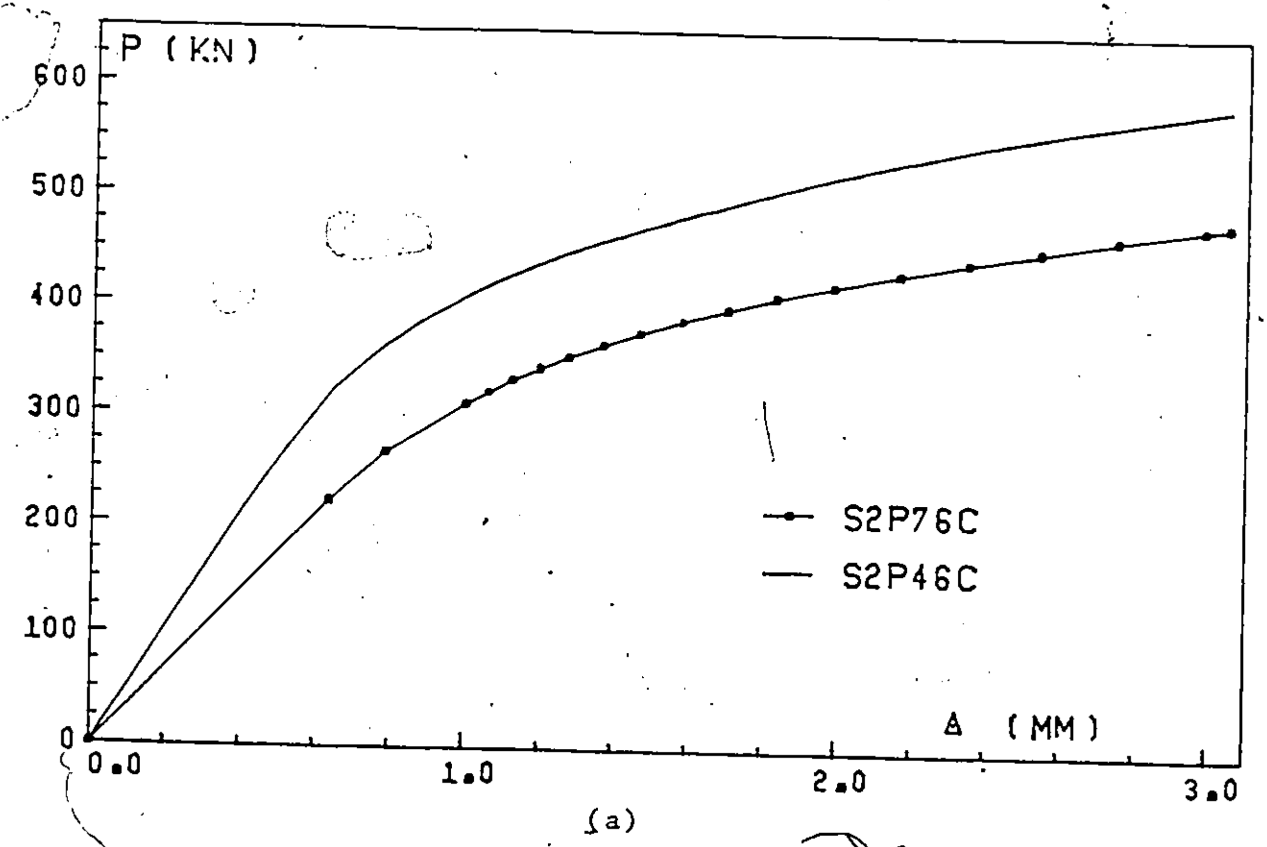

(a)

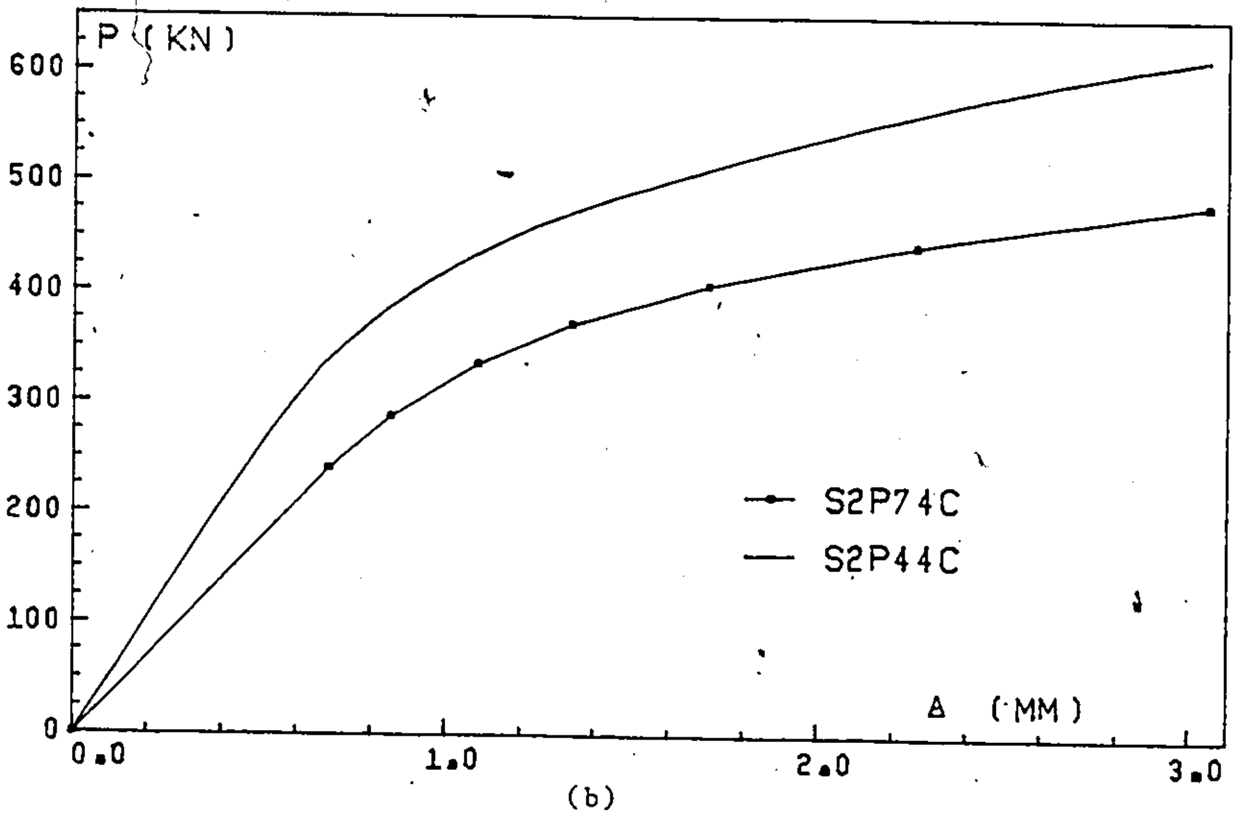

(b)

FIGURE 7.10 : EFFECT OF K-JOINT ECCENTRICITY ON ITS ELASTO-PLASTIC BEHAVIOR

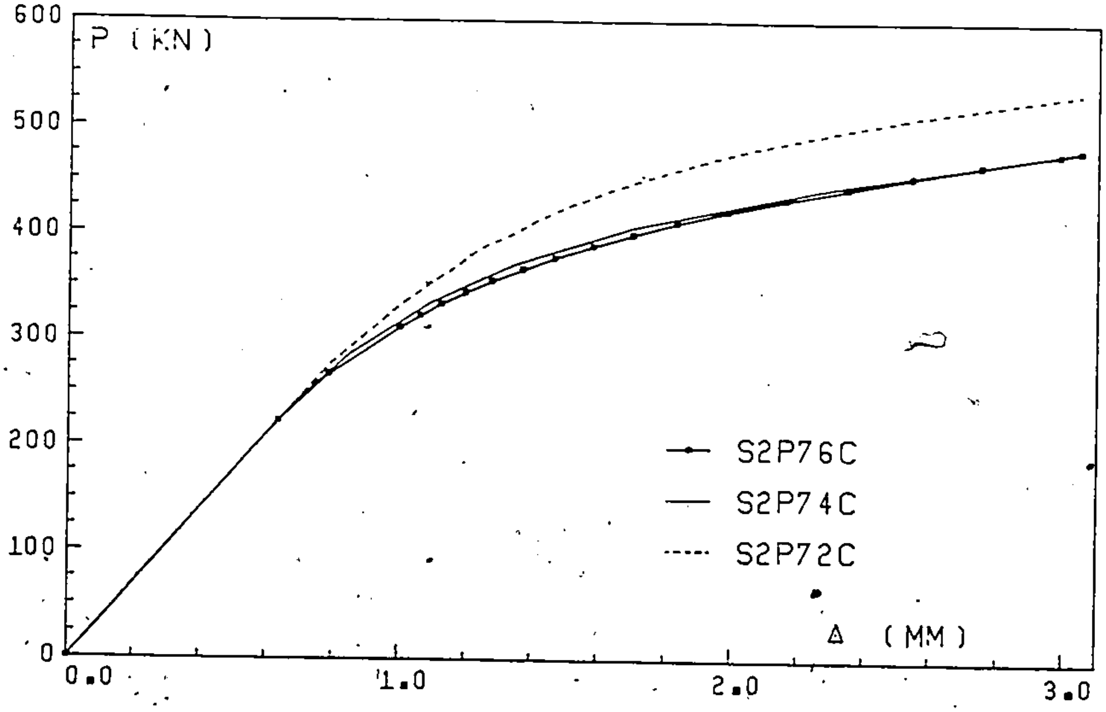

FIGURE 7.11 : EFFECT OF CHORD AXIAL PRELOAD ON THE BEHAVIOUR OF K-JOINT

CHAPTER 8

CONCLUSIONS

8.1 Summary and Conclusions

The research programme presented has aimed at establishing a better understanding of the strength and stiffness characteristics of separated double chord joints employed in truss systems of steel rectangular hollow sections. Due to their flexibilities, such joints may precipitate premature failure and hence disrupt the anticipated function of the truss. In the process of evaluating their strength and behaviour, the notion of the twin member shear beam evolved as a simple means for simulating the shearing action ocurring in double chord gap K or N joints on which the emphasis has been placed.

The main objective of this investigation was then to develop a finite element model for separated double chord RHS joints in steel that would be computationally efficient and yet capable of predicting the behaviour accurately. It was also desirable to cast the developments in a general format that would be applicable to various separated double chord joint configurations.

The finite element model developed in this study involves idealization of the RHS chord member as a thin plate representing the inner web and a channel grillage of beam elements representing the top and bottom flanges and the outer web. The restraining effect of the channel portion on the inner web plate was incorporated through a condensation of the former into a boundary stiffness matrix and augmenting it to the global stiffness matrix of the latter. The model incorporates material nonlinearities of the joint material that is presumed to be isotropic; its plastic behaviour can be adequately described by the Von Mises yield criterion and the associated plastic flow rule. The stress-strain relationship has been idealized by a bilinear behaviour to account for varying degree of strain hardening. Joint deformations are assumed small and hence geometric nonlinearities are neglected. This latter assumption was deemed satisfactory for the range of deformations considered in this study. Furthermore, no account is made either of the weakening effect of residual stresses due to fabrication and weldment or of the stiffening effect of the added weld material itself around the chord-branch member inclusion. The two effects were presumed to cancel one another.

The four node rectangular element, with both in-plane and out-of-plane actions, is employed in discretizing the inner web plate of the joint. While a beam-column element is used in subdividing the channel's cross sections, a combined beam bending-pure shear element is selected in its longitudinal direction, thus resulting in a grillage of beam elements.

To validate the finite element model, it was important to compare predicted joint behaviour and strength with experimental results. As such, a number of experiments were undertaken on twin shear beams with a view to making definitive statements about failure modes and deformation patterns to be anticipated for the finite element model proposed. Twin shear beams formed a simple alternative and enhanced the understanding of the more complex K or N joints which are associated with popular Warren and Pratt truss construction. Twenty-four specimens were tested in the Applied Dynamics Laboratory of McMaster University. As expected, all twin beams failed by shearing action in which a pronounced distortion of their inner webs was exhibited. The amount of deformation of the outer web and flange portions varied according to the selected geometry of the beams. Principally, it was concluded that deep beams with small gap-to-depth ratio exhibit superior performance in terms of strength and stiffness.

In view of the experimental results, a local deflection limit criterion was proposed to provide a unified basis for prescribing the maximum permissible deformation in a separated double chord joint. The criterion, which is also consistent with that described in the literature for single chord joints, suggests that the relative deflection in a gap joint may not exceed 1% $(h_0 + b_0)$. Beyond this limit, gains in strength would be relatively small and inevitably are accompanied by large increments of deflection.

The finite element model was then verified through a comparison of its prediction with twin shear beam experimental results in the range of displacements described above. Correlation between theory and experiments was found to be reasonably good for most of the geometrical configurations analysed. It could therefore be ascertained that the model is promising and could well be extended to truss joint applications. A sensitivity analysis was also carried out on a number of hypothetical twin beams. It was evident that improved behaviour is obtained for larger chord depth and thickness and smaller gap distance. It was also found that changing the branch member geometry or the chord member width had little influence on the behaviour.

An extension of the finite element model was made to the general model called EPAC-RHS (Elasto-Plastic Analysis of RHS Connections). The nonconforming triangular plate bending element and the constant strain triangle were combined for application in the model. With a combination of rectangular and triangular elements, joints with branches arbitrarily positioned could be simulated. In addition, the model accounts for the member preloads. The model was rendered more efficient by introducing the skyline technique to assemble and solve the global system of the inner web. The method of dynamic storage was also employed in the source coding of EPAC-RHS for additional savings on storage.

Relevant experimental data extracted from the literature were compared with EPAC-RHS simulated K-joints. It is concluded from such a comparison that elastic response prediction is very good; however, conservative strength estimates were generally observed at the deflection limit. It may be emphasized that by giving appropriate consideration to the simulation scheme of the inner web - branch member inclusion, it is possible to use EPAC-RHS for the analysis of RHS single, two or three branch member joints of the separated type.

Another aspect of this study involved the use of yield line theory to derive theoretical strength expressions for separated double chord gap joints. In this analysis, the joint material is assumed rigid-perfectly plastic. For loadings transverse to the plate, the effect of shear force on the plastic moment capacity is assumed to be negligible. Furthermore, deflections are small and as such, membrane stresses developed in the plate may be ignored.

With these assumptions, two plastic failure mechanism models, trapezoidal and conical, were proposed for the twin beam. Based upon a comparison with twin shear beam experiments, both models proved satisfactory. Theoretical expressions were then applied to K-joints after making provision to account for chord preloading. Comparison with test results from a previous study was successfully made. It was concluded that both trapezoidal and conical strength models provide a good basis for predicting the deflection limit strength of separated double chord joints of K or N type.

8.2 Suggestions for Future Research

A number of research areas are suggested to broaden the scope of application of the EPAC-RHS model developed in this study. These are:

1. Incorporation of large deformation theory for ultimate strength prediction and identification of failure modes. This would account for tension field action that was observed to develop in the gap spacing of the inner webs and the stretching action in the flanges around the inclusion.

2. Better models for material behaviour such as the trilinear stress-strain model.

On the other hand, to enhance our knowledge about the behaviour of double chord RHS connections, further research is needed in several topics of which the following are suggested.

1. Undertake a study on the effect of residual stresses due to weldments on the joint behaviour. Given their distribution, the locked-in stresses due to welding can be simulated in EPAC-RHS in the form of a preload vector. It is also desirable to determine the effect that weld material itself has as a resisting element by employing thicker elements along the welded portions between the chord and branch members.
2. EPAC-RHS can also be used in an analytical study to search for optimum joint configuration (K or N) leading to minimum stress concentrations at its toes. This can be accomplished by cutting the end of diagonal members at different angles and varying the eccentricities. A comparison of numerical results would then form a basis for selecting the best configuration to be adopted in practice.
3. Another objective to be achieved through the finite element model is the development of characteristic equations to describe the joint behaviour. Such equations can then be incorporated into an elasto-plastic model for truss analysis.
4. Finite element modelling of back-to-back double chord K-

joints is also possible through the present model. In this case, however, the top flange plate would be the candidate for discretization into rectangular and/or triangular plate elements. The channel frame would represent the inner and outer webs and the bottom flange.

APPENDIX A

A.1 Shape Functions for the Retangular Plate Bending Element

If $w = N_{b1}w_1 + N_{b2}\Theta_{x1} + N_{b3}\Theta_{y1} + \dots\ N_{12}\Theta_{y4}$, then

$$N_{b1} = 1-\xi\eta-(3-2\xi)\xi^2(1-\eta)-(1-\xi)(3-2\eta)\eta^2$$

$$N_{b2} = (1-\xi)\eta(1-\eta)^2 b$$

$$N_{b3} = -\xi(1-\xi)^2(1-\eta)a$$

$$N_{b4} = (3-2\xi)\xi^2(1-\eta)+\xi\eta(1-\eta)(1-2\eta)$$

$$N_{b5} = \xi\eta(1-\eta)^2 b$$

$$N_{b6} = (1-\xi)\xi^2(1-\eta)a$$

$$N_{b7} = (3-2\xi)\xi^2\eta-\xi\eta(1-\eta)(1-2\eta)$$

$$N_{b8} = -\xi(1-\eta)\eta^2 b$$

$$N_{b9} = (1-\xi)\xi^2\eta a$$

$$N_{b10} = (1-\xi)(3-2\eta)\eta^2+\xi(1-\xi)(1-2\xi)\eta$$

$$N_{b11} = -\ (1-\xi)(1-\eta)\eta^2 b$$

$$N_{b12} = -\xi(1-\xi)^2\eta a$$

A.2 Shape Functions for the Rectangular Plane Stress Element

$$N_{p1} = (1-\xi)(1-\eta)$$

$$N_{p2} = \xi(1-\eta)$$

$$N_{p3} = \xi\eta$$

$$N_{p4} = (1-\xi)\eta$$

A.3 Shape Functions for the Boundary Spring Element

$$\underset{6\times 40}{[N^*]} = \begin{bmatrix} \underset{3\times 20}{[N_{sp}]} & \underset{3\times 20}{[0]} \\ \underset{3\times 20}{[0]} & \underset{3\times 20}{[N_{sp}]} \end{bmatrix}$$

where

$$[N_{sp}] = \left[\begin{array}{cccccccccccccccccccc} 0 & N_{p_1} & 0 & 0 & 0 & 0 & N_{p_2} & 0 & 0 & 0 & 0 & N_{p_3} & 0 & 0 & 0 & 0 & N_{p_4} & 0 & 0 & 0 \\ 0 & 0 & N_{b_1} & N_{b_2} & N_{b_3} & 0 & 0 & N_{b_4} & N_{b_5} & N_{b_6} & 0 & 0 & N_{b_7} & N_{b_8} & N_{b_9} & 0 & 0 & N_{b_{10}} & N_{b_{11}} & N_{b_{12}} \\ 0 & 0 & N_{r_1} & N_{r_2} & N_{r_3} & 0 & 0 & 0 & 0 & 0 & 0 & 0 & N_{r_7} & N_{r_8} & N_{r_4} & 0 & 0 & N_{r_{10}} & N_{r_{11}} & N_{r_{12}} \end{array}\right]$$

where N_{bi} and N_{pi} are defined in Sections A.1 and A.2, respectively. The shape functions N_{ri} correspond to Θ_x and can be obtained using Equation 5.6. These are:

$$N_{r1} = \frac{1}{b}\,[-\xi + \xi^2(3-2\xi) - 6(1-\xi)\eta(1-\eta)]$$

$$N_{r2} = (1-\xi)(1-\eta)(1-3\eta)$$

$$N_{r3} = \frac{a}{b}\,\xi(1-\xi)^2$$

$$N_{r4} = \frac{1}{b}\,[-\xi^2(3-2\xi) + \xi(1-2\eta)^2 - 2\xi\eta(1-\eta)]$$

$$N_{r5} = \xi(1-\eta)(1-3\eta)$$

$$N_{r6} = -\frac{a}{b}\,\xi^2(1-\xi)$$

$$N_{r7} = -N_{r_4}$$

$$N_{r8} = \xi[\eta^2 - 2\eta(1-\eta)]$$

$$N_{r9} = N_{r6}$$

$$N_{r10} = \frac{1}{b}\,[\xi(1-\xi)(1-2\xi) + 6(1-\xi)\eta(1-\eta)]$$

$$N_{r11} = (1-\xi)[\eta^2 - 2\eta(1 - \eta)]$$

$$N_{r12} = -N_{r3}$$

APPENDIX B

B.1 Shape Functions for the Triangular Plate Bending Element (Ref. 34)

If $w = N_{b_1} w_1 + N_{b_2} \Theta_{x_1} + N_{b_3} \Theta_{y_1} + \ldots\ldots N_{b_9} \Theta_{y_3}$, then

$$N_{b_1} = L_1 + L_1^2 L_2 + L_1^2 L_3 - L_1 L_2^2 - L_1 L_3^2$$

$$N_{b_2} = b_3 (L_1^2 L_2 + \tfrac{1}{2} L_1 L_2 L_3) - b_2 (L_3 L_1^2 + \tfrac{1}{2} L_1 L_2 L_3)$$

$$N_{b_3} = c_3 (L_1^2 L_2 + \tfrac{1}{2} L_1 L_2 L_3) - c_2 (L_3 L_1^2 + \tfrac{1}{2} L_1 L_2 L_3)$$

$$N_{b_4} = L_2 + L_2^2 L_3 + L_2^2 L_1 - L_2 L_3^2 - L_2 L_1^2$$

$$N_{b_5} = b_1 (L_2^2 L_3 + \tfrac{1}{2} L_1 L_2 L_3) - b_3 (L_1 L_2^2 + \tfrac{1}{2} L_1 L_2 L_3)$$

$$N_{b_6} = c_1 (L_2^2 L_3 + \tfrac{1}{2} L_1 L_2 L_3) - c_3 (L_1 L_2^2 + \tfrac{1}{2} L_1 L_2 L_3)$$

$$N_{b_7} = L_3 + L_3^2 L_1 + L_3^2 L_2 - L_3 L_1^2 - L_3 L_2^2$$

$$N_{b_8} = b_2(L_3^2L_1 + \frac{1}{2}L_1L_2L_3) - b_1(L_2L_3^2 + \frac{1}{2}L_1L_2L_3)$$

$$N_{b_9} = c_2(L_3^2L_1 + \frac{1}{2}L_1L_2L_3) - c_1(L_2L_3^2 + \frac{1}{2}L_1L_2L_3)$$

where

$$b_i = y_j - y_k$$

and $c_i = x_k - x_j$.

The suffices i,j and k take up the value of 1-2-3 respectively in cyclic order.

B.2 Transformation between Bending Slopes and Triangular Element Nodal Displacements (Ref. 41)

$$\begin{bmatrix}
\frac{c_1}{2\Delta} & 1 & 0 & \frac{c_2}{2\Delta} & 0 & 0 & \frac{c_3}{2\Delta} & 0 & 0 \\
\frac{-b_1}{2\Delta} & 0 & 1 & \frac{-b_2}{2\Delta} & 0 & 0 & \frac{-b_3}{2\Delta} & 0 & 0 \\
\frac{c_1}{2\Delta} & 0 & 0 & \frac{c_2}{2\Delta} & 1 & 0 & \frac{c_3}{2\Delta} & 0 & 0 \\
\frac{-b_1}{2\Delta} & 0 & 0 & \frac{-b_2}{2\Delta} & 0 & 1 & \frac{-b_3}{2\Delta} & 0 & 0 \\
\frac{c_1}{2\Delta} & 0 & 0 & \frac{c_2}{2\Delta} & 0 & 0 & \frac{c_3}{2\Delta} & 1 & 0 \\
\frac{-b_1}{2\Delta} & 0 & 0 & \frac{-b_2}{2\Delta} & 0 & 0 & \frac{-b_3}{2\Delta} & 0 & 1
\end{bmatrix}$$

B.3 Matrix $[\bar{B}]$ of Triangular Plate Bending Element (Ref. 42)

The matrix $[\bar{B}]$ is 7 × 6 in size and can be defined in terms of six submatrices as follows.

$$[\bar{B}] = [\{BX\}^{(1)}\{BY\}^{(1)}\{BX\}^{(2)}\{BY\}^{(2)}\{BX\}^{3}\{BY\}^{3}]\ldots \qquad (B.1)$$

Each submatrix is 7 × 1 and has an ℓ^{th} entry of

$$(BX)_\ell^{(i)} = X_\ell^{(i)} \cdot b_k - Y_\ell^{(i)} \cdot b_j + E_\ell \cdot F^{(i)}$$

or (B.2)

$$(BY)_\ell^{(i)} = X_\ell^{(i)} \cdot c_k - Y_\ell^{(i)} \cdot c_j + E_\ell \cdot G^{(i)}$$

where $(i) = 1,2,3$

and $\ell = 1,2,\ldots 7.$

Therefore, twenty-one expressions are needed to define E_ℓ, $X_\ell^{(i)}$ and $Y_\ell^{(i)}$ (7 each). The E_ℓ functions are:

$$E_1 = a \sum_{i=1,3} (b_i b_j)$$

$$E_2 = a \sum_{i=1,3} (c_i b_j + b_i c_j)$$

$$E_3 = a \sum_{i=1,3} (c_i c_j)$$

$$E_4 = b_i b_j b_k$$

$$E_5 = \sum_{i=1,3} c_i b_j b_k$$

$$E_6 = \sum_{i=1,3} c_i c_j b_k \qquad (B.3)$$

$$E_7 = c_i c_j c_k$$

where $a = 1.5\ \Delta$ and i,j and k are assumed to take up the values 1-2-3 respectively in cyclic order. The formulae for $X_\ell^{(i)}$ are:

$$X_1^{(i)} = b_i^2 a + 2ab_i b_j$$

$$X_2^{(i)} = 2b_i c_i a + 2b_j c_i a + 2b_i c_j a$$

$$X_3^{(i)} = c_i^2 a + 2ac_i c_j$$

$$X_4^{(i)} = b_i^2 b_j \qquad (B.4)$$

$$X_5^{(i)} = 2b_i c_i b_j + b_i^2 c_j$$

$$X_6^{(i)} = c_i^2 b_j + 2b_i c_i c_j$$

$$X_7^{(i)} = c_i^2 c_j,$$

and those for $Y_\ell^{(i)}$ are given by:

$$Y_1^{(i)} = b_i^2 a + 2ab_i b_k$$

$$Y_2^{(i)} = 2b_i c_i a + 2b_k c_i a + 2b_i c_k a$$

$$Y_3^{(i)} = c_i^2 a + 2ac_i c_k$$

$$Y_4^{(i)} = b_i^2 b_k \tag{B.5}$$

$$Y_5^{(i)} = 2b_i c_i b_k + b_i^2 c_k$$

$$Y_6^{(i)} = c_i^2 b_k + 2b_i c_i c_k$$

$$Y_7^{(i)} = c_i^2 c_k.$$

The six functions $F^{(i)}$ and $G^{(i)}$ (3 each) can be condensed as

$$F^{(i)} = (b_k - b_j)/2$$

$$G^{(i)} = (c_k - c_j)/2. \tag{B.6}$$

BIBLIOGRAPHY

[1] Korol, R.M. and Chidiac, M.A., K-Joints of double chord square hollow sections. Can. Jour. Civ. Eng., Vol. 7, No. 3, 1980, pp. 523-539.

[2] Chidiac, M.A., K-Joints of double chord hollow sections. Ph.D. Thesis, McMaster University, Canada, 1979.

[3] Chidiac, M.A. and Korol, R.M., Rectangular Hollow Section Double Chord T-Joints; Technical Note, Jour. Struct. Div., ASCE, Vol. 105, No. ST8, 1979, pp. 1717-1721.

[4] Korol, R.M., El-Zanaty, M. and Brady, F-J., Unequal width connections of square hollow sections in Vierendeel trusses, Can. Jour. Civ. Eng., Vol. 4; No. 2, 1979, pp. 190-201.

[5] Korol, R.M. and Keen, R.G., Parametric study of standard RHS double chord K-joints. Can. Jour. Civ. Eng., Vol. 8, No. 4, 1981, pp. 456-463.

[6] Chiu, E.C., Experimental and Analytical Investigation of Double Chord HSS trusses. M. Eng. Thesis, McMaster University, 1982.

[7] Korol, R.M.; Mirza, F.A. and Chiu, E.C., An investigation into the behaviour of double chord HSS trusses. CIDECT Report, 1982.

[8] Korol, R.M.; Mirza, F.A. an Chiu, E.C., An experimental investigation of double chord HSS trusses. Can. Jour. Civ. Eng., Vol. 10, 1983, pp. 248-260.

[9] Korol, R.M., Mirza, F.A. and Chiu, E.C., Predicting the behaviour of HSS double chord trusses - a comparison with test results. Can. Jour. Civ. Eng., Vol. 10, 1983, pp. 261-270.

[10] Shehata, A.A., Finite element modelling and elasto plastic analysis of RHS double chord T-joints. Ph.D. Thesis, McMaster University, 1983.

[11] Mirza, F.A.; Shehata, A.A. and Korol, R.M., Modelling of double chord rectangular hollow section T-joints by finite element method. Computers and Structures, Vol. 15, No. 2, 1982, pp. 123-129.

[12] Mouty, J., Calcul des charges ultimes des assemblages soudes de profils creux carres et rectangulaires. Construction Metallique, No. 2, June 1976, pp. 37-58.

[13] Redwood, R.G., The behaviour of joints between rectangular hollow structural members. Civil Eng. and Public Works Review,

October 1965, pp. 1463-1469.

[14] Korol, R.M. and Mansour, M.H., Theoretical analysis of haunch reinforced T-joints in square hollow sections. Can. Jour. Civ. Eng., Vol. 6, No. 4, 1979, pp. 601-609.

[15] El-Hifnawy, L., Elasto-plastic finite element analysis of rectangular hollow section T-joints. M. Eng. Thesis, McMaster University, 1980.

[16] Korol, R.M. and Mirza, F.A., Finite element analysis of RHS T-joints. Jour. Struct. Div., ASCE, Vol. 108, No. ST9, September 1982, pp. 2081-2098.

[17] Ostrowski, P., Finite element modelling of single chord gap K-joints. M. Eng. Thesis, McMaster University, 1984.

[18] Packer, J.A.; Korol, R.M.; Mirza, F.A. and Ostrowski, P., A finite element study of the flexibility of rectangular hollow section truss gapped K-joints. Proc. Ninth Australian Conf. on the Mechanics of Structures and Materials, Sydney, August 29-31, 1984.

[19] Wood, R.H., Plastic and elastic design of slabs and plates. Ronald Press Co., New York, N.Y., 1961.

[20] Johansen, K.W., Yield line theory. Cement and Concrete Assoc., London, 1962.

[21] Jubb, J.E.M. and Redwood, R.G., Design of joints to box sections. Instn. of Struct. Eng. Conf. on Industrialized Buildings, London, May 17-19, 1966.

[22] Patel, N.M., Punching Shear characteristics of RHS joints. ASCE National Structural Eng. Meeting, San Francisco, April 9-13, 1973.

[23] Davies, G. and Roper, C.G., Gap joints with tubular members - A yield line approach. Building Science, Vol. 10, 1975, pp. 199-205.

[24] Davies, G. and Roper, C.G., Gap joints with tubes - A yield line modified by shear approach. Building and Environment, Vol. 12, 1977, pp. 31-38.

[25] Packer, J.A.; Davies, G. and Coutie, N.G., Ultimate strength of gapped joints in RHS trusses. Jour. Struct. Div., ASCE, Vol. 108, No. ST2, February 1982, pp. 411-429.

[26] Korol, R.M.; Mitri, H.S. and Mirza, F.A., Plate reinforced square hollow section T-joints of unequal width. Can. Jour. Civ. Eng., Vol. 9, No. 2, June 1982, pp. 143-148.

[27] Korol, R.M. and Mitri, H.S., Strength analysis of RHS double

chord connection. Ninth Canadian Cong. for Appl. Mech., Saskatoon, June 1-2, 1983, pp. 201-202.

[28] Mitri, H.S. and Korol, R.M., The strength of beam-to-staggered column connections of rectangular hollow sections. Int. Jour. Mech. Sci., October 1984, 11 pp.

[29] Johnson, W., Upper bounds to the load for the transverse bending of flat rigid-perfectly plastic plates. Int. Jour. Mech. Sci., Vol. 11, 1969.

[30] Lau, W. C-P. and Dawe, J.L., Elasto-plastic finite element analysis of welded truss connections. Can. Jour. Civ. Eng., Vol. 9, 1982, pp. 399-412.

[31] Strömmen, Z.N., Ultimate strength of welded K-joints of rectangular setions. Norwegian Inst. of Tech., Div. of Steel Struct., 1983.

[32] Galambos, T.V., Structural members and frames. Prentice-Hall, Englewood Cliffs, N.J., 1968.

[33] Prezemieniecki, J.S., Theory of matrix structural analysis. McGraw-Hill Book Co., 1968.

[34] Zienkiewicz, O.C., The finite element method, McGraw-Hill Book Co., 3rd ed., 1977.

[35] Mendelson, A., Plasticity-theory and applications. MacMillan, 1968.

[36] Yamada, Y.; Yishimura, N. and Sakurai, T., Plastic stress-strain matrix and its application for the solution of elastic-plastic problems by the finite element method. Int. Jour. Mech. Sci., Vol. 10, 1968, pp. 343-354.

[37] Zienkiewicz, O.C.; Valliappen, S. and King, I.P., Elastic-plastic solutions of engineering problems. Initial stress, finite element approach. Int. Jour. Num. Meth. Eng., Vol. 1, 1968, pp. 75-100.

[38] Timoshenko, S.P. and Goodier, J.N., Theory of elasticity. McGraw Hill Book Co., 3rd ed., 1970.

[39] Cook, R.D., Concepts and applications of finite element analysis. John Wiley and Sons Inc., 1974.

[40] Bathe, K-J., Finite Element Procedures in Engineering Analysis. Prentice-Hall, Inc., New Jersey, 1982.

[41] Bazeley, G.P., Cheung, Y.K.; Irons, B.M. and Zienkiewicz, O.C., Triangular elements in plate bending - conforming and nonconforming solutions. Proc. Conf. Matrix Methods in Structural

Mechanics, Wright-Patterson Air Force Base, Ohio, 1965, pp. 547-572.

[42] Cheung, Y.K.; King, I.P. and Zienkiewicz, O.C., Slab bridges with arbitrary shape and support conditions: a general method of analysis based on finite elements. Proc. Inst. Civ. Eng., Vol. 40, 1968, pp. 9-37.

[43] Bathe, K-J. and Cimento, A.P., Some practical procedures for the solution of nonlinear finite element equations. Comp. Meth. in Appl. Mech. and Eng., Vol. 22, 1980, pp. 59-85.

[44] Irons, B.M. and Tuck, R.C., A version of the Aitken accelerator for computer iteration. Int. Jour. Num. Meth. in Eng., Vol. 1, 1969, pp. 275-277.

[45] Stanton, E.L. and Schmit, L.A., A discrete element stress and displacement analysis of elastoplastic plates. AIAA, Vol. 8, No. 7, 1970, pp. 1245-1251.

[46] Basler, K., Strength of plate girders in shear. Jour. Struct. Div. ASCE, Vol. 97, No. ST7, 1961, pp. 151-180.

[47] Mitri, H.S.; Mirza, F.A. and Korol, R.M., Program EPAC-RHS: Elasto-plastic analysis of RHS connections. Dept. Civil Eng., McMaster University, Report No. 84-5, 1984, 86 pp.